Mesoscale Wind and Temperature Changes over Peatlands of the Hudson Bay Lowlands: Impacts on the Surface Energy Balance and Net CO_2 Exchange

OLALEKAN BALOGUN

A dissertation submitted to the Faculty of Graduate Studies
in partial fulfilment of the requirements for the Degree of Doctor of Philosophy

Graduate Program in Geography

York University

Toronto, Ontario

November 2021

Abstract

Although northern peatlands in general are currently a net carbon sink, there is still considerable uncertainty in the long-term combined response of plant productivity and ecosystem respiration to global warming and moisture changes. The Hudson Bay Lowlands (HBL) region of Canada is the second largest peat-accumulating complex in the world that is strongly influenced by the cold air masses originating off the Hudson Bay. Recent warming has caused observed changes in the sea ice dynamics and energy budget of the Hudson Bay, yet it is presently unknown how these climatic changes in the Bay will impact the surface energy and carbon balance of the adjacent HBL. As a globally significant peatland carbon pool, the HBL will play an important role in future climate warming and permafrost carbon feedback. The primary aim of this study is to improve our understanding of the warming-induced changes in the advective influence of the Hudson Bay and its linkage to the changes in the surface energy and carbon balance over peatlands of the HBL. I use a combined model and assimilated climate dataset to investigate the mesoscale wind and temperature changes in the HBL and their impacts on the surface energy balance (1979–2018). Furthermore, I employ a satellite data-driven light-use efficiency model, calibrated and validated with eddy covariance tower measurements at a fen and bog to examine the response of net ecosystem CO_2 exchange to climatic changes (2000–2019). The results reveal that differential rates of warming between offshore and onshore winds have produced significant changes in the advective role of the Hudson Bay as evident in the increased frequency and strength of onshore winds. Also, the results show contrasting net CO_2 exchange between the fen and bog sites. The anomalies in gross primary production and ecosystem respiration were associated with strong trends in temperature and moisture, and the Hudson Bay had a more pronounced advective influence on peatland respiration than photosynthesis.

"The fastest runner doesn't always win the race, and the strongest warrior doesn't always win the battle. The wise sometimes go hungry, and the skillful are not necessarily wealthy. And those who are educated don't always lead successful lives. It is all decided by chance, by being in the right place at the right time."

—The Teacher (Ecclesiastes 9:11)

Dedication

First: To my parents, Mr. Nosiru Adetola and Mrs. Esther Oluranti Balogun

Second: To humankind, in hopes that—in your foolishness—you will not destroy the planet. And yourselves

Acknowledgements

Dr. Richard Bello and Dr. Kaz Higuchi—my supervisors, mentors and academic fathers. I am deeply grateful for all you have done.

Yvonne Yim—you are so amazing. Thank you for always being there for me.

Prof. Kathy Young—you have taught me a lot about teaching and research. Thank you for supporting me throughout this journey.

Dr. Tarmo Remmel, Dr. Ranu Basu, Dr. Jennifer Korosi, Dr. Joseph Mensah, Dr. Patricia (Ellie) Perkins and Dr. Roderick MacRae—you inspired me much more than you know.

Dr. Huaiping Zhu and Dr. Peter Lafleur—thank you for your constructive feedback.

Hanis, K., Tenuta, M., Amiro, B., Papakyriakou, T., Helbig, M., Humphreys, E., Todd A., Zhang, Y., and Hilton, T.—I couldn't have done this research without your datasets. Thank you.

LeeAnn Fishback, the Churchill Northern Studies Centre and the Town of Churchill, Manitoba—I look forward to seeing you (and the polar bears) again.

Dr. Christiana Egbinola, Dr. Olutoyin Fashae, Dr. Adeniyi Gbadegesin, Prof. Ayoade and Prof. Aweto—I would not have embarked on this journey without your help. Thank you.

Aunty Maggie, Melody Duggan, Shandana Khan, Rosa Pereira, Connie Ko and Laura Walton—you are the nicest people I know.

Tasnuva (Belle) Rashid, Kimisha Ghunowa, Ryan Rimas, Katerina Sofos, Devin Ali, Ratiba Munir and Patrick Mojdehi—the lightning lab would not have been the same without you!

Vivien Bediako, DMoi Keen, Mandy Huynh, Yolanda Weima, Tewodros Asfaw, Lord-Emmanuel Achidago and Rachael Abulu—I appreciate your friendship.

Jarren Richards, Aida Afrazeh, Rosanna Chowdhury and Justin Podur—the EUC dream team. I can basically work for free just for you all!

Ayo Mbah, Mumsy Dara and Uncle Ade Ayoola, Queen Iroko, Victoria and Wale Ajayi, Anjola Oluwole-Rotimi, Senator Femi Adekoya and Tosin Adegboyega—Friends in High Places.

Rex Agbajor (Bishop) and Ousmane Balde (Mountain Vanisher)—possibly two of the greatest thinkers of our time. Mr. Fresh, it is a Banana Republic after all.

Oluwatosin Faith Olagesin—Nita, you will always be his gift of grace to me.

Desiree Musa, Ekemini Etim, Seyi Jegele, Mofe Olagesin, Debbi Dada and Emmanuel Adeyemo—I care about you more than you know.

Daniel Generation (D~GEN)—you have won your battle with the world.

Dr. Amos and Maama Eyitayo Dada, P. Emmanuel and Aunty Abiodun Ojo—the teachers and shepherds that keep watch over my soul.

Dcn. Omolara Ajayi and the boys (Anjola and Nifemi), Mummy Owaseye, Sis. Susan Olaborede, Dcn. Funmi Olagesin and Dcn. Bolanle Oluwole-Rotimi—I sincerely appreciate you.

Wasiu Afolabi, Johnson Ahmed, Yemi Ogunmola, Adeyinka Gbadebo, Amobi Amanambu and Tomilola Olatinwo—I know you have always got my back.

David Cheung, Asem Azar, Dongdong (Daniel) Li and Luyuan (Richard) Li—thank you for giving me a home away from home.

Mr. Walter (Wally) Hopkins—my Canadian dad and elderly friend. You are one of the kindest humans on the planet.

Aunty Mosun Victoria Adesina, Mrs. Evelyn Tilley, and Mr. and Mrs. Awolusi—beloved citizens of the city that has no need of sun or moon. You are always in my heart.

Dr. Tunji Odubela, Olawale Balogun, Damilola Babalola, Seun Babalola, Kolade and Femi Kalejaye, and the Adesinas (Ayo, Bayo, Gbolawa and Ola)—I miss you all so much.

Engr. Kole and Mrs. Raolat Ayoola (Aunti mi) Kalejaye, and Aunty Kemi (née Awolusi)—thank you for your support and encouragement.

Kolawole and Modupeola Balogun, Michael and Abimbola Michael-Taiwo, and Adebowale and Olufunke Awojide—you gave me the strength that I needed throughout this journey.

Monjola, Monjore, Monjayo, Titilayomi, AyoOluwa, Emmanuel, Sharon, Tamilore and Tomi—you have made me the world's happiest uncle. I love you so much.

Mr. Nosiru Adetola and Mrs. Esther Oluranti Balogun—I couldn't have achieved this without your unwavering love and encouragement. Thank you for believing in me.

The People of Saturn—waiting does not diminish us, any more than waiting diminishes a pregnant mother. We are enlarged in the waiting.

Jasper and Sapphire—I loved you before you were formed.

Princess Adaline Caspirelle—my love for you is eternal.

King Melchizedek (and his order), king of Salem, ruler of justice and mediator of the new covenant—may your kingdom know no end.

Table of Contents

List of Tables

List of Figures

Acronyms

EC	Eddy Covariance
ER	Ecosystem Respiration
ET	Evapotranspiration
EVI	Enhanced Vegetation Index
GPP	Gross Primary Production
HBL	Hudson Bay Lowlands
LSWI	Land Surface Water Index
LUE	Light Use Efficiency
MBE	Mean Bias Error
MODIS	Moderate Resolution Imaging Spectroradiometer
NARR	North American Regional Reanalysis
NDVI	Normalized Difference Vegetation Index
NEE	Net Ecosystems Exchange
OCO-2	Orbiting Carbon Observatory-2
OFF	Offshore Winds originating from Inland
ON	Onshore Winds originating from the Hudson Bay
PAR	Photosynthetically Active Radiation
PFT	Plant Functional Type
Q_E	Latent Heat Flux
Q_G	Ground Heat Flux
Q_H	Sensible Heat Flux
RMSE	Root Mean Square Error
SIF	Solar-Induced Chlorophyll Fluorescence
TSA	Theil-Sen Slope Approach
VPD	Vapour Pressure Deficit
VPRM	Vegetation Photosynthesis and Respiration Model

Chapter 1

Introduction

1.1 Background

1.1.1 Climatic Changes in Arctic and Subarctic Regions

Greenhouse gases such as water vapour, carbon dioxide (CO_2), methane (CH_4), and nitrous oxide (N_2O) help regulate the Earth's temperature due to their ability to absorb and trap heat in the atmosphere. The greenhouse gases play a vital role in the sustenance of life on the Earth, maintaining an average global surface air temperature of about 15 °C. Without this so-called "natural greenhouse effect", the earth would be much colder with an average temperature of about -18 °C. However, the rise in the atmospheric concentration of greenhouse gases since the mid-19th century due to the burning of fossil fuels, agriculture and urbanization, has resulted in unprecedented warming of the atmosphere and terrestrial ecosystems (Shukla et al., 2019). The globally averaged temperature over land for the period 1880–2018 have increased by 1.41 °C (Jia et al., 2019), which is primarily attributable to the anthropogenic greenhouse effect. The rise in air temperatures has varied considerably across regions of the world.

Warmer temperatures have led to a dramatic reduction in snow cover and sea ice extent in the Arctic and Subarctic region, reducing the Earth's surface albedo and amplifying the rate of warming (Derksen et al., 2018; Mudryk et al., 2018). In addition to the positive snow- and sea ice-albedo feedback, the Arctic amplification is also produced by aerosol concentration changes and black carbon deposits on snow or ice (Shindell and Faluvegi, 2009), changes in arctic cloud feedback and water vapour content (Vavrus, 2004; Graversen and Wang 2009), and the poleward atmospheric and oceanic heat transport from lower latitudes (Spielhagen et al., 2011). Research studies have shown that temperature trends in the high-latitudes have been higher than trends for the northern hemisphere as a whole (van Wijngaarden, 2008; Serreze and Barry, 2011; Walsh et al., 2011), and the Arctic has warmed over twice as much as the global average (Screen and Simmonds, 2010; Cowtan and Way, 2013). The warming-induced changes in the Arctic and Subarctic have impacted the soil thermal dynamics, freeze-thaw regimes, and permafrost carbon stability (Euskirchen et al., 2006; Fan et al., 2013).

1.1.2 Terrestrial Ecosystems and the Global Carbon Cycle

The growth rate of atmospheric greenhouse gases, particularly CO_2 and CH_4 is determined by anthropogenic sources (e.g. fossil fuel combustion and land-use change) and natural sinks (e.g. ocean and land ecosystems). Long-term measurements of atmospheric CO_2 concentrations indicate that the upward secular trend in CO_2 is produced primarily by fossil fuel burning, while the presence of a seasonal cycle is due to photosynthetic-decay processes of the terrestrial biosphere (Keeling et al., 1976; Keeling et al., 1989). The current capacity of North American terrestrial ecosystems to absorb more CO_2 and offset some of the human emissions is not guaranteed to persist into the future. The net ecosystem carbon (C) exchange (NEE) depends on the balance between gross primary production (GPP, which removes C from the atmosphere) and ecosystem respiration (ER, which releases C to the atmosphere). Organic carbon is stored on land by living vegetation biomass (450–650 Pg C; Prentice et al., 2001), dead organic matter in litter and soils (1500–2400 Pg C; Batjes, 1996), wetlands (300–700 Pg C; Bridgham et al., 2006) and permafrost soils (~1700 Pg C; Tarnocai et al., 2009).

There is a strong relationship between climate and terrestrial ecosystems, and the exchange of carbon between the land and atmosphere plays an important role in the global climate. Changes in the climate influence vegetation dynamics and ecosystem processes, and the terrestrial biosphere exerts important feedbacks on the climate through various biogeophysical and biogeochemical cycles. The climate–ecosystem interaction is influenced by the rising atmospheric CO_2 concentration, enhanced photosynthesis, and higher heterotrophic respiration (Prentice et al., 2001; Bindof et al., 2013). Widespread changes in vegetation structure, community composition and biogeography due to human-induced changes in temperature and precipitation have been reported (Dieleman et al., 2015; IPCC 2021). The vegetation feedback on climate includes physiological effects related to a lower stomatal conductance with higher atmospheric CO_2 concentrations. This leads to a decrease in evapotranspiration and precipitation, further accelerating climate warming (Lemordant et al., 2018).

Although the relationship between the terrestrial ecosystem and climate has been well-studied, the direction and magnitude of climate-carbon cycle feedback remain uncertain (Friedlingstein et al., 2006; Gallego-Sala et al., 2018). The response of the carbon cycle to the anthropogenic increase in atmospheric CO_2 has been characterized into two strong and opposing feedbacks (Friedlingstein et al., 2006; Boer and Arora 2009). First, there is the negative carbon–concentration feedback which is a measure of the carbon cycle response to higher atmospheric CO_2 concentration that will result in greater C uptake by the land and ocean. Second, there exists a positive carbon–temperature feedback which is a measure of the carbon cycle response to a warmer climate that will decrease land and ocean carbon sinks (Arora et al., 2013). In northern high-latitudes, Earth System Models suggest that climate warming may increase land carbon sequestration, though there are considerable uncertainties in both the sign and magnitude of the carbon-temperature response in this region (Bindof et al., 2013).

1.1.3 Response of Permafrost Peatland Carbon to Climate Change

Northern permafrost soils contain approximately 1700 Pg C, which represents about one-third of the world's soil organic carbon, and is equivalent to twice as much carbon as there is in the atmosphere (Zimov et al., 2006; Tarnocai et al., 2009; Schuur et al., 2015). Permafrost peatlands can store large amounts of carbon due to wet and cold soil conditions, and slow rates of organic matter decomposition. Peat accumulation has occurred over millennia, resulting in the removal of carbon from the atmosphere, as organic carbon was stabilized by decay-resistant conditions (Dorrepaal et al., 2009).

The arctic and subarctic peatlands are highly sensitive to climate change (Koven et al., 2017), climate warming of about 0.755 °C/decade (Huang et al., 2017) has resulted in extensive permafrost thawing over the region (Camill, 2005; Vallée and Payette 2007; Grosse et al., 2011). Warmer soil temperatures and deeper active layer thaw accelerate the decomposition of organic matter, resulting in the release of carbon to the atmosphere. Surface and subsurface hydrology is also influenced by permafrost thaw. Moreover, wetland drainage in some areas promotes aerobic conditions which lead to higher peat respiration and CO_2 losses. In other areas that were previously dry, waterlogged conditions due to ground thaw and subsidence promote anaerobic soil conditions that enhance CH_4 release to the atmosphere (Treat et al., 2014; Schädel et. al, 2016). The response of permafrost peatland to climate warming has been inconsistent, with some areas showing increased C accumulation and others experiencing decreased C accumulation

(Euskirchen et al., 2014; Sim et al., 2021). The long-term stability of northern peatland C will depend on the combined response of GPP and ER to temperature and moisture changes. Warmer spring conditions, earlier snowmelt, and longer growing seasons may lead to higher rates of primary production and stronger carbon uptake (Churkina et al., 2005; Loisel and Yu, 2013), but this may be offset by carbon losses from increased ER and CH_4 emissions (Parmentier et al., 2011; Schuur et al., 2015; Nzotungicimpaye and Zickfeld, 2017). Also, the short-term response of northern peatlands to climatic changes (Aurela et al., 2004) have been shown to differ considerably from the long-term trends (Mack et al., 2004; Swindles et al., 2015).

1.1.4 The Hudson Bay and Adjacent Lowlands

The Hudson Bay Lowlands (HBL) of Canada is a globally significant ecological region, storing over 30 Pg of carbon that have accumulated since the mid-Holocene (Packalen et al., 2014). Peat growth in the HBL is promoted by the anomalously cold temperatures, permafrost presence, isostatic rebound, and expansive flatland areas with waterlogged conditions. The HBL is located between the Canadian Shield and the southern shores of Hudson Bay and James Bay. The entire region drains into the Bay through rivers such as the Churchill, Severn, and Attawapiskat. The climate of the HBL is strongly influenced by the Hudson Bay, which at its core is 6 °C colder than the average for its latitude (Harvey, 1978). The effect of the Bay on the adjacent lowlands is evident in the intense, cold winters and the short, cool summers.

The Hudson Bay undergoes a full cryogenic cycle each year, being completely ice-covered in the winter and becoming ice-free during the summer. The formation of ice starts in late October or early November and peak ice thickness occurs around April and May. Traditionally, sea ice break-up is complete by the first week of August (Saucier and Dionne, 1998; Gagnon and Gough, 2005). Polar bears have adapted to the seasonality of sea-ice cover over the Bay. In winters and springs, the bears live on the ice platforms feeding on seal pups or hibernating. In summer when the sea-ice begins to retreat, the polar bears migrate to the land where they bear and raise their young. The survival of the polar bear population in western Hudson Bay depends on the presence of sea-ice cover with reliable breakup and freeze-up periods.

It has been shown that there is strong interannual variability in the timing of freeze-up and breakup over the Bay (Gagnon and Gough, 2005). The magnitude of the variability is higher for the breakup dates than for the freeze-up period, and the largest variability in the timing of breakup occurs close to the western shore of the Hudson Bay. In recent decades, climate warming has resulted in significant trends toward earlier sea ice breakup in the western half and along the southern shore of Hudson Bay and in James Bay. The magnitude of the breakup trend was greatest in western Hudson Bay, decreasing eastward. Trends toward later freeze-up occurred in the northern and northeastern parts of the Hudson Bay (Gagnon and Gough, 2005).

Research studies have demonstrated that the recent increase in spring and early summer temperatures coincide with earlier breakup trends in sea-ice over the Hudson Bay (Gagnon and Gough, 2005; Hochheim and Barber, 2014). Also, there is a strong relationship between positive temperature anomalies in late summer and autumn and later sea ice freeze-up over the Bay. Hochheim and Barber (2014) found trends toward a longer ice-free season, with freeze-up dates delayed by ~1.6 weeks and break up occurring 1.5 weeks earlier. It is anticipated that the trend towards a longer ice-free season over the Hudson Bay will impact both the climate and ecology of the adjacent HBL.

1.2 Motivation

Recent changes in the sea ice dynamics and energy budget of the Hudson Bay can be attributed to the increase in global temperatures and Arctic amplification (Hochheim and Barber 2014; Kowal et al. 2017; Bello and Higuchi 2019). The impact of these climatic changes in the Bay on the adjacent HBL is presently unknown. The advective influence of the Bay on the HBL is largely determined by the relative frequency of offshore (warmer and drier) and onshore (cooler and wetter) wind regimes. Changes in the distribution of large-scale air masses in the Hudson Bay region has been linked to positive temperature trends (Leung and Gough (2016); yet, the implications of these changes on the advective role of the Bay and the surface energy balance of the HBL remain speculative (Rouse and Bello, 1985; Delidjakova et al., 2016). Moreover, despite our knowledge of short-term peatland carbon exchange in the HBL, there are still substantial uncertainties in the longer-term combined response of plant productivity and ecosystem respiration to global, regional and local climatic changes.

Previous studies have mostly focused on the advective influence of the Hudson Bay on the HBL using eddy covariance (EC) measurements collected over a relatively short period. Furthermore, the existing networks of EC tower sites (e.g. FLUXNET and AmeriFlux) have sparse coverage over northern peatlands, particularly the HBL, due to the high cost of tower setup and maintenance (Lees et al., 2018). Process-based terrestrial ecosystem models can serve as powerful tools to address the limited temporal and spatial coverage of peatland NEE but are computationally intensive. These models also have considerable uncertainties in flux outputs which are difficult to diagnose due to model complexity (Lin et al., 2011; Bonan, 2019; Xiao et al., 2019). There is a need for relatively simple yet accurate terrestrial ecosystem models that can provide reliable estimates of NEE in the HBL region.

Long-term temporal analyses of the surface energy and carbon balance of the HBL are crucial to gaining a better understanding of the linkage between climate change in the Hudson Bay and the surrounding HBL. It is also imperative to provide insights into the spatial variations in the magnitude and strength of these climatic changes across the HBL. As a globally significant peatland C reservoir, the HBL region will play a vital role in future climate warming and permafrost carbon feedback.

1.3 Research Objectives

The central aim of this research work is to improve our understanding of the long-term warming-induced changes in the surface energy balance and net CO_2 exchange over the HBL, and how they have been influenced by climate change in the Hudson Bay. The overall aim is achieved by developing specific research objectives that are grouped under Chapters 2–5 in this dissertation. The four chapters are structured as four distinct manuscripts in preparation for submission or already submitted to peer-reviewed scientific journals. All four manuscripts are written sequentially and connected by the central aim of this research work. As a result of this linkage between chapters, there are some similarities in research methods and study locations.

Generally, Chapters 2 and 3 employ a combined model and assimilated dataset (North American Regional Reanalysis, NARR) to investigate the mesoscale wind and temperature changes in the HBL and their impact on the surface energy balance from 1979–2018. Chapters 4 and 5 use the satellite data-driven land surface model (Vegetation Photosynthesis and Respiration Model, VPRM) to examine the suitability of light-use efficiency models for studying the long-term response of peatland CO_2 exchange to climatic changes in the HBL and the Hudson Bay from 2000–2019. More precisely, the research objectives are as follows:

Chapter 2: Climatic Changes in the Mesoscale Wind and Temperatures in the Hudson Bay Lowlands: Impact on the Surface Energy Balance

1) investigate the climatic changes in the mesoscale wind regimes in the HBL

2) examine the trends in temperatures between offshore and onshore winds

3) assess the advective influence of the Hudson Bay on the surface energy balance in the adjacent lowlands under global warming

Chapter 3: Spatial Heterogeneity in the Magnitude and Strength of the Impacts of Wind and Temperature Changes across the Hudson Bay Lowlands

1) examine the spatial variations in wind and temperature changes across the HBL region

2) analyze the spatial heterogeneity in the magnitude and strength of the resulting changes in the surface energy balance

3) discuss the potential implications for permafrost thaw and peatland carbon dynamics

Chapter 4: Terrestrial CO_2 Exchange Diagnosis using a Peatland-Optimized Vegetation Photosynthesis and Respiration Model (VPRM) for the Hudson Bay Lowlands

1) evaluate a peatland-optimized LUE-based model at a fen and bog site

2) compare an EVI-driven model and a SIF-driven model to determine which modelling approach can provide more reliable estimates of peatland photosynthesis

3) examine how LUE and other model parameter values vary within and between different peatland types

Chapter 5: Long-term response of peatland carbon exchange to climatic changes in the Hudson Bay Lowlands

1) extend the limited EC carbon flux data over a fen and bog site in the HBL and examine the net CO_2 exchange during the growing season

2) investigate the 20-year response of peatland C balance to changes in temperature and moisture conditions

3) quantify the relative importance of environmental controls on peatland C balance

4) assess the advective influence of the Hudson Bay on the C dynamics of the HBL under global warming

Chapter 2

Climatic Changes in the Mesoscale Wind and Temperatures in the Hudson Bay Lowlands: Impact on the Surface Energy Balance

Abstract

The Hudson Bay exerts a strong advective influence on the surface energy balance in the Hudson Bay Lowlands (HBL) region of Canada. The onshore winds blowing from the Bay towards the HBL are relatively cold and moist compared to the warm and dry offshore winds. The contrasting thermal and humidity properties of these two wind regimes affect the partitioning of net radiation between the sensible, latent and ground heat fluxes over the HBL. Offshore wind regimes are characterized by significantly larger latent and ground heat fluxes, while onshore winds have significantly higher sensible heat flux. In this study, it is shown that recent global warming has caused significant changes in the mesoscale wind regimes and the advective role of the Hudson Bay on the surface energy balance over the HBL. I found a strong increasing trend in onshore wind frequency of about 7% over the past 40 years. The most rapid changes occur in June when the onshore winds have increased by 17% over the study period. These significant changes in June are quite striking, as it implies that the average difference in frequency between the two wind regimes has decreased by about 35% over the study period. Consequently, there has been a shift from offshore to onshore winds dominance in June over the HBL. The results also demonstrate that the offshore air temperatures are increasing at a faster rate than the onshore temperatures, producing significant distinctive trends in the surface energy fluxes that are considerably different between the wind regimes. The results reveal that the changes in the mesoscale wind regimes and surface energy balance of the HBL under present and projected climate warming are markedly different than was previously thought.

2.1 Introduction

The Arctic and Subarctic regions have experienced significant climatic changes since the mid-20th century due to the human-induced increases in the atmospheric concentrations of greenhouse gases (GHGs), particularly carbon dioxide (van Wijngaarden, 2008; Serreze and Barry, 2011; Walsh et al., 2011; Bindof et al., 2013). Arctic surface air temperatures have risen at over twice the global mean rate (Serreze et al., 2009; Screen and Simmonds, 2010; Cowtan and Way, 2013). This disproportionately substantial rate of warming in the region has been attributed not only to the snow- and sea ice-albedo feedbacks (Hall, 2004; Serreze and Francis, 2006; Taylor et al., 2013), but also, recently, ozone-depleting substances, particularly Chlorofluorocarbons (CFCs) emitted over the second half of the twentieth century (Polvani et al., 2020). Extreme warming in the Arctic and Subarctic has been accompanied by a dramatic reduction in sea-ice cover and thickness (Parkinson et al., 1999; Rothrock et al., 1999; Comiso, 2002), as well as thawing permafrost and changing wetlands (Camill, 2005; Vallée and Payette 2007; Grosse et al., 2011).

The Hudson Bay has been referred to as the cold tongue of the Arctic Ocean plunging into southern Canada (Bello and Higuchi, 2019). The Bay is a large, relatively shallow, inland subarctic sea covering an area of approximately 8.04×10^5 km^2, with a mean depth of 150 m (Prinsenberg, 1986). The Hudson Bay, together with James Bay to the South, Foxe Basin to the North and Hudson Strait to the East, forms the largest inland sea in the world (Etkin, 1991; Gagnon and Gough, 2005). The Hudson Bay system drains an area of 3.7×10^6 km^2, with a freshwater discharge of $\sim$760 km^3 per year (Dery et al. 2011). The Hudson Bay is completely ice-covered each winter and becomes ice-free during the summer. Typically, ice formation begins in late October and November, the ice cover reaches its peak thickness in April and May, and breakup is complete by the first week of August (Saucier and Dionne, 1998; Gagnon and Gough, 2005). The persistence of sea ice in the Hudson Bay until late July contributes to the presence of permafrost along the western coast of the Hudson Bay Lowlands (HBL), where the southern limit of continuous permafrost lies parallel to the coast (Gough and Leung, 2002). Indeed, Hudson Bay exerts an advective influence on the adjacent lowlands.

The HBL region lies within the provinces of Ontario, Manitoba and to lesser extent Quebec, covering about 250,000 km^2. It is the second-largest wetland region in the world accounting for an estimated 12% of the Earth's total wetlands (Riley, 2011). The region is characterized by a wide variety of hydro-geomorphic features such as fens, bogs, peat plateaus, ponds, lakes, swamps and marshes. The extensive wetlands are supported by the expansive flatland areas with gentle gradients and sluggish flow which prolong surface water retention, the cold temperatures that allow peat accumulation with a catotelm layer that is essentially impervious, and the presence of permafrost with a thin active layer in summer which impedes percolation (Woo, 2012). The area is part of the tundra and boreal forest transition zone, and the vegetation consists of open stands of stunted white spruce, tamarack and black spruce. The shrub layer features dwarf birch, willow, and a ground cover of sedge, lichen and moss. Common wildlife includes barren-ground caribou, polar bear, arctic fox, brown lemming, snow and Canada goose, swan, sea ducks, and shorebirds (ESWG, 1995).

The strong advective influence of the Hudson Bay on the surface energy balance of the Hudson Bay Lowlands has been well studied. During the growing season in Churchill, Manitoba, Rouse and Bello (1985) found that onshore winds originating from the Bay resulted in larger sensible heat fluxes (Q_H) over the HBL compared to offshore winds. On the other hand, the evaporative or latent heat fluxes (Q_E) were usually greater during offshore winds. Therefore, the

Bowen ratios ($\beta = Q_H/Q_E$) were higher for onshore wind regimes. The Bowen ratios also decreased away from the Hudson Bay for both onshore and offshore wind regimes (Weick and Rouse, 1991). The decrease in Bowen ratios inland during onshore and offshore winds are in response to boundary layer adjustments to the new land surface and the development of the convective internal boundary layer. This demonstrates that a large vertical temperature gradient exists between the warm land surface and the cold overlying marine air mass during onshore winds; the usage of the available net radiation, therefore, favours sensible heating of the atmosphere. In addition, the cold and moist onshore winds also decrease the vapour pressure gradient which suppresses the evaporative flux. The opposite conditions prevail during offshore wind regimes. At a coastal site near southern James Bay, Rouse et al. (1987) found that the ground heat flux (Q_G) was about twice as large for offshore compared to onshore winds. This strong dependence of the energy balance in the HBL region on the advective wind direction around the Hudson Bay has been confirmed by other research studies (Lafleur and Rouse, 1988; Delidjakova et al., 2016).

Beyond that, however, these previous studies were limited both in their temporal and spatial extent, as they were constrained by data obtained from a small number of study sites over a few years. Consequently, some crucial questions about the advective influence of the Hudson Bay on the HBL still remain largely unanswered. With climatic warming in the Hudson Bay, the disappearance of sea ice—11% per decade between 1968 and 2008 (Henry, 2011; Tivy et al. 2011), the lengthening of the open water season—3.1 weeks (Hochheim and Barber 2014; Kowal et al. 2017), and the increase in net radiation driven by lower summer albedo (Bello and Higuchi 2019), one is led to ask whether there are significant changes in the Hudson Bay's advective influence and trends in the surface energy balance over the HBL.

The primary objectives of this study are to 1) investigate the climatic changes in the mesoscale wind regimes in the HBL; 2) examine the trends in temperatures between offshore and onshore winds; and 3) assess the advective influence of the Hudson Bay on the surface energy balance in the adjacent lowlands under global warming.

2.2 Methodology

2.2.1 Atmospheric and Energy Balance Data

The climatological data used in this study were obtained from NOAA's North American Regional Reanalysis (NARR) model, produced by the National Centers for Environmental Prediction (NCEP). NARR is a long-term, dynamically consistent, high-resolution, high-frequency, atmospheric and land surface hydrology dataset for the entire North American domain (Mesinger et al., 2006). NARR was developed as a major improvement upon the earlier NCEP–NCAR Global Reanalysis (Kalnay et al., 1996; Kistler et al., 2001), with lateral boundary conditions provided by the NCEP–DOE GR2 (Kanamitsu et al., 2002). The key features of the NARR system include the NCEP regional Eta model and its Data Assimilation System, an upgraded Noah land-surface model, improved precipitation assimilation, and direct assimilation of radiances. The NARR model employs a fully cycled analysis-forecast system with 3-hourly weather observations feeding into the 3-hourly forecasts. This three-dimensional variational data assimilation (3DVAR) technique ensures that the model first guess is reanalyzed and optimized with observations to generate more realistic and accurate results. NARR input observation datasets are obtained from various sources including surface weather stations, ships, buoys, rawinsondes, aircraft and satellites (Shafran et al, 2004). The NARR dataset is available from 1979–present, on a 3 hourly, 32 km horizontal grid spacing, with 29 pressure levels.

For this study, the meteorological variables obtained from NARR covering the HBL include (i) Air temperature at 2 m (ii) U and V component of wind at 10 m (iii) Sensible heat flux at the surface (iv) Latent heat flux at the surface, and (v) Ground heat flux at the surface. The NARR datasets are provided in PSD standard NetCDF4 file format for the entire North American domain. The coordinates information and grid points corresponding to the HBL region were carefully extracted using Esri's ArcGIS. The climate and energy flux data for the HBL were extracted from the NetCDF using R programming (R Core Team, 2019). Furthermore, the NARR wind data consist of the zonal and meridional wind components. To calculate the meteorological wind speed and wind direction from the zonal (U) and meridional (V) wind components, the NCAR Command Language (NCL, 2019) was employed.

The data used in this study are daily averages from June to September, for the period 1979-2018. A total of 194 grid locations (only 181 grid locations available for the ground heat flux) were used to examine the climatic changes in the mesoscale wind regimes in the HBL and their impact on the surface energy balance over a 40-year period (Figure 2.1).

2.2.2 Surface Energy Balance and Advection

For each grid point, the surface energy balance is given by:

$$Q^* = Q_H + Q_E + Q_G \qquad (1)$$

where Q^* is the net surface radiation, Q_H is the sensible heat flux—energy used for warming the atmosphere, Q_E is the latent heat flux—energy used for evaporating water from the surface, and Q_G is the ground heat flux—energy for warming the underlying soil. Q^* along with all the other energy fluxes are positive during the day indicating that the surface has a radiant energy surplus, but they are negative at night due to the surface radiation deficit. The daytime surface radiative surplus is partitioned into atmospheric and sub-surface energy sinks—energy moves away from the surface, while the nocturnal surface deficit must be offset by heat gained from the available sub-surface and atmospheric sources—energy moves towards the surface. The radiation and energy fluxes are all in units of $W\,m^{-2}$.

The nature of the surface and the overlying atmosphere are the most important determinants of the exact partitioning of Q* between sensible, latent and ground heat fluxes. In particular, the relative significance of latent verse sensible heat is mainly governed by the availability of surface water for evaporation and the moisture content of the atmosphere. The partitioning of the convective fluxes, therefore, depends strongly on the quantitative relation between the vertical air temperature and vapour pressure gradients. Another important factor that affects energy partitioning at any given location is the influence of upwind air masses arriving from adjacent locations possessing different surface characteristics. The horizontal transport of heat energy (advection) between different locations with dissimilar surface radiative, thermal, and moisture properties may alter the vertical gradient of temperature and vapour pressure in the downwind region. Indeed, the effect of advection is particularly important in coastal environments such as the HBL region, where the land and the Bay surfaces possess different energy balances due to their contrasting thermal and moisture properties.

To examine the advective role of the Hudson Bay on the HBL and the climatic changes over time, the temperature, wind speed and heat flux data from NARR were separated into onshore and offshore wind regimes based on the wind direction. Onshore winds are defined as winds blowing from the Bay towards the HBL, while offshore winds blow from inland over the

HBL. Generally, winds originating from the west and south are mostly offshore winds, while winds originating from the north and east are mostly onshore winds. Temporal analysis (1979–2018) of the variability in the surface energy fluxes averaged over the HBL region were carried out for both the study period (June–September) average and the individual monthly averages. The study is primarily focused on the June–September period because it is the typical growing season in the HBL and the sea ice melt season when the advective influence of the Hudson Bay is most noticeable.

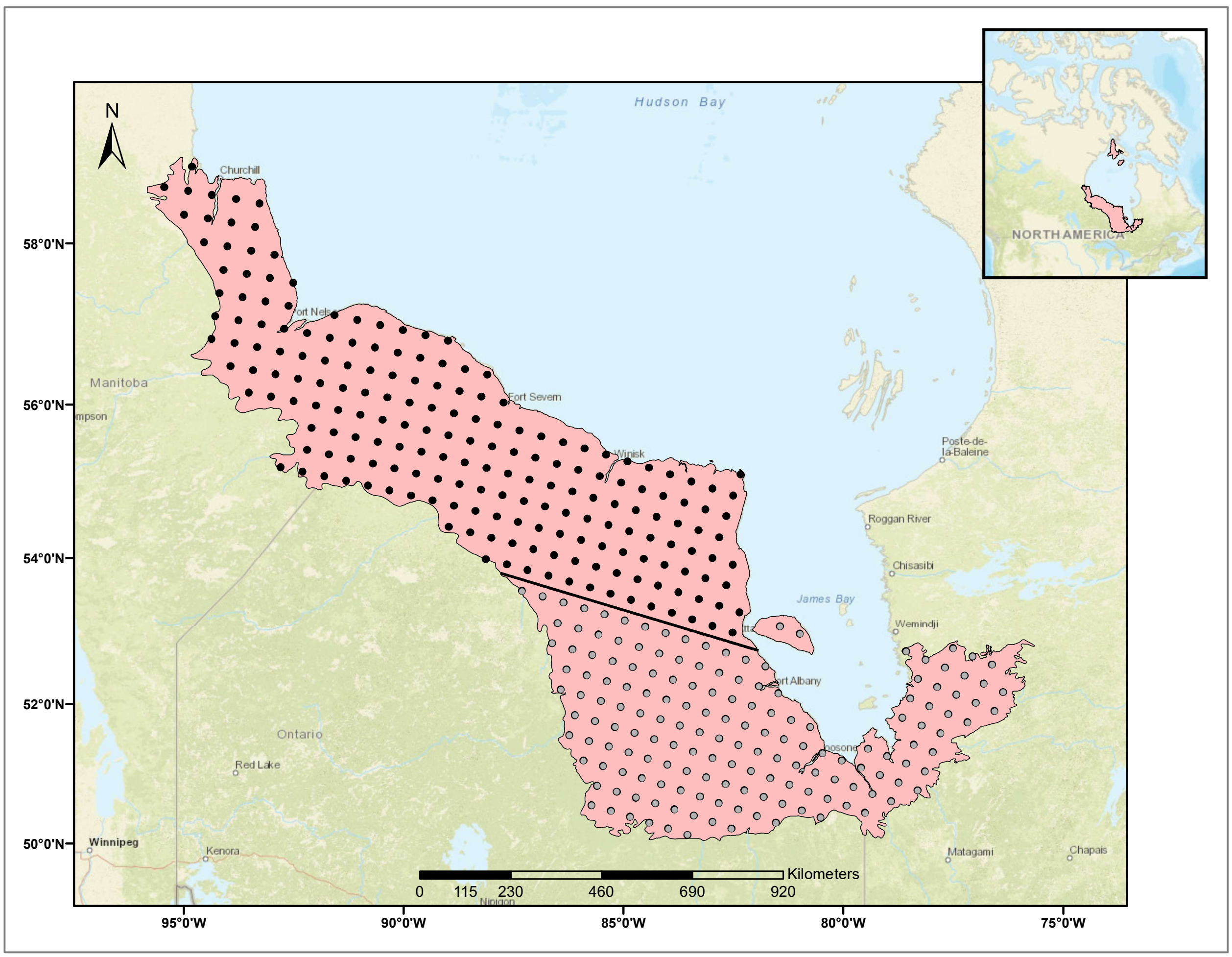

Figure 2. 1. Map of the study region including the Hudson Bay Lowlands (pink) and the Hudson Bay. The dots are the locations of all the NARR data grid points over the Hudson Bay Lowlands region. A total of 194 grid locations covering the "true" Hudson Bay Lowlands were used (black dots above the thick black line). The area below the thick black line is technically referred to as the James Bay Lowlands and was not included in this study.

2.2.3 Statistical Analysis

The Shapiro–Wilk (Shapiro and Wilk, 1965) and Kolmogorov-Smirnov (Massey, 1951) tests for normality and Q-Q plots were used to determine if the data were normally distributed. Since the datasets were not normally distributed (Kolmogorov–Smirnov, $p < 0.05$; Shapiro–Wilk, $p < 0.05$), non-parametric statistical methods were employed to analyze the climatological and energy flux data. These non-parametric tests do not require the assumptions of a normal distribution and are more robust in situations where there are outliers in the time series. The Mann-Kendall test (McLeod, 2011) was used for the detection of trends in the time series. The Kendall tau, (–1 to +1) represents the direction and strength of the linear trend while the p-value indicates the significance of the trend. In addition, the Theil-Sen slope approach (TSA; Sen, 1968; Hirsch et al., 1982) was used to compute estimates of the magnitude or rate of change of the trend. The trends are expressed as anomalies relative to the climate normal period, 1981–2010.

The climate time series was not corrected for autocorrelation and the pre-whitening technique by Yue et al. (2002) was not applied to the data. Even though pre-whitening may reduce the influence of serial dependence and the probability of rejecting the no-trend hypothesis (von Storch, 1995), it also reduces the magnitude of the real trend. Yue & Wang, (2004a) cautioned that pre-whitening a time series may be fundamentally wrong because the presence of a trend in the time series will produce spurious or increased estimates of serial correlation. Moreover, research studies have shown that when an explicit trend exists in a time series and the sample size is large (as in this present study), pre-whitening would cause a false assessment of the significance of the trend (Yue & Wang, 2002; Yue & Wang, 2004b; Bayazit & Önöz, 2007).

For the difference of means test, the Mann–Whitney *U* test was employed to test for significance. All statistical analyses were conducted using R programming (R Core Team, 2019).

2.3 Results

2.3.1 Wind Frequency

The spatially averaged offshore and onshore wind frequency over the HBL during the study period, June through September 1979–2018 show the dominance of the offshore winds throughout. (Figure 2.2). It is important to note the exception in 2009 when onshore wind frequency exceeded that of the offshore winds. The wind frequency anomalies for the study period reveal a clear downward trend in offshore winds and a corresponding increase in the frequency of onshore winds (Figure 2.3). The overall shift from positive to negative offshore wind anomalies becomes apparent by the beginning of the 21st century. Onshore winds shifted from negative to positive anomalies around that same time. Statistical analysis shows that these trends in wind frequency are significant (tau = 0.29, p = 0.009) with a total increase (decrease) of 6.8% in onshore (offshore) winds during the study period. As a result, there is a significant downward trend (TSA = -13.5%) in the difference between offshore and onshore wind frequency during the study period (Figure 2.4), though the wind frequency difference (Offshore – Onshore) remains positive. Again, it is important to note that 2009 was the only year when onshore winds exceeded offshore winds, with a difference of about 10%.

The monthly wind frequencies for the spatially averaged offshore and onshore winds over the HBL for the 1979–2018 period indicates that offshore winds are much higher than onshore winds in July, August and September (Figure 2.5; Table 2.1). In June, offshore wind frequency is approximately equal to that of onshore winds. The average offshore wind frequency for the study period is 63% compared to 37% for onshore winds (mean of the differences = 26%, $p < 0.0001$).

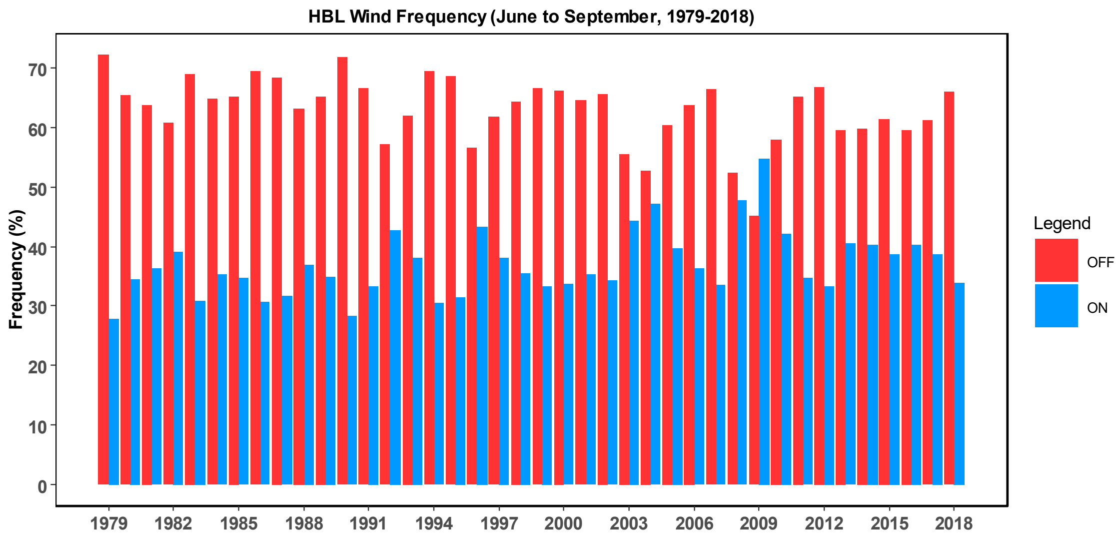

Figure 2. 2. Spatially averaged offshore and onshore wind frequency over the HBL (June–September) for the period 1979–2018.

Time series analysis of the individual months provides further insights into the trends in the spatially averaged offshore and onshore wind frequency over the past 40 years (Figure 2.6). The increase in the occurrence of onshore winds in June is particularly noticeable and the onshore winds appear to have, generally, surpassed offshore winds by 2003. Statistical results for all the study months reveal that the anomalies in wind frequency are only significant in June. The upward trend in June onshore wind frequency is striking, with an increase of 17.4% (tau = 0.24, $p = 0.03$) over the past 40 years. Offshore winds in June have decreased by the same percentage. In July, offshore (onshore) winds have declined (risen) by 10.7% over the study period, though this result is not statistically significant (tau = -0.18, $p = 0.11$). The results in August (4.8%) and September (2.2%) are also non-significant.

(a)

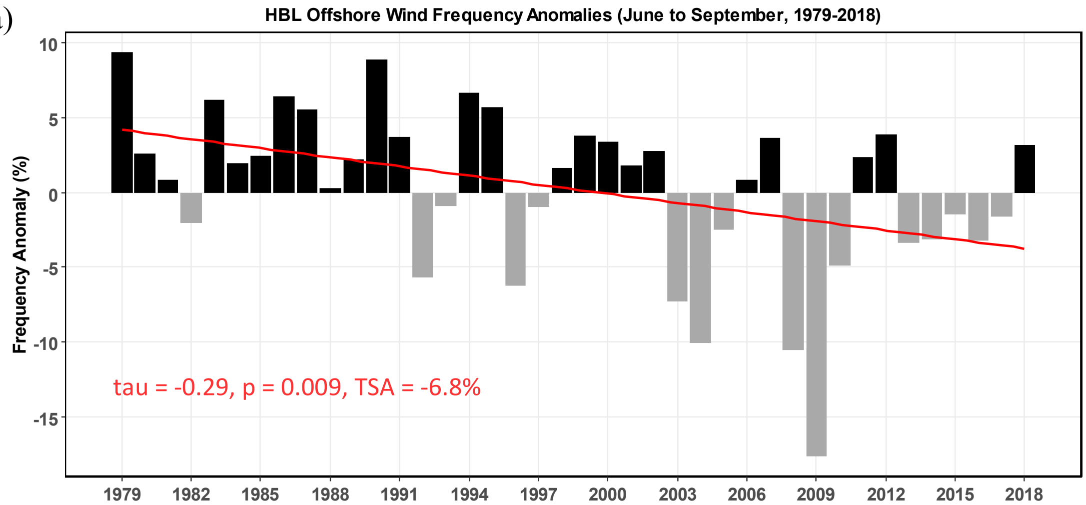

(b)

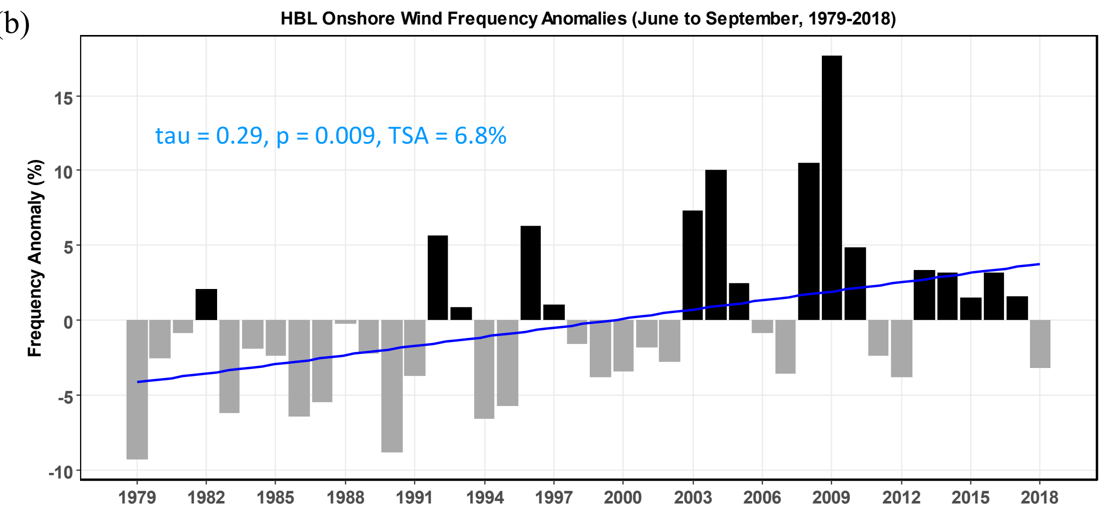

Figure 2. 3. Spatially averaged wind frequency anomalies over the HBL (June–September) during the period 1979–2018, for (a) Offshore and (b) Onshore winds. The anomalies are calculated as the observed value in any given year minus the average, for the climate normal period 1981-2010

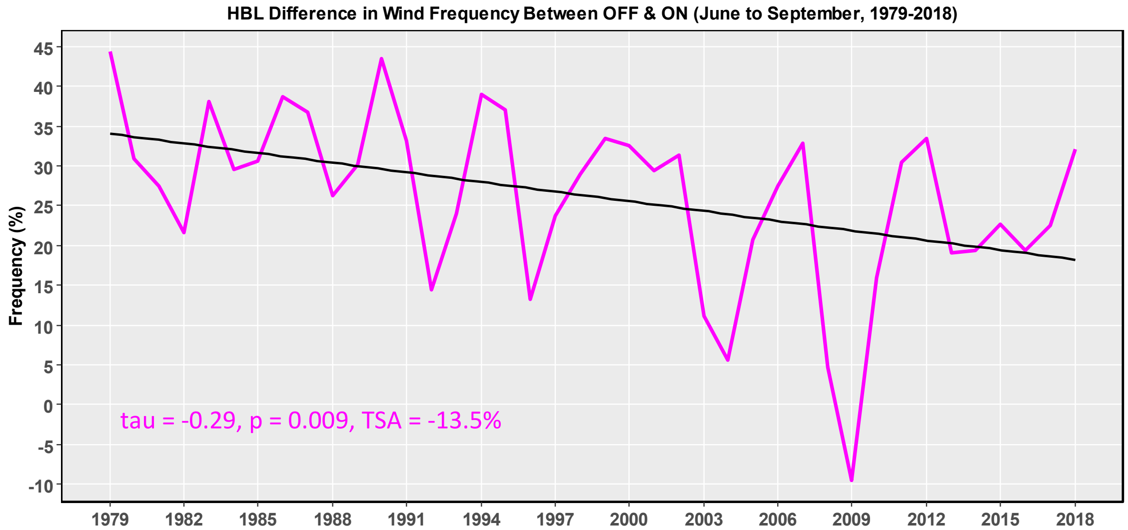

Figure 2. 4. Difference between offshore and onshore wind frequency over the HBL (June–September) for the period 1979–2018. The difference is calculated as offshore wind frequency minus onshore wind frequency.

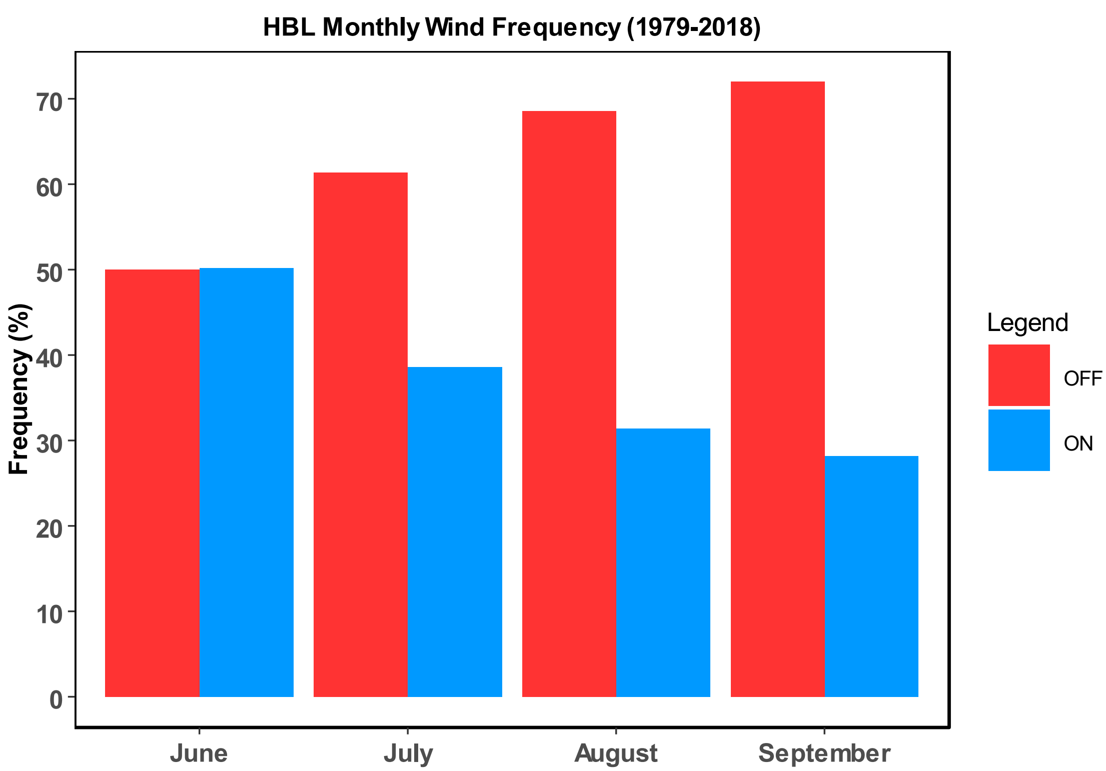

Figure 2. 5. Average monthly wind frequency (June–September) for the spatially averaged offshore and onshore winds over the HBL for the 1979–2018 period.

Table 2. 1. Monthly mean wind frequency and medians for temperature and energy fluxes for the period 1979–2018. The seasonal values are the means over the four months as a whole.

Wind Frequency (%)	June	July	August	September	Seasonal Mean	p-value
Offshore Mean	49.9	61.4	68.6	71.9	63.0	< 0.0001
Onshore Mean	50.1	38.6	31.4	28.1	37.0	
Temperature (°C)						
Offshore Median	13.4	16.2	14.4	8.0	13.1	< 0.0001
Onshore Median	8.0	11.7	11.0	7.0	9.6	
Wind Speed (ms^{-1})						
Offshore Median	3.7	3.6	3.7	4.3	4.0	0.03
Onshore Median	3.9	3.4	3.5	3.9	3.9	
Sensible Heat Flux ($W\ m^{-2}$)						
Offshore Median	61.2	39.1	29.3	19.6	37.5	< 0.0001
Onshore Median	87.5	64.1	47.6	27.9	54.5	
Latent Heat Flux ($W\ m^{-2}$)						
Offshore Median	82.6	91.4	71.0	39.2	68.6	< 0.0001
Onshore Median	60.6	71.9	56.2	30.9	52.7	
Ground Heat Flux ($W\ m^{-2}$)						
Offshore Median	20.5	14.5	10.3	2.7	11.4	< 0.0001
Onshore Median	10.5	8.3	3.3	-2.7	4.0	

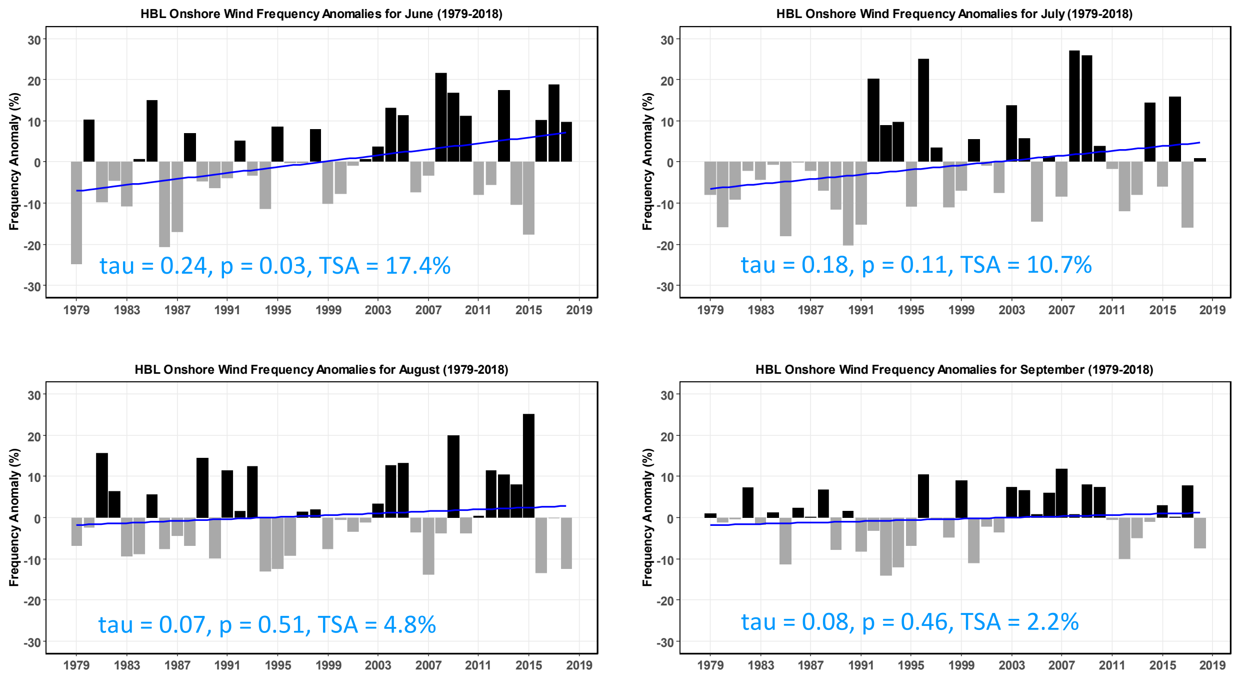

Figure 2. 6. Monthly wind frequency anomalies (June–September) for the spatially averaged onshore winds over the HBL for the period 1979–2018.

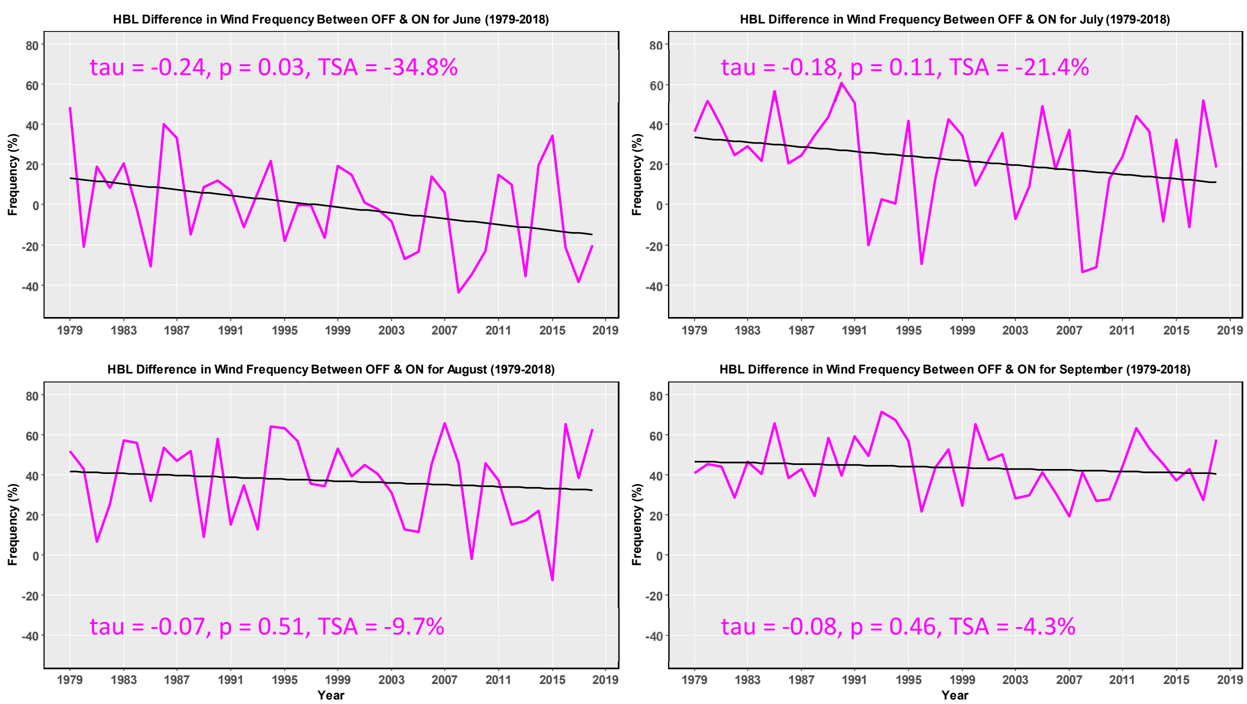

Figure 2. 7. Difference between offshore and onshore wind frequency over the HBL for each of the four study months for the period 1979–2018. The difference is calculated as offshore wind frequency minus onshore wind frequency.

The aforementioned trends imply that the difference between offshore and onshore wind frequency has decreased by as much as 34.8% (tau = -0.24, p = 0.03) in June during the study period (Figure 2.7). All the other months have experienced non-significant, yet notable, declines in the wind frequency difference (21.4% in July, 9.7% in August and 4.3% in September). It is important to emphasize that the dominant wind regime in June over the HBL has now shifted from offshore winds to onshore winds. On average, June offshore winds were approximately 17% dominant in 1979, but by 2018 onshore winds are now dominant by nearly 18%. Furthermore, a similar shift in wind regimes is becoming apparent in July as the linear trend in the wind frequency difference potentially approaches zero.

2.3.2 Temperature

The spatially averaged air temperature anomalies over the HBL during the period 1979–2018 show statistically significant increasing trends for both offshore and onshore winds (Figure 2.8). The mean temperatures during offshore winds have risen by about 2.1 °C (tau = 0.36, p = 0.001), while onshore temperatures have increased by 1.7 °C (tau = 0.39, p = 0.0004). This suggests that air masses originating inland are warming faster than those originating over Hudson Bay. At the beginning of the study period, there were overall negative temperature anomalies—compared to the climatological normal period, 1981-2010—for both offshore and onshore winds, but a general shift to positive temperature anomalies occurred around the early 2000s. The difference between offshore and onshore temperatures is positive throughout the study period, indicating that the average temperatures during offshore winds are always higher than their onshore counterpart (Figure not shown). Additionally, there is an upward trend in the difference between offshore and onshore temperatures averaged for June to September, though this trend is not statistically significant (tau = 0.13, p = 0.24, TSA = 0.6 °C).

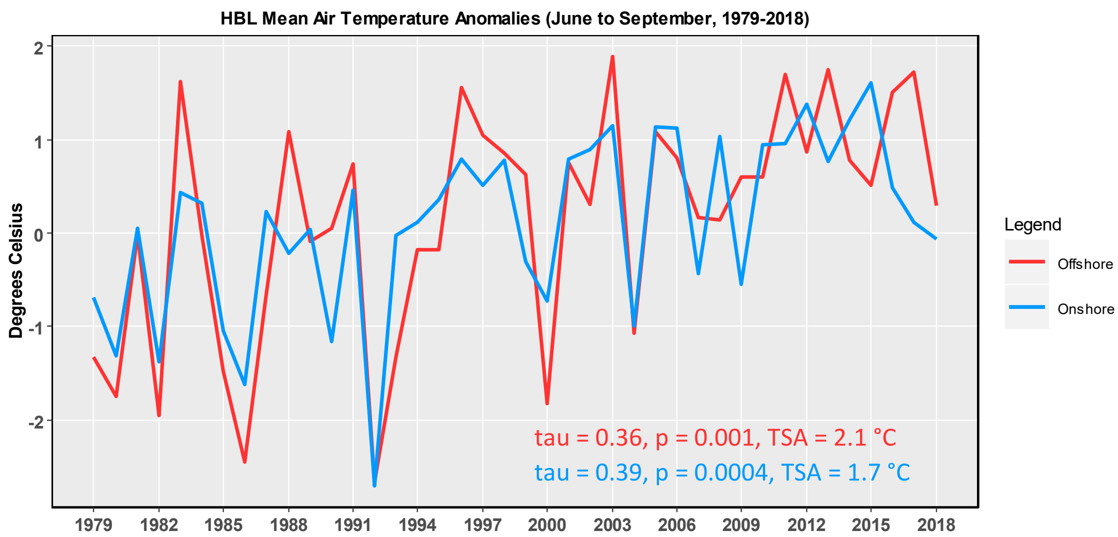

Figure 2. 8. Spatially averaged temperature anomalies over the HBL (June–September) during the period 1979–2018.

The monthly average temperatures for each of the study months during the 1979–2018 period demonstrate that offshore temperatures (median = 13.4 °C for June, 16.2 °C for July, 14.4 °C for August, and 8.0 °C for September) are much higher than onshore temperatures (median = 8.0 °C for June, 11.7 °C for July, 11.0 °C for August, and 7.0 °C for September) in all months (Table 2.1). For the study period, the average temperature during offshore winds is 13.1 °C compared to 9.6 °C during onshore winds (mean of the differences = 3.5 °C, $p < 0.0001$).

Further time series analysis of the individual months provides more insights into the offshore and onshore temperature trends in the HBL over the last 40 years (Figure not shown). The greatest difference in the mean temperatures between offshore and onshore winds occurs in June (mean of the differences = 5.1 °C; $p < 0.0001$) and July (mean of the differences = 4.2 °C; $p < 0.0001$). Statistically significant temperature differences between offshore and onshore wind regimes also persist in August (mean of the differences = 3.2 °C; $p < 0.0001$) and September (mean of the differences = 1.5 °C; $p < 0.0001$). Indeed, the advective influence of the Hudson Bay on the adjacent HBL is obvious. The spatially averaged monthly temperature anomalies over the HBL for the 1979–2018 period reveal that the most rapid warming is occurring in June and September for both offshore and onshore wind regimes (Figure 2.9). Moreover, the temperature anomalies are much higher for offshore winds than onshore winds, particularly in June (Offshore—tau = 0.29, p = 0.009, TSA = 3.2 °C; Onshore—tau = 0.34, p = 0.002, TSA = 2.2 °C) and September (Offshore—tau = 0.36, p = 0.001, TSA = 3.4 °C; Onshore—tau = 0.35, p = 0.002, TSA = 2.8 °C). In July, there is a statistically significant upward trend in offshore wind temperature (tau = 0.30, p = 0.007, TSA = 1.8 °C), while the trend in onshore temperatures is much smaller and not significant (tau = 0.14, p = 0.22, TSA = 0.6 °C). In August, the positive trend in temperature is not statistically significant for either offshore (tau = 0.17, p = 0.13, TSA = 1.2 °C) or onshore (tau = 0.20, p = 0.08, TSA = 1.2 °C) wind regimes.

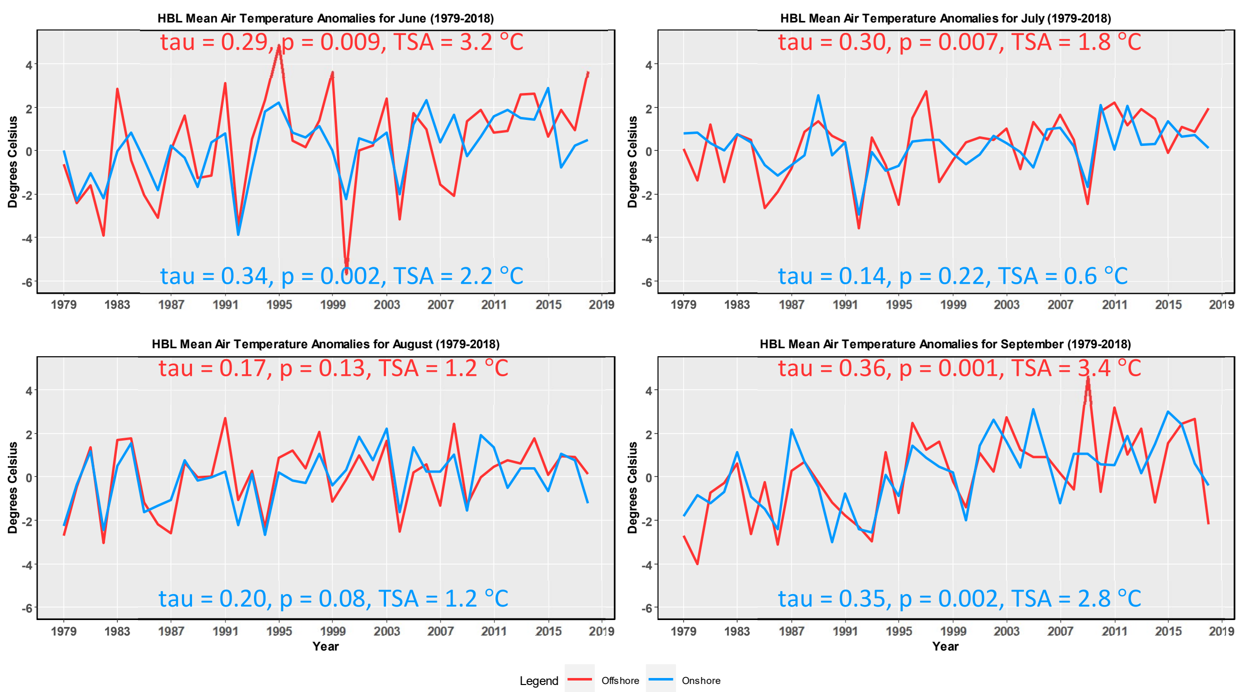

Figure 2. 9. Spatially averaged monthly temperature anomalies (June–September) over the HBL for the 1979–2018 period.

Although the above-mentioned trends in monthly temperature suggest a larger warming rate for offshore winds than onshore winds, there is no statistically significant trend in the average difference between offshore and onshore temperatures for all the study months (Figure not shown). Nonetheless, positive trends do exist in all the months (June TSA = 0.9 °C, July TSA = 1.3 °C, August TSA = 0.1 °C and September TSA = 0.9 °C). It is noteworthy that the most substantial changes in the temperature difference between offshore and onshore winds occur in July (tau = 0.19, p = 0.08, TSA = 1.3 °C). This underscores the large, statistically significant increase in the July offshore temperature anomalies (1.8 °C) compared to a relatively small, non-significant increase in the onshore temperature anomalies (0.6 °C).

2.3.3 Wind Speed

The HBL during the period 1979–2018 show non-significant increasing trends in the spatially averaged wind speed for both offshore (tau = 0.11, p = 0.33, TSA = 0.1 ms^{-1}) and onshore (tau = 0.16, p = 0.15, TSA = 0.2 ms^{-1}) wind regimes (Figure not shown). Similarly, there is no significant trend in the mean difference between offshore and onshore wind speeds over the study period (Figure not shown).

The daily average wind speeds for each of the study months during the 1979–2018 period show that offshore and onshore wind speeds are rather similar, with a mean of 4.0 ms^{-1} and 3.9 ms^{-1} for offshore and onshore winds, respectively (Table 2.1). One could argue that the offshore winds are marginally faster than onshore winds in all the study months, except June (Figure not shown); though the mean difference is only about 0.3 ms^{-1} in July (p = 0.01) and September (p = 0.002), and 0.1 ms^{-1} in August (p = 0.36). The average onshore wind speeds exceed those of offshore winds by approximately 0.2 ms^{-1} in June (p = 0.07). Arguably, the highest wind speeds in the HBL are in September during offshore wind regimes (about 0.6 ms^{-1} higher than the other months).

The spatially averaged monthly wind speed anomalies for offshore and onshore wind regimes indicate that there are no distinguishable trends in wind speeds over the HBL in all the study months, except July (Figure 2.10). The average wind speed anomalies in July have risen by about 0.5 ms^{-1} for offshore winds (tau = 0.20, p = 0.07) and 0.6 ms^{-1} (tau = 0.38, p = 0.001) for onshore winds over the study period. The overall shift from negative to positive wind speed anomalies in July occurred around the year 1999. This reveals that there are important changes in the wind speeds over the HBL in July, particularly during onshore wind regimes. Evidently, the statistically significant trends in July onshore wind speeds underscore the relevance of the large disproportionate warming rate during July offshore winds, where offshore mean temperature anomalies are 1.3 °C higher than their onshore counterpart over the study period.

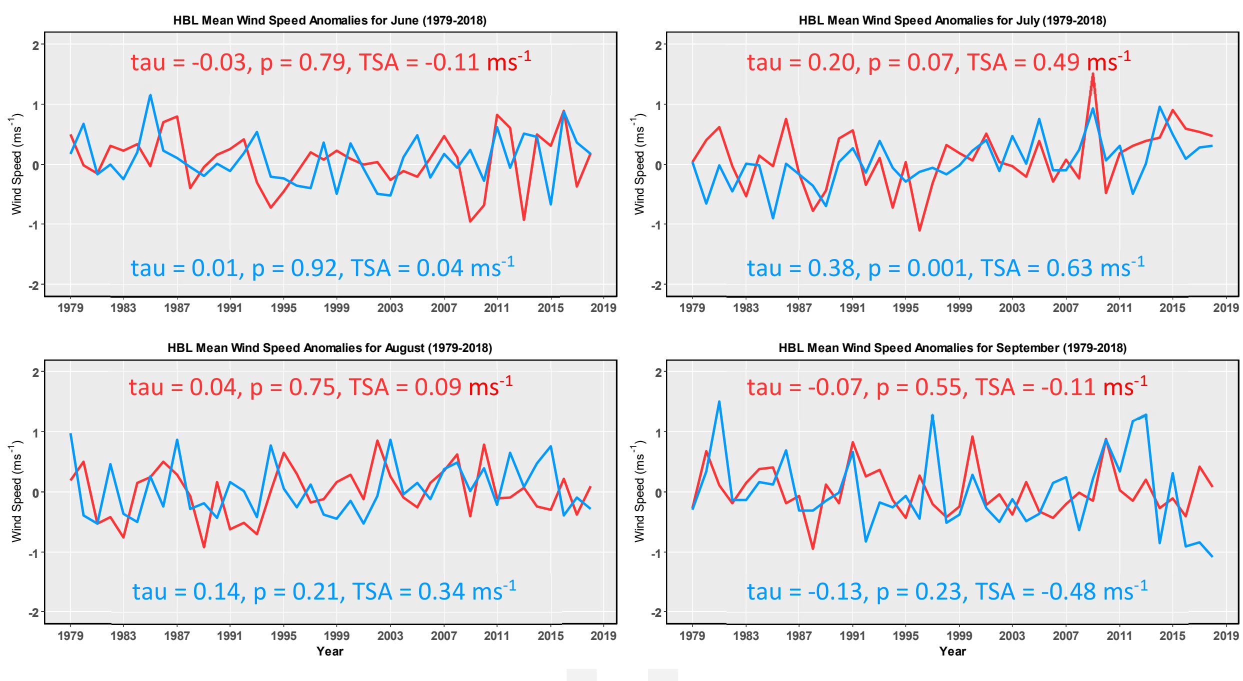

Figure 2. 10. Spatially averaged monthly wind speed anomalies (June–September) over the HBL for the 1979–2018 period.

2.3.4 Sensible Heat Flux

The spatially averaged sensible heat flux (Q_H) anomalies over the HBL during the period 1979–2018 show considerable and statistically significant rising trends for both offshore and onshore winds (Figure 2.11). The average Q_H anomalies during offshore winds have increased by 5.4 W m^{-2} (tau = 0.32, p = 0.004), while onshore Q_H anomalies have risen by 11.4 W m^{-2} (tau = 0.43, p = 0.0001). This reveals that the onshore Q_H anomalies have increased over twice as much as the offshore Q_H anomalies in the HBL over the study period. The earlier years of the study period are overall characterized by negative Q_H anomalies for both offshore and onshore winds, but a general shift to positive Q_H anomalies occurred around the beginning of the 21st century. Interestingly, this transition from negative to positive Q_H anomalies around 2000 is analogous to those of the wind frequency, temperature and wind speed trends over the HBL. The mean difference between onshore and offshore Q_H is positive throughout the study period, signifying that the average Q_H during onshore winds is consistently larger than their offshore counterpart (Figure 2.12). Furthermore, there is a statistically significant positive trend in the mean difference between onshore and offshore Q_H (tau = 0.32, p = 0.004, TSA = 8.0 W m^{-2}) over the 1979–2018 period.

The daily average Q_H for each of the study months during the period 1979–2018 show that onshore Q_H (median = 87.5 W m^{-2} for June, 64.1 W m^{-2} for July, 47.6 W m^{-2} for August, and 27.9 W m^{-2} for September) are considerably larger than offshore Q_H (median = 61.2 W m^{-2} for June, 39.1 W m^{-2} for July, 29.3 W m^{-2} for August, and 19.6 W m^{-2} for September) in all months (Table 2.1). For the entire study period, the average Q_H during onshore winds is 54.5 W m^{-2} compared to 37.5 W m^{-2} during offshore winds (mean of the differences = 16.9 W m^{-2}, $p < 0.0001$).

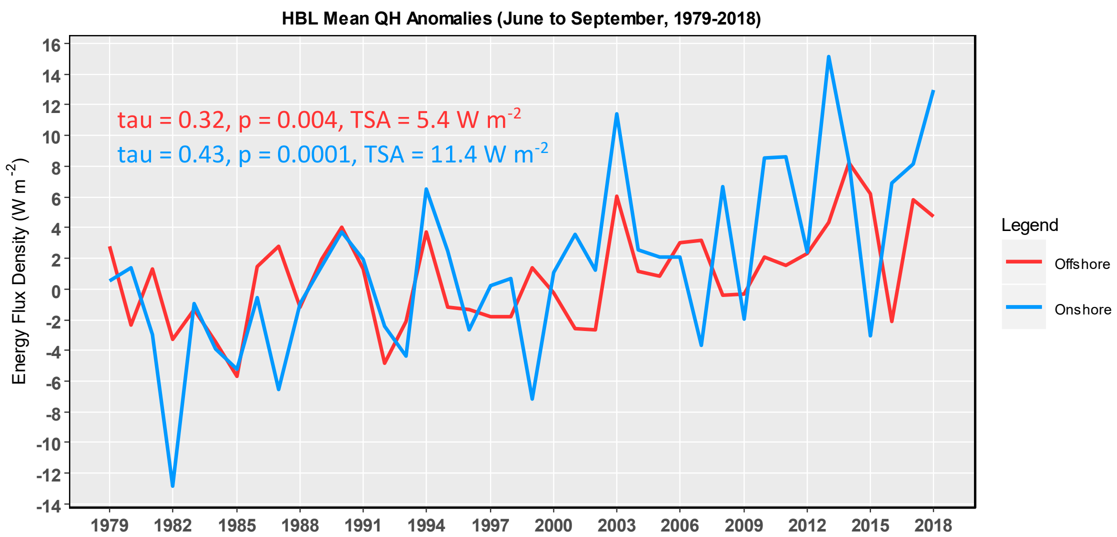

Figure 2. 11. Spatially averaged sensible heat flux anomalies over the HBL (June–September) during the period 1979–2018.

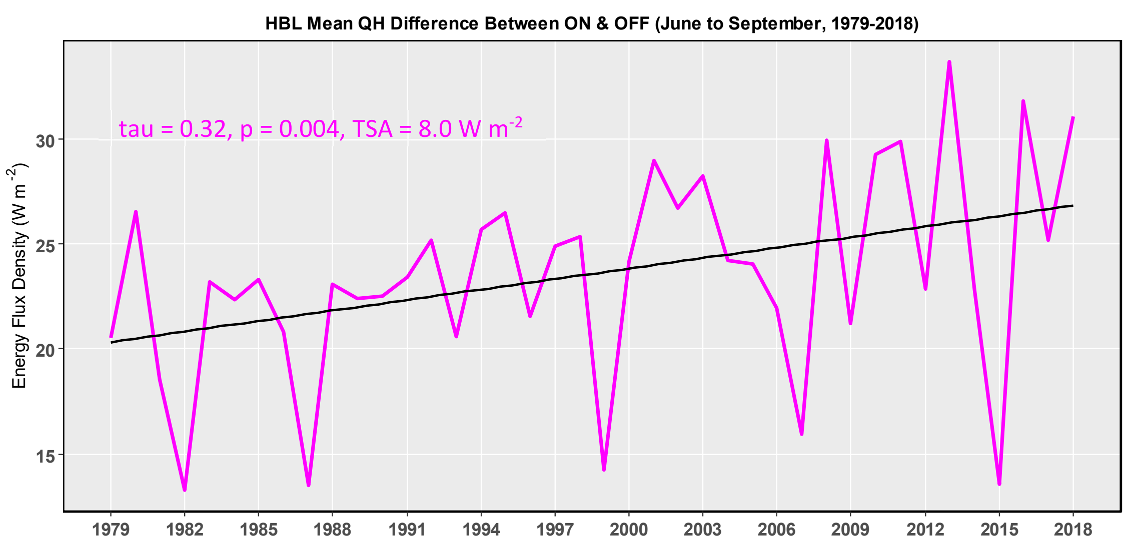

Figure 2. 12. Difference between the mean onshore and offshore sensible heat fluxes for the four study months over the HBL during the period 1979–2018. The difference is calculated as mean onshore sensible heat flux minus mean offshore sensible heat flux.

The greatest difference between the mean onshore Q_H and offshore Q_H occurs in June (mean of the differences = 22.0 W m^{-2}; $p < 0.0001$) and July (mean of the differences = 21.6 W m^{-2}; $p < 0.0001$), which are markedly larger than the average difference of 16.9 W m^{-2} for the entire study months (Figure not shown). Statistically significant differences between onshore and offshore Q_H averages are also present in August (mean of the differences = 15.9 W m^{-2}; $p < 0.0001$) and September (mean of the differences = 8.2 W m^{-2}; $p < 0.0001$). Overall, this significant difference between the means of the onshore and offshore Q_H highlights, once again, the strong advective influence of the Hudson Bay on the adjacent HBL region.

The spatially averaged monthly Q_H time series for offshore and onshore winds demonstrate the varying magnitude of Q_H anomalies over the four study months (Figure 2.13). The most rapid increase in Q_H occurs in June when the trends in offshore and onshore anomalies are 17.2 W m^{-2} (tau = 0.45, p = 0.00004) and 19.1 W m^{-2} (tau = 0.36, p = 0.001), respectively. The magnitude of the June offshore Q_H anomalies far exceeds all the other study months (July: tau = 0.27, p = 0.01, TSA = 6.2 W m^{-2}; August: tau = 0.26, p = 0.02, TSA = 4.9 W m^{-2}; September: tau = 0.04, p = 0.75, TSA = 0.5 W m^{-2}), and is more than a factor of three larger than the average for the entire study months (5.4 W m^{-2}). Similarly, the magnitude of the June onshore Q_H anomalies is over twofold greater than that of July (tau = 0.32, p = 0.004, TSA = 9.3 W m^{-2}), over fourfold greater than August (tau = 0.16, p = 0.15, TSA = 4.4 W m^{-2}) and over threefold that of September (tau = 0.28, p = 0.01, TSA = 6.0 W m^{-2}). Overall, these trends in Q_H anomalies are significant in all study months except August for onshore winds and September for offshore winds. Even though the trends in the monthly Q_H anomalies generally suggest larger trends for onshore winds compared to offshore winds, there is no statistically significant trend in the mean difference between onshore and offshore Q_H for all the study months (Figure not shown). Nevertheless, it is important to note the positive trend of 4.1 W m^{-2} in September (tau = 0.19, p = 0.08) that is due to the differential trends in onshore (TSA = 6.0 W m^{-2}) and offshore (TSA = 0.5 W m^{-2}) Q_H anomalies.

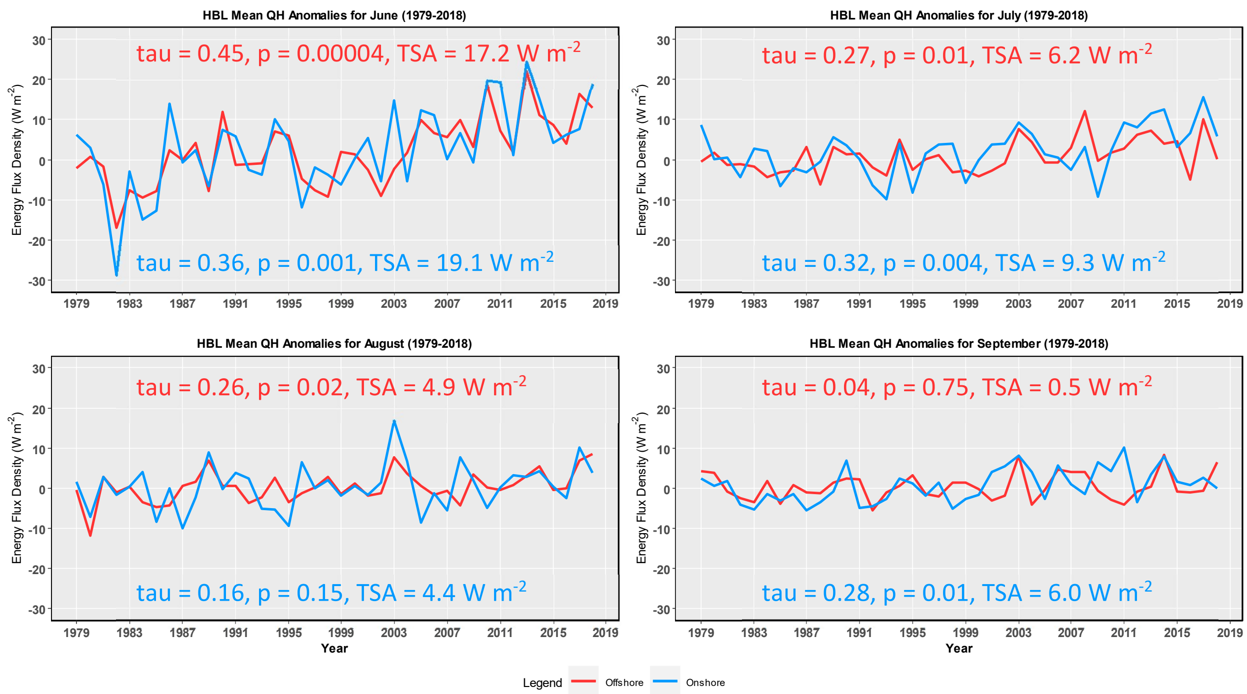

Figure 2. 13. Spatially averaged monthly sensible heat flux anomalies (June–September) over the HBL for the 1979–2018 period.

2.3.5 Latent Heat Flux

The spatially averaged latent or evaporative heat flux (Q_E) anomalies over the HBL during the period 1979–2018 show statistically significant upward trends for both offshore and onshore winds (Figure 2.14). The average Q_E anomalies during offshore winds have increased by 7.2 W m^{-2} (tau = 0.29, p = 0.01), while onshore Q_E anomalies have risen by 6.1 W m^{-2} (tau = 0.27, p = 0.01). The trends in offshore Q_E are only slightly larger than the onshore Q_E anomalies, and therefore, there are no significant trends in the mean differences between onshore and offshore Q_E (tau = -0.08, p = 0.49, TSA = -1.1 W m^{-2}) over the study period (Figure not shown).

However, the mean difference between onshore and offshore Q_E is negative throughout the study period, indicating that the average Q_E during onshore winds are consistently smaller than their offshore counterpart.

The monthly average Q_E for each of the four study months show that offshore Q_E (median = 82.6 W m^{-2} for June, 91.4 W m^{-2} for July, 71.0 W m^{-2} for August, and 39.2 W m^{-2} for September) are considerably larger than onshore Q_E (median = 60.6 W m^{-2} for June, 71.9 W m^{-2} for July, 56.2 W m^{-2} for August, and 30.9 W m^{-2} for September) in all months (Table 2.1). For the study months, average Q_E during onshore winds is 52.7 W m^{-2} compared to 68.6 W m^{-2} during offshore winds (mean of the differences = -15.9 W m^{-2}, $p < 0.0001$). The time-series analysis of the individual study months over the past 40 years (Figure not shown) demonstrates that the largest difference between the mean onshore and offshore Q_E occurs in June (mean of the differences = -20.8 W m^{-2}; $p < 0.0001$) and July (mean of the differences = -19.1 W m^{-2}; $p < 0.0001$). Statistically significant differences between onshore and offshore Q_E averages also persists in August (mean of the differences = -15.0 W m^{-2}; $p < 0.0001$) and September (mean of the differences = -8.6 W m^{-2}; $p < 0.0001$). It is important to observe here that the magnitude of these monthly differences between the mean onshore and offshore Q_E are similar to those of the sensible heat flux, though the sign of the difference is reversed.

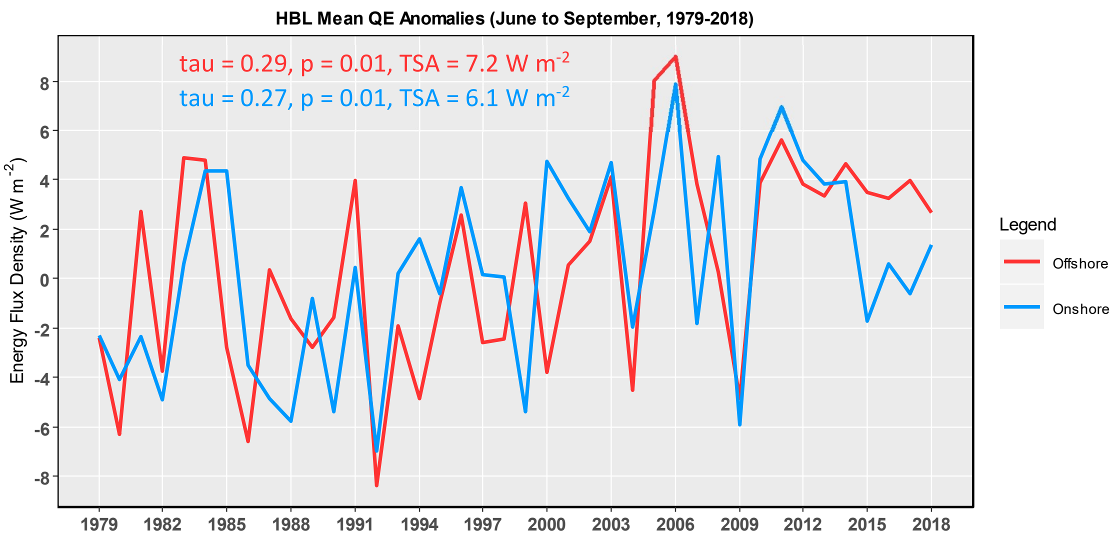

Figure 2. 14. Spatially averaged latent heat flux anomalies over the HBL (June–September) during the period 1979–2018.

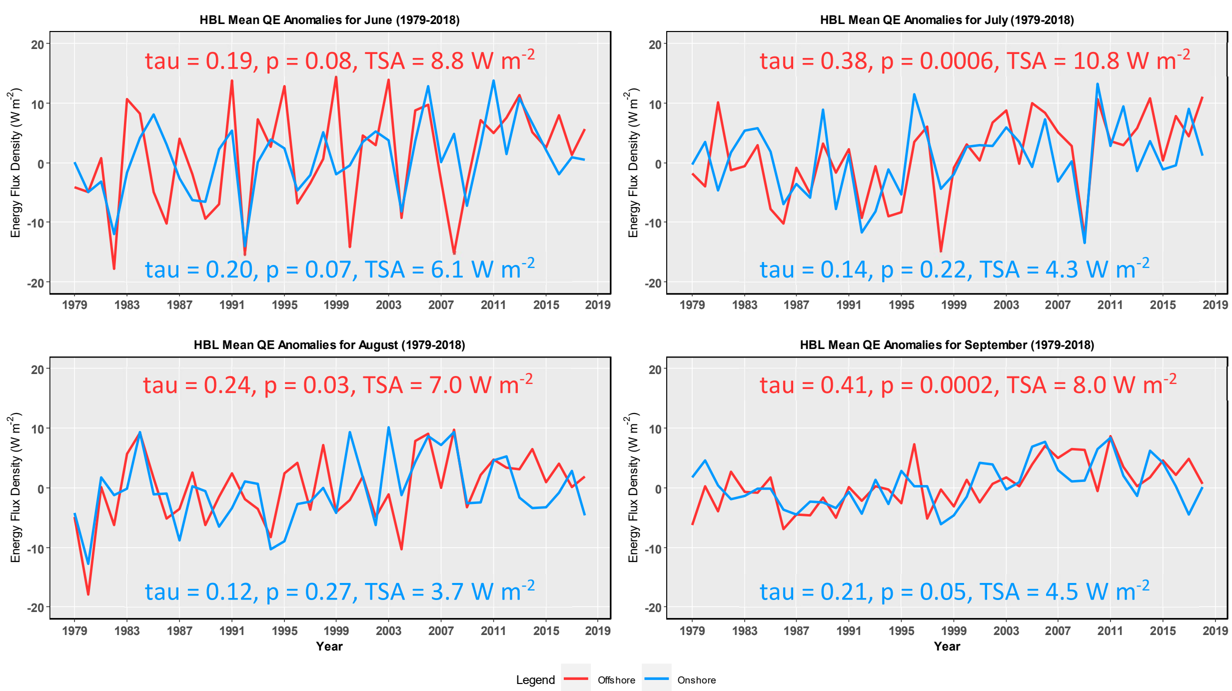

Figure 2. 15. Spatially averaged monthly latent heat flux anomalies (June–September) over the HBL for the 1979–2018 period.

The spatially averaged monthly Q_E time series for offshore and onshore winds demonstrate the varying magnitude and significance of Q_E anomalies over the individual study months (Figure 2.15). The largest increase in Q_E trends occurs during offshore winds where Q_E anomalies have risen by about 8 to 11 W m^{-2} over the forty-year study period. These offshore Q_E trends are significant in the months of July (tau = 0.38, p = 0.0006, TSA = 10.8 W m^{-2}), August (tau = 0.24, p = 0.03, TSA = 7.0 W m^{-2}) and September (tau = 0.41, p = 0.0002, TSA = 8.0 W m^{-2}), but marginally non-significant in June (tau = 0.19, p = 0.08, TSA = 8.8 W m^{-2}). On the other hand, the trends in the monthly onshore Q_E anomalies are overall not statistically significant at the 95% confidence level, though it is noteworthy to highlight the trends in June (tau = 0.20, TSA = 6.1 W m^{-2}) and September (tau = 0.21, TSA = 4.5 W m^{-2}), where p = 0.07 and 0.05, respectively. Although the trends in monthly Q_E indicate larger trends for offshore winds compared to onshore winds in all the study months, only the mean difference for July between onshore and offshore Q_E (tau = -0.23, p = 0.04, TSA = -7.1 W m^{-2}) has a significant trend (Figure not shown). This implies that in July, offshore evaporation rates are rising faster than their onshore counterpart over the 40-year study period.

2.3.6 Ground Heat Flux

The spatially averaged ground heat flux (Q_G) anomalies over the four months combined during the period 1979–2018 show a statistically significant upward trend for onshore winds (tau = 0.28, p = 0.01, TSA = 2.1 W m^{-2}), while the upward trend for offshore winds (tau = 0.19, p = 0.08, TSA = 1.5 W m^{-2}) is marginally non-significant (Figure 2.16). This suggests that the onshore anomalies in ground heating have increased faster than the offshore anomalies. Arguably, the first half of the study period is overall characterized by negative Q_G anomalies for both offshore and onshore winds, but a general shift to positive Q_G anomalies occurred around the beginning of the 21st century. Once again, this transition from negative to positive Q_G anomalies roughly around the year 2000 is analogous to those of the wind frequency, temperature, wind speed and sensible heat flux trends over the HBL.

Since the trend in onshore Q_G is only slightly larger than that of the offshore winds, there is no significant trend in the mean difference between onshore and offshore Q_G (tau = 0.06, p = 0.60, TSA = 0.3 W m^{-2}) over the study period (Figure not shown). However, the mean difference between onshore and offshore Q_G is negative throughout the study period, indicating that the average Q_G during onshore winds is systematically smaller than the offshore counterpart.

The daily average Q_G for each of the four study months show that offshore Q_G (median = 20.5 W m^{-2} for June, 14.5 W m^{-2} for July, 10.3 W m^{-2} for August, and 2.7 W m^{-2} for September) are considerably larger than onshore Q_G (median = 10.5 W m^{-2} for June, 8.3 W m^{-2} for July, 3.3 W m^{-2} for August, and -2.7 W m^{-2} for September) in all months except September when the fluxes are equal, but opposite (Table 2.1). Here, the negative onshore Q_G in September signifies that the flux is moving towards the surface, in the direction of lower temperatures. Under both wind regimes, the pattern exhibited shows maximum ground warming in June with diminishing ground heat fluxes as the season progresses. For the study months as a whole, average Q_G during onshore winds is 4.0 W m^{-2} compared to 11.4 W m^{-2} during offshore winds (mean of the differences = -7.3 W m^{-2}, $p < 0.0001$). The mean differences between onshore and offshore Q_G averages are statistically significant in all the study months (Figure not shown). The largest difference of -10.1 W m^{-2} ($p < 0.0001$) between the mean onshore and offshore Q_G occurs in June, compared to -6.6 W m^{-2}, -7.1 W m^{-2} and -5.6 W m^{-2} in July, August and September, respectively.

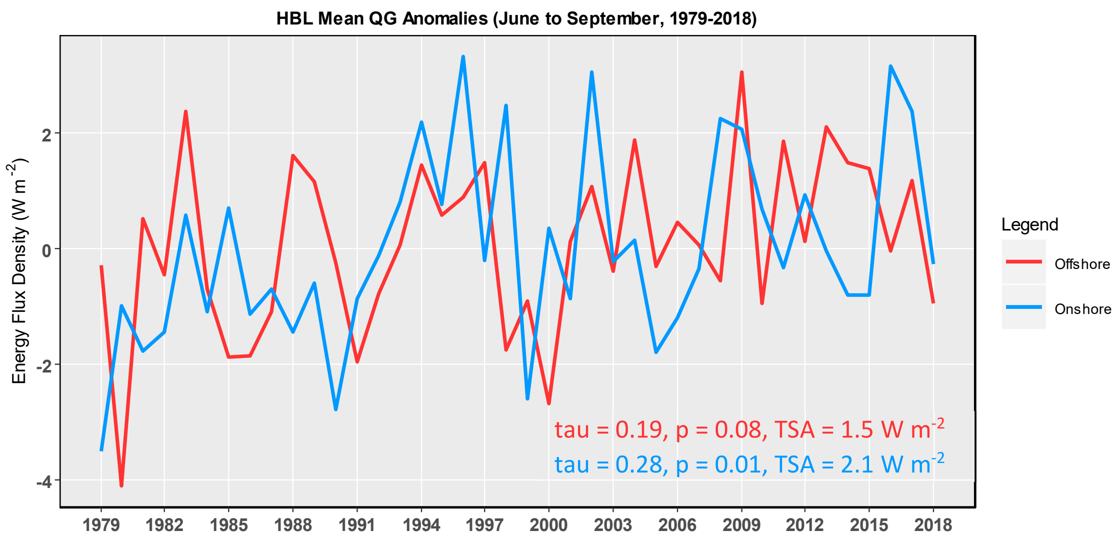

Figure 2. 16. Spatially averaged ground heat flux anomalies over the HBL (June–September) during the period 1979–2018.

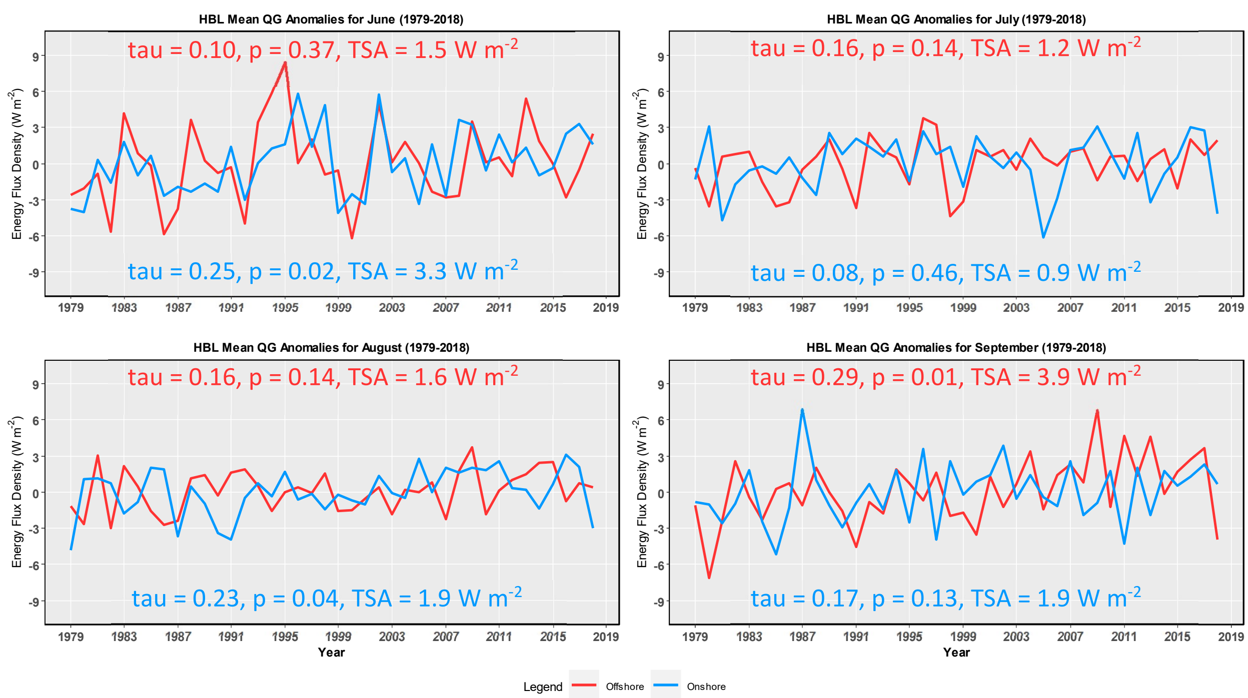

Figure 2. 17. Spatially averaged monthly ground heat flux anomalies (June–September) over the HBL for the 1979–2018 period.

The spatially averaged monthly Q_G time series for offshore and onshore winds demonstrate the varying magnitude and significance of Q_G anomalies over the four study months (Figure 2.17). On the one hand, the upward trends in offshore Q_G are only significant in September, corresponding to a reduction in the active layer cooling/refreezing rates, where the Q_G anomalies have increased by approximately 4 W m^{-2} (tau = 0.29, p = 0.01) over the 40 years; this is more than a factor of two larger than the Q_G average for the entire season. On the other hand, the upward trends in the monthly onshore Q_G are significant in June and August where the Q_G anomalies have increased by 3.3 W m^{-2} (tau = 0.25, p = 0.02) and 1.9 W m^{-2} (tau = 0.23, p = 0.04), respectively, corresponding to an enhancement of active layer warming/melting rates. Overall, there is no statistically significant trend in the difference between onshore and offshore Q_G in any of the study months (Figure not shown).

2.4 Discussion

2.4.1 Contrasting Thermal and Moisture Properties of Wind Regimes

The results of this study provide valuable insights into the climatic changes in the advective role of the Hudson Bay on the Hudson Bay Lowlands over the 1979–2018 study period. Here, it is quite certain that global warming is causing significant changes in the mesoscale wind regimes and consequently, impacting the surface energy balance in the study region. The results show that offshore winds are characterized by significantly higher air temperatures compared to onshore winds. This is because the land surface during the summer months heats up more rapidly than the Bay due to its lower heat capacity and a faster thermal response. On the other hand, the solar radiation incident on the Bay must be transmitted to great depths and used for warming the entire water column, which delays a rise in water and air temperature. The energy absorbed by the Bay is also largely diffused by convective mixing and horizontal advection within the water body.

The contrasting thermal and moisture properties between the HBL and the Hudson Bay strongly influences the partitioning of net radiation between Q_H, Q_E and Q_G. The spatially averaged convective and ground heat fluxes over the study period demonstrate that offshore wind regimes are characterized by significantly larger Q_E and Q_G fluxes, while the onshore winds have significantly higher Q_H fluxes in all months throughout the study period. This energy partitioning is a result of the quantitative relationship between the vertical air temperature and vapour pressure gradients during offshore and onshore wind regimes in the HBL. A stronger atmospheric temperature gradient promotes Q_H, while a stronger vapour pressure gradient favours Q_E.

The onshore winds are relatively cool and moist compared to the warm and dry offshore winds. On the one hand, the arrival of the relatively cool and moist onshore winds over the HBL increases the vertical air temperature gradient over the land (cold air mass aloft, warm land surface beneath), but decreases the vapour pressure gradient (moist air mass above, wet surface below). As a result, onshore winds enhance Q_H and suppress Q_E. On the other hand, the arrival of offshore winds decreases the vertical air temperature gradient over the HBL (warm air mass aloft, hot surface beneath), but increases the vapour pressure gradient (dry air mass above, wet surface below). Consequently, offshore winds strengthen Q_E and repress Q_H. Additionally, Q_G is lower during onshore winds since the regime promotes an increase in the upward sensible heat flux via convection and a corresponding decrease in the downward ground heat flux via conduction. These results are consistent with previous studies in the HBL (Delidjakova et al., 2016)

2.4.2 Differential Warming Trends and Increased Frequency of Onshore Winds

The present study demonstrates that the HBL has long been dominated by offshore wind regimes which are characterized by significantly higher air temperatures, evaporation and ground heat fluxes compared to the onshore winds. However, the wind frequency anomalies for the 1979–2018 period reveal a strong and significant downward trend (-6.8%, $p < 0.01$) in offshore winds and a corresponding increase in the frequency of onshore winds. The overall shift from negative to positive onshore wind anomalies became apparent by the beginning of the 21st century. Even more striking is the monthly wind frequency over the study period which reveals that offshore wind occurrences are much higher than onshore winds in July, August and September, but not in June. In fact, the trends in onshore wind frequency are only significant in June when the onshore winds have increased by a staggering 17.4% ($p = 0.03$) over the past 40 years. The equivalent decrease in the offshore wind frequency anomalies implies that the difference between offshore and onshore wind frequency has decreased by as much as 34.8% in June over the study period. Therefore, it is crucial to note that the dominant wind regime in the HBL has shifted from offshore to onshore winds in June. One can reasonably argue that a similar situation is emerging in July.

Temperature anomalies over the HBL during the period 1979–2018 show statistically significant upward trends for both offshore and onshore winds. However, the offshore temperature anomalies (TSA = 2.1 °C) are increasing at a faster rate than the onshore temperature anomalies (1.7 °C). The monthly average temperature anomalies further demonstrate that the most rapid warming is occurring in June and September for both offshore and onshore winds. These trends in temperatures are much higher for offshore winds than onshore winds—June (Offshore TSA = 3.2 °C; Onshore TSA = 2.2 °C) and September (Offshore TSA = 3.4 °C; Onshore TSA = 2.8 °C). Here, two interesting features are revealed. First, the increase in temperature for both offshore and onshore winds is evidently due to global warming and the Arctic amplification. Second, the differential warming trends between offshore and onshore winds can be attributed to the land-ocean contrast in surface warming. These two key features of the temperature trends in the HBL are discussed separately.

The rising trends in temperature anomalies for both offshore and onshore winds over the HBL are consistent with warming trends across the Arctic and Subarctic regions, where the annual mean temperatures have increased by about twice the rate of the global average (ACIA 2005; Richter-Menge et al., 2019). The polar amplification is due primarily to the snow- and sea ice-albedo feedback, triggered by an increase in the atmospheric concentration of greenhouse gases and the associated rise in air temperatures (Serreze and Barry, 2011). The temperature changes have influenced the onset of snowfall and the accumulation of seasonal snow, as well as the timing, duration and intensity of snowmelt periods (Derksen et al., 2018). Consequently, the most rapid warming trends have occurred in the shoulder seasons (October–November and May–June) and snow cover fraction and seasonal snow accumulation have both decreased by 5% to 10% per decade between 1981–2015, due to later snow onset and earlier spring melt in the Canadian high latitudes (Vincent et al., 2015; Thackeray et al., 2016; Mudryk et al., 2018). In this present study, the strongest warming trends over the HBL are in June and September—which are the transition periods in the four study months.

Similar changes in the cryosphere during late spring and autumn have occurred over the Hudson Bay, where the seasonal sea ice is particularly sensitive to climate warming. Sea ice typically starts to form in the Hudson Bay around late October to early November, while melting begins around late May to early June (Gagnon and Gough, 2005). However, a significant increase in surface air temperatures over the Bay since the mid-1990s has resulted in changing patterns of seasonal sea ice breakup and freeze-up. Hochheim and Barber (2014) demonstrated that for every 1 °C increase in surface air temperatures, the sea ice extent decreases by 14% (% of the basin area) within the Hudson Bay. The research study by Kowal et al. (2017) concluded that the breakup date is occurring earlier, on average −0.49 days per year, and the freeze-up occurring later, on average 0.46 days per year. These trends towards earlier sea ice breakup and later freeze-up have led to a significantly longer ice-free season, on average 0.91 days per year. These previous findings are consistent with the rapid warming trends shown here in this study, particularly during the June and September transition months.

Previous studies have also shown that surface temperatures over the land have been increasing more rapidly than over the sea in response to rising levels of greenhouse gases as demonstrated here in the HBL (Cubasch et al., 2001; Braganza et al., 2003, 2004). The enhanced warming over land is a robust feature of climate model simulations over the twenty-first century, where the global mean land/sea warming ratios are in the range of 1.36–1.84 (Sutton et al., 2007; Joshi et al., 2008). The land–sea contrast in surface temperature response to climatic change is partially attributable to the differing thermal inertias of the two surface types since the sea has a larger heat capacity and mixes heat more readily. However, this land–sea warming contrast is not simply a transient effect but also persists in equilibrium simulations of climate change. The phenomenon is therefore not primarily a consequence of the large effective thermal inertia of the sea, rather, it is predominantly due to moisture availability and feedbacks in the hydrological cycle (Manabe et al., 1991; Joshi et al., 2008).

Under global warming, the increase in atmospheric CO_2 concentration and direct radiative forcing, as well as increased trapping of outgoing longwave radiation and reduction in surface albedo, cause an anomalous energy absorption by the land and ocean surfaces. This anomalous surface energy gain must be balanced by an equivalent anomalous surface energy loss. Sutton et al. (2007) argued that to balance the anomalous surface energy budget over the sea, it is more probable that most of the additional energy will be used to increase evaporation and therefore enhance the upward Q_E. Conversely, the limited surface moisture availability over land promotes surface cooling by dry Q_H and longwave radiative flux. The additional energy is therefore used to raise the surface air temperature in order to balance the anomalous surface energy budget over the land. Thus, the differences in the surface energy budget over the land and sea reasonably accounts for the existence of a warming contrast between the offshore and onshore winds in the HBL.

Furthermore, Joshi et al. (2008) argued that the limited moisture availability over land causes differential changes in the lapse rates upon warming over the land and sea. This is because the tropospheric lapse rate is strongly dependent on temperature and humidity. The atmospheric humidity profile over the sea is often saturated and thus the lapse rate ($\Gamma = -dT/dz$) is usually lower over the sea compared to land—since the saturated adiabatic lapse rate (Γ_S) is less than the dry adiabatic lapse rate (Γ_D). On the one hand, an increase in temperature under global warming causes an exponential increase in the saturation vapour pressure (due to the Clausius–Clapeyron relationship) resulting in a decrease in Γ_S (Holton, 1992). On the other hand, Γ_D is independent of the saturation vapour pressure and does not decrease when the climate is warmed. This implies that the so-called moist adiabatic lapse rate (Γ_M) over land, being closer to Γ_D, decreases less than the Γ_S. Hence, the magnitude of the decline in the lapse rate over the sea due to climate warming is larger than the decrease over the land. The air surface temperature will consequently increase more slowly over the sea than over land (Joshi et al., 2008).

The land–sea contrast in surface temperature response to climatic change can also be caused by elevated atmospheric CO_2 concentrations which increases stomatal resistance and thus inhibits evaporation over the land (Sellers et al., 1996; Cox et al., 1999). Climate model simulations have shown that this dependence of stomatal resistance on CO_2 concentration amplifies the magnitude of the land–sea temperature contrast, and the reduction in evaporation from vegetation results in more rapid warming over the land surface (Joshi and Gregory, 2008; Joshi et al., 2008). This is because to offset the restricted evaporative cooling, a higher land surface temperature is required to increase Q_H and upward longwave radiation.

The differential warming trends between offshore and onshore winds in the HBL suggests that the enhanced temperature contrast between the land and sea is very likely responsible for the significant increase (decrease) in the frequency of onshore (offshore) winds. The higher trend in the offshore temperature anomalies strengthens the horizontal temperature and pressure gradient between the land and sea surfaces (the pressure gradient is directed towards the land at low levels) thereby increasing the frequency and strength of sea breezes. This argument is further supported by the fact that the daily average temperatures for each of the study months which shows that the mean temperature difference between offshore and onshore winds is greatest in June (5.1 °C), decreasing through July (4.2 °C), August (3.2 °C) and September (1.5 °C), corresponds to the monthly average wind frequency where the occurrence of onshore (offshore) winds decreases (increases) from June to September. The strong horizontal temperature gradient in June is due to the land–sea albedo difference and can be attributed to the presence of sea ice over the Hudson Bay—breakup starts in late May to early June, and sea ice persists until late July—while the snowmelt season over the adjacent HBL is essentially over.

In addition, the monthly average temperature anomalies show that the most rapid warming for both offshore and onshore winds is occurring in June and September, but the largest mean difference between the warming trends is in June when the offshore temperature trend exceeds that of onshore winds by 1 °C. The month of June thus has both a higher mean temperature difference between offshore and onshore winds, as well as a stronger land–sea surface warming contrast. Consequently, the largest and most significant upward trend in onshore wind frequency (17.4%) over the study period occurred in June, when the dominant wind regime in the HBL has now shifted from offshore to onshore winds. The frequency of onshore winds in the HBL is therefore largely influenced by the magnitude of the temperature difference between offshore and onshore winds, as well as the land/ocean warming ratio in response to climate change. This simple argument to explain the considerable increase in the frequency of onshore winds in the HBL is consistent with the view of Sutton et al. (2007) who suggested that the land–sea temperature difference would increase as the global climate warms and could have local effects such as stronger sea breezes.

It is important to recognize that other factors could also contribute to the increased frequency of onshore winds in the HBL, such as changes in the distribution of large-scale air masses in the region. Leung and Gough (2016) examined the linkages between changes in air mass distribution and warmer temperature trends in the Hudson Bay/Foxe Basin region and found a declining frequency of the dry polar (DP) air mass—originating from northern Canada or the Arctic, with a corresponding increase in the moist polar (MP) air mass—originating from North Atlantic Ocean or probably generated locally over the Hudson Bay. The decrease in the frequency of DP air mass in the fall season coincides with an increasing ice-free season, indicating that DP is being replaced by locally produced MP air mass. Leung and Gough (2016) argued that the reduction of DP air mass in winter could be related to changing atmospheric dynamics due to climate warming and Arctic amplification, and associated shifts in the locations of atmospheric Rossby waves (Francis and Vavrus 2012; Francis and Vavrus, 2015).

Not much has changed in the wind speeds in the HBL over the study period. The increasing trends in the four study months average wind speed for both offshore and onshore winds is not significant. However, the results show noticeable trends in July when wind speeds have risen by about 0.5 ms^{-1} for offshore winds (tau = 0.20, p = 0.07) and 0.6 ms^{-1} (tau = 0.38, p = 0.001) for onshore winds over the study period. The occurrence of the most significant and strongest wind speed trend in July during onshore regimes is probably due to the large disproportionate warming rate of the offshore winds. Over the study period, the offshore mean temperature anomalies in July are 1.3 °C (p = 0.08) higher than their onshore counterpart, and this is the largest difference in the temperature trends between offshore and onshore winds during the four-study months. This slower onshore warming rate in July could be attributed to a lag in surface warming over the Hudson Bay as the enhanced net radiation is used entirely for melting the sea ice. Bello and Higuchi (2019) also found evidence for this so-called zero-curtain effect during the active melt period over the Hudson Bay, when the energy that would otherwise warm the atmosphere is largely consumed by the latent heat of fusion. The higher trend in the July offshore temperatures would intensify the horizontal temperature and pressure gradient between the land and sea and consequently, increase onshore (and to a lesser extent, offshore) wind speeds. This has also contributed to the considerable increase (10.7%) in the frequency of onshore winds in July over the study period.

2.4.3 Changes in the Advective Influence of the Hudson Bay

Important changes have occurred in the energy balance of the HBL over the last 40 years. The average Q_H anomalies for the four study months have risen by 5.4 W m^{-2} and 11.4 W m^{-2} during offshore and onshore winds, respectively. The highest and most significant Q_H trends of 17.2 W m^{-2} and 19.1 W m^{-2} are found in June for offshore and onshore winds, respectively. The general increase in Q_H trends corresponds to the positive temperature trends in the study region. Climate warming and the decline in surface albedo in the High latitudes not only increase the amount of available net radiation (Q*) but also increase the vertical temperature gradient ($\Delta T/\Delta Z$) since the atmosphere is stable and warming is mainly confined to the lower troposphere (Screen et al., 2012; Pithan and Mauritsen, 2014). As a result, more energy is directed towards warming the atmosphere via Q_H. The average onshore Q_H anomalies have increased over twice as much as the offshore Q_H anomalies over the study period. This is in agreement with the dominant role Q_H plays during onshore winds—due to the greater vertical temperature gradient compared to offshore wind regimes—as shown in the average Q_H for all the study months. Moreover, the higher land warming rates during offshore winds, caused by the land–sea warming contrast, further strengthens the vertical temperature gradient during onshore wind regimes.

Significant trends in evaporation exist over the study period where the average Q_E anomalies for the four study months have increased by 7.2 W m^{-2} and 6.1 W m^{-2} during offshore and onshore winds, respectively. The overall increase in the Q_E trends corresponds to the positive trends in the temperature anomalies over the study region. Significant differences between onshore and offshore Q_E averages are found in all the study months, decreasing from June to September. The magnitude of these differences between onshore and offshore Q_E are similar—but opposite—to those of Q_H, suggesting that the energy that would otherwise be directed towards Q_H (Q_E) during offshore (onshore) winds has been used for Q_E (Q_H). The trends in the average offshore Q_E are much higher than those of the onshore winds, particularly in July, August and September. This is consistent with the overriding role of Q_E during offshore winds—due to the stronger vertical vapour pressure gradient—as shown in the daily Q_E averages for all the study months. The largest, and only significant trend, in the mean difference between onshore and offshore Q_E occurred in July (-7.1 W m^{-2}). This corresponds with the trends in temperature and wind speed anomalies in July as described earlier, where there was a large disproportionate warming rate for offshore winds and increased wind speeds over the study period.

The energy that goes into warming the ground is particularly important in the HBL due to its role in melting the active layer of permafrost during the summer. The average Q_G anomalies for the four study months have increased by 1.5 W m^{-2} and 2.1 W m^{-2} during offshore and onshore winds, respectively, over the past 40 years. The larger subsurface warming trend for onshore winds is contrary to what was initially expected. However, it is clear from the foregoing analysis that June dominates active layer development, contributing approximately 44% of the net seasonal flux over the past 40 years. The 17% increase in the frequency of onshore winds during this month has been accompanied by an increase in Q_G of 3.3 W m^{-2} and therefore the influence on seasonal ground warming could be anticipated given the increased likelihood of onshore winds during the summer solstice. Nevertheless, this has been dwarfed by the increase in the onshore sensible heat flux of 19.1 W m^{-2}, which suggests that the advective influence of the Bay, favours energy loss to the atmosphere by a factor of approximately 5.8.

The seasonal average Q_G for the period 1979–2018 shows that offshore Q_G averages are almost threefold greater than onshore Q_G averages over the HBL. This is because of the considerably larger vertical soil temperature gradient during offshore wind regimes owing to higher surface temperatures. One would expect therefore that as the climate warms and more radiant energy is available, the trends in offshore Q_G would be larger than their onshore counterpart. Although this is the case in September when the trends in offshore Q_G are over twofold that of the onshore winds, the month of June is characterized by onshore Q_G trends that are more than a factor of two larger than the offshore trends.

So what has been the net impact of the changing wind regimes? The non-directional energy budget analysis (Figures not shown) indicates that the mean air temperature anomalies have increased by 1.6 °C ($p < 0.001$) over the last 40 years in the HBL. The mean Q_H anomalies have increased by 8.9 W m^{-2} (or 20%, $p < 0.0001$) over the same period. Also, there has been an increase in evaporation over the study period with Q_E anomalies showing a positive trend of about 6.5 W m^{-2} (or 10%, $p < 0.01$). There has also been a seasonal increase in ground warming of about 1.6 W m^{-2} (or 18%, $p = 0.02$) over the 1979–2018 study period. These trends suggest that the shift in wind regimes are having a considerable net impact on the HBL. Additionally, the largest changes in the combined (on- and off-shore) temperature and surface energy fluxes are, overall, occurring in September. This is in agreement with previous studies which showed that the biggest change in the open water season over the Hudson Bay is occurring in the fall, not in the spring period (Hochheim and Barber 2014; Bello and Higuchi 2019). It has also been reported that in the last decade there is an accelerated warming trend in fall temperatures and a dramatic delay in sea ice freeze-up dates (on average by 0.46 days per year) over the Hudson Bay (Hochheim and Barber 2014; Kowal et al. 2017). This present study suggests that the permafrost active layer in the HBL does not seem to be responding much to warming in the spring and summer, whereas it is taking longer for it to freeze back in the fall.

2.5 Conclusion

It is well-known that the Hudson Bay exerts a strong advective influence on the adjacent HBL region. Until now, the temporal and spatial impact of climate change on the mesoscale wind regimes in the HBL and the associated consequences on the surface energy balance was poorly understood. This research study addresses these pressing concerns and provides insights into potential implications of future climate changes in the HBL.

First, this study demonstrates that there are significant changes in the advective role of the Hudson Bay. The spatially averaged wind frequency anomalies over the HBL reveal a strong increasing (decreasing) trend in onshore (offshore) winds of about 7% over the study period. The four study month average difference between offshore and onshore wind frequency suggests the dominance of the offshore wind regimes persists to the present day, but have significantly declined by about 14% over the past 40 years. The most rapid changes occur in June when the frequency of onshore winds have increased by about 17% over the study period. These significant changes in the wind regimes in June is quite striking, as it implies that the average difference between offshore and onshore wind frequency has decreased by as much as 35% over the study period. Consequently, there has been a shift from offshore winds dominance to onshore winds dominance in June over the HBL.

Previously published research studies (Rouse and Bello, 1985; Delidjakova et al., 2016) had anticipated that global warming and sea ice decline would cause an increase in the frequency of offshore winds in the HBL. It was suggested that a higher frequency of offshore winds would diminish the advective role of the Hudson Bay on the HBL, giving rise to much higher temperatures, accelerated permafrost degradation and a weakening of the carbon sink in the region. This present study provides evidence that, on the contrary, there has been a significant and profound increase in the frequency of onshore winds due to the land–sea warming contrast in response to climate change. The study results show that the changes in the mesoscale wind regimes and surface energy balance of the HBL under present and projected climate warming are markedly different than was previously thought.

Second, this research study demonstrates that there are significant positive trends in the temperature, sensible, latent and ground heat fluxes over the HBL, and the magnitude and strength of these trends vary considerably between offshore and onshore wind regimes. The offshore temperatures are increasing at a faster rate than onshore temperatures as a consequence of the land–sea contrast in surface temperature response to climatic change. The most rapid temperature increase occurs in June and September, and the largest warming contrast between offshore and onshore winds is found in July. The much slower onshore warming rate in July is attributed to a lag in surface warming over the Hudson Bay caused by the zero-curtain effect during sea ice melt. The wind speed anomalies suggest that though offshore and onshore winds exhibit no significant trends in the four study month averages as a whole, there is a statistically significant trend in the July onshore wind speeds due to the large disproportionate warming of offshore winds.

The spatially averaged surface energy fluxes show that the onshore Q_H anomalies are over twice as high as the offshore anomalies. The most rapid increase in Q_H occurs in June, and the largest difference between onshore and offshore Q_H trends is found in September. By contrast, the trends in the offshore Q_E are slightly greater than the onshore trends, and the largest difference between onshore and offshore Q_E anomalies is found in July. Additionally, the trend in the onshore Q_G is higher than the offshore trend. The most rapid increase in onshore Q_G occurs in June when the onshore Q_G trend is more than a factor of two higher than the offshore trend. In September, however, the offshore Q_G anomalies are over twofold that of the onshore anomalies.

These research findings have important implications for permafrost thaw, evaporation, soil moisture changes and peatland carbon losses across the HBL. It is uncertain if there will be significant spatial variations in the magnitude and strength of the observed changes in mesoscale winds and temperatures over the HBL, given the diverse hydro-geomorphic landscape and peatland types in the region. Moreover, the changes in the advective influence of the Hudson Bay on the adjacent lowlands may vary considerably across the region due to the spatial pattern of sea ice breakup and freeze-up over the Bay, and proximity to the coast. Further research is therefore needed to address these uncertainties.

Chapter 3

Spatial Heterogeneity in the Magnitude and Strength of the Impacts of Wind and Temperature Changes across the Hudson Bay Lowlands

Abstract

The climate of the Hudson Bay Lowlands (HBL) is strongly influenced by the adjacent Hudson Bay. The persistence of sea ice in the Hudson Bay until late July contributes to the presence of permafrost along the western coast of the HBL where the southern limit of continuous permafrost lies parallel to the coast. Onshore winds originating from the Bay are comparatively cold and wet relative to the warm and dry offshore winds. The contrasting temperature and humidity properties of the wind regimes influence the partitioning of net radiation between the sensible, latent and ground heat fluxes over the HBL. This study builds on the earlier work (Chapter 2; Balogun et al. (2021), manuscript under review) on the mesoscale wind and temperature trends in the HBL as a whole. The previous study showed that climate warming has resulted in significant changes in the advective influence of the Hudson Bay on the surface energy balance in the HBL. This present study examines the spatial variations in the observed changes in winds and temperatures, given the diverse hydro-geomorphic landscape and peatland types in the region during the snow-free season of June through September. The results show that there is considerable spatial heterogeneity in the magnitude and strength of these climatic trends across the HBL region. I found that the onshore winds have not only increased in frequency but also penetrated further inland over the 1979–2018 study period. The largest and most statistically significant positive trends in the onshore winds occur in June, particularly in the inland areas of central and southern HBL. Spatial analyses of the trends in temperature and surface energy fluxes reveal several prominent hotspots found mostly along the coast and at the mouths of rivers such as Churchill, Severn and Winisk, as well as in an extensive narrow belt along the Ekwan and Attawapiskat Rivers in southern HBL. These research findings have important implications for permafrost dynamics and peatland carbon exchange in the HBL region.

3.1 Introduction

Recent climate warming has resulted in observed changes in the atmosphere, ocean, and land surface, though these changes have not occurred uniformly across the globe. The northern high-latitudes have experienced the most severe climatic changes due to the Arctic amplification, associated with decreases in sea ice and snow cover, northward advection of heat and moisture, and changes in summer cloud cover (Serreze and Barry, 2011; Pithan and Mauritsen, 2014; Stuecker et al., 2018). Warming in the Arctic and Subarctic has led to changes in seasonal sea ice breakup and freeze-up in the Hudson Bay, and the lengthening of the open water season (Gagnon and Gough, 2005; Hochheim and Barber 2014; Kowal et al. 2017).

The Hudson Bay Lowlands (HBL) is a vast wetland region where the climate and ecology are strongly regulated by the presence of sea ice on the Hudson Bay. The onshore winds blowing from the Bay towards the HBL are comparatively cold and moist relative to the warm and dry offshore winds. These contrasting thermal and moisture properties of the wind regimes have been shown to influence the surface energy balance of the HBL (Rouse and Bello, 1985; Lafleur and Rouse, 1988; Delidjakova et al., 2016). The research studies found that onshore winds were associated with higher sensible heat flux (Q_H) compared to offshore winds, while the latent heat flux (Q_E) was higher during offshore winds over the HBL. Rouse et al. (1987) demonstrated at a coastal site near southern James Bay that the ground heat flux (Q_G) was about twice as large for offshore winds compared to onshore winds, with important implications for permafrost dynamics.

More recently, it was demonstrated that the warming-induced trends in sea ice duration over the Hudson Bay have resulted in significant changes in the advective influence of the Bay over the last 40 years, including increased frequency of onshore winds and greater warming during offshore winds (Chapter 2; Balogun et al. (2021), manuscript under review). That study found that the largest changes in wind frequency during the 1979–2018 period have occurred in June when the onshore winds have increased by 17%. Also, the highest temperature increases of over 3 °C were found in June and September during offshore winds. This has resulted in significant impacts on the surface energy balance, with contrasting trends between offshore and onshore wind regimes.

Although the mesoscale wind and temperature changes in the HBL have been studied, the spatial variations in the magnitude and strength of the observed climatic trends have not yet been investigated. It remains uncertain the extent to which various locations across the region have been impacted by the changes in the advective role of the Hudson Bay. The uneven rates of isostatic rebound and peat accumulation across the HBL (Martini, 2006; Packalen et al., 2014) have resulted in the development of diverse peatland types (e.g. fens and bogs) and microforms (e.g. hummocks, lawns and hollows) (Belyea and Clymo 2001; Harris et al., 2020). Moreover, the spatial variability of sea ice breakup and freeze-up over the Hudson Bay (Markham, 1986; Maxwell, 1986; Gagnon and Gough, 2005) suggests that its advective influence may vary substantially across the HBL.

In this study, I investigate the spatio-temporal pattern of the climatic trends induced by the changing advective influence of the Hudson Bay on the surrounding lowlands. The primary objectives of this study are to 1) examine the spatial variations in wind and temperature changes across the HBL region, 2) analyze the spatial heterogeneity in the magnitude and strength of the resulting changes in the surface energy balance, and 3) discuss the potential implications for permafrost thaw and peatland carbon dynamics.

3.2 Methodology

3.2.1 Climate Data

This study builds on the earlier research work from Chapter 2 (Balogun et al. (2021), manuscript under review) and thus shares a similar methodology. Briefly, climate data were obtained from the North American Regional Reanalysis (NARR)— a combined model and assimilated dataset, available on a 3 hourly, 32 km horizontal resolution (Mesinger et al., 2006). Daily averages of NARR meteorological variables used for this HBL study from June to September (1979-2018) include (i) Air temperature at 2 m (ii) U and V component of wind at 10 m (iii) Sensible heat flux at the surface (iv) Latent heat flux at the surface, and (v) Ground heat flux at the surface. The coordinates information and grid points corresponding to the HBL region were carefully extracted using ArcGIS. The climate and energy flux data for the HBL were extracted using R programming (R Core Team, 2019).

NARR datasets were partitioned into onshore and offshore winds based on the wind direction. Onshore winds were defined as winds blowing from the Bay towards the HBL, while offshore winds originated from inland. Generally, winds coming from the west and south were mostly offshore, while winds originating from the north and east were mostly onshore. Spatial analyses of the trends in the climate data were performed for a total of 194 grid locations (181 grid locations for Q_G) over the HBL for the 40-year study period for the months of June, July, August and September corresponding to the snow-free season.

3.2.2 Study Region Subdivisions

To assist in the description and interpretation of the results, the HBL region is roughly subdivided into three sections—with each boundary defined by a line perpendicular to the coastline and extending from the shore to the inland border of the HBL (Figure 3.1). First, the northern section or upper HBL, including the town of Churchill (Churchill River), Wapusk National Park, Port Nelson (Nelson River) and the York Factory (Hayes River). Second, the central section or middle HBL, extending from just south of the York Factory to Fort Severn (Severn River) and its environs. Third, the southern section or lower HBL, including the Polar Bear Provincial Park, Winisk and Peawanuck (Winisk River), Ekwan (Ekwan River) and Attawapiskat (Attawapiskat River), west of the Akimiski Island. In addition, the term *coastal HBL* is also used to distinguish the narrow subregion that occurs along the southern coast of the Hudson Bay from the rest of the broader HBL study region.

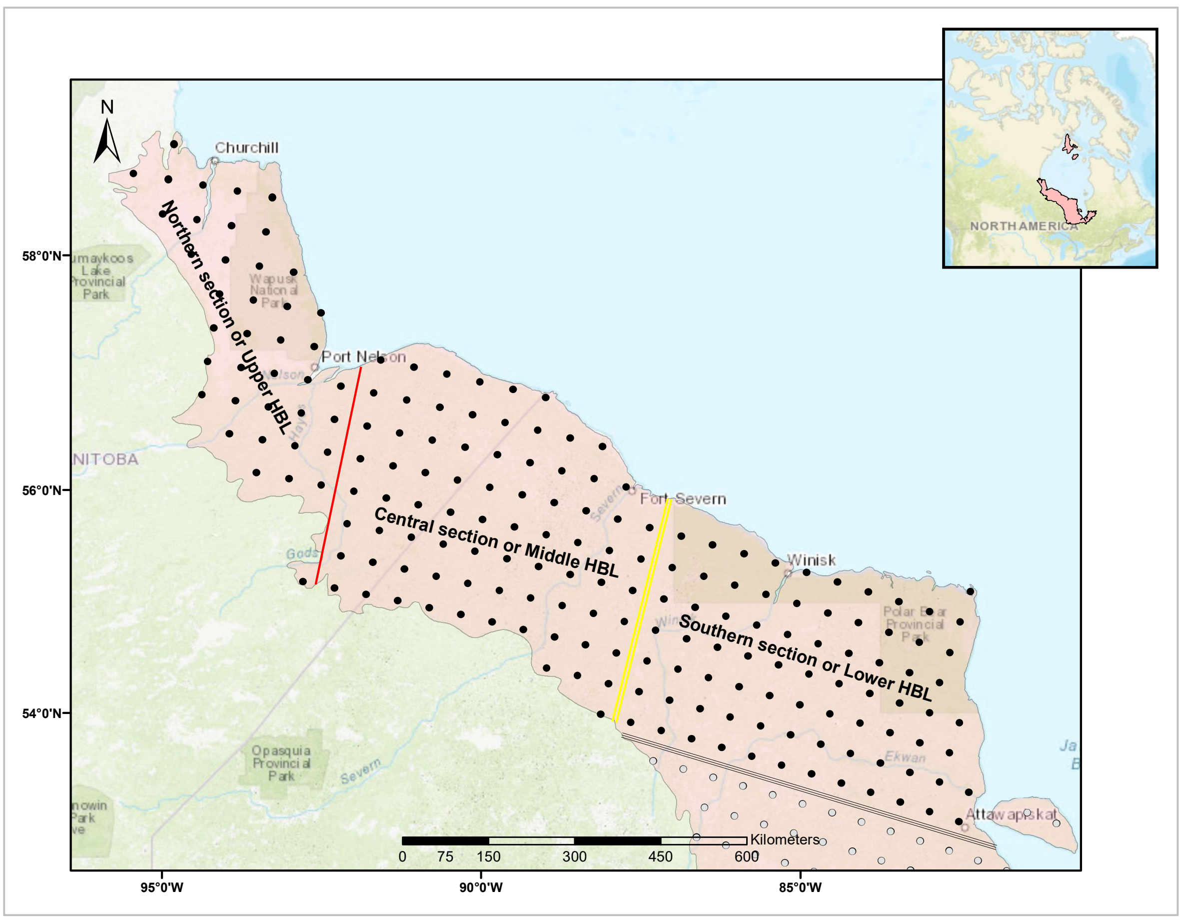

Figure 3. 1. Map showing the subdivision of the study region into roughly three sections: (i) Northern section or upper HBL, (ii) Central section or middle HBL, (iii) Southern section or lower HBL. Each boundary is defined by a line perpendicular to the coastline and extending from the shore to the inland border of the HBL. A total of 194 grid locations covering the "true" Hudson Bay Lowlands were used (black dots above the triple black line). The area below the triple black line with the grey dots is technically referred to as the James Bay Lowlands and was not included in this study.

3.2.3 Statistical Analysis

The Shapiro–Wilk (Shapiro and Wilk, 1965) and Kolmogorov-Smirnov (Massey, 1951) tests for normality and Q-Q plots were used to determine if the data were normally distributed. Since the datasets were not normally distributed (Kolmogorov–Smirnov, $p < 0.05$; Shapiro–Wilk, $p < 0.05$), non-parametric statistical methods were employed to analyze the data. The Mann-Kendall test (McLeod, 2011) was used for the detection of trends in the time series. The Kendall tau, (–1 to +1) represents the direction and strength of the linear trend while the p-value indicates the significance of the trend. In addition, the Theil-Sen slope approach (TSA; Sen, 1968; Hirsch et al., 1982) was used to compute estimates of the magnitude or rate of change of the trend. The trends are expressed as anomalies relative to the climate normal period 1981-2010. For the difference of means test, the Mann–Whitney *U* test was employed to test for significance. The trend and spatial analyses were conducted using the R environment for statistical computing (R Core Team, 2019). The statistical maps were created using the rworldmap and rworldxtra packages in R (South, 2011; South, 2012).

3.3 Results

3.3.1 Wind Frequency

The four study months average wind frequency anomalies for the 1979–2018 period show positive trends in onshore winds throughout the HBL (Figure 3.2, Table 3.1). The strength of these positive trends varies across the region with a median tau of 0.24 (Min tau = 0.15, Max tau = 0.32). The magnitude of the onshore wind frequency anomalies also varies spatially with a median increase of about 7.2% (Min TSA = 4.7%, Max TSA = 9.7%) over the study period. The grid locations which have the largest trends are described as areas above the upper quartile with onshore wind frequency anomalies exceeding about 7.9%. These positive trends in onshore winds are statistically significant (median p-value = 0.03) at 134 grid locations (out of 194) in the HBL.

Furthermore, the monthly spatial analysis demonstrates the varying magnitude and significance of onshore wind frequency anomalies during the study months. In June, there are positive trends in the onshore wind anomalies throughout the HBL, with a median tau of 0.21 (Min tau = 0.06, Max tau = 0.35) (Figure 3.3, Table 3.1). There are considerable spatial variations in the magnitude of the trends with a median increase of about 16% (Min TSA = 2.8%, Max TSA = 25.2%) over the study period. The grid locations that have the highest trends are shown as areas with onshore wind frequency anomalies exceeding 18.7%. The northern section (or upper HBL) is generally characterized by non-significant positive trends, while significant positive trends are present in parts of the central section (or middle HBL) and the southern section (or lower HBL). Overall, these positive anomalies (median p-value = 0.06) in June onshore wind frequency are statistically significant ($p < 0.05$) at 92 grid locations in the HBL.

In July, positive trends persist in the onshore wind frequency throughout the HBL, with a median tau of 0.15 (Min tau = 0.06, Max tau = 0.24) (Table 3.1). The magnitude of the trends ranges from 3.8% to 17.3% (median TSA = 10.4%) over the region. The highest trends are mostly along the coastal HBL, with the onshore wind frequency anomalies exceeding 12.3%. Overall, these positive trends (median p-value = 0.17) in July onshore wind frequency are statistically significant ($p < 0.05$) only at 8 grid locations in the HBL—3 locations along the coast around Winisk and the Polar Bear Provincial Park, and 5 locations further inland around the Severn River in central HBL.

Table 3. 1. Mann-Kendall trends for the onshore wind frequency anomalies for the period 1979–2018.

June	Minimum	Lower Quartile	Median	Upper Quartile	Maximum	Significance #*
tau	0.06	0.17	0.21	0.26	0.35	-
TSA (%)	2.8	12.1	16.0	18.7	25.2	-
p-value	0.002	0.02	0.06	0.13	0.28	92
July						
tau	0.06	0.13	0.15	0.18	0.24	-
TSA (%)	3.8	8.3	10.4	12.3	17.3	-
p-value	0.01	0.11	0.17	0.24	0.43	8
August						
tau	-0.08	0.02	0.07	0.11	0.21	-
TSA (%)	-5.8	0.7	4.8	7.2	12.9	-
p-value	0.001	0.30	0.51	0.80	1.00	2
September						
tau	-0.09	0.03	0.07	0.11	0.19	-
TSA (%)	-4.9	0.8	2.9	4.8	9.3	-
p-value	0.10	0.33	0.51	0.70	1.00	0
Study Months Average						
tau	0.15	0.21	0.24	0.26	0.32	-
TSA (%)	4.7	6.3	7.2	7.9	9.7	-
p-value	0.004	0.02	0.03	0.06	0.10	134

Statistics are derived from boxplot summaries showing the distribution of trends across the HBL. TSA indicates the Theil-Sen approach estimate of the slope expressed here as the 40-year trend. *The number of grid locations out of 194 in the HBL with statistically significant trends (<0.05).

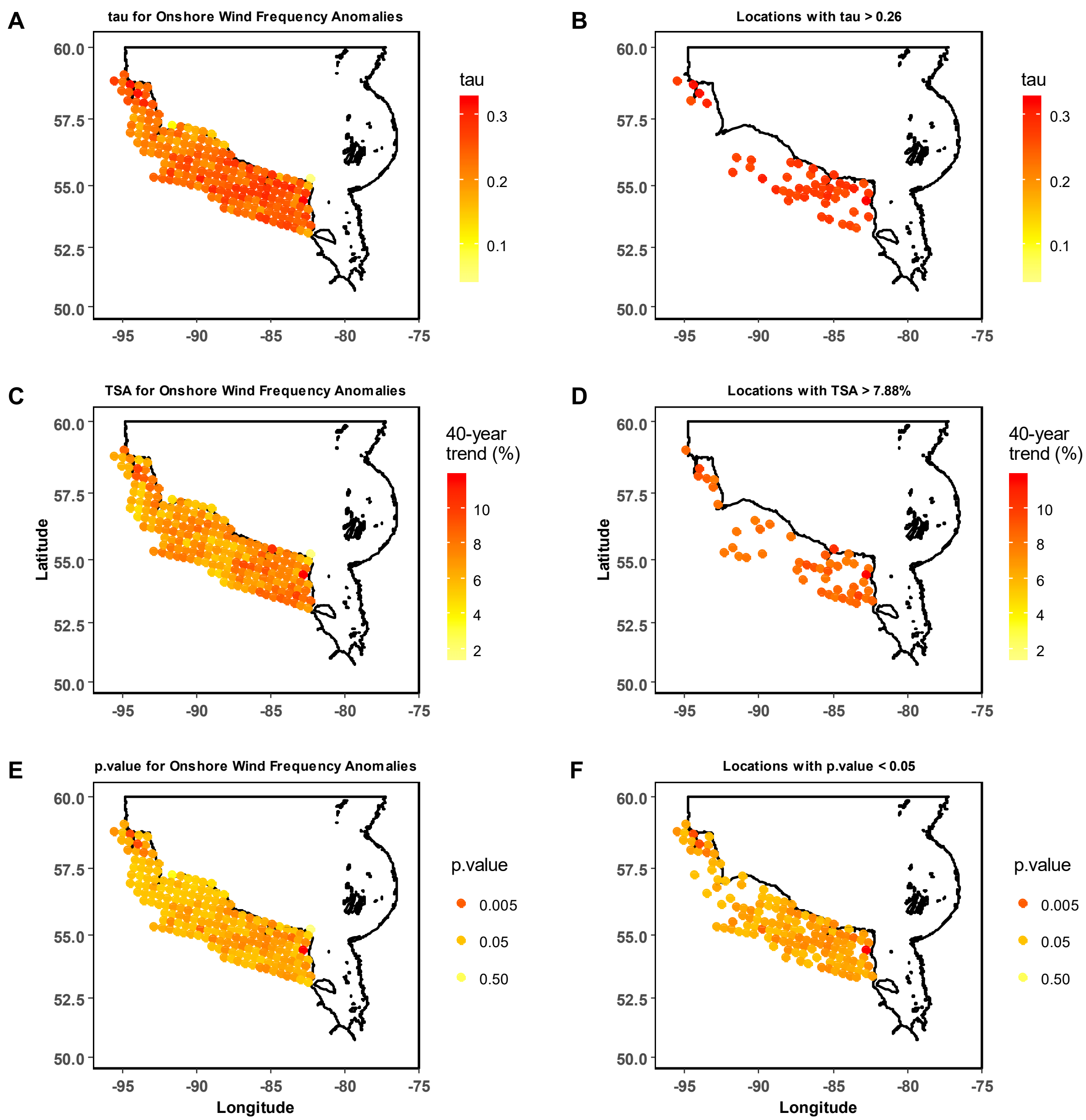

Figure 3. 2. Mann-Kendall trends for the four study months (June to September) average onshore wind frequency anomalies over the HBL during the 1979–2018 period. (A) tau for all grid locations, and (B) the top 25% of the grid locations with the highest tau. (C) Theil-Sen slope for all grid locations, and (D) the top 25% of the grid locations with the highest TSA. (E) p-value for all grid locations, and (F) the grid locations with statistically significant p-values (<0.05).

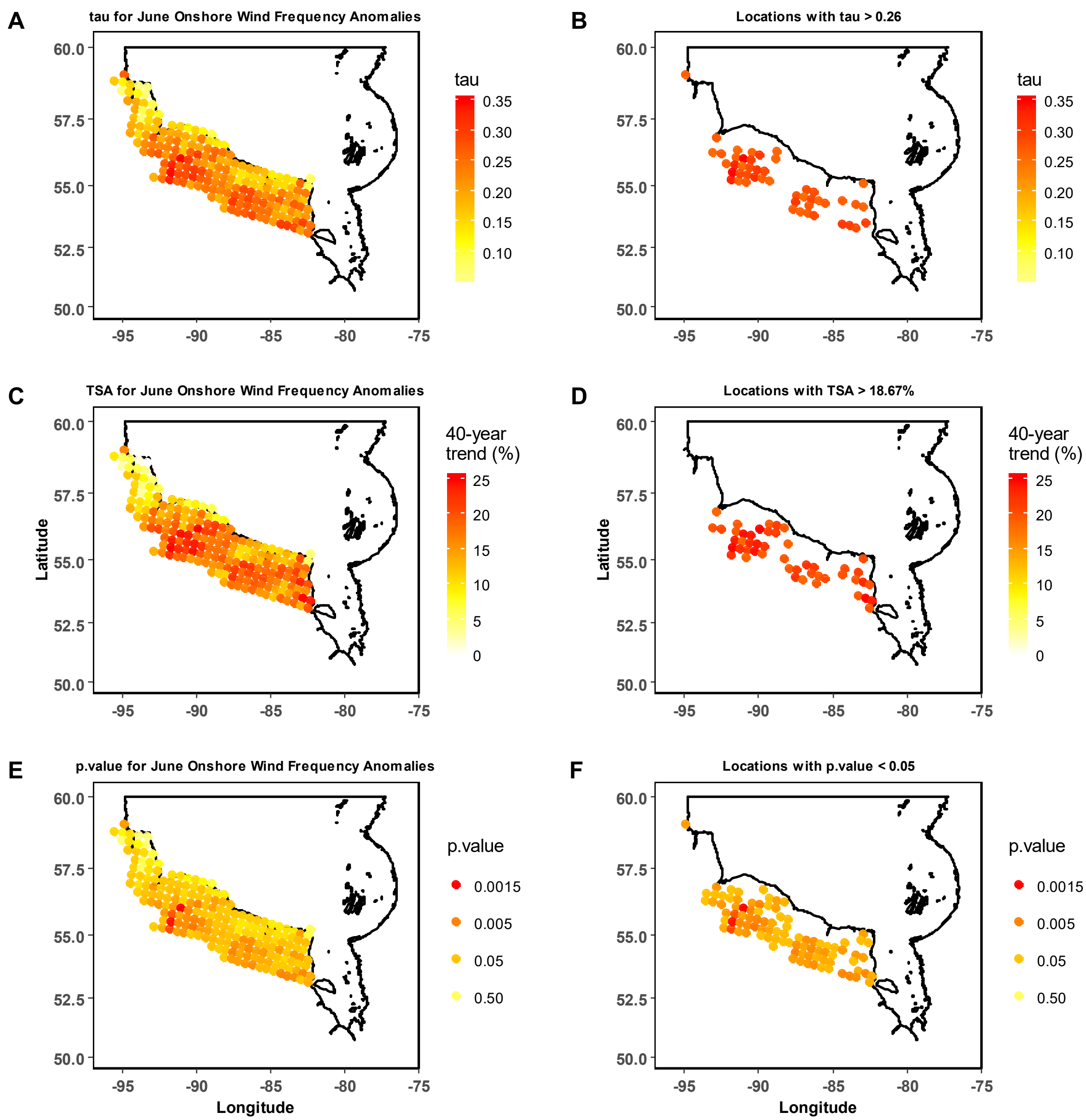

Figure 3. 3. Mann-Kendall trends for the onshore wind frequency anomalies over the HBL for June during the 1979–2018 period. (A) tau for all grid locations, and (B) the top 25% of the grid locations with the highest tau. (C) Theil-Sen slope for all grid locations, and (D) the top 25% of the grid locations with the highest TSA. (E) p-value for all grid locations, and (F) the grid locations with statistically significant p-values (<0.05).

In August, the onshore wind anomalies are mostly characterized by positive trends (median tau = 0.07), though some grid locations have negative or no trends at all (Table 3.1). The magnitude of the trends ranges from -5.8% to 12.9% (median TSA = 4.8%) over the HBL. The largest positive trends generally occur in the northern and southern sections of HBL, where the onshore wind frequency anomalies exceed 7.2%. Nevertheless, these trends (median p-value = 0.51) in August onshore wind frequency are not statistically significant, except at 2 grid locations ($p < 0.05$) in the Wapusk National Park and Polar Bear Provincial Park.

In September, the onshore wind anomalies are mainly characterized by positive trends (median tau = 0.07), though some grid locations have negative or no trends at all (Table 3.1). The magnitude of the trends ranges from -4.9% to 9.3% (median TSA = 2.9%) over the HBL. Regardless, the trends (median p-value = 0.51) in the September onshore wind frequency are not statistically significant at all grid locations in the HBL.

The results demonstrate that the largest and most significant trends in the onshore wind frequency occur in June, particularly at 92 grid locations in the HBL. These significant positive trends are mostly found at inland grid locations of central and southern HBL. It is important to mention here that the offshore wind frequency anomalies in the HBL show identical but opposite trends during the study period.

3.3.2 Temperature

The four study months average temperature anomalies during offshore wind regimes for the period 1979–2018 show positive trends over the entire HBL (Figure 3.4, Table 3.2). The strength of these positive trends varies considerably across the region with a median tau of 0.33 (Min tau = 0.22, Max tau = 0.48). The magnitude of the trends in offshore temperatures also varies spatially with a median increase of 2.1 °C (Min TSA = 1.6 °C, Max TSA = 2.7 °C) over the study period. The grid locations that have the largest trends are described as areas with offshore temperature anomalies exceeding 2.3 °C (upper quartile). These positive offshore temperature trends are statistically significant (median p-value = 0.003) at 193 grid locations (out of 194) in the HBL. The most significant warming trends ($p < 0.001$) are occurring along the coast, at the mouths of rivers—such as around Churchill, Fort Severn and Winisk, as well as in southern HBL in an extensive narrow belt along the Ekwan and Attawapiskat Rivers.

There are also substantial monthly variations in the magnitude and significance of the offshore temperature anomalies. In June, there are positive offshore temperature trends throughout the HBL, with a median tau of 0.25 (Min tau = 0.17, Max tau = 0.33) (Figure 3.5, Table 3.2). The magnitude of the trends varies between 2.1 °C and 4.2 °C (median TSA = 3.2 °C) over the study region. The grid locations that have the highest trends are characterized by offshore temperature anomalies exceeding 3.4 °C (upper quartile). These positive offshore temperature trends in June are statistically significant (median p-value = 0.02) at 166 grid locations in the HBL.

In July, the positive trends persist in the offshore temperature anomalies throughout the HBL, with a median tau of 0.23 (Min tau = 0.12, Max tau = 0.38) (Table 3.2). The magnitude of the trends ranges from 0.9 °C to 2.8 °C (median TSA = 1.8 °C) over the HBL. The highest trends mostly occur along the coastal HBL, where offshore temperature anomalies exceed 2.1 °C. Overall, these positive trends (median p-value = 0.04) in July offshore temperatures are statistically significant ($p < 0.05$) at 112 grid locations in the HBL. The majority of the non-significant temperature trends are found in the central HBL.

In August, the offshore temperature anomalies are typically characterized by positive trends (median tau = 0.12) over the HBL (Table 3.2). The magnitude of the trends ranges from -0.1 °C to 2.4 °C (median TSA = 1.0 °C) over the study region. Overall, statistically significant positive trends ($p < 0.05$) in the August offshore temperatures occur at 20 grid locations, predominantly along the coastal HBL.

In September, there are significant positive offshore temperature trends throughout the HBL, with a median tau of 0.35 (Min tau = 0.23, Max tau = 0.49) (Figure 3.6, Table 3.2). The magnitude of the trends varies between 2.5 °C and 4.6 °C (median TSA = 3.4 °C) over the study region. The grid locations that have the highest trends are usually found in southern HBL along the mouth of the Winisk River and in a swath along the Ekwan and Attawapiskat Rivers, where offshore temperature anomalies exceed 3.8 °C. The positive offshore temperature trends in September are statistically significant (median p-value = 0.002) at all 194 grid locations in the HBL. The results show that the largest and most significant trends in the offshore temperatures over the HBL occur in September, followed by June.

Table 3. 2. Mann-Kendall trends for the offshore temperature anomalies for the period 1979–2018

June	Minimum	Lower Quartile	Median	Upper Quartile	Maximum	Significance #*
tau	0.17	0.23	0.25	0.27	0.33	-
TSA (°C)	2.1	2.9	3.2	3.4	4.2	-
p-value	0.001	0.01	0.02	0.04	0.07	166
July						
tau	0.12	0.19	0.23	0.27	0.38	-
TSA (°C)	0.9	1.5	1.8	2.1	2.8	-
p-value	0.000	0.02	0.04	0.09	0.18	112
August						
tau	-0.02	0.09	0.12	0.18	0.29	-
TSA (°C)	-0.1	0.8	1.0	1.5	2.4	-
p-value	0.000	0.11	0.28	0.40	0.65	20
September						
tau	0.23	0.29	0.35	0.38	0.49	-
TSA (°C)	2.5	3.2	3.4	3.8	4.6	-
p-value	0.0000	0.001	0.002	0.01	0.02	194
Study Months Average						
tau	0.22	0.30	0.33	0.38	0.48	-
TSA (°C)	1.6	2.0	2.1	2.3	2.7	-
p-value	0.000	0.001	0.003	0.007	0.016	193

Statistics are derived from boxplot summaries showing the distribution of trends across the HBL. TSA indicates the Theil-Sen approach estimate of the slope expressed here as the 40-year trend. *The number of grid locations out of 194 in the HBL with statistically significant trends (<0.05).

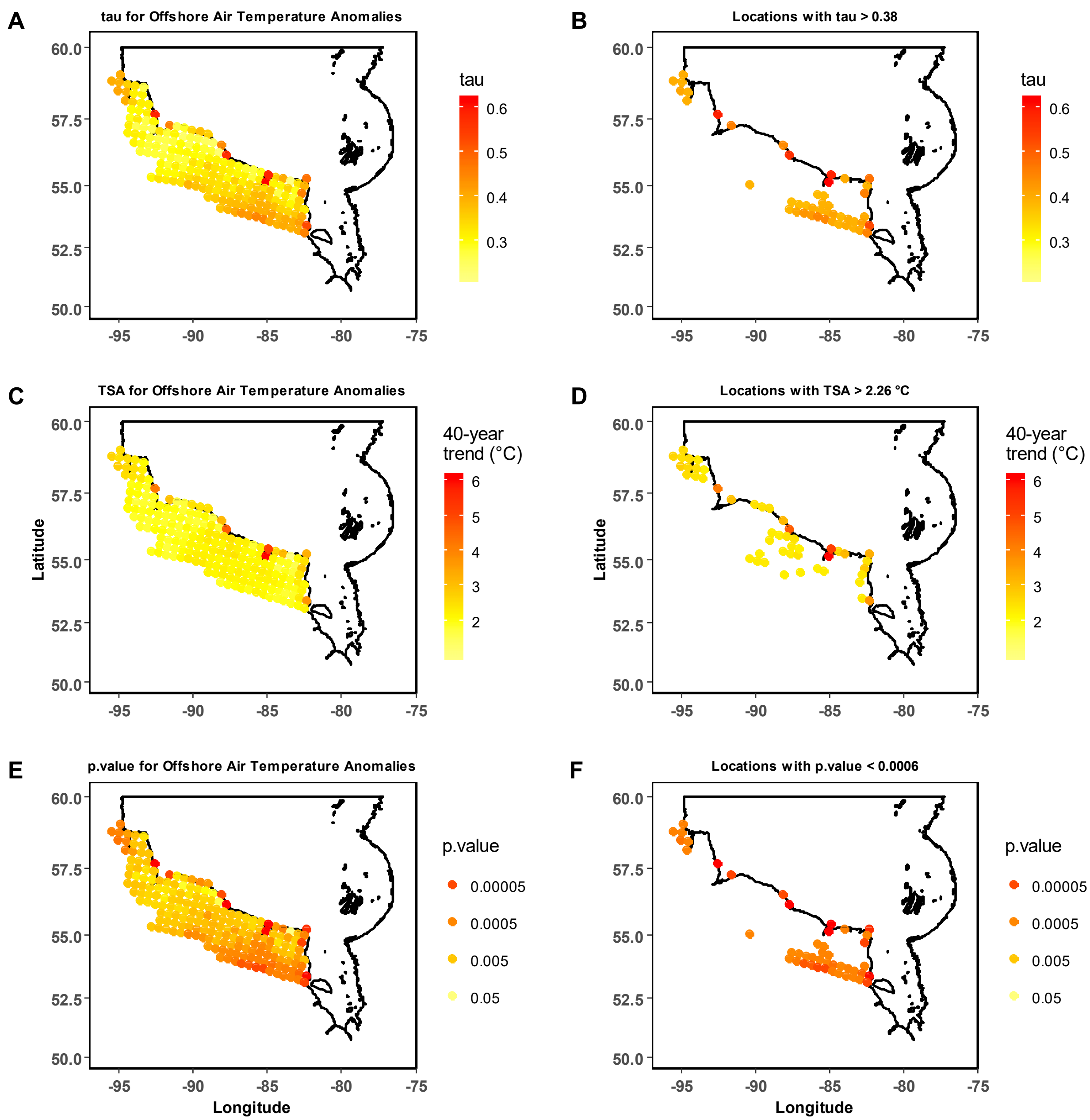

Figure 3. 4. Mann-Kendall trends for the four study months (June to September) average offshore air temperature anomalies over the HBL during the 1979–2018 period. (A) tau for all grid locations, and (B) the top 25% of the grid locations with the highest tau. (C) Theil-Sen slope for all grid locations, and (D) the top 25% of the grid locations with the highest TSA. (E) p-value for all grid locations, and (F) the bottom 25% of the grid locations with the lowest p-value.

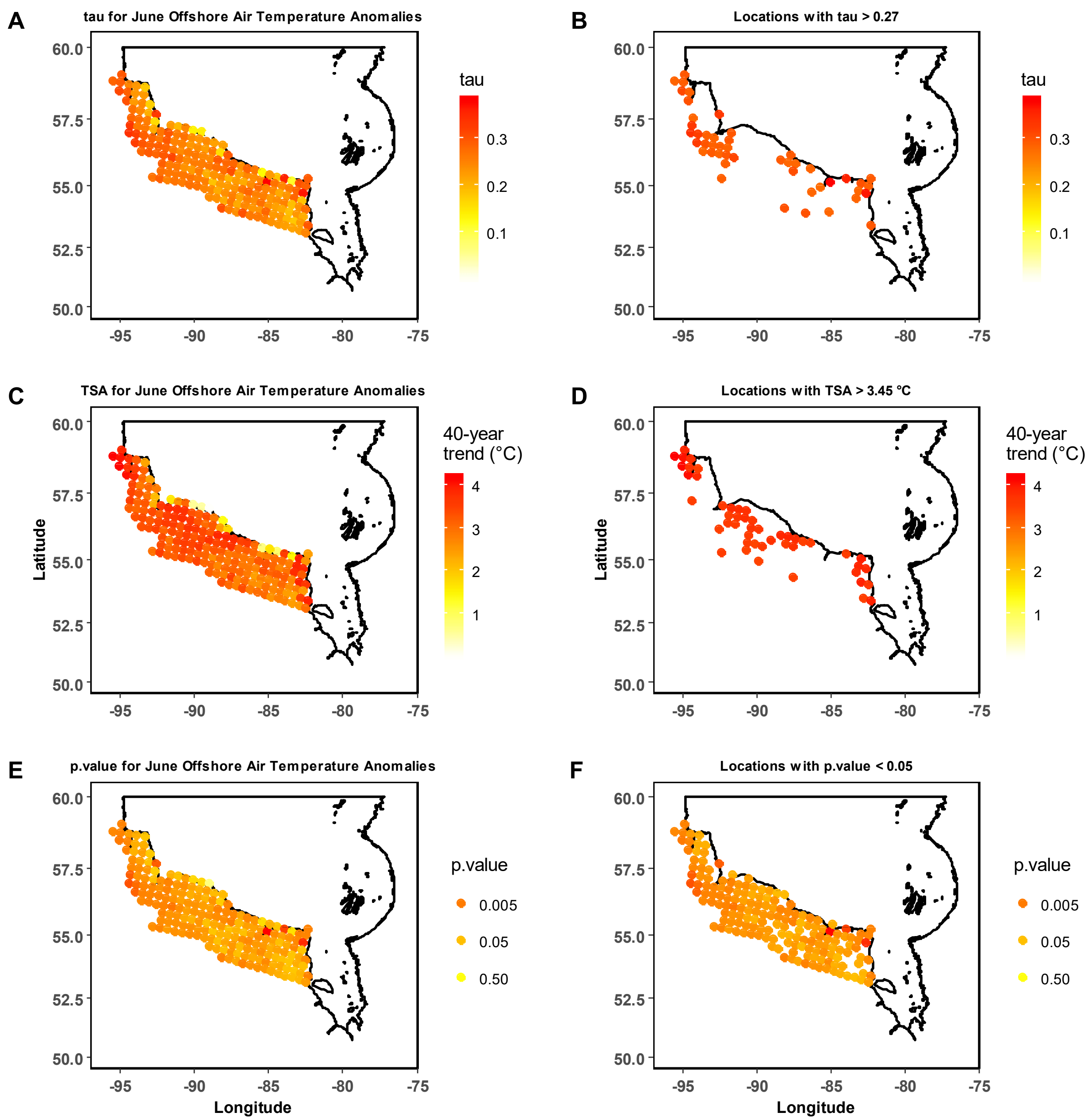

Figure 3. 5. Mann-Kendall trends for the offshore air temperature anomalies over the HBL for June during the 1979–2018 period. (A) tau for all grid locations, and (B) the top 25% of the grid locations with the highest tau. (C) Theil-Sen slope for all grid locations, and (D) the top 25% of the grid locations with the highest TSA. (E) p-value for all grid locations, and (F) the grid locations with statistically significant p-values (<0.05).

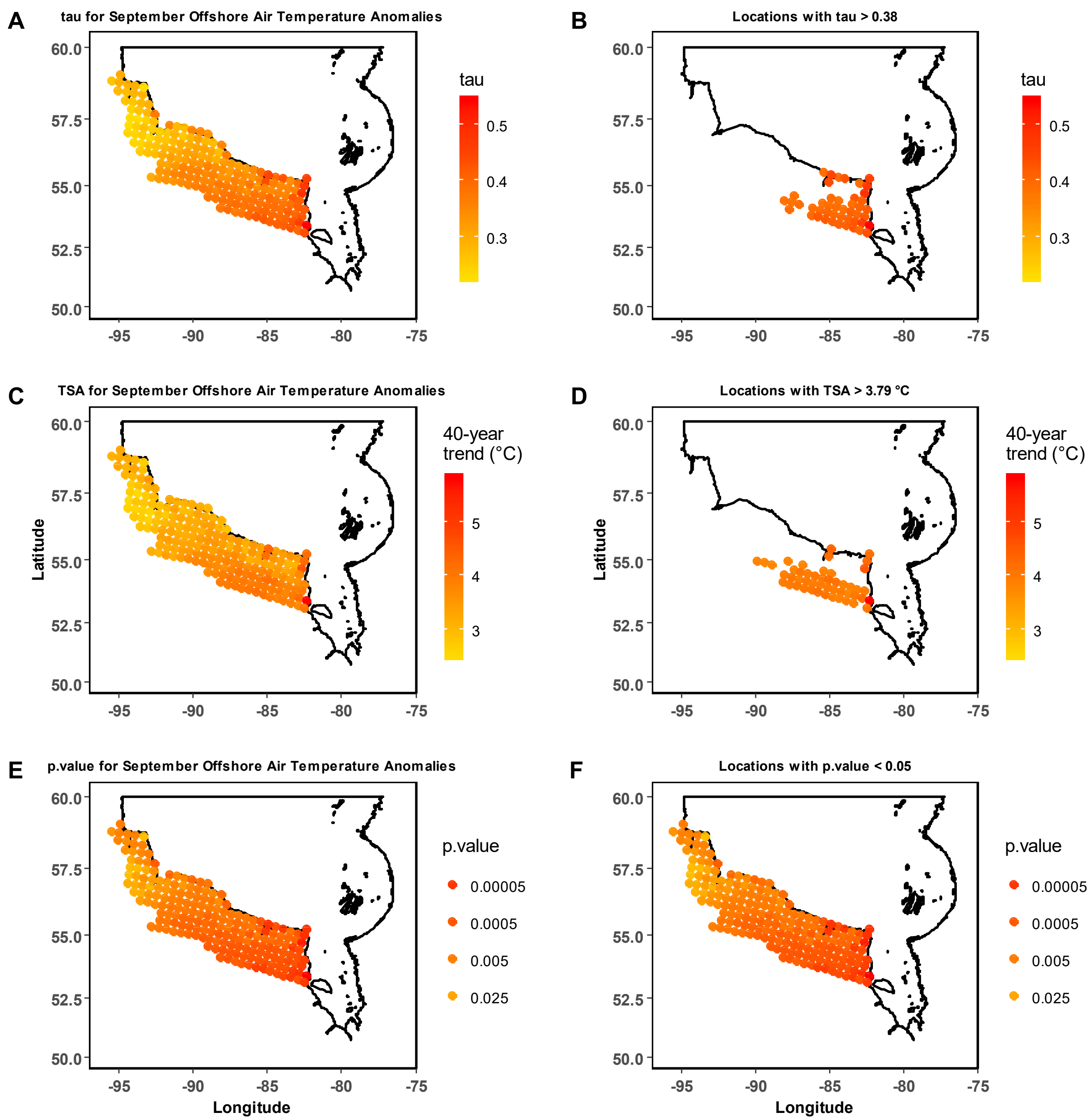

Figure 3. 6. Mann-Kendall trends for the offshore air temperature anomalies over the HBL for September during the 1979–2018 period. (A) tau for all grid locations, and (B) the top 25% of the grid locations with the highest tau. (C) Theil-Sen slope for all grid locations, and (D) the top 25% of the grid locations with the highest TSA. (E) p-value for all grid locations, and (F) the grid locations with statistically significant p-values (<0.05).

The four study months average temperature anomalies during onshore wind regimes for the period 1979–2018 show positive trends over the entire HBL (Figure 3.7, Table 3.3). The strength of these positive trends varies considerably across the study region with a median tau of 0.30 (Min tau = 0.14, Max tau = 0.46). The magnitude of the trends in onshore temperatures also varies spatially with a median increase of 1.6 °C (Min TSA = 0.9 °C, Max TSA = 2.2 °C) over the study period. The grid locations that have the largest trends are described as areas with onshore temperature anomalies exceeding about 1.8 °C (upper quartile). These positive onshore temperature trends are statistically significant (median p-value = 0.006) at 186 grid locations (out of 194) in the HBL. The most significant warming trends ($p < 0.002$) occur around the Churchill area in upper HBL, around Fort Severn and the Severn River in central HBL, as well as at the mouths of the Winisk, Ekwan and Attawapiskat Rivers, and in parts of the Polar Bear Provincial Park in the lower HBL.

There are also substantial monthly variations in the magnitude and significance of the onshore temperature anomalies. In June, the HBL region is usually characterized by positive onshore temperature trends, with a median tau of 0.26 (Min tau = 0.10, Max tau = 0.42) (Figure 3.8, Table 3.3). The magnitude of the trends varies considerably between 0.1 °C and 3.8 °C (median TSA = 2.2 °C) over the region. The grid locations that have the highest trends are mostly found in the central HBL and, to a lesser extent, around the Churchill area in northern HBL, where the onshore temperature anomalies exceed 2.9 °C. Overall, the positive onshore temperature trends in June are statistically significant (median p-value = 0.02) at 138 grid locations in the HBL.

In July, the onshore temperature anomalies generally have weak positive trends over the study region, with a median tau of 0.08 (Min tau = -0.06, Max tau = 0.22) (Table 3.3). The magnitude of the trends ranges from -0.5 °C to 1.5 °C (median TSA = 0.5 °C) over the HBL. Overall, the positive trends (median p-value = 0.48) in July onshore temperatures are statistically significant ($p < 0.05$) at only 10 grid locations along the coastal HBL.

In August, the onshore temperature anomalies are typically characterized by positive trends (median tau = 0.14) over the HBL (Table 3.3). The magnitude of the trends ranges from -0.3 °C to 2.9 °C (median TSA = 1.1 °C) over the study region. Overall, statistically significant positive trends ($p < 0.05$) in the August onshore temperatures occur at 38 grid locations, predominantly along the coastal HBL.

In September, there are strong positive onshore temperature trends throughout the HBL, with a median tau of 0.31 (Min tau = 0.20, Max tau = 0.44) (Figure 3.9, Table 3.3). The magnitude of the trends varies considerably between 2.0 °C and 4.0 °C (median TSA = 2.9 °C) over the study region. The positive onshore temperature trends in September are statistically significant (median p-value = 0.01) at 187 grid locations in the HBL. Indeed, the results demonstrate that the largest and most significant onshore temperature anomalies over the HBL occur in September, followed by June.

Table 3. 3. Mann-Kendall trends for the onshore temperature anomalies for the period 1979–2018.

June	Minimum	Lower Quartile	Median	Upper Quartile	Maximum	Significance #*
tau	0.10	0.21	0.26	0.31	0.42	-
TSA (°C)	0.1	1.7	2.2	2.9	3.8	-
p-value	0.0002	0.005	0.02	0.06	0.13	138
July						
tau	-0.06	0.04	0.08	0.12	0.22	-
TSA (°C)	-0.5	0.2	0.5	0.8	1.5	-
p-value	0.0001	0.29	0.48	0.72	1.00	10
August						
tau	-0.04	0.08	0.14	0.19	0.34	-
TSA (°C)	-0.3	0.7	1.1	1.7	2.9	-
p-value	0.0000	0.08	0.22	0.46	1.00	38
September						
tau	0.20	0.27	0.31	0.35	0.44	-
TSA (°C)	2.0	2.6	2.9	3.2	4.0	-
p-value	0.0001	0.002	0.01	0.02	0.04	187
Study Months Average						
tau	0.14	0.26	0.30	0.34	0.46	-
TSA (°C)	0.9	1.4	1.6	1.8	2.2	-
p-value	0.000	0.002	0.006	0.018	0.041	186

Statistics are derived from boxplot summaries showing the distribution of trends across the HBL. TSA indicates the Theil-Sen approach estimate of the slope expressed here as the 40-year trend.
*The number of grid locations out of 194 in the HBL with statistically significant trends (<0.05).

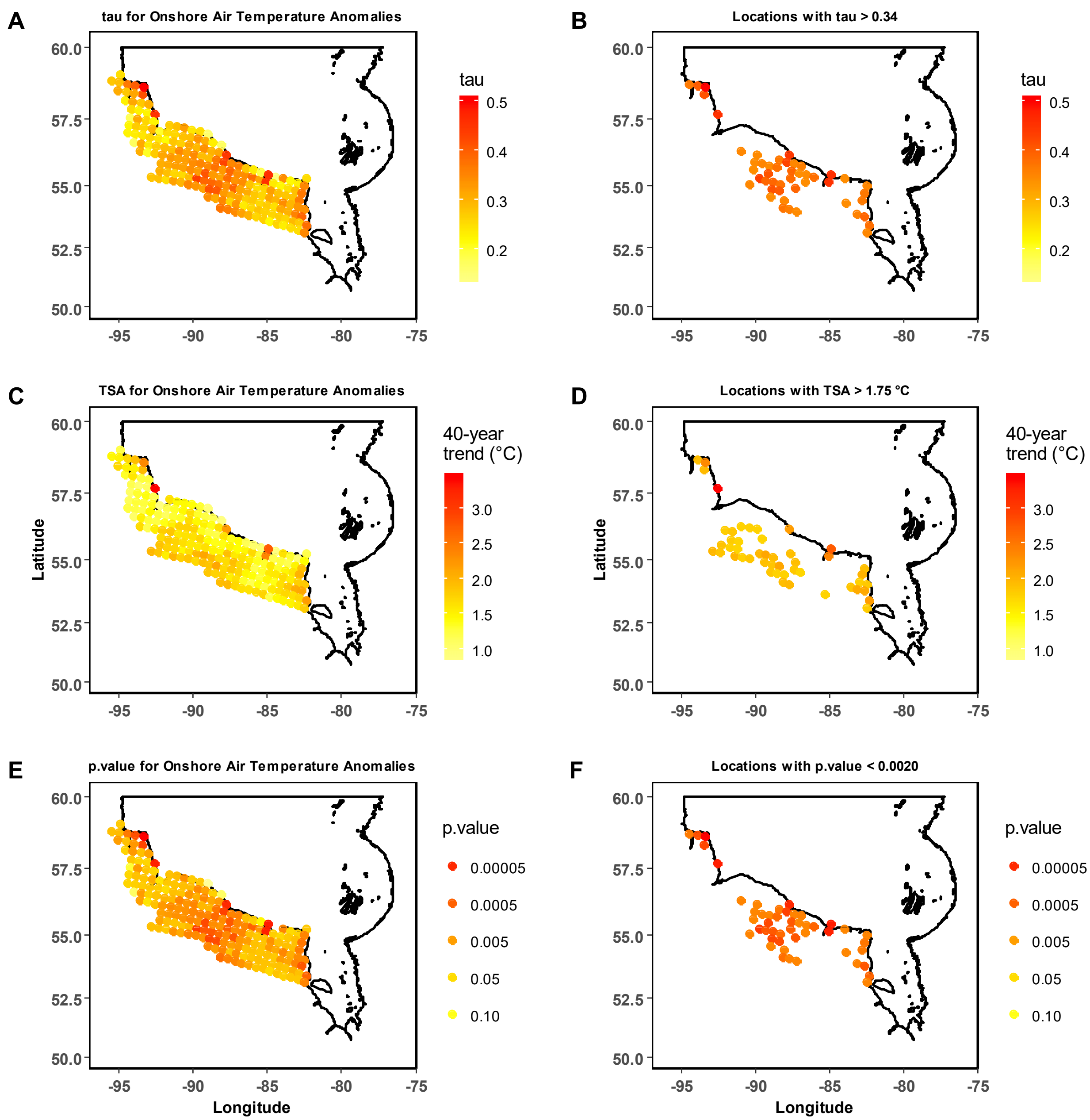

Figure 3. 7. Mann-Kendall trends for the four study months (June to September) average onshore air temperature anomalies over the HBL during the 1979–2018 period. (A) tau for all grid locations, and (B) the top 25% of the grid locations with the highest tau. (C) Theil-Sen slope for all grid locations, and (D) the top 25% of the grid locations with the highest TSA. (E) p-value for all grid locations, and (F) the bottom 25% of the grid locations with the lowest p-value.

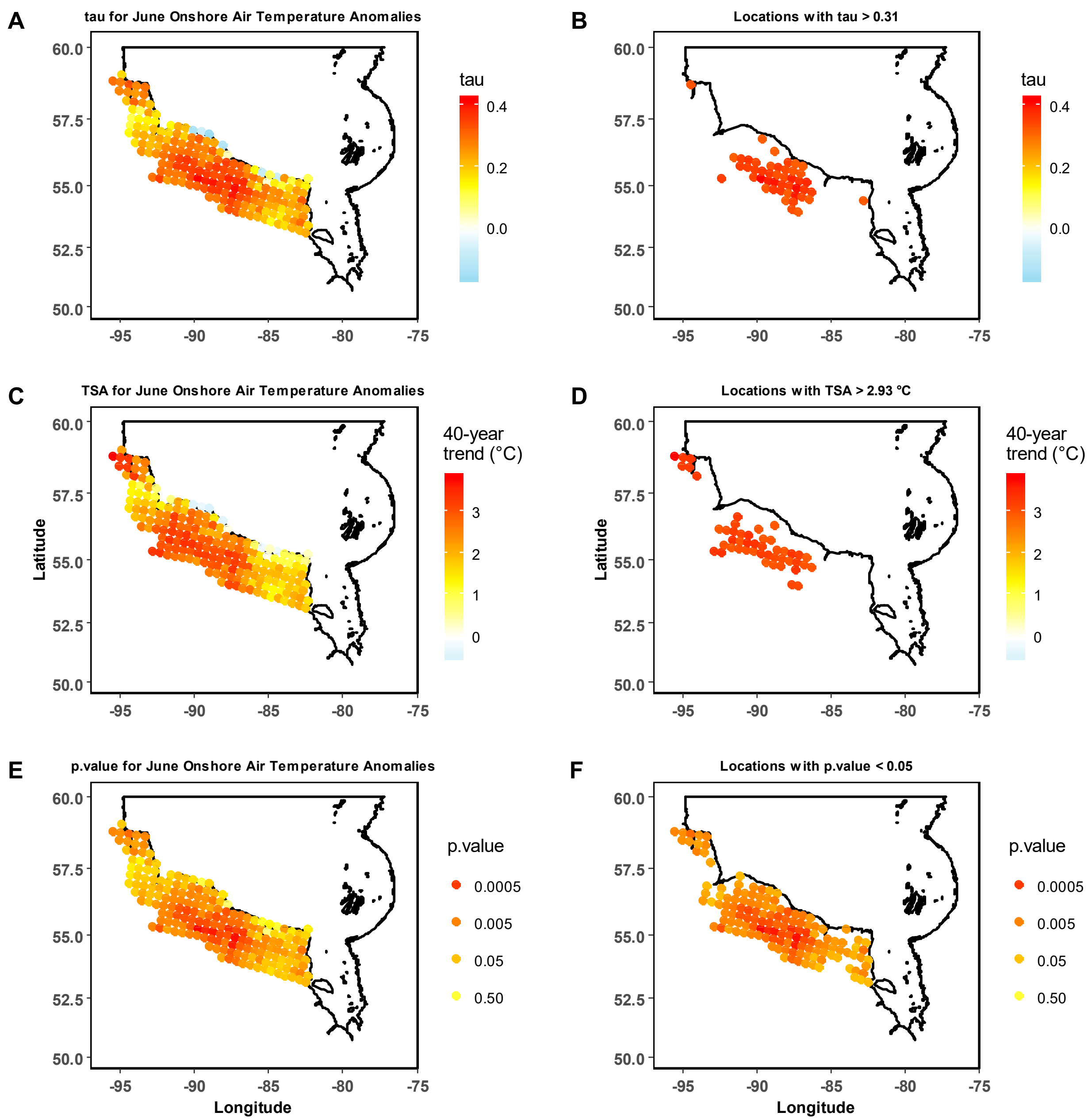

Figure 3. 8. Mann-Kendall trends for the onshore air temperature anomalies over the HBL for June during the 1979–2018 period. (A) tau for all grid locations, and (B) the top 25% of the grid locations with the highest tau. (C) Theil-Sen slope for all grid locations, and (D) the top 25% of the grid locations with the highest TSA. (E) p-value for all grid locations, and (F) the grid locations with statistically significant p-values (<0.05).

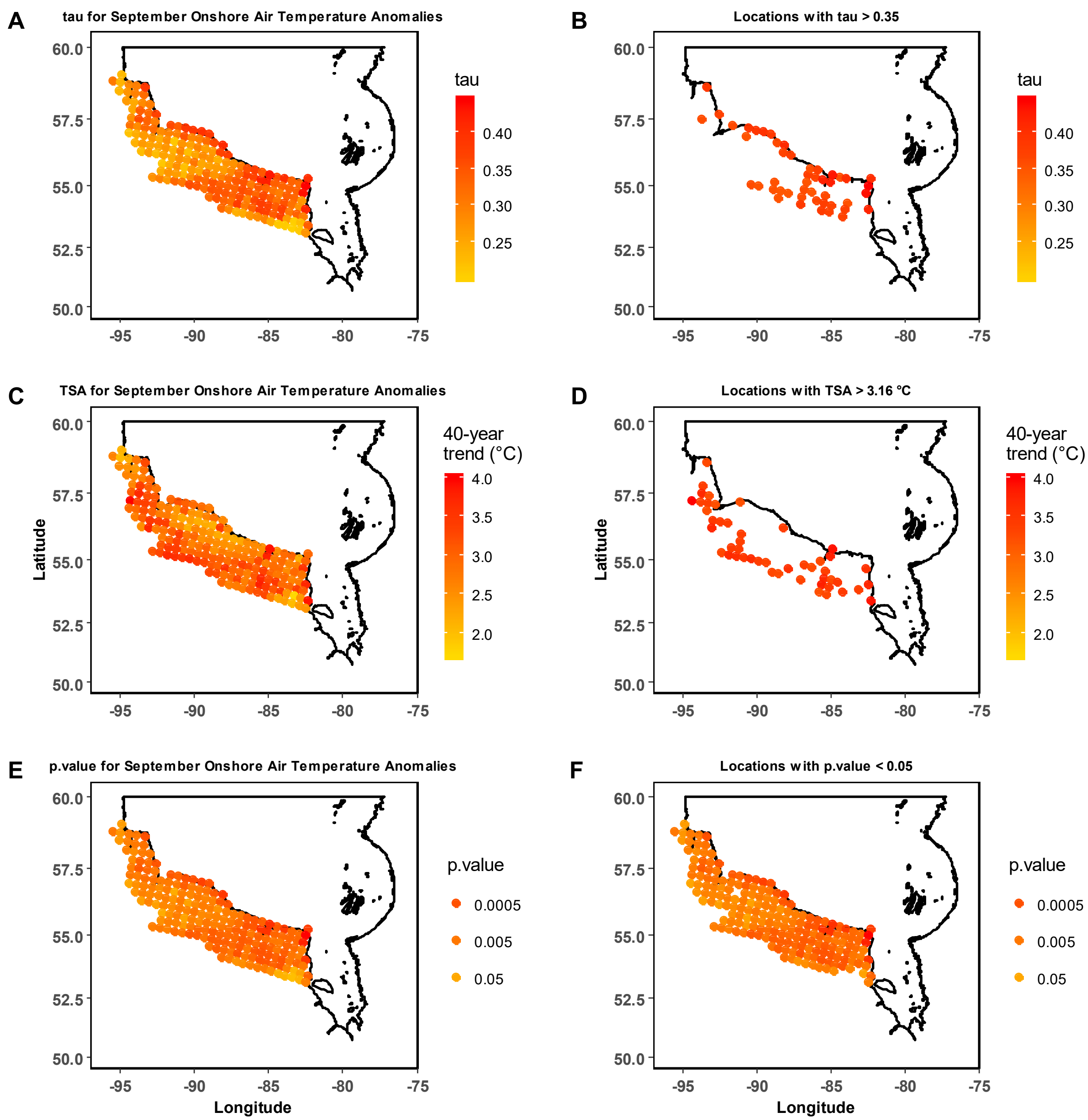

Figure 3. 9. Mann-Kendall trends for the onshore air temperature anomalies over the HBL for September during the 1979–2018 period. (A) tau for all grid locations, and (B) the top 25% of the grid locations with the highest tau. (C) Theil-Sen slope for all grid locations, and (D) the top 25% of the grid locations with the highest TSA. (E) p-value for all grid locations, and (F) the grid locations with statistically significant p-values (<0.05).

3.3.3 Wind Speed

The four study months average wind speed anomalies during offshore wind regimes for the period 1979–2018 generally show weak positive trends over the HBL (Table 3.4). The strength of these trends varies across the region with a median tau of 0.07 (Min tau = -0.06, Max tau = 0.23). The magnitude of the offshore wind speed anomalies also varies spatially with a median increase in wind speed of 0.08 ms^{-1} over the study period. The largest trends are found at grid locations where the offshore wind speed anomalies have increased by over 0.14 ms^{-1}. The offshore wind speed trends (median p-value = 0.54) are statistically significant ($p < 0.05$) at only 17 grid locations (out of 194) along the coastal HBL, where the wind speed anomalies have increased by 0.32 ms^{-1} to 1.90 ms^{-1} over the study period.

The monthly average offshore wind speed anomalies show both weak positive and negative trends (median tau = -0.03) in June over the HBL (Table 3.4). The magnitude of the trends varies between -0.6 ms^{-1} and 0.4 ms^{-1} (median TSA = -0.1 ms^{-1}). Nevertheless, these offshore wind speed trends (median p-value = 0.65) in June are not statistically significant, except at 1 grid location ($p < 0.05$) on the Ekwan River in southern HBL—where the wind speed anomalies have decreased by 0.7 ms^{-1} over the study period.

In July, the offshore wind speed anomalies are typically positive across the HBL, with a median tau of 0.17 (Min tau = -0.05, Max tau = 0.36) (Figure 3.10, Table 3.4). The magnitude of the trends also varies spatially with a median increase in wind speed anomalies of 0.4 ms^{-1} over the study period. The offshore wind speed trends (median p-value = 0.12) in July are statistically significant ($p < 0.05$) at 45 grid locations, found mostly along the coastal HBL and at inland locations in central HBL, where the wind speed anomalies have increased by 0.4 ms^{-1} to 2.0 ms^{-1} over the study period.

Table 3. 4. Mann-Kendall trends for the offshore wind speed anomalies for the period 1979–2018.

June	Minimum	Lower Quartile	Median	Upper Quartile	Maximum	Significance #*
tau	-0.19	-0.08	-0.03	0.01	0.13	-
TSA (ms^{-1})	-0.6	-0.2	-0.1	0.0	0.4	-
p-value	0.05	0.41	0.65	0.84	1.00	1
July						
tau	-0.05	0.11	0.17	0.21	0.36	-
TSA (ms^{-1})	-0.2	0.3	0.4	0.6	1.1	-
p-value	0.000	0.05	0.12	0.30	0.67	45
August						
tau	-0.10	0.00	0.04	0.07	0.16	-
TSA (ms^{-1})	-0.3	0.0	0.1	0.2	0.5	-
p-value	0.09	0.52	0.68	0.82	1.00	11
September						
tau	-0.22	-0.12	-0.08	-0.03	0.10	-
TSA (ms^{-1})	-0.5	-0.3	-0.2	-0.1	0.2	-
p-value	0.001	0.26	0.39	0.62	1.00	4
Study Months Average						
tau	-0.06	0.02	0.07	0.11	0.23	-
TSA (ms^{-1})	-0.09	0.03	0.08	0.14	0.30	-
p-value	0.00	0.35	0.54	0.79	1.00	17

Statistics are derived from boxplot summaries showing the distribution of trends across the HBL. TSA indicates the Theil-Sen approach estimate of the slope expressed here as the 40-year trend. *The number of grid locations out of 194 in the HBL with statistically significant trends (<0.05).

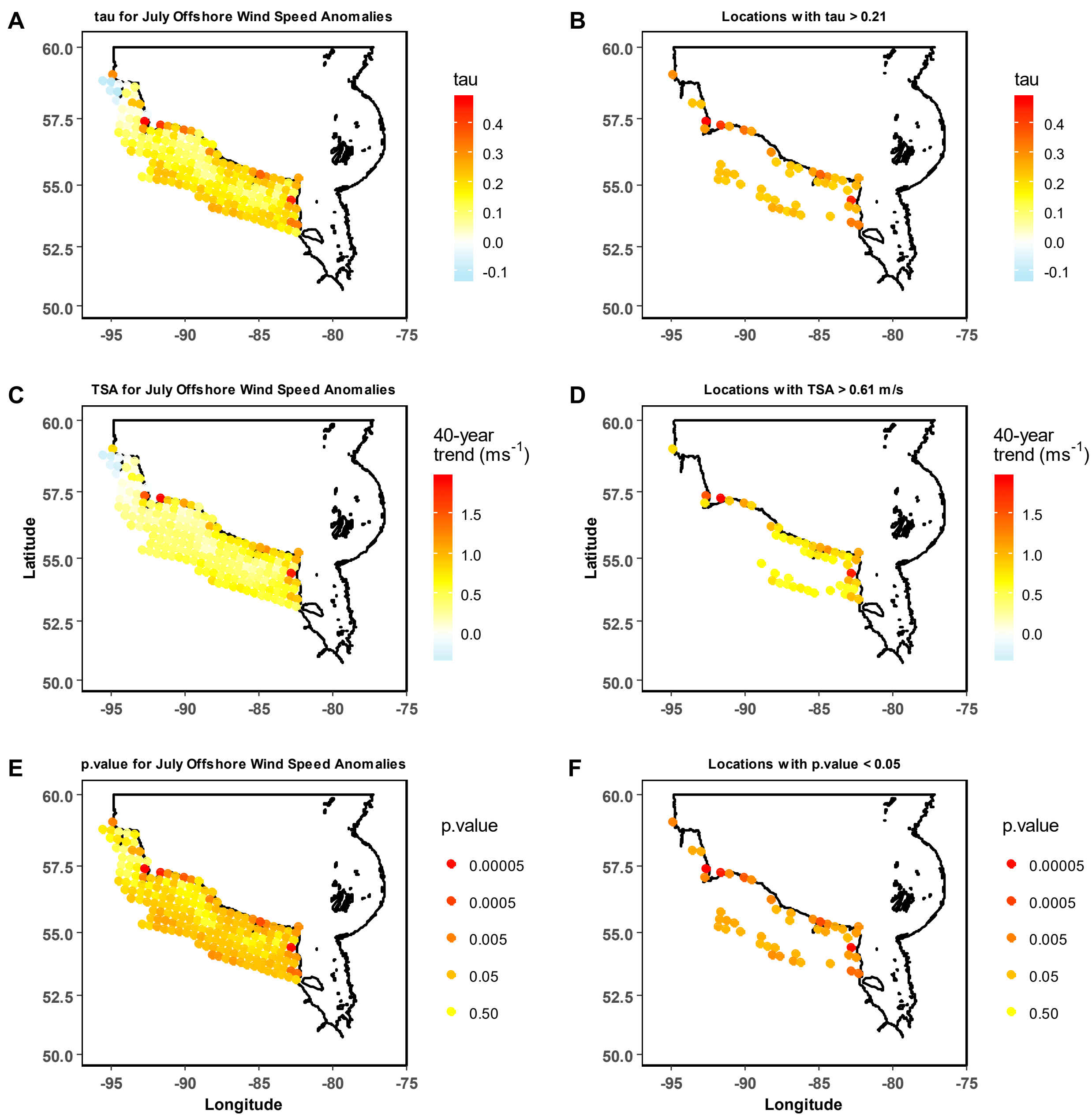

Figure 3. 10. Mann-Kendall trends for the offshore wind speed anomalies over the HBL for July during the 1979–2018 period. (A) tau for all grid locations, and (B) the top 25% of the grid locations with the highest tau. (C) Theil-Sen slope for all grid locations, and (D) the top 25% of the grid locations with the highest TSA. (E) p-value for all grid locations, and (F) the grid locations with statistically significant p-values (<0.05).

The August offshore wind speed anomalies show both weak positive and negative trends (median tau = 0.04) over the HBL (Table 3.4). The magnitude of the trends varies spatially with a median increase in wind speed anomalies of 0.1 ms^{-1} over the study period. The offshore wind speed trends (median p-value = 0.68) in August are statistically significant ($p < 0.05$) at only 11 grid locations along the coastal areas of central and southern HBL, where the wind speed anomalies have increased by 0.6 ms^{-1} to 2.3 ms^{-1} over the study period.

In September, there are generally weak negative trends (median tau = -0.08) in the offshore wind speeds over the HBL, though 26 grid locations show positive trends (Table 3.4). The positive trends generally occur along the coastal parts of southern HBL, with statistically significant trends ($p < 0.05$) at only 4 grid locations, where the offshore wind speed anomalies have increased by 0.9 ms^{-1} to 2.2 ms^{-1} over the study period. Overall, the results suggest that the most significant and widespread increase in offshore wind speeds occur in July, particularly along the coastal HBL.

The four study months average wind speed anomalies during onshore wind regimes for the period 1979–2018 generally show positive trends over the HBL (Table 3.5). The strength of these trends varies substantially across the region with a median tau of 0.10 (Min tau = -0.12, Max tau = 0.33). The magnitude of the onshore wind speed anomalies also varies spatially with a median increase in wind speed of 0.17 ms^{-1} over the study period. The highest trends are found at grid locations where the onshore wind speed anomalies have increased by over 0.26 ms^{-1}. The onshore wind speed trends (median p-value = 0.35) are statistically significant ($p < 0.05$) at 24 grid locations (out of 194), found mostly around the Nelson and Hayes Rivers in upper HBL, as well as around the southern edge of the Polar Bear Provincial Park and the mouth of the Ekwan

River in lower HBL. Here, the wind speed anomalies have increased by 0.28 ms^{-1} to 1.32 ms^{-1} over the study period.

The monthly average onshore wind speed anomalies for June show both positive and negative trends, with the tau ranging from -0.19 to 0.25 over the HBL (Table 3.5). The magnitude of the trends varies between -0.6 ms^{-1} and 0.8 ms^{-1} over the study region. These onshore wind speed trends (median p-value = 0.60) in June are statistically significant ($p < 0.05$) only at 5 grid locations—4 around the mouths of the Nelson and Hayes Rivers in northern HBL, and 1 at the Polar Bear Provincial Park in southern HBL. Here, the onshore wind speeds have increased by 0.55 ms^{-1} to 1.26 ms^{-1} over the study period.

In July, the onshore wind speed anomalies are usually positive across the HBL, with a median tau of 0.21 (Min tau = 0.00, Max tau = 0.43) (Figure 3.11, Table 3.5). The magnitude of the trends also varies spatially with a median increase in wind speed anomalies of 0.6 ms^{-1} over the study period. The onshore wind speed trends (median p-value = 0.05) in July are statistically significant ($p < 0.05$) at 96 grid locations, where the wind speeds have increased by 0.52 ms^{-1} to 2.25 ms^{-1} over the study period.

The August onshore wind speed anomalies show both weak positive and negative trends ranging from a tau of -0.21 to 0.24 (median tau = 0.02) over the HBL (Table 3.5). The magnitude of the trends varies spatially with a median increase in wind speed anomalies of 0.1 ms^{-1} over the study period. The highest trends in the August onshore wind speeds are generally found along the coastal HBL, with statistically significant trends ($p < 0.05$) at 7 grid locations, where the wind speeds have increased by 0.73 ms^{-1} to 1.96 ms^{-1} over the study period.

In September, onshore wind speed anomalies show both positive and negative trends ranging from a tau of -0.27 to 0.23 (median tau = -0.04) over the HBL (Table 3.5).

Table 3. 5. Mann-Kendall trends for the onshore wind speed anomalies for the period 1979–2018.

June	Minimum	Lower Quartile	Median	Upper Quartile	Maximum	Significance #*
tau	-0.19	-0.04	0.01	0.09	0.25	-
TSA (ms^{-1})	-0.6	-0.1	0.0	0.2	0.8	-
p-value	0.0001	0.33	0.60	0.84	1.00	5
July						
tau	0.00	0.14	0.21	0.26	0.43	-
TSA (ms^{-1})	0.2	0.5	0.6	0.7	1.1	-
p-value	0.000	0.02	0.05	0.20	0.45	96
August						
tau	-0.21	-0.05	0.02	0.08	0.24	-
TSA (ms^{-1})	-0.8	-0.2	0.1	0.3	0.9	-
p-value	0.0003	0.30	0.56	0.75	1.00	7
September						
tau	-0.27	-0.11	-0.04	0.04	0.23	-
TSA (ms^{-1})	-1.5	-0.5	-0.2	0.2	1.2	-
p-value	0.0006	0.24	0.48	0.72	1.00	16
Study Months Average						
tau	-0.12	0.04	0.10	0.16	0.33	-
TSA (ms^{-1})	-0.15	0.08	0.17	0.26	0.52	-
p-value	0.00	0.15	0.35	0.67	1.00	24

Statistics are derived from boxplot summaries showing the distribution of trends across the HBL. TSA indicates the Theil-Sen approach estimate of the slope expressed here as the 40-year trend.
*The number of grid locations out of 194 in the HBL with statistically significant trends (<0.05).

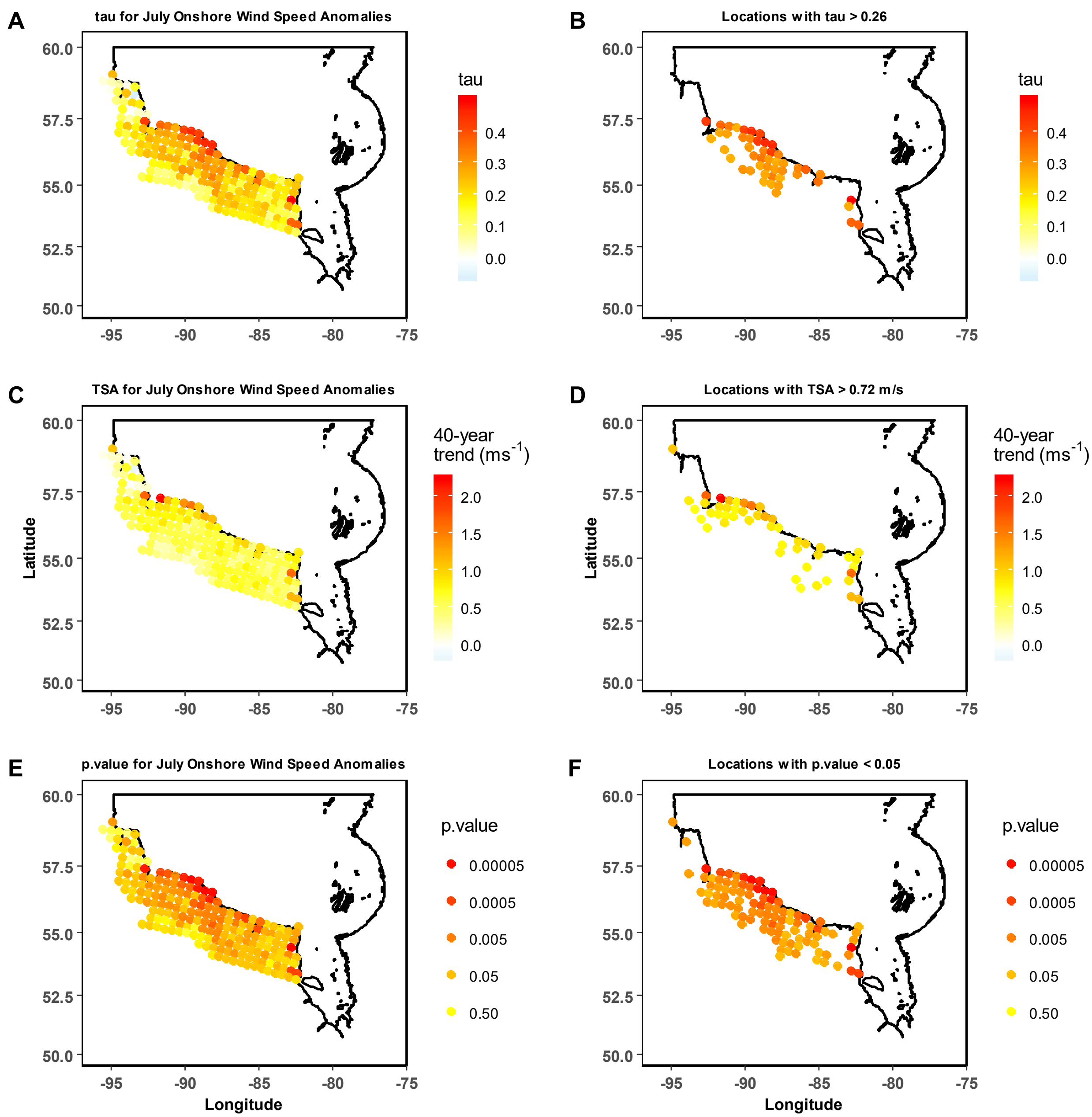

Figure 3. 11. Mann-Kendall trends for the onshore wind speed anomalies over the HBL for July during the 1979–2018 period. (A) tau for all grid locations, and (B) the top 25% of the grid locations with the highest tau. (C) Theil-Sen slope for all grid locations, and (D) the top 25% of the grid locations with the highest TSA. (E) p-value for all grid locations, and (F) the grid locations with statistically significant p-values (<0.05).

The negative trends are relatively close to the coast while the positive trends are generally found farther inland. Overall, the onshore wind speed trends (median p-value = 0.48) in September are statistically significant ($p < 0.05$) at 16 grid locations—4 with positive trends at the southern edge of the Polar Bear Provincial Park and the mouth of the Ekwan River, and 12 with negative trends mainly along the coast of central HBL. These significant wind speed trends range between -1.64 ms^{-1} and 2.71 ms^{-1} over the study region. The monthly average onshore wind speed anomalies, in general, suggest that the most significant and widespread increase in the onshore wind speeds over HBL occur in July.

3.3.4 Sensible Heat Flux

The four study months average Q_H anomalies during offshore wind regimes for the period 1979–2018 are generally characterized by positive trends over the HBL (Figure 3.12, Table 3.6). The strength of these positive trends varies considerably across the region with a median tau of 0.20 (Min tau = -0.01, Max tau = 0.36). The magnitude of the offshore Q_H anomalies also varies spatially with a median increase of 3.9 W m^{-2} over the study period. The largest trends are found at grid locations where the offshore Q_H have risen by over 6.2 W m^{-2}. The positive offshore Q_H trends (median p-value = 0.07) are statistically significant ($p < 0.05$) at 71 grid locations (out of 194), where the Q_H have increased by 3.0 W m^{-2} to 28.4 W m^{-2} over the study period.

The monthly average offshore Q_H anomalies for June mostly show strong positive trends over the study region., with a median tau of 0.32 (Min tau = 0.15, Max tau = 0.47) (Figure 3.13, Table 3.6). The magnitude of the trends varies considerably between 4.6 W m^{-2} and 30.1 W m^{-2} (median TSA = 16.6 W m^{-2}) over the HBL. The highest trends are found at grid locations where

Table 3. 6. Mann-Kendall trends for the offshore Q_H anomalies for the period 1979–2018.

June	Minimum	Lower Quartile	Median	Upper Quartile	Maximum	Significance #*
tau	0.15	0.27	0.32	0.36	0.47	-
TSA (W m^{-2})	4.6	13.4	16.6	20.2	30.1	-
p-value	0.00001	0.001	0.004	0.01	0.03	178
July						
tau	-0.16	0.05	0.14	0.22	0.45	-
TSA (W m^{-2})	-5.1	1.6	3.7	6.6	13.9	-
p-value	0.0000	0.05	0.21	0.52	1.00	46
August						
tau	-0.11	0.08	0.15	0.23	0.43	-
TSA (W m^{-2})	-3.3	2.3	3.8	6.1	11.3	-
p-value	0.0000	0.04	0.16	0.44	0.99	58
September						
tau	-0.18	-0.02	0.05	0.12	0.28	-
TSA (W m^{-2})	-4.0	-0.4	1.2	2.5	5.9	-
p-value	0.01	0.25	0.51	0.77	1.00	9
Study Months Average						
tau	-0.01	0.14	0.20	0.24	0.36	-
TSA (W m^{-2})	-1.7	3.0	3.9	6.2	10.9	-
p-value	0.00	0.03	0.07	0.20	0.46	71

Statistics are derived from boxplot summaries showing the distribution of trends across the HBL. TSA indicates the Theil-Sen approach estimate of the slope expressed here as the 40-year trend. *The number of grid locations out of 194 in the HBL with statistically significant trends (<0.05).

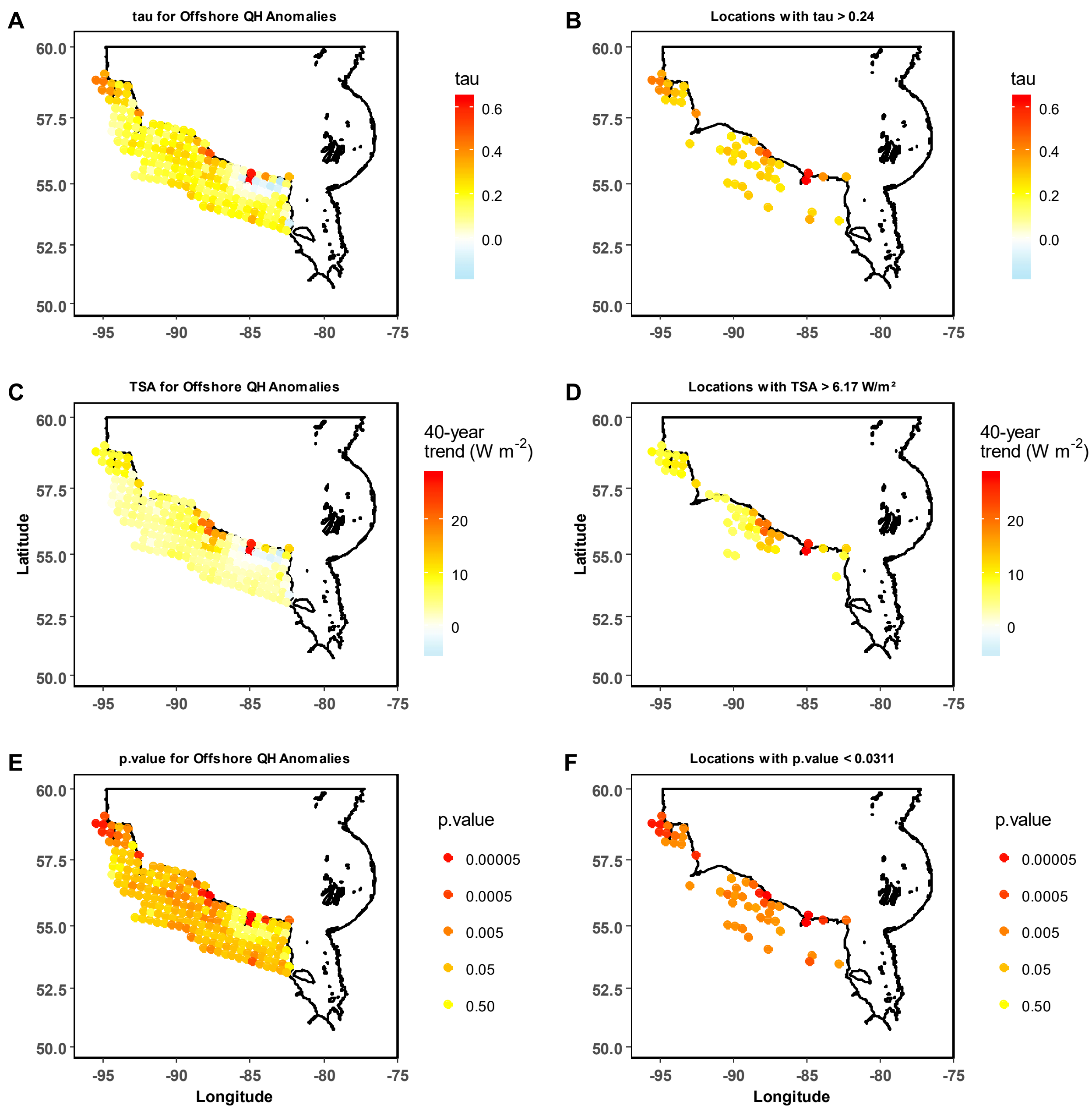

Figure 3. 12. Mann-Kendall trends for the four study months (June to September) average offshore sensible heat flux anomalies over the HBL during the 1979–2018 period. (A) tau for all grid locations, and (B) the top 25% of the grid locations with the highest tau. (C) Theil-Sen slope for all grid locations, and (D) the top 25% of the grid locations with the highest TSA. (E) p-value for all grid locations, and (F) the bottom 25% of the grid locations with the lowest p-value.

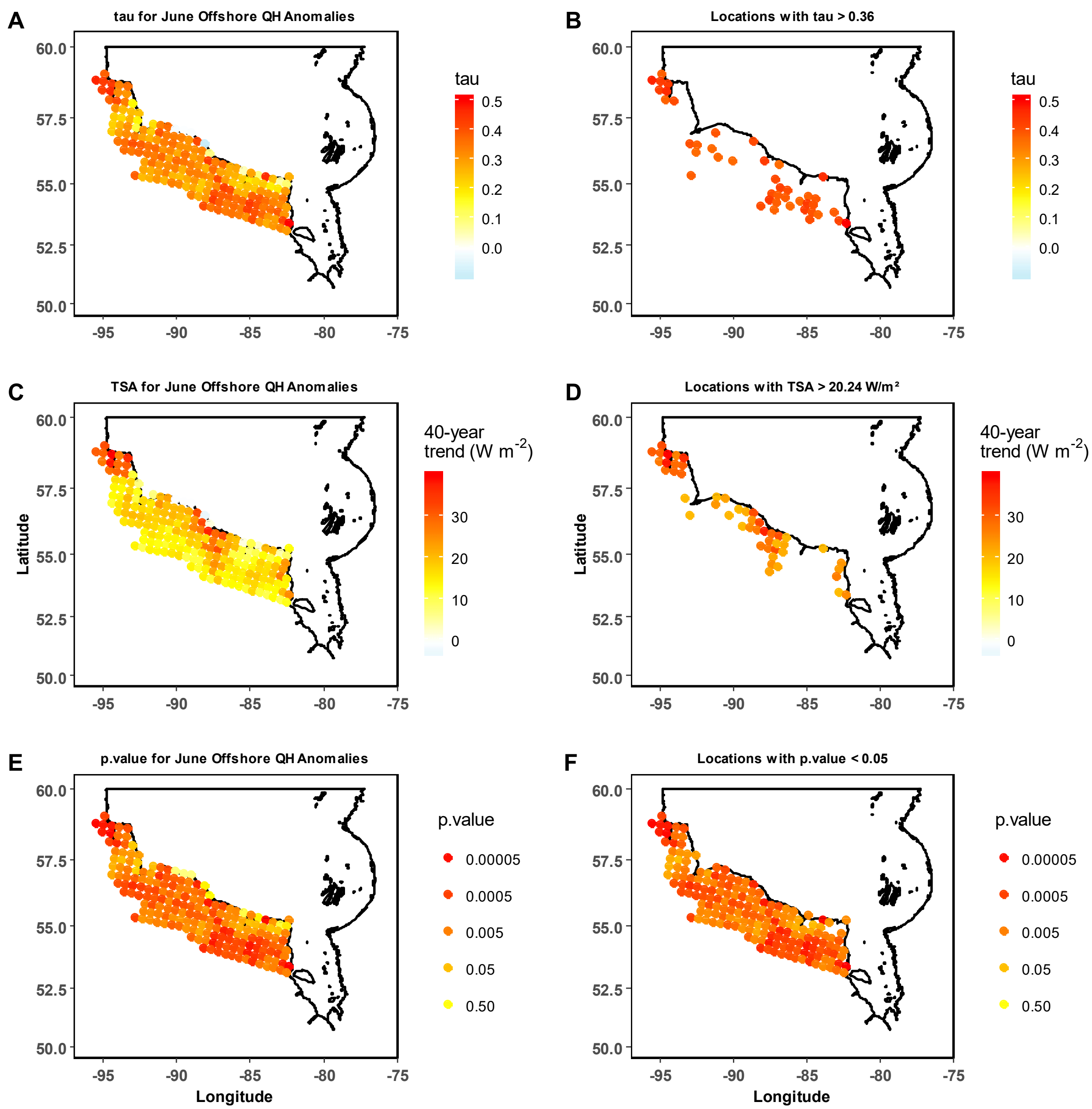

Figure 3. 13. Mann-Kendall trends for the offshore sensible heat flux anomalies over the HBL for June during the 1979–2018 period. (A) tau for all grid locations, and (B) the top 25% of the grid locations with the highest tau. (C) Theil-Sen slope for all grid locations, and (D) the top 25% of the grid locations with the highest TSA. (E) p-value for all grid locations, and (F) the grid locations with statistically significant p-values (<0.05).

the offshore Q_H anomalies have risen by over 20.2 W m^{-2}, such as around the Churchill area in upper HBL and along the coast of middle and lower HBL. These positive offshore Q_H trends in June are statistically significant (median p-value = 0.004) at 178 grid locations in the HBL.

In July, most of the trends in the offshore Q_H are positive over the HBL, with a median tau of 0.14 (Min tau = -0.16, Max tau = 0.45) (Table 3.6). The magnitude of the trends varies spatially with a median increase in Q_H of 3.7 W m^{-2} over the study period. The grid locations that have the highest trends are characterized by offshore Q_H anomalies exceeding 6.6 W m^{-2}. These positive trends (median p-value = 0.21) in July are statistically significant ($p < 0.05$) at 46 grid locations, especially along the coast of central HBL where the offshore Q_H have increased by over 17.9 W m^{-2} during the study period.

In August, the offshore Q_H anomalies are typically characterized by positive trends over the study region, with a median tau of 0.15 (Min tau = -0.11, Max tau = 0.43) (Table 3.6). The magnitude of the trends ranges between -3.3 W m^{-2} and 11.3 W m^{-2} (median TSA = 3.8 W m^{-2}) over the HBL, with a few hotspots at the mouths of the Severn and Winisk Rivers, where the offshore Q_H have increased by about 49.0 W m^{-2} during the study period. Overall, these positive trends in August are statistically significant ($p < 0.05$) at 58 grid locations, predominantly in the central HBL.

In September, the offshore Q_H anomalies show both weak positive and negative trends ranging from a tau of -0.18 to 0.28 (median tau = 0.05) over the study region (Table 3.6). The magnitude of the trends varies spatially with a median increase of 1.2 W m^{-2} (Min TSA = -4.0 W m^{-2}, Max TSA = 5.9 W m^{-2}) over the study period. The positive offshore Q_H trends are statistically significant ($p < 0.05$) at only 9 grid locations—along the coast just west of the Severn River in central HBL, and along the Ekwan and Attawapiskat Rivers and the Polar Bear

Provincial Park in southern HBL. Overall, the results of the monthly average offshore Q_H anomalies demonstrate that the most extensive and significant trends over the HBL occur in June.

The four study months average Q_H anomalies during onshore wind regimes for the period 1979–2018 typically show positive trends over the HBL (Figure 3.14, Table 3.7). The strength of the trends varies considerably across the region with a median tau of 0.29 (Min tau = 0.10, Max tau = 0.48). The magnitude of the trends in onshore Q_H also varies spatially with a median increase of 11.3 W m^{-2} (Min TSA = 0.2 W m^{-2}, Max TSA = 21.2 W m^{-2}) over the study period. The largest trends are found at grid locations where the onshore Q_H anomalies exceed 13.7 W m^{-2}. These positive onshore Q_H trends are statistically significant (median p-value = 0.01) at 155 grid locations (out of 194) in the HBL. The most significant trends in the onshore Q_H occur primarily in the central section of the HBL.

The monthly average onshore Q_H anomalies for June mainly show strong positive trends over the study region., with a median tau of 0.24 (Min tau = -0.11, Max tau = 0.48) (Figure 3.15, Table 3.7). The magnitude of the trends varies considerably with a median increase in Q_H of 18.1 W m^{-2} over the study period. The largest trends are found at grid locations where the onshore Q_H anomalies are between 24.2 W m^{-2} and 36.2 W m^{-2}, such as in the coastal areas of upper and middle HBL. The onshore Q_H trends in June are statistically significant (median p-value = 0.03) at 112 grid locations—including 2 locations with significant negative trends.

In July, most of the trends in the onshore Q_H anomalies are positive over the HBL, with a median tau of 0.17 (Min tau = -0.02, Max tau = 0.36) (Table 3.7). The magnitude of the trends varies considerably over the study region with a median increase in Q_H of 8.1 W m^{-2}. The highest trends are found at grid locations where the onshore Q_H have risen by between 10.5 W m^{-2} and

18.0 W m^{-2}. The positive trends (median p-value = 0.14) in July are statistically significant ($p < 0.05$) at 47 grid locations—mainly found in central and southern HBL.

In August, the onshore Q_H anomalies show both positive and negative trends ranging widely from a tau of -0.25 to 0.37 (median tau = 0.13) over the HBL (Table 3.7). The magnitude of the trends varies between -12.0 W m^{-2} and 17.2 W m^{-2} (median TSA = 5.0 W m^{-2}) over the HBL, with a few hotspots at the mouths of the Severn and Winisk Rivers, where the onshore Q_H anomalies are about 36.2 W m^{-2} during the study period. The negative trends are generally found in the upper HBL, while the positive trends occur mainly in the middle and lower HBL. Overall, the onshore Q_H trends (median p-value = 0.20) in August are statistically significant ($p < 0.05$) at 36 grid locations—29 with positive trends and 7 with negative trends over the study period.

In September, there are generally positive onshore Q_H trends over the HBL, with a median tau of 0.20 (Min tau = -0.05, Max tau = 0.39) (Figure 3.16, Table 3.7). The magnitude of the trends varies considerably with a median increase in onshore Q_H of 7.2 W m^{-2} over the study period. The highest trends are found at grid locations where the onshore Q_H have risen by between 9.1 W m^{-2} and 14.8 W m^{-2}. The positive trends (median p-value = 0.07) in September are statistically significant ($p < 0.05$) at 85 grid locations—predominantly in southern HBL and, to a lesser extent, central HBL. Overall, the results demonstrate that the most significant and widespread onshore Q_H anomalies occur in June, followed by September.

Table 3. 7. Mann-Kendall trends for the onshore Q_H anomalies for the period 1979–2018

June	Minimum	Lower Quartile	Median	Upper Quartile	Maximum	Significance #*
tau	-0.11	0.14	0.24	0.34	0.48	-
TSA (W m^{-2})	-2.7	9.9	18.1	24.2	36.2	-
p-value	0.00001	0.002	0.03	0.17	0.40	112
July						
tau	-0.02	0.11	0.17	0.21	0.36	-
TSA (W m^{-2})	-0.8	5.4	8.1	10.5	18.0	-
p-value	0.0000	0.05	0.14	0.31	0.68	47
August						
tau	-0.25	0.01	0.13	0.18	0.37	-
TSA (W m^{-2})	-12.0	0.1	5.0	8.2	17.2	-
p-value	0.0000	0.07	0.20	0.51	0.99	36
September						
tau	-0.05	0.12	0.20	0.26	0.39	-
TSA (W m^{-2})	-2.4	4.1	7.2	9.1	14.8	-
p-value	0.0003	0.02	0.07	0.28	0.60	85
Study Months Average						
tau	0.10	0.23	0.29	0.33	0.48	-
TSA (W m^{-2})	0.2	8.2	11.3	13.7	21.2	-
p-value	0.000	0.003	0.01	0.03	0.08	155

Statistics are derived from boxplot summaries showing the distribution of trends across the HBL. TSA indicates the Theil-Sen approach estimate of the slope expressed here as the 40-year trend. *The number of grid locations out of 194 in the HBL with statistically significant trends (<0.05).

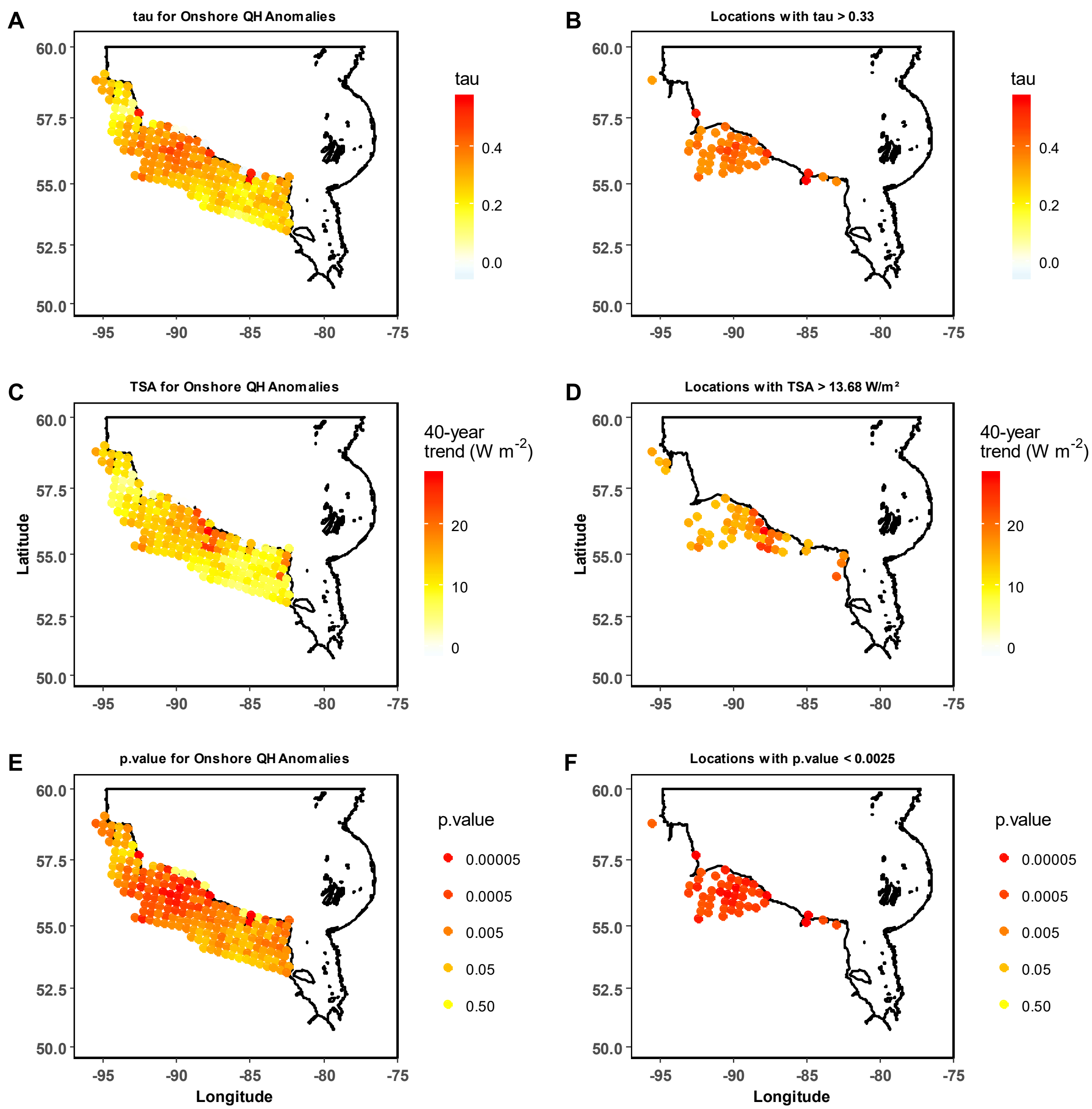

Figure 3. 14. Mann-Kendall trends for the four study months (June to September) average onshore sensible heat flux anomalies over the HBL during the 1979–2018 period. (A) tau for all grid locations, and (B) the top 25% of the grid locations with the highest tau. (C) Theil-Sen slope for all grid locations, and (D) the top 25% of the grid locations with the highest TSA. (E) p-value for all grid locations, and (F) the bottom 25% of the grid locations with the lowest p-value.

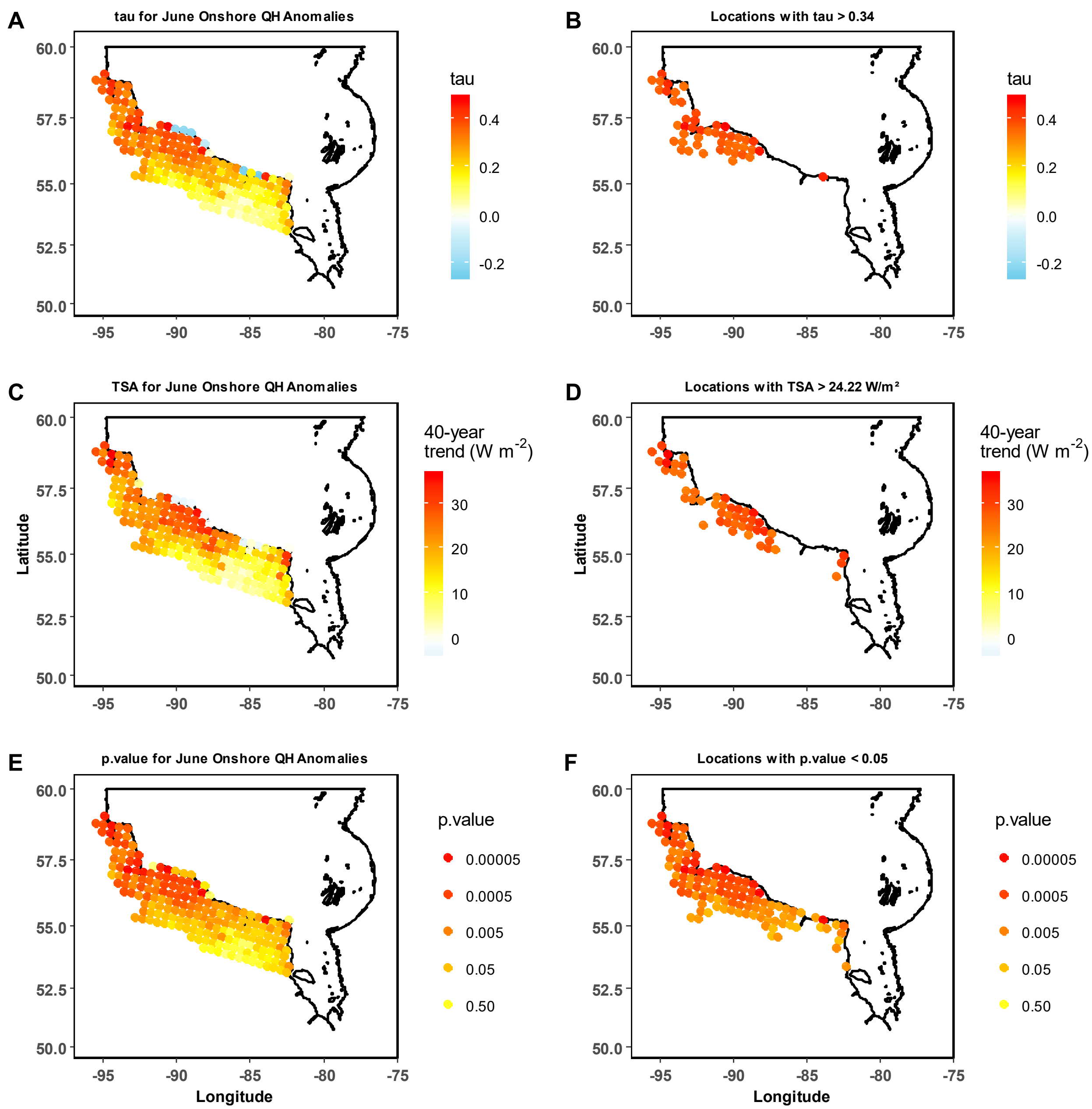

Figure 3. 15. Mann-Kendall trends for the onshore sensible heat flux anomalies over the HBL for June during the 1979–2018 period. (A) tau for all grid locations, and (B) the top 25% of the grid locations with the highest tau. (C) Theil-Sen slope for all grid locations, and (D) the top 25% of the grid locations with the highest TSA. (E) p-value for all grid locations, and (F) the grid locations with statistically significant p-values (<0.05).

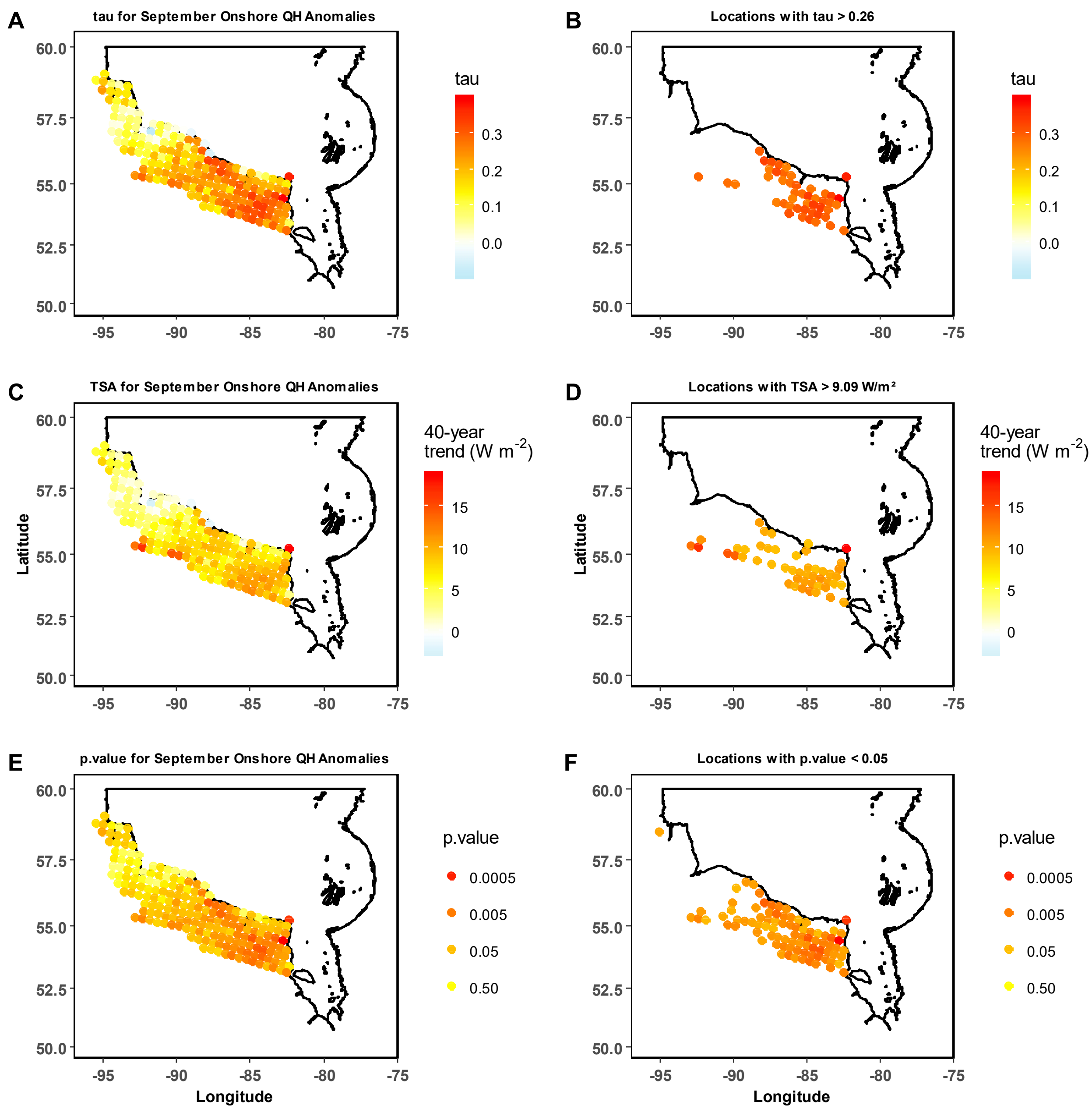

Figure 3. 16. Mann-Kendall trends for the onshore sensible heat flux anomalies over the HBL for September during the 1979–2018 period. (A) tau for all grid locations, and (B) the top 25% of the grid locations with the highest tau. (C) Theil-Sen slope for all grid locations, and (D) the top 25% of the grid locations with the highest TSA. (E) p-value for all grid locations, and (F) the grid locations with statistically significant p-values (<0.05).

3.3.5 Latent Heat Flux

The four study months average Q_E anomalies during offshore wind regimes for the period 1979–2018 are mostly characterized by positive trends over the HBL (Figure 3.17, Table 3.8). The strength of the positive trends varies considerably across the region with a median tau of 0.26 (Min tau = 0.08, Max tau = 0.43). The magnitude of the trends in offshore Q_E also varies spatially with a median increase of 7.6 W m^{-2} (Min TSA = 2.4 W m^{-2}, Max TSA = 10.8 W m^{-2}) over the study period. The offshore Q_E trends (median p-value = 0.02) are statistically significant ($p < 0.05$) at 147 grid locations (out of 194)—including 3 grid locations with significant negative trends roughly around the Severn River in the coastal areas of central HBL. The most significant positive trends in the Q_E are mainly found in southern HBL and, to a lesser extent, in the central HBL.

The offshore Q_E anomalies for June are mostly positive—with some non-significant negative trends along the coast of northern and central HBL (Table 3.8). The strength of the trends varies spatially with a median tau of 0.17 (Min tau = -0.22, Max tau = 0.41). The magnitude of the trends ranges between -11.4 W m^{-2} and 23.2 W m^{-2} (median TSA = 9.2 W m^{-2}) over the study region. The largest positive trends are mainly found at grid locations in southern HBL where the offshore Q_E have risen by over 16.8 W m^{-2}. The positive offshore Q_E trends (median p-value = 0.13) in June are statistically significant ($p < 0.05$) at 63 grid locations in the HBL.

In July, the trends in the offshore Q_E anomalies are strongly positive over much of the HBL, though some notable negative trends are present mainly around Fort Severn and its environs (Figure 3.18, Table 3.8). The strength of the trends varies spatially with a median tau of 0.27 (Min tau = 0.09, Max tau = 0.45). The magnitude of the trends ranges between 2.0 W m^{-2}

and 18.2 W m^{-2} (median TSA = 11.1 W m^{-2}) over the study region. The offshore Q_E trends (median p-value = 0.01) in July are statistically significant ($p < 0.05$) at 144 grid locations—including 8 grid locations with significant negative trends, ranging from -13.7 W m^{-2} to -24.2 W m^{-2}.

In August, the offshore Q_E anomalies are generally characterized by positive trends over the study region, with a median tau of 0.18 (Min tau = -0.05, Max tau = 0.36) (Table 3.8). The magnitude of the trends ranges between -1.7 W m^{-2} and 13.5 W m^{-2} (median TSA = 6.5 W m^{-2}) over the HBL, with a few hotspots at the mouths of the Severn and Winisk Rivers, where the offshore Q_E anomalies are approximately 37.0 W m^{-2} during the study period. Overall, the positive trends (median p-value = 0.10) in August are statistically significant ($p < 0.05$) at 61 grid locations, predominantly around inland areas of central and southern HBL.

In September, there are mostly strong positive offshore Q_E trends over the HBL, with a median tau of 0.36 (Min tau = 0.06, Max tau = 0.49) (Figure 3.19, Table 3.8). The magnitude of the trends varies between 1.8 W m^{-2} and 13.3 W m^{-2} (median TSA = 9.0 W m^{-2}) over the study region. The largest trends are generally found at grid locations in the southern HBL where the offshore Q_E have increased by over 10.3 W m^{-2}. The positive offshore Q_E trends in September are statistically significant (median p-value = 0.001) at 152 grid locations in the HBL. It is noteworthy that most of the non-significant Q_E trends occur in the coastal areas of central HBL, approximately around Fort Severn. The results show that overall, the most widespread and significant trends in the offshore Q_E over the HBL occur in September, followed by July.

Table 3. 8. Mann-Kendall trends for the offshore Q_E anomalies for the period 1979–2018.

June	Minimum	Lower Quartile	Median	Upper Quartile	Maximum	Significance #*
tau	-0.22	0.06	0.17	0.27	0.41	-
TSA (W m^{-2})	-11.4	3.2	9.2	16.8	23.2	-
p-value	0.0002	0.02	0.13	0.41	0.99	63
July						
tau	0.09	0.20	0.27	0.31	0.45	-
TSA (W m^{-2})	2.0	8.6	11.1	13.5	18.2	-
p-value	0.0000	0.005	0.01	0.05	0.12	144
August						
tau	-0.05	0.12	0.18	0.23	0.36	-
TSA (W m^{-2})	-1.7	4.3	6.5	8.4	13.5	-
p-value	0.0000	0.03	0.10	0.28	0.60	61
September						
tau	0.06	0.26	0.36	0.40	0.49	-
TSA (W m^{-2})	1.8	6.9	9.0	10.3	13.3	-
p-value	0.00001	0.0003	0.001	0.02	0.04	152
Study Months Average						
tau	0.08	0.21	0.26	0.30	0.43	-
TSA (W m^{-2})	2.4	5.9	7.6	8.4	10.8	-
p-value	0.000	0.006	0.02	0.05	0.11	147

Statistics are derived from boxplot summaries showing the distribution of trends across the HBL. TSA indicates the Theil-Sen approach estimate of the slope expressed here as the 40-year trend. *The number of grid locations out of 194 in the HBL with statistically significant trends (<0.05).

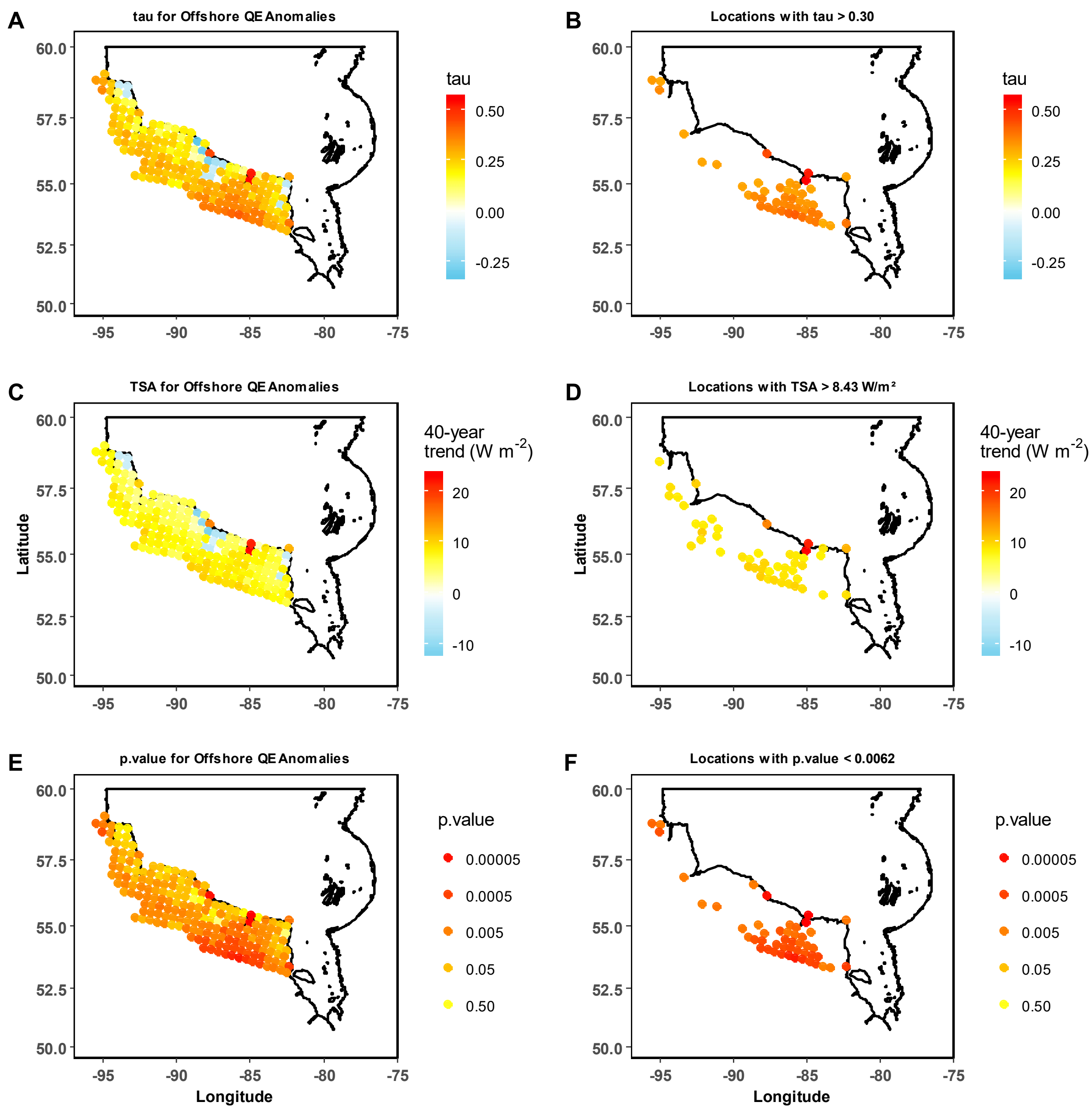

Figure 3. 17. Mann-Kendall trends for the four study months (June to September) average offshore latent heat flux anomalies over the HBL during the 1979–2018 period. (A) tau for all grid locations, and (B) the top 25% of the grid locations with the highest tau. (C) Theil-Sen slope for all grid locations, and (D) the top 25% of the grid locations with the highest TSA. (E) p-value for all grid locations, and (F) the bottom 25% of the grid locations with the lowest p-value.

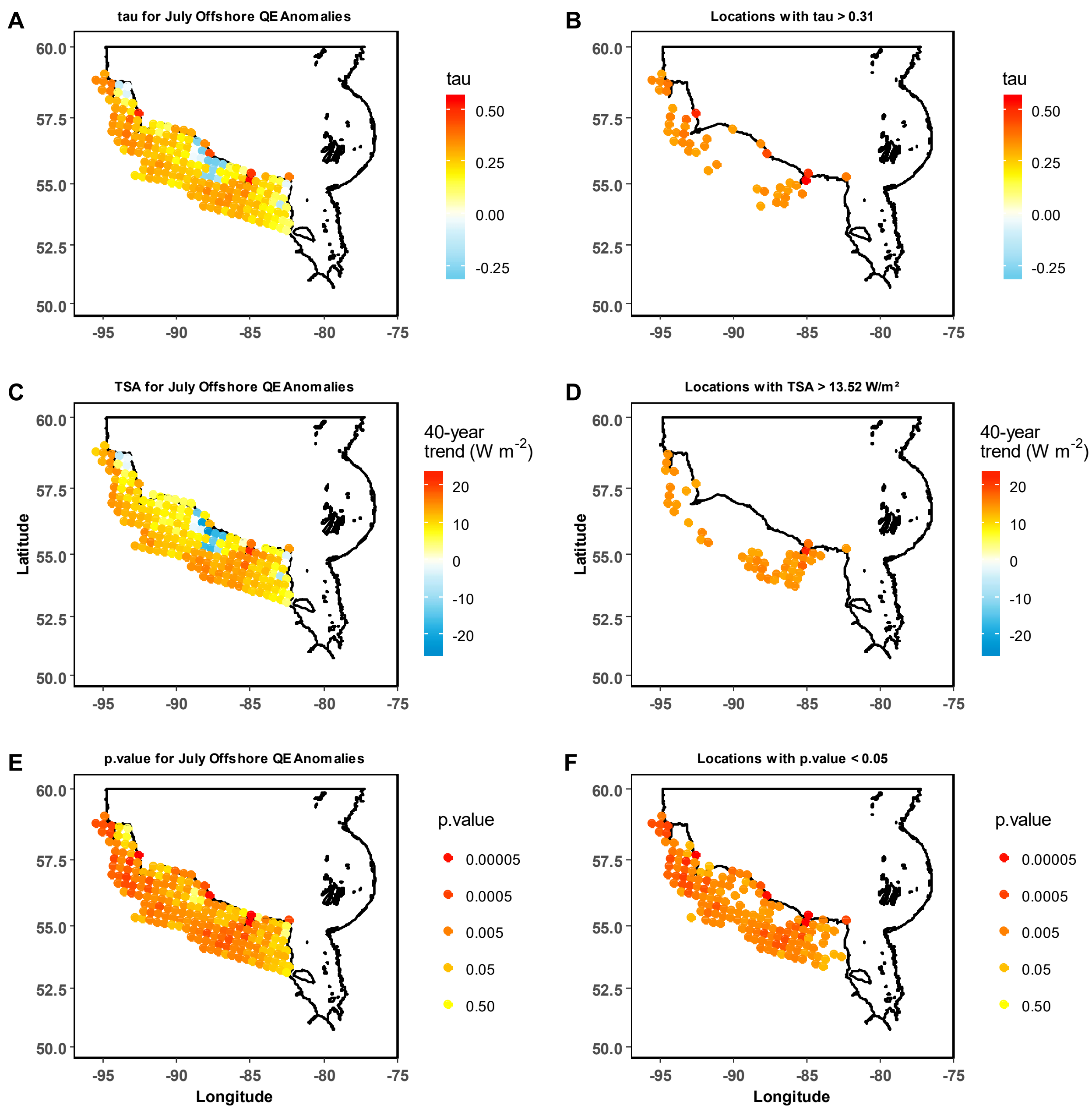

Figure 3. 18. Mann-Kendall trends for the offshore latent heat flux anomalies over the HBL for July during the 1979–2018 period. (A) tau for all grid locations, and (B) the top 25% of the grid locations with the highest tau. (C) Theil-Sen slope for all grid locations, and (D) the top 25% of the grid locations with the highest TSA. (E) p-value for all grid locations, and (F) the grid locations with statistically significant p-values (<0.05).

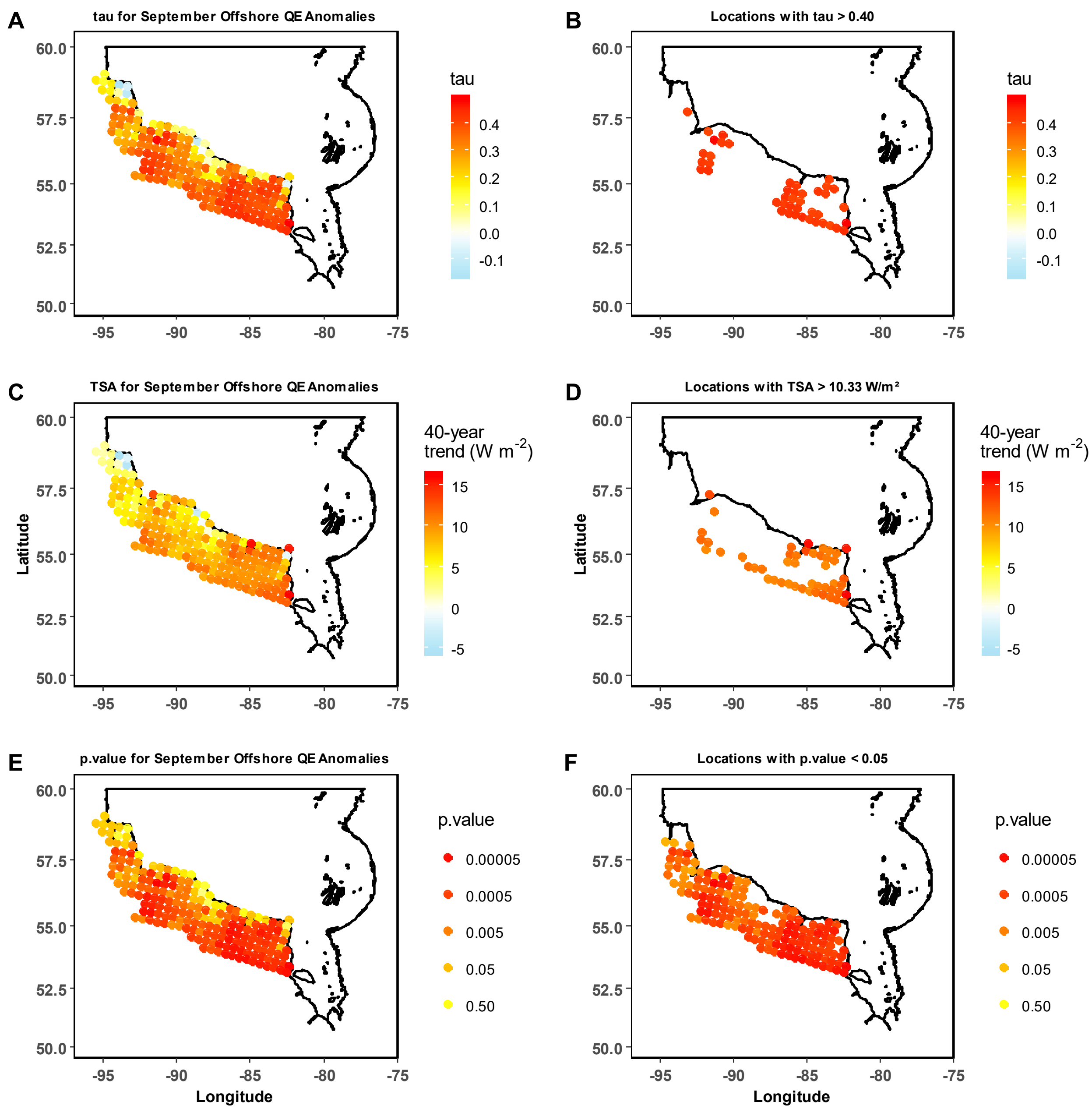

Figure 3. 19. Mann-Kendall trends for the offshore latent heat flux anomalies over the HBL for September during the 1979–2018 period. (A) tau for all grid locations, and (B) the top 25% of the grid locations with the highest tau. (C) Theil-Sen slope for all grid locations, and (D) the top 25% of the grid locations with the highest TSA. (E) p-value for all grid locations, and (F) the grid locations with statistically significant p-values (<0.05).

The four study months average Q_E anomalies during onshore wind regimes for the period 1979–2018 typically show positive trends over the HBL, although some prominent negative trends are present mostly around Fort Severn in the central HBL (Figure 3.20, Table 3.9). The strength of the trends ranges from a tau of -0.11 to 0.47 (median tau = 0.23) over the study region. The magnitude of the trends also varies spatially with a median increase in Q_E anomalies of 7.4 W m^{-2}. The highest trends are mostly found at grid locations farther inland in the middle and lower HBL where the onshore Q_E have risen by between 9.4 W m^{-2} and 14.5 W m^{-2} over the study period. The onshore Q_E trends (median p-value = 0.03) are statistically significant ($p < 0.05$) at 116 grid locations (out of 194)—including 5 grid locations with significant negative trends, ranging from -8.4 W m^{-2} to -13.2 W m^{-2}. The most significant positive trends in the Q_E are mainly found in southern HBL.

The monthly average onshore Q_E anomalies for June show both positive and negative trends which range between a tau of -0.26 and 0.39 (median tau = 0.18) over the HBL (Figure 3.21, Table 3.9). The negative trends are relatively close to the coast while the positive trends are generally found farther inland. The magnitude of the onshore Q_E anomalies varies considerably across the HBL with a median increase of 8.0 W m^{-2} (Min TSA = -7.9 W m^{-2}, Max TSA = 22.1 W m^{-2}) over the study period. The largest trends are found at grid locations where the onshore Q_E anomalies exceed 11.1 W m^{-2}. Overall, the onshore Q_E trends (median p-value = 0.09) in June are statistically significant ($p < 0.05$) at 72 grid locations, particularly in inland areas of central HBL and much of southern HBL—including 2 negative trends along the coast in upper and middle HBL.

In July, the trends in the onshore Q_E are positive over the vast majority of the HBL, though some notable negative trends occur mainly around Fort Severn and its environs in central

HBL (Table 3.9). The strength of the trends varies spatially with a median tau of 0.11 (Min tau = -0.15, Max tau = 0.38). The magnitude of the trends ranges between -6.0 W m^{-2} and 14.3 W m^{-2} (median TSA = 5.2 W m^{-2}) over the study region. The largest positive trends are mainly found at inland grid locations in southern HBL, and to a lesser extent, central HBL where the onshore Q_E have risen by over 8.5 W m^{-2}. The onshore Q_E trends (median p-value = 0.23) in July are statistically significant ($p < 0.05$) at 39 grid locations—including 8 grid locations with significant negative trends, ranging from -15.6 W m^{-2} to -27.18 W m^{-2}.

In August, the onshore Q_E anomalies generally show positive trends over much of the HBL, but a few prominent negative trends occur mainly in the coastal areas of northern HBL and around Fort Severn in central HBL (Table 3.9). The strength of the trends varies considerably with a median tau of 0.13 (Min tau = -0.23, Max tau = 0.29). The magnitude of the trends ranges between -11.1 W m^{-2} and 13.2 W m^{-2} (median TSA = 5.5 W m^{-2}) over the HBL, with a few hotspots at the mouths of the Severn and Winisk Rivers, and along the southeastern coast of the Wapusk National Park, where the onshore Q_E anomalies are about 27.1 W m^{-2}. The onshore Q_E trends (median p-value = 0.22) in August are statistically significant ($p < 0.05$) at 28 grid locations—including 3 grid locations with significant negative trends. The most significant positive trends in the Q_E are mainly found in southern HBL.

In September, there are typically positive onshore Q_E trends over the HBL, with a median tau of 0.16 (Min tau = -0.07, Max tau = 0.42) (Figure 3.22, Table 3.9). The magnitude of the trends varies spatially with a median increase of 5.4 W m^{-2}. The largest trends are found at grid locations where the onshore Q_E have risen by between 7.4 W m^{-2} and 13.7 W m^{-2}.

Table 3. 9. Mann-Kendall trends for the onshore Q_E anomalies for the period 1979–2018.

June	Minimum	Lower Quartile	Median	Upper Quartile	Maximum	Significance #*
tau	-0.26	0.04	0.18	0.25	0.39	-
TSA (W m^{-2})	-7.9	1.4	8.0	11.1	22.1	-
p-value	0.0005	0.02	0.09	0.33	0.77	72
July						
tau	-0.15	0.05	0.11	0.18	0.38	-
TSA (W m^{-2})	-6.0	2.3	5.2	8.5	14.3	-
p-value	0.0000	0.07	0.23	0.45	0.99	39
August						
tau	-0.23	0.02	0.13	0.19	0.29	-
TSA (W m^{-2})	-11.1	0.8	5.5	8.7	13.2	-
p-value	0.0000	0.08	0.22	0.62	1.00	28
September						
tau	-0.07	0.10	0.16	0.23	0.42	-
TSA (W m^{-2})	-2.0	3.2	5.4	7.4	13.7	-
p-value	0.0001	0.04	0.14	0.33	0.75	51
Study Months Average						
tau	-0.11	0.14	0.23	0.33	0.47	-
TSA (W m^{-2})	-4.9	3.5	7.4	9.4	14.5	-
p-value	0.000	0.003	0.03	0.15	0.36	116

Statistics are derived from boxplot summaries showing the distribution of trends across the HBL. TSA indicates the Theil-Sen approach estimate of the slope expressed here as the 40-year trend. *The number of grid locations out of 194 in the HBL with statistically significant trends (<0.05).

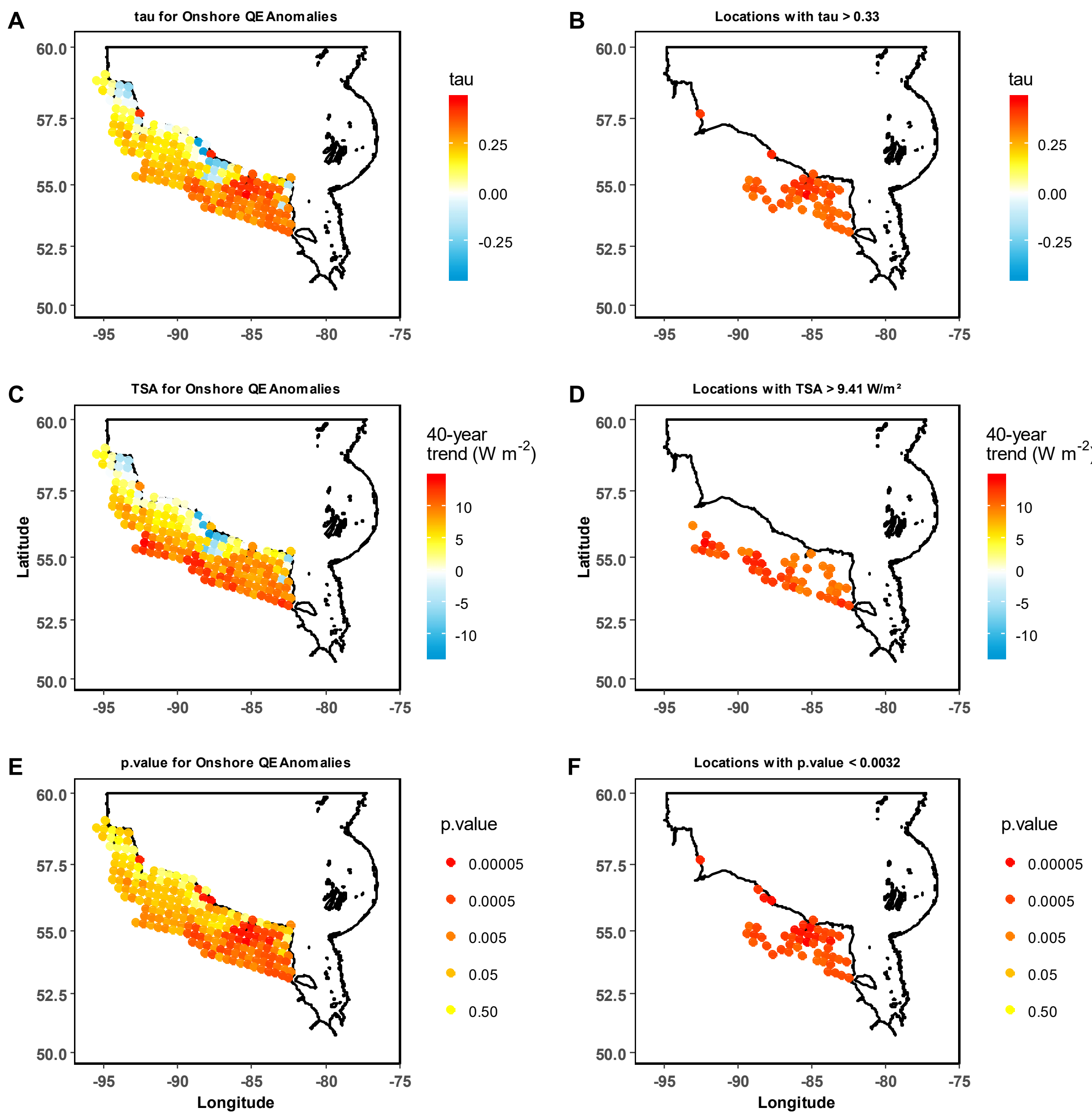

Figure 3. 20. Mann-Kendall trends for the four study months (June to September) average onshore latent heat flux anomalies over the HBL during the 1979–2018 period. (A) tau for all grid locations, and (B) the top 25% of the grid locations with the highest tau. (C) Theil-Sen slope for all grid locations, and (D) the top 25% of the grid locations with the highest TSA. (E) p-value for all grid locations, and (F) the bottom 25% of the grid locations with the lowest p-value.

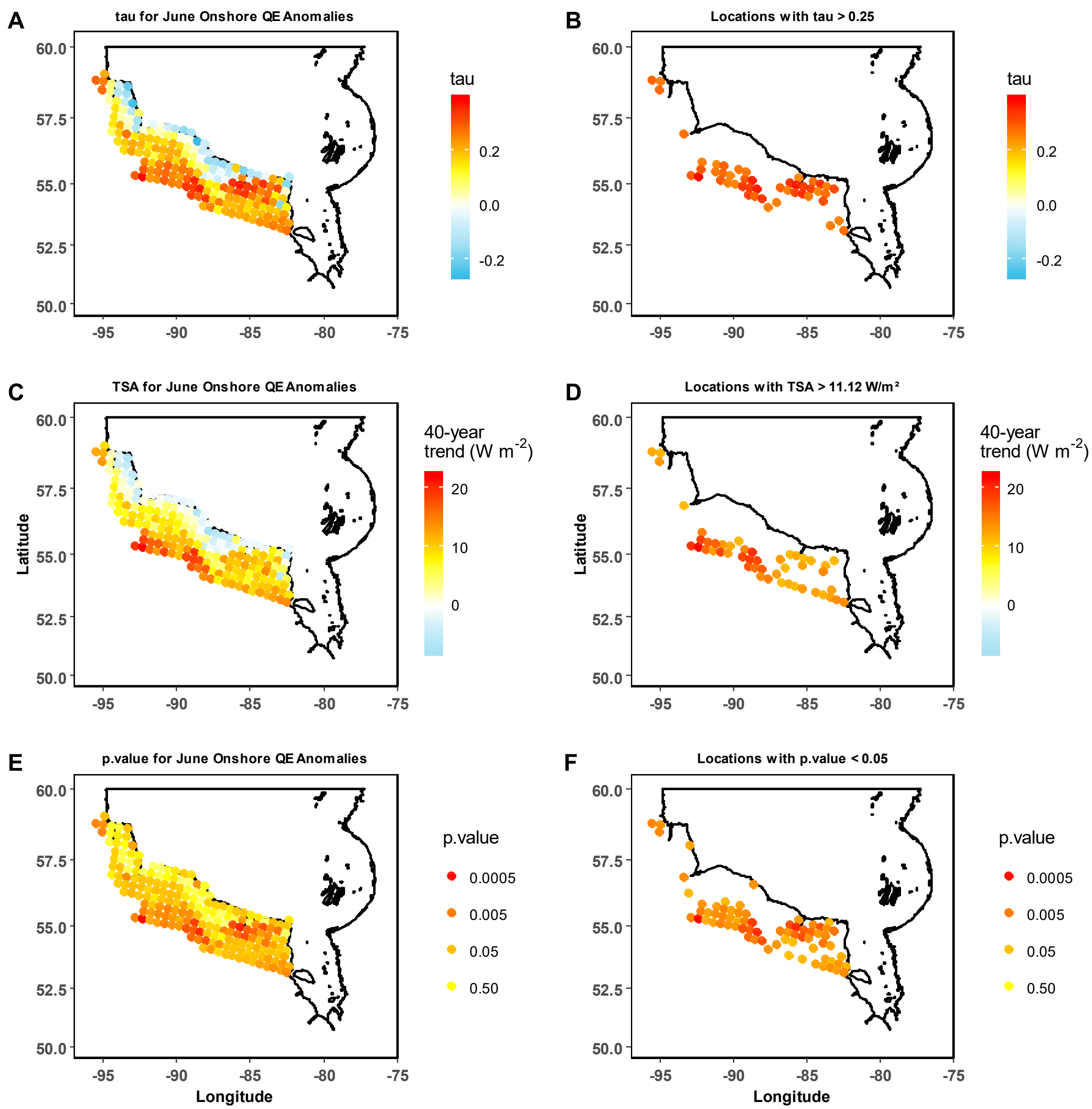

Figure 3. 21. Mann-Kendall trends for the onshore latent heat flux anomalies over the HBL for June during the 1979–2018 period. (A) tau for all grid locations, and (B) the top 25% of the grid locations with the highest tau. (C) Theil-Sen slope for all grid locations, and (D) the top 25% of the grid locations with the highest TSA. (E) p-value for all grid locations, and (F) the grid locations with statistically significant p-values (<0.05).

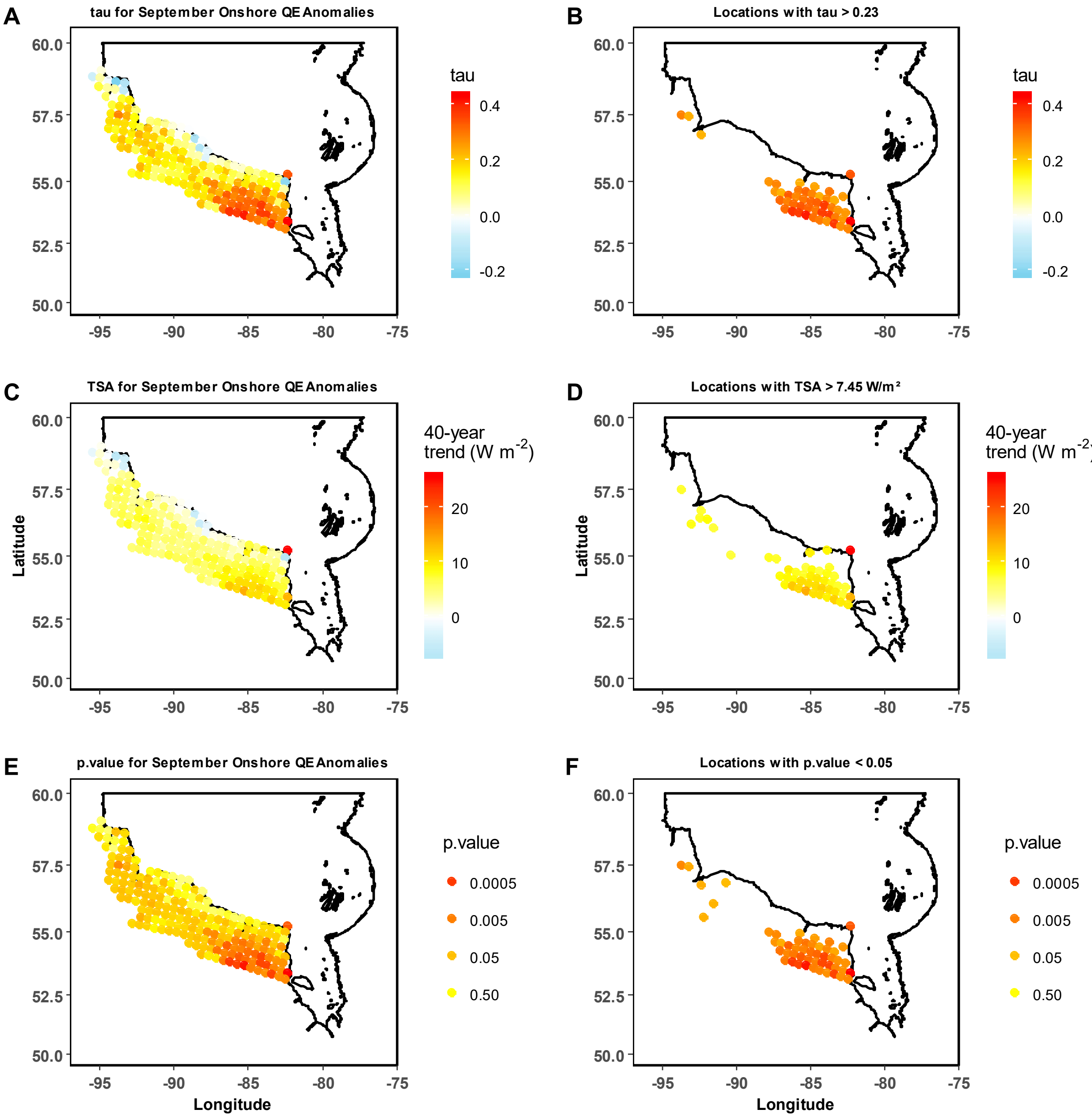

Figure 3. 22. Mann-Kendall trends for the onshore latent heat flux anomalies over the HBL for September during the 1979–2018 period. (A) tau for all grid locations, and (B) the top 25% of the grid locations with the highest tau. (C) Theil-Sen slope for all grid locations, and (D) the top 25% of the grid locations with the highest TSA. (E) p-value for all grid locations, and (F) the grid locations with statistically significant p-values (<0.05).

The positive onshore Q_E trends (median p-value = 0.14) in September are statistically significant ($p < 0.05$) at 51 grid locations. The most significant trends in the Q_E are mainly found in southern HBL. Overall, the results demonstrate that the most widespread and significant onshore Q_E anomalies over the HBL occur in June.

3.3.6 Ground Heat Flux

The four study months average Q_G anomalies during offshore wind regimes for the period 1979–2018 show positive trends over the HBL (Figure 3.23, Table 3.10). The strength of these positive trends varies considerably across the region with a median tau of 0.17 (Min tau = 0.03, Max tau = 0.33). The magnitude of the trends in offshore Q_G also varies spatially with a median increase of 1.6 W m^{-2} (Min TSA = 0.02 W m^{-2}, Max TSA = 3.1 W m^{-2}) over the study period. These positive offshore Q_G trends (median p-value = 0.12) are statistically significant ($p < 0.05$) at 40 grid locations in the HBL. The most significant ground warming trends are occurring mainly at grid locations around Churchill and the Wapusk National Park in upper HBL.

There are also substantial monthly variations in the magnitude and significance of the offshore Q_G anomalies. In June, the offshore Q_G anomalies show both weak positive and negative trends ranging from a tau of -0.09 to 0.23 (median tau = 0.08) over the HBL (Table 3.10). The magnitude of the trends varies spatially between -2.1 W m^{-2} and 6.2 W m^{-2} (median TSA = 1.5 W m^{-2}). The highest positive trends are found around Churchill and the northern edge of Wapusk National Park in upper HBL, as well as over much of lower HBL, where the offshore Q_G have increased by over 3.6 W m^{-2}. The offshore Q_G trends (median p-value = 0.48) in June indicate statistically significant ($p < 0.05$) positive trends at only 2 grid locations in the coastal areas of northern HBL. On the other hand, non-significant negative trends in the offshore Q_G occur mainly in central HBL.

In July, the offshore Q_G anomalies are generally characterized by weak positive trends over the study region, with a median tau of 0.13 (Min tau = -0.01, Max tau = 0.24) (Table 3.10). The magnitude of the trends varies spatially with a median increase of 1.5 W m^{-2}. The largest trends are primarily found at grid locations along the coastal HBL, where the offshore Q_G have increased by between 2.0 W m^{-2} and 3.4 W m^{-2} over the study period. However, these positive trends (median p-value = 0.26) in the July offshore Q_G are statistically significant ($p < 0.05$) at only 4 grid locations.

In August, the offshore Q_G anomalies generally have positive trends over the study region, with a median tau of 0.17 (Min tau = 0.04, Max tau = 0.28) (Table 3.10). The magnitude of the trends varies spatially with a median increase of 1.9 W m^{-2}. The highest trends mainly occur at grid locations along the coastal HBL, where the offshore Q_G anomalies are between 2.2 W m^{-2} and 3.3 W m^{-2} over the study period. Overall, the positive offshore Q_G trends (median p-value = 0.13) in August are statistically significant ($p < 0.05$) at 27 grid locations in the HBL.

In September, there are strong positive offshore Q_G trends over the vast majority of HBL, with a median tau of 0.26 (Min tau = 0.13, Max tau = 0.39) (Figure 3.24, Table 3.10). The magnitude of the trends varies between 2.1 W m^{-2} and 5.7 W m^{-2} (median TSA = 3.9 W m^{-2}), and the highest trends are generally found at grid locations in southern HBL. The positive offshore Q_G trends in September are statistically significant (median p-value = 0.02) at 143 grid locations in the HBL. Indeed, the results demonstrate that the most significant and extensive trends in the offshore Q_G over the HBL occur in September.

Table 3. 10. Mann-Kendall trends for the offshore Q_G anomalies for the period 1979–2018.

June	Minimum	Lower Quartile	Median	Upper Quartile	Maximum	Significance #*
tau	-0.09	-0.01	0.08	0.15	0.23	-
TSA (W m^{-2})	-2.1	-0.3	1.5	3.6	6.2	-
p-value	0.04	0.17	0.48	0.77	1.00	2
July						
tau	-0.01	0.08	0.13	0.16	0.24	-
TSA (W m^{-2})	-0.1	1.1	1.5	2.0	3.4	-
p-value	0.01	0.15	0.26	0.45	0.84	4
August						
tau	0.04	0.13	0.17	0.20	0.28	-
TSA (W m^{-2})	0.3	1.4	1.9	2.2	3.3	-
p-value	0.01	0.07	0.13	0.23	0.46	27
September						
tau	0.13	0.23	0.26	0.29	0.39	-
TSA (W m^{-2})	2.1	3.3	3.9	4.3	5.7	-
p-value	0.0003	0.008	0.02	0.04	0.09	143
Study Months Average						
tau	0.03	0.13	0.17	0.21	0.33	-
TSA (W m^{-2})	0.02	1.1	1.6	2.0	3.1	-
p-value	0.000	0.06	0.12	0.24	0.51	40

Statistics are derived from boxplot summaries showing the distribution of trends across the HBL. TSA indicates the Theil-Sen approach estimate of the slope expressed here as the 40-year trend. *The number of grid locations out of 181 in the HBL with statistically significant trends (<0.05).

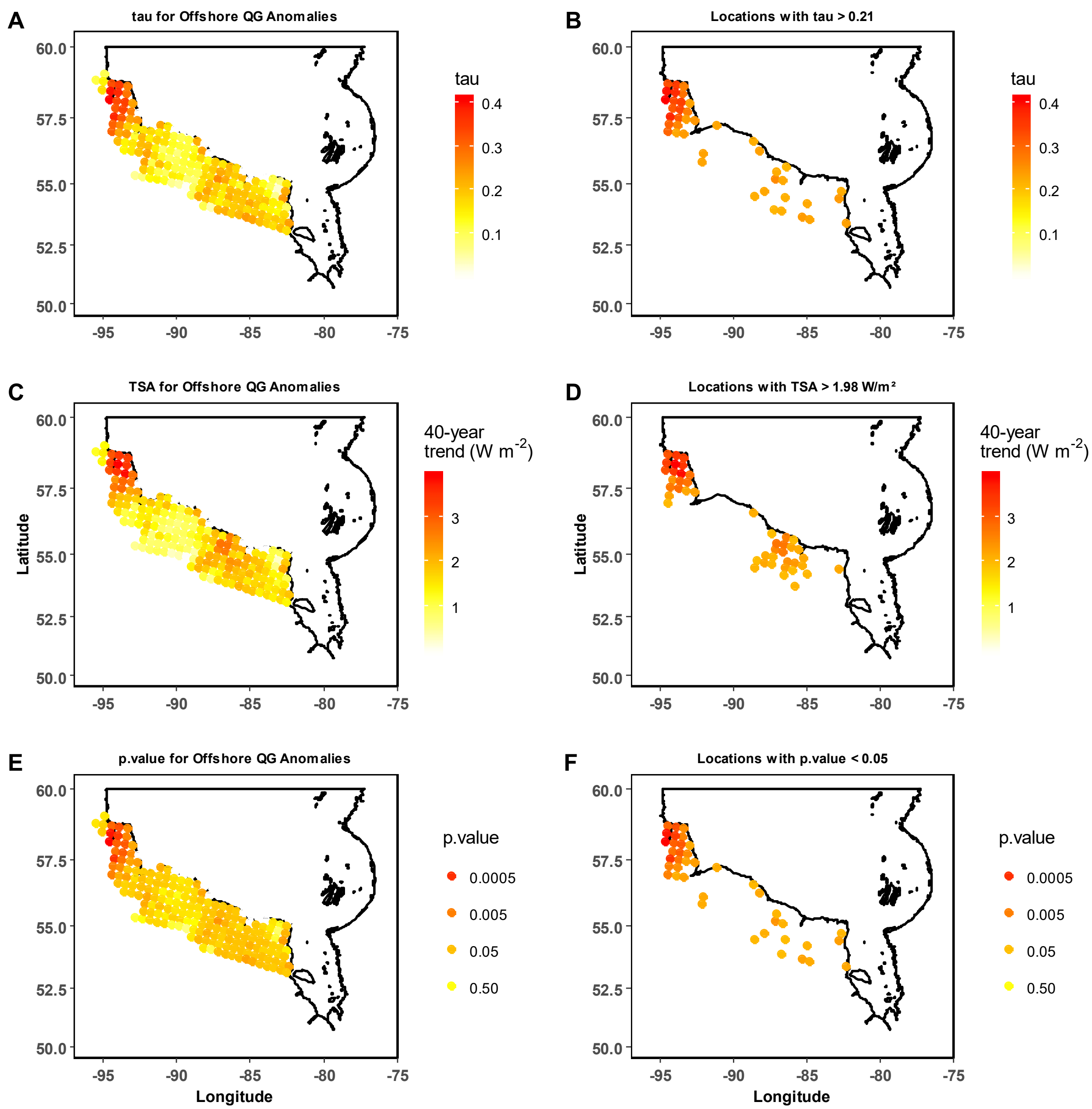

Figure 3. 23. Mann-Kendall trends for the four study months (June to September) average offshore ground heat flux anomalies over the HBL during the 1979–2018 period. (A) tau for all grid locations, and (B) the top 25% of the grid locations with the highest tau. (C) Theil-Sen slope for all grid locations, and (D) the top 25% of the grid locations with the highest TSA. (E) p-value for all grid locations, and (F) the grid locations with statistically significant p-values (<0.05).

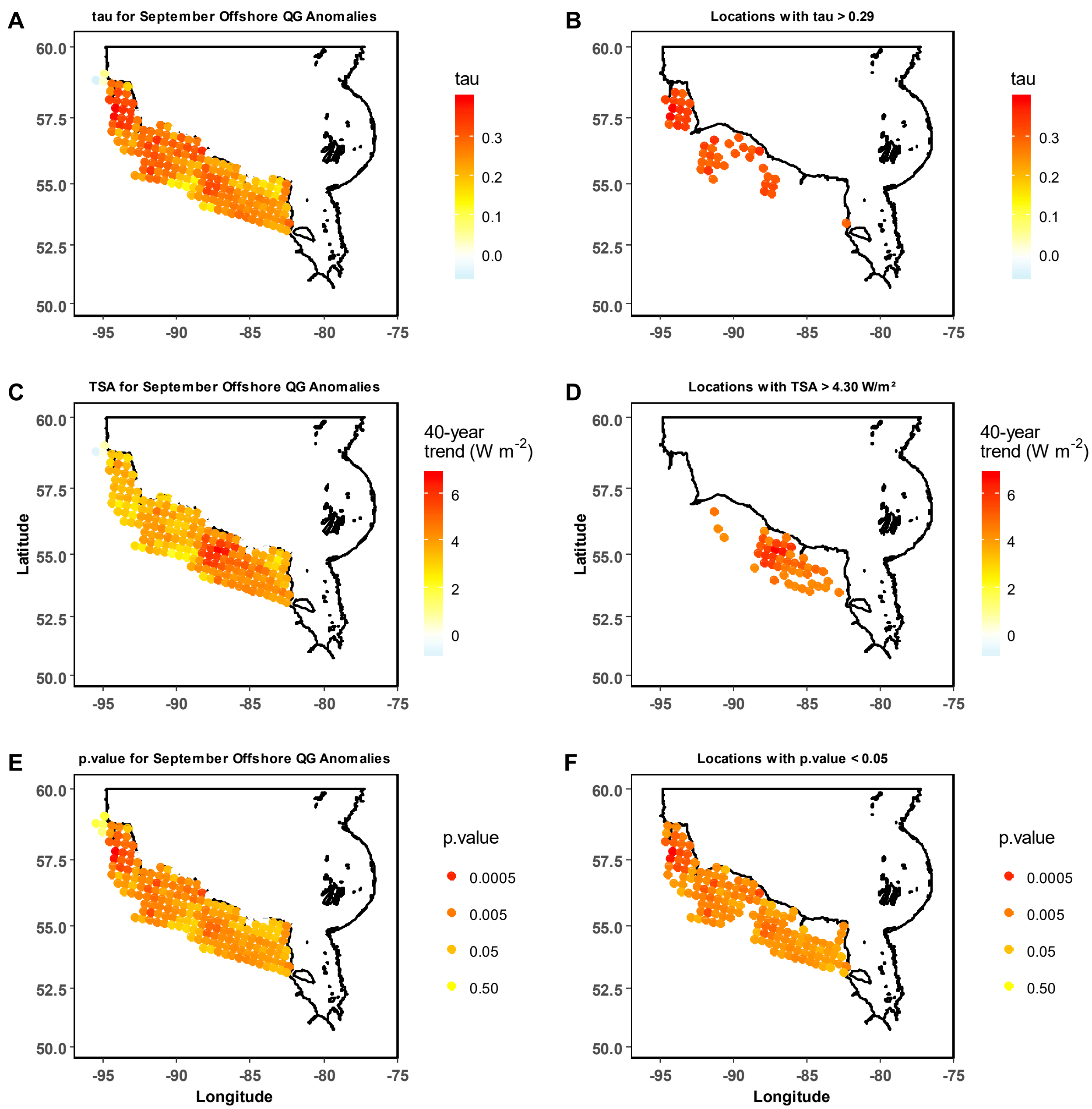

Figure 3. 24. Mann-Kendall trends for the offshore ground heat flux anomalies over the HBL for September during the 1979–2018 period. (A) tau for all grid locations, and (B) the top 25% of the grid locations with the highest tau. (C) Theil-Sen slope for all grid locations, and (D) the top 25% of the grid locations with the highest TSA. (E) p-value for all grid locations, and (F) the grid locations with statistically significant p-values (<0.05).

The average Q_G anomalies during onshore wind regimes for the period 1979–2018 generally show positive trends over the HBL (Figure 3.25, Table 3.11). The strength of these positive trends varies considerably across the study region with a median tau of 0.22 (Min tau = 0.08, Max tau = 0.34). The magnitude of the trends in onshore Q_G also varies spatially with a median increase of 2.3 W m^{-2} (Min TSA = 0.9 W m^{-2}, Max TSA = 3.5 W m^{-2}) over the study period. The positive onshore Q_G trends (median p-value = 0.05) are statistically significant ($p < 0.05$) at 92 grid locations, particularly in central and southern HBL.

The onshore Q_G anomalies show considerable spatial variations in the magnitude and significance of the trends over the four study months. In June, the HBL region is characterized by positive onshore Q_G trends, with a median tau of 0.22 (Min tau = 0.04, Max tau = 0.35) (Figure 3.26, Table 3.11). The magnitude of the trends varies between 1.1 W m^{-2} and 6.5 W m^{-2} (median TSA = 3.9 W m^{-2}) over the study region. These positive onshore Q_G trends (median p-value = 0.05) in June are statistically significant ($p < 0.05$) at 88 grid locations—predominantly in central HBL and, to a lesser extent, southern HBL.

In July, onshore Q_G anomalies show both weak positive and negative trends ranging from a tau of -0.07 to 0.18 (median tau = 0.04) over the HBL (Table 3.11). The magnitude of the trends varies between -0.9 W m^{-2} and 3.1 W m^{-2} (median TSA = 0.6 W m^{-2}). The positive onshore Q_G trends (median p-value = 0.70) in July are statistically significant ($p < 0.05$) at only 2 coastal grid locations around the northern edge of Wapusk National Park in upper HBL.

In August, there are generally positive onshore Q_G trends over the study region, with a median tau of 0.14 (Min tau = -0.05, Max tau = 0.32) (Table 3.11). The magnitude of the trends in onshore Q_G varies spatially with a median increase of 2.1 W m^{-2} over the study period. The highest trends are found at grid locations where the onshore Q_G have increased by between

Table 3. 11. Mann-Kendall trends for the onshore Q_G anomalies for the period 1979–2018.

June	Minimum	Lower Quartile	Median	Upper Quartile	Maximum	Significance #*
tau	0.04	0.16	0.22	0.25	0.35	-
TSA (W m^{-2})	1.1	3.0	3.9	4.4	6.5	-
p-value	0.002	0.02	0.05	0.14	0.29	88
July						
tau	-0.07	0.00	0.04	0.07	0.18	-
TSA (W m^{-2})	-0.9	0.0	0.6	1.3	3.1	-
p-value	0.02	0.51	0.70	0.84	1.00	2
August						
tau	-0.05	0.08	0.14	0.20	0.32	-
TSA (W m^{-2})	-1.4	1.1	2.1	3.1	5.7	-
p-value	0.004	0.07	0.20	0.50	1.00	30
September						
tau	-0.12	0.05	0.12	0.17	0.34	-
TSA (W m^{-2})	-1.7	0.9	1.9	2.9	5.5	-
p-value	0.002	0.12	0.28	0.55	1.00	22
Study Months Average						
tau	0.08	0.18	0.22	0.25	0.34	-
TSA (W m^{-2})	0.9	1.8	2.3	2.6	3.5	-
p-value	0.002	0.03	0.05	0.11	0.23	92

Statistics are derived from boxplot summaries showing the distribution of trends across the HBL. TSA indicates the Theil-Sen approach estimate of the slope expressed here as the 40-year trend. *The number of grid locations out of 181 in the HBL with statistically significant trends (<0.05).

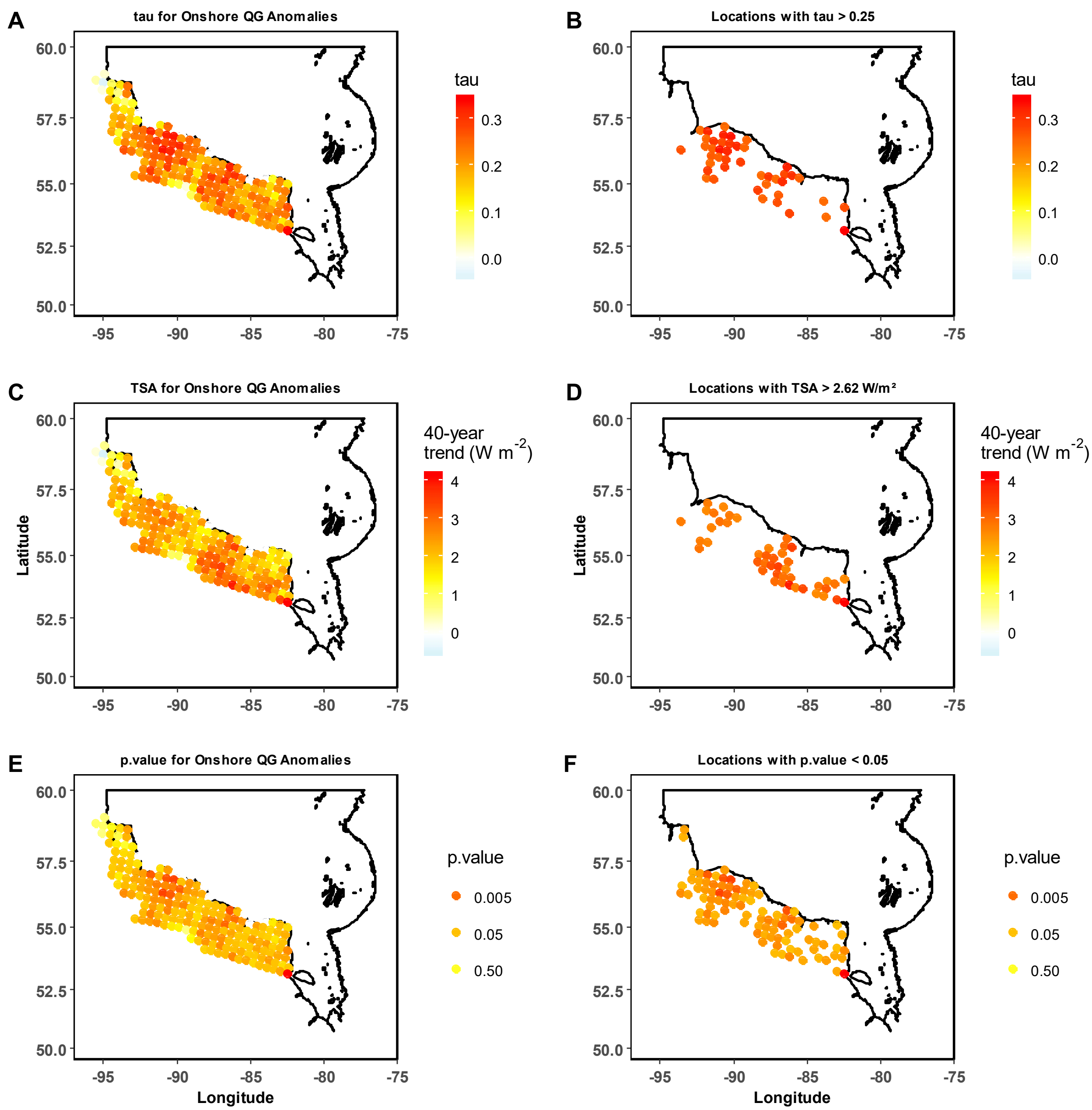

Figure 3. 25. Mann-Kendall trends for the four study months (June to September) average onshore ground heat flux anomalies over the HBL during the 1979–2018 period. (A) tau for all grid locations, and (B) the top 25% of the grid locations with the highest tau. (C) Theil-Sen slope for all grid locations, and (D) the top 25% of the grid locations with the highest TSA. (E) p-value for all grid locations, and (F) the grid locations with statistically significant p-values (<0.05).

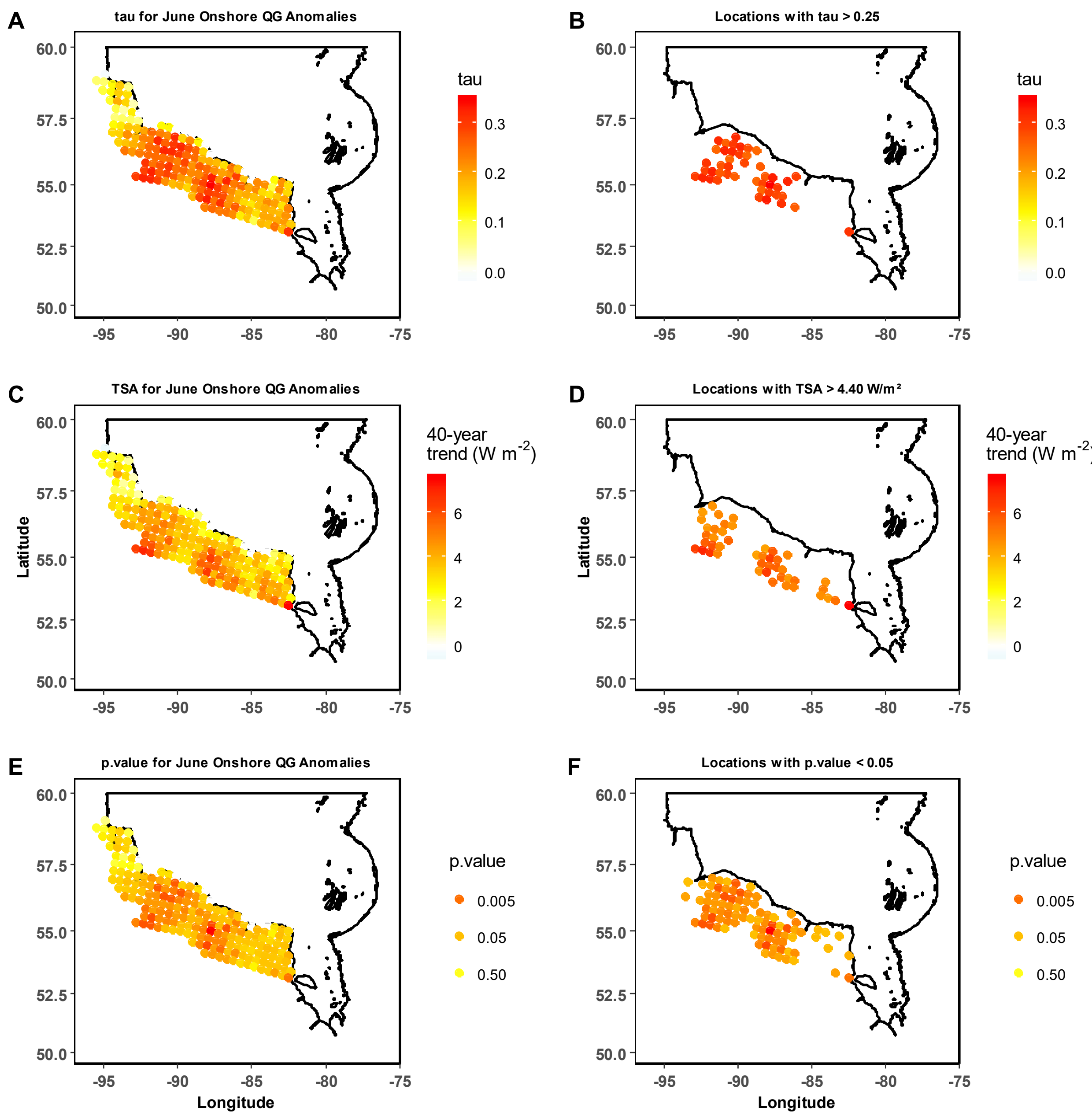

Figure 3. 26. Mann-Kendall trends for the onshore ground heat flux anomalies over the HBL for June during the 1979–2018 period. (A) tau for all grid locations, and (B) the top 25% of the grid locations with the highest tau. (C) Theil-Sen slope for all grid locations, and (D) the top 25% of the grid locations with the highest TSA. (E) p-value for all grid locations, and (F) the grid locations with statistically significant p-values (<0.05).

3.1 W m^{-2} and 5.7 W m^{-2}, especially at inland grid locations in southern HBL. The onshore Q_G trends (median p-value = 0.20) in August are statistically significant ($p < 0.05$) at 30 grid locations in the HBL.

In September, the trends in the onshore Q_G anomalies are mostly positive over the study region, with a median tau of 0.12 (Min tau = -0.12, Max tau = 0.34) (Table 3.11). The magnitude of the onshore Q_G anomalies varies spatially with a median increase of 1.9 W m^{-2} over the study period. The largest trends primarily occur in the coastal areas of northern and central HBL, where the onshore Q_G have risen by between 2.9 W m^{-2} and 5.5 W m^{-2}. The onshore Q_G trends (median p-value = 0.28) in September are statistically significant ($p < 0.05$) at 22 grid locations in the HBL. Overall, the results indicate that the most widespread and significant trends in the onshore Q_G over the HBL occur in June.

3.4 Discussion

3.4.1 Spatial Variations in Wind and Temperature Changes Across the HBL

The positive (negative) trends in the four study months average onshore (offshore) wind frequency are widespread over the study region, with a total of 134 out of 194 grid locations showing significant trends ($p < 0.05$). The monthly spatial analysis shows that the number of grid locations that have significant positive trends ($p < 0.05$) is 92 in June, 8 in July, 2 in August and 0 in September. It is important to recall here that the spatially averaged results discussed earlier in Chapter 2 indicate that the trends in wind frequency are only significant in June. Here, a detailed spatial analysis highlights not only the specific areas that have significant trends in June but also shows a few grid locations with significant trends in July and August. Overall, the results demonstrate that the highest and most significant trends in the onshore winds occur in June, particularly in the inland areas of central and southern HBL. The general absence of significant onshore trends in parts of the coastal areas during this month probably reflects the fact that locations relatively close to the shore traditionally have the highest onshore winds frequency (results not shown). Thus, as the climate warms, the significant wind frequency trends found only at inland locations simply demonstrates that the onshore winds now penetrate further inland. The statistically significant trends in June are also conspicuously absent in the northern—predominantly coastal—section of the study region. Indeed, Sutton et al. (2007) suggested that the land–sea temperature contrast would increase as the global climate warms resulting in stronger sea breezes.

The four study months average offshore temperature anomalies show significant positive trends ($p < 0.05$) at 193 out of 194 grid locations (the remaining one actually has a p-value = 0.05). Although there is a considerable warming trend over the study period, it is important to note the heterogeneous pattern of the trend across the study region. Some prominent hotspots can be seen along the coast—at the mouths of rivers such as around Churchill, Fort Severn and Winisk. In addition, there is an extensive narrow belt of hotspots along the Ekwan and Attawapiskat Rivers in southern HBL. Bello and Higuchi (2019) also highlighted the significance of similar areas of enhanced energy budget activities, where severe ice loss during the spring and summer has led to large reductions in albedo. Other research studies have shown that climate warming is driving an earlier onset of upstream discharge and weakening the strength of downstream river ice cover, thereby promoting an earlier ice breakup during the spring season (Cooley and Pavelsky, 2016). Thermally-induced, accelerated river ice breakup is caused by positive temperature anomalies and enhanced net radiation, while mechanical breakup events could occur during periods of high upstream discharge even if the downstream ice cover is not directly melted by radiative energy.

The monthly spatial analysis shows that the number of grid locations with significant warming trends ($p < 0.05$) during offshore winds is 166 in June, 112 in July, 20 in August and 194 in September. This is consistent with the spatially averaged monthly temperature anomalies described earlier in Chapter 2 which showed that the largest and most significant warming trends during offshore wind regimes occur in September, followed by June.

Furthermore, the seasonal average onshore temperature anomalies show significant positive trends ($p < 0.05$) at 186 out of 194 grid locations. The monthly spatial analysis shows that the number of grid locations with significant warming trends ($p < 0.05$) during onshore winds is 138 in June, 10 in July, 38 in August and 187 in September. These results are in agreement with the spatially averaged monthly temperature anomalies for onshore winds as discussed earlier in Chapter 2 where the largest and most significant warming trends are found in September, followed by June. It is noteworthy that the spatially averaged results show no significant temperature trends in July and August, while the detailed spatial analysis reveals a few grid locations with significant trends.

The seasonal average offshore wind speed anomalies show significant positive trends ($p < 0.05$) at 17 out of 194 grid locations, in contrast with the spatially averaged results discussed earlier in Chapter 2, where there was no significant trend. The significant increase in wind speed trends is found along the coast where there is enhanced climate warming and a decrease in surface albedo near coastal polynyas and shore leads in the Hudson Bay (Hannah et al. 2009; Dery et al. 2011). These areas of open water or thin ice within otherwise contiguous pack ice are undergoing the most rapid declines in sea ice under a warmer Hudson Bay climate (Bello and Higuchi, 2019).

The monthly spatial analysis shows that the number of grid locations that have significant positive trends ($p < 0.05$) in offshore wind speeds is 0 in June (and 1 significant negative trend), 45 in July, 11 in August and 4 in September. This demonstrates that the significant increase in wind speeds are most extensive in July, which is consistent with the trends found in the spatially averaged wind speeds (Chapter 2; Balogun et al., Manuscript under review). Overall, significant trends occur along the coast and the inland boundary of the HBL.

For the onshore wind regimes, the four study months average wind speed trends show significant positive trends ($p < 0.05$) at 24 out of 194 grid locations. Recall, by contrast, that the spatially averaged results show no significant trends in the four study months average wind speeds over the HBL. The significant increase in wind speeds are found in areas around river channels and at/near the mouths of rivers, where enhanced climate warming and the associated changes in upstream discharge and downstream mechanical ice resistance may be playing an important role (Cooley and Pavelsky, 2016). The monthly spatial analysis shows that the number of grid locations that have significant increases ($p < 0.05$) in onshore wind speeds is 5 in June, 96 in July, 7 in August and 4 in September (which also has 12 grid locations with significant negative trends). The most significant and widespread wind speeds found in July are due to the large disproportionate warming rate of the offshore winds compared to onshore winds, caused by the zero-curtain effect during active melt over the Hudson Bay (Chapter 2).

3.4.2 Heterogeneity in the Magnitude and Strength of Climate Warming Signals

The seasonal average offshore Q_H anomalies show significant positive trends ($p < 0.05$) at 71 out of 194 grid locations. The monthly spatial analysis shows that the number of grid locations that have significant positive trends ($p < 0.05$) in offshore Q_H are 178 in June, 46 in July, 58 in August and 9 in September. This is consistent with the spatially averaged result which showed that the largest offshore Q_H trend of 17.2 W m^{-2} is found in June (Chapter 2). Remarkably, there are many areas in the HBL where the June Q_H trends far exceed the spatially averaged trend, including about 50 grid locations where the Q_H have risen by between 20.2 W m^{-2} and 30.1 W m^{-2}, over the study period. These areas with the highest Q_H increase in June occur mostly around the Churchill area in upper HBL and along the coast of middle and lower HBL. In addition, while the spatially averaged study showed no significant trends in September offshore Q_H, the detailed spatial analysis highlights 9 grid locations with significant positive Q_H trends over the study period. These grid locations are found along the coast just west of the Severn River in central HBL, and along the Ekwan and Attawapiskat Rivers and the Polar Bear Provincial Park in southern HBL.

For the onshore wind regimes, the four study months average Q_H anomalies show significant positive trends ($p < 0.05$) at 155 out of 194 grid locations. The monthly spatial analysis shows that the number of grid locations that have significant positive trends ($p < 0.05$) in onshore Q_H is 110 in June (as well as 2 with significant negative trends), 47 in July, 29 in August (and 7 with significant negative trends) and 85 in September. This is consistent with the spatially averaged results which reported that the highest onshore Q_H trend of 19.1 W m^{-2} was in June (Chapter 2). Notably, there are as many as 50 grid locations in the study region where the June Q_H trends surpass the spatially averaged trend and have increased by between 24.2 W m^{-2}

and 36.2 W m^{-2} over the study period. Such grid locations with enhanced Q_H trends in June occur predominantly in the coastal areas of northern and central HBL. Furthermore, even though the spatially averaged onshore Q_H anomalies showed no significant trends in August, here the results reveal that there are 29 grid locations with significant positive Q_H trends over the study period.

The seasonal average offshore Q_E anomalies show significant positive trends ($p < 0.05$) at 144 out of 194 grid locations—besides 3 with significant negative trends. The monthly spatial analysis shows that the number of grid locations that have significant positive trends ($p < 0.05$) in offshore Q_E are 63 in June, 136 in July (besides 8 with significant negative trends), 61 in August and 152 in September. This is generally consistent with the spatially averaged results which showed that the highest offshore Q_E trends were found in July and September (Chapter 2; Balogun et al., Manuscript under review). One should note here that though the spatially averaged offshore Q_E anomalies suggest marginally non-significant positive trends in June ($p = 0.08$), the detailed spatial analysis reveals that there are as many as 63 grid locations in the study region with statistically significant increases ($p < 0.05$) in the evaporative heat flux. These grid locations—mostly found in southern HBL—have positive offshore Q_E trends ranging from about 11.0 W m^{-2} to 23.2 W m^{-2} over the study period, which far exceeds the spatially averaged trend of 8.8 W m^{-2}. Furthermore, the spatially averaged offshore Q_E results mask the presence of statistically significant negative Q_E trends ($p < 0.05$) at 8 grid locations in July. These areas—mainly around Fort Severn and its environs—reveal a decrease in offshore Q_E ranging between -13.7 W m^{-2} to -24.2 W m^{-2} over the study period. In the other study months, most of these 8 grid locations also show atypical Q_E trends compared to other locations in the HBL, with non-significant negative trends in June and August, and non-significant positive trends in September.

For the onshore wind regimes, the four study months average Q_E anomalies show significant positive trends ($p < 0.05$) at 111 out of 194 grid locations—besides 5 with significant negative trends. The monthly spatial analysis shows that the number of grid locations that have significant positive trends ($p < 0.05$) in onshore Q_E is 70 in June (besides 2 with significant negative trends), 31 in July (besides 8 with significant negative trends), 25 in August (besides 3 with significant negative trends) and 51 in September. It is imperative to remember that the spatially averaged monthly onshore Q_E anomalies showed non-significant positive trends ($p > 0.05$) in July and August, and marginally significant trends in June ($p = 0.07$) and September ($p = 0.05$). However, the spatial analysis here reveals that there are many grid locations in the HBL with statistically significant positive onshore Q_E trends ($p < 0.05$) in all the study months. In fact, the significant positive trends in June at 70 grid locations range from about 7.7 W m^{-2} to 22.1 W m^{-2} over the HBL, far exceeding the spatially averaged trend of 6.1 W m^{-2}. This underscores the spatial heterogeneity of the surface energy balance over the study region. Moreover, the spatially averaged onshore Q_E results conceal the existence of statistically significant negative Q_E trends ($p < 0.05$) in June, July and August (Chapter 2; Balogun et al., Manuscript under review). This is particularly important in July when there are 8 grid locations with significant declines in the onshore evaporative heat flux—an atypical trend identical to the July offshore Q_E anomalies.

The four study months average offshore Q_G anomalies show significant positive trends ($p < 0.05$) at 40 out of 181 grid locations. In contrast, the spatially averaged results showed a marginally non-significant positive trend ($p = 0.08$) for offshore Q_G in the HBL (Chapter 2; Balogun et al., Manuscript under review). The most significant ground warming trends occur mostly around Churchill and Wapusk National Park in northern HBL. It is pertinent to mention that there are an additional 39 grid locations that are statistically significant at the 90%

confidence level ($p < 0.10$). The monthly spatial analysis demonstrates that the number of grid locations that have significant positive trends ($p < 0.05$) in offshore Q_G is only 2 in June, 4 in July, 27 in August and as many as 143 in September. Recall that the spatially averaged monthly offshore Q_G anomalies showed the upward trends are only significant ($p < 0.05$) in September, however, it is revealed here that there are also a few grid locations in June, July and particularly August, where the positive Q_G trends are statistically significant ($p < 0.05$) over the study period.

For the onshore wind regimes, the four study months average Q_G anomalies show significant positive trends ($p < 0.05$) at 92 out of 181 grid locations—generally occurring in central and southern HBL. It is noteworthy that an additional 33 grid locations have positive trends that are statistically significant at the 90% confidence level ($p < 0.10$). The monthly spatial analysis indicates that the number of grid locations that have significant positive trends ($p < 0.05$) in onshore Q_G is 88 in June, 2 in July, 30 in August and 22 in September. Previously, the spatially averaged Q_G anomalies showed that the positive trends during onshore wind regimes were significant ($p < 0.05$) only in June and August (Chapter 2; Balogun et al., Manuscript under review). Here, the spatial analysis reveals that there are also a few grid locations in July and September, where the positive Q_G trends averaging approximately 3.6 W m^{-2} and 3.8 W m^{-2}, respectively, are statistically significant ($p < 0.05$).

The spatial investigation of the trends in the mesoscale wind regimes and surface energy balance over the study period provides important insights into the heterogeneity of climate warming signals in the HBL. The results of the study demonstrate that the magnitude and strength of the climate anomalies and the number of grid locations with significant trends vary considerably over the study region. Indeed, the effects of climatic change are not expected to be uniform over the HBL as the region is climatologically and ecologically complex, featuring a wide range of permafrost systems, mineral wetlands and organic peatlands—including ice wedge polygons, thermokarst lakes, peat plateaus, bogs, fens, swamps and marshes (Riley, 2011). These diverse and often patterned systems have distinct temperature, precipitation, humidity and vegetation characteristics which influence the surface radiation and energy balance. Moreover, the results of this study suggest that the distance from the coast, as well as the temporal trends and spatial patterns in the breakup and freeze-up periods of Hudson Bay sea ice probably play an important role in the heterogeneity of climate change signals in the HBL.

We can anticipate that the HBL will very likely experience further climatic and ecological changes with continued global warming—changes that are unique to the region due to both the land/sea warming ratio and the modification in the advective role of the Hudson Bay. These changes will have considerable and unprecedented environmental impacts well beyond the region.

The spatial heterogeneity identified here raises issues for field-based ground validation experiments which have commonly been located near centers which offer logistical support. It is clear, that past studies have tended to be located in regions which now appear to have been undergoing accelerated change. While no single experiment should be considered as being representative of the Hudson Bay Lowlands as a whole, experiments in certain locations may serve as the *canary in the coal mine,* offering insights into how landscape processes my evolve with persistent climate change. This spatial analysis also allows for the identification of *hot-spots* where reviews of management practices may take on heightened importance.

3.5 Conclusion

3.5.1 Key Findings

This study provides a comprehensive spatial analysis of the changes in the frequency and advective influence of offshore and onshore winds over the HBL. It demonstrates that there are significant spatial variations in the magnitude and strength of the climatic changes in the mesoscale wind regimes over the region. The number of grid locations with significant trends in wind frequency varies considerably among the four study months. The results suggest that the onshore winds have not only increased in frequency but also penetrated further inland over the 1979–2018 study period.

Additionally, the magnitude and strength of the trends in temperatures, wind speeds and surface energy fluxes exhibit significant spatial heterogeneity over the HBL. The detailed spatial analysis reveals significant—and sometimes contrasting—climatic trends at some grid locations that were otherwise obscured by the previously reported spatially averaged results. Moreover, several prominent hotspots were found mostly along the coast and at the mouths of rivers such as Churchill, Severn and Winisk, as well as in an extensive narrow belt along the Ekwan and Attawapiskat Rivers in southern HBL. The heterogeneous climate warming signals over the study region can be attributed to both the presence of complex and patterned systems of hydro-geomorphic features in the HBL, as well as the spatial pattern of sea ice breakup and freeze-up trends in the Hudson Bay.

Overall, the research findings emphasize the importance of employing detailed spatial analysis to more fully understand the climatic changes in the HBL. It is recommended that future studies should involve long-term, regional-scale approaches to provide further insights into the impact of global warming on the mesoscale wind regimes in the HBL.

3.5.2 Implications for Permafrost and Peatland Carbon Dynamics

The HBL has long been characterized by anomalously cold temperatures in comparison with other regions at similar latitudes. The climate of the HBL is largely regulated by the presence of sea ice over the Hudson Bay—which at its core is 6 °C colder than the average for its latitude (Harvey, 1978). The advective influence of the Bay on the HBL region is particularly important during the growing season when the sea-ice cover persists into mid-summer. The region is therefore sensitive to climate warming and the associated negative trends in sea ice extent, and earlier breakup and later freeze-up dates in the Hudson Bay. Indeed, this study demonstrates that global warming and changes in the sea ice dynamics over the Hudson Bay have caused significant shifts in the mesoscale wind regimes and impacted the surface energy balance across the HBL region.

Nevertheless, the positive implications are that the changes in the climate over the HBL has resulted in a considerable increase in the frequency of onshore wind regimes in all the study months, and a complete shift towards onshore wind dominance in June. The onshore winds are relatively cool and moist and have warmed at a slower rate than the offshore winds over the last 40 years. One can argue therefore that the increased frequency of onshore winds and the corresponding decrease in offshore winds has helped to slow down the overall warming trend in the HBL. If the rise in global temperatures had led to an increase in the offshore wind frequency over the HBL—as was previously thought—there would have been a much faster rate of warming in the region (Rouse and Bello, 1985; Delidjakova et al., 2016). Moreover, the onshore wind regimes are characterized by significantly lower Q_G, thereby reducing ground warming and restricting permafrost melt. The increased frequency of onshore winds over the study period will help delay the loss of permafrost in the region. The presence of a permafrost layer also impedes water percolation from rain and snowmelt, so that during the spring-summer period, the energy that would otherwise warm the ground is used for evaporation. The persistence of wetlands and frozen soil in the HBL will help preserve the extensive peatland cover in the region, which are sensitive to moisture and temperature changes. This will inhibit carbon losses from peatlands and slow down the permafrost carbon feedback in response to global warming. It may also impede erosion arising from melt-driven river discharge and slumping. The increasing trend in the frequency of onshore winds would probably continue in the future provided the zero-curtain effects of lingering sea-ice continue. Given this, a shift from offshore to onshore wind dominance in July seems imminent.

The observed climatic changes in the mesoscale wind regimes in the HBL will further impact the terrestrial ecosystem carbon dynamics. The rise in temperatures for both onshore and offshore wind regimes coupled with the changes in the advective influence of the Hudson Bay will likely affect gross primary production and ecosystem respiration. In addition, the peatlands of the HBL feature a ground layer that is dominated by extensive coverage of bryophytes, especially *Sphagnum* mosses, and lichens, which play a crucial role in water and nutrient cycling in the region. The overall response of peatland net carbon exchange to climatic changes in the study region remains uncertain. This is an important research area that requires further investigation.

Chapter 4

Terrestrial CO_2 Exchange Diagnosis using a Peatland-Optimized Vegetation Photosynthesis and Respiration Model (VPRM) for the Hudson Bay Lowlands

Abstract

Satellite-based light use efficiency (LUE) models have been widely used to estimate gross primary production in various terrestrial ecosystems such as forests and croplands, but northern peatlands have received less attention. Peatland ecosystems in Arctic and Subarctic regions have accumulated large stocks of organic carbon over many millennia, and they play a vital role in the global carbon cycle. The Hudson Bay Lowlands (HBL) is a massive peatland-rich region in Canada that has been largely ignored in previous LUE-based studies. The ability of LUE models to capture the variations in net ecosystem exchange (NEE) over peatlands of the HBL depends on the use of appropriate LUE parameter, ε, and other model parameter values. In this study, I used the satellite data-driven Vegetation Photosynthesis and Respiration Model (VPRM) to examine the suitability of LUE models for carbon flux diagnosis in the HBL. VPRM was driven alternately with the satellite-derived enhanced vegetation index (EVI) and solar-induced chlorophyll fluorescence (SIF) datasets. The model parameter values were constrained by eddy covariance tower observations from the Churchill fen and Attawapiskat River bog sites. The main objectives of the study were to (i) investigate if site-specific parameter optimization improved NEE estimates, (ii) determine which satellite-based proxy of photosynthesis produced more reliable estimates of peatland net carbon exchange, and (iii) examine how LUE and other model parameters vary within and between the study sites. The results showed that the VPRM mean diurnal and monthly estimates of NEE had strong agreement (R^2 ranged between 0.84 and 0.99) with EC tower fluxes at the two study sites. A comparison of the site-optimized VPRM against a generic peatland PFT-optimized version of the model revealed that the site-optimized VPRM provided better estimates of NEE only during the calibration period at the Churchill fen. The diurnal and seasonal cycles of peatland carbon exchange were better captured by the SIF-driven VPRM demonstrating that SIF is a more accurate proxy for photosynthesis compared to EVI. This study suggests that satellite-based LUE models have the potential to be applied on a larger scale to the HBL region.

4.1 Introduction

Vegetation gross primary production is the largest component flux of the global carbon cycle, and it is approximately 20 times greater than anthropogenic carbon sources (Canadell et al., 2007). The exchange of carbon between the atmosphere and the terrestrial biosphere plays an important role in the Earth's climate. The magnitude and direction of the feedback between climate warming and vegetation carbon exchange represent one of the most significant uncertainties in climate change projections (Huntingford et al., 2009), particularly in the northern high-latitudes (Koven et al., 2013; Schuur et al., 2015; Nzotungicimpaye and Zickfeld, 2017).

Northern peatlands store approximately one-third of the global soil C pool (Gorham, 1991; Limpens et al., 2008), accumulating about 550 Gt C since the end of the last glaciation (Tarnocai et al., 2009; Yu et al., 2010; Loisel et al., 2014). The storage of huge amounts of carbon in peatland ecosystems results from moderate primary production rates but slow decomposition rates of organic matter due to cold temperatures and waterlogged, anaerobic conditions (Davidson & Janssens, 2006; Dorrepaal et al., 2009). However, global warming and human disturbance have caused changes in temperature and moisture conditions in peatlands. Some studies have suggested that warming in northern high latitudes will lead to an increase in terrestrial CO_2 sink due to earlier snowmelt, longer growing seasons and enhanced productivity (Churkina et al., 2005). Other studies have argued that losses from permafrost peat decomposition in high latitudes may offset the gains from vegetation growth (Koven et al., 2013; Schuur et al., 2015; Nzotungicimpaye and Zickfeld, 2017). Furthermore, the response of peatland ecosystems to climatic changes may also vary considerably over time. Short-term field and laboratory studies found that climate warming benefits rather than threaten the carbon pool of subarctic peatlands (Aurela et al., 2004), but longer-term trends show quite different results

(Euskirchen et al., 2006; Kittler et al., 2016). It remains uncertain if the northern peatlands will continue to be a net sequester of carbon or shift to a carbon source under climate and land-use change. The combined response of ecosystem respiration (R or ER) and gross primary production (GPP) to climate change will determine the overall stability of net ecosystem exchange (NEE) in northern peatland regions.

Estimating the spatial-temporal variations in peatland carbon fluxes is crucial to improve our understanding of the global climate-carbon cycle feedback. Terrestrial carbon exchange studies of northern peatlands at local, regional and global scales have experienced several challenges. These peatlands mainly occur in cold, remote locations and typically cover extensive areas. The most common technique of estimating carbon exchange in peatlands involves the use of flux chambers and eddy covariance (EC) towers. Flux chamber measurements lack both the temporal and spatial resolution needed for a thorough understanding of the carbon dynamics of peatland ecosystems (Humphreys et al., 2006; Marushchak et al., 2013), while they do shed light on the individual component communities making up an ecosystem. EC tower measurements of NEE provide a much larger CO_2 footprint, with continuous measurement at a fine temporal scale, but are unable to differentiate between GPP and R. Moreover, the existing networks of EC tower sites such as those within the FLUXNET and AmeriFlux have sparse coverage over northern peatlands due to the high cost of tower setup and maintenance. EC tower flux data for peatland sites are also prone to large gaps due to frequent equipment malfunctions, the difficulty of taking continuous measurements all year round and diminished turbulence under conditions of strong stability. Besides, many research studies that provide EC estimates of peatland NEE are limited to one single growing season or a few years, mainly due to the short EC measurement record currently available (Lees et al., 2018).

Terrestrial ecosystem models can serve as powerful tools to address the limited temporal and spatial coverage of peatland carbon exchange. Process-based terrestrial ecosystem models such as the McGill Wetland Model (MWM, St-Hilaire et al., 2010), peatland version of the Dynamic Organic Soil Terrestrial Ecosystem Model (peatland DOS-TEM, Fan et al., 2013), Lund-Potsdam-Jena General Ecosystem Simulator (LPJ-GUESS, Chaudhary et al., 2017) and Canadian Land Surface Scheme Including Biogeochemical Cycles (CLASSIC, Melton et al., 2020) have been used to investigate the long-term sensitivity of peatland carbon accumulation to climate changes. These complex process-based models incorporate a full mechanistic calculation of the terrestrial carbon balance and typically represent a large number of processes and parameters. As a result, the model simulations are computationally intensive, experimentation to isolate critical model processes may be difficult, and uncertainty in modelled carbon flux outputs may increase considerably (Lin et al., 2011; Bonan, 2019; Xiao et al., 2019).

Satellite-based light use efficiency (LUE) models are one class of terrestrial ecosystem models that have demonstrated great potential in estimating CO_2 fluxes in peatlands (Connolly et al., 2009; Kross et al., 2016). Remote sensing techniques have several advantages over field-based methods such as EC towers and process-based terrestrial biosphere models, particularly over peatland ecosystems. Historical satellite-derived carbon flux datasets are freely available and provide spatially and temporally continuous observations of the global vegetation. Data-driven LUE models have a relatively simple model structure with a minimum number of parameters, yet have been able to provide estimates of GPP or NEE which show comparable or better statistical agreement with EC tower observations than the complex, process-based models (Keenan et al., 2012; Raczka et al., 2013; Luus and Lin, 2015).

Ecosystem carbon fluxes have been commonly estimated using passive optical remote sensors that detect surface reflectance in the visible, near-infrared (NIR), and shortwave infrared (SWIR) wavelength range of the electromagnetic spectrum. Global vegetation optical measurements have been made possible using instruments such as the Advanced Very High Resolution Radiometer (AVHRR) onboard the National Oceanic and Atmospheric Administration's (NOAA) satellites, and Moderate Resolution Imaging Spectroradiometer (MODIS) aboard National Aeronautics and Space Administration's (NASA) Terra and Aqua satellites. Several satellite-derived vegetation indices (VI) including the Normalized Difference Vegetation Index (NDVI) and Enhanced Vegetation Index (EVI) have been widely employed to estimate GPP over various terrestrial ecosystems (Xiao and Moody, 2004; Rahman et al., 2005; Zhang et al., 2014, Huang et al., 2019). In recent years, solar-induced chlorophyll fluorescence (SIF) retrieved from the Orbiting Carbon Observatory-2 (OCO-2) has provided an unprecedented approach for estimating plant primary production (Frankenberg et al., 2014; Li et al., 2018a; Sun et al., 2018; Mohammed et al., 2019), and high resolution (i.e., 0.05°, 4-day or 8-day) SIF products have become available (Zhang et al., 2018; Li and Xiao, 2019).

Remote sensing data are integrated into LUE models to provide crucial information about vegetation "greenness", phenology, land cover type, and water stress (Xiao et al., 2019). Over the past three decades, different LUE models have been developed including the Carnegie-Ames-Stanford Approach model (CASA, Potter et al., 1993), MODIS GPP algorithm (MOD17, Running et al., 2004), Vegetation Photosynthesis Model (VPM, Xiao et al., 2004), and Eddy Covariance-Light Use Efficiency model (EC-LUE, Yuan et al., 2007). These satellite data-driven LUE models have been used to estimate carbon fluxes for many ecosystem types such as forests and cropland (Turner et al. 2003; Sims et al., 2008; Yuan et al., 2010), but northern peatlands have been largely ignored (Lees et al., 2018).

A few studies have used the MODIS LUE-based GPP product (MOD17) to examine carbon fluxes over peatlands (Schubert et al., 2010; Harris and Dash, 2011; Kross et al., 2013). The MOD17 estimates showed reasonable agreement with EC tower fluxes (explained 44% to 89% of the variability), but systematically underestimated GPP at most of the study sites in Canada and Finland. Kross et al. (2013) suggested that one possible cause of the observed biases could be associated with the MODIS GPP algorithm which employs a biome-specific, constant maximum LUE parameter (ε_{max}); unfortunately, peatlands or wetlands are not included in the MOD17 land cover types. Furthermore, the MODIS GPP algorithm uses vapour pressure deficit (VPD) as a proxy for water availability to modify the $\varepsilon_{max.}$ It has been argued that the use of VPD in LUE models may be ineffective over peatlands since carbon exchange is strongly dependent on soil moisture which is not well captured by VPD (Connolly et al., 2009; Harris and Dash, 2011).

Yuan et al. (2010) calibrated and validated the EC-LUE model at 54 EC flux tower sites, covering six major terrestrial biomes, excluding peatlands. Similarly, Yuan et al. (2014) evaluated the performance of seven LUE models (including CASA, EC-LUE, MODIS and VPM) using 157 EC flux towers covering six major vegetation types, but did not include any peatland or wetland site. Kross et al. (2016) evaluated the variability and environmental controls of ε, and the suitability of LUE models for the estimation of GPP in peatlands. The results of their study suggest that it is crucial for models to use a unique maximum LUE parameter value (ε_{max}) that are derived specifically from peatland ecosystems, but few studies provide information on ε_{max} values for peatlands. Moreover, they argued that although environmental scalars can be used to determine the actual ε value, it is necessary for model scalars to adequately capture changes in seasonal water availability. These studies underscore a major limitation of current LUE models as they require a well-constrained ε value, but have not been adequately calibrated within peatland ecosystems.

In this study, I examine the terrestrial carbon exchange in the Hudson Bay Lowlands (HBL) using a peatland-optimized LUE model. The HBL is a massive peatland-rich region containing an estimated 33 Gt of soil carbon (Martini, 2006), which is approximately 25% of the Canadian peatland C pool (McLaughlin and Webster, 2014) and 6% of the northern peatland C pool (Packalen et al., 2014). Despite the critical importance of the HBL to our understanding of peatland C exchange and the potential for large climate-carbon feedback (Lafleur et al., 2001; Rouse et al., 2002; Bunbury et al., 2012; Holmquist et al., 2014), little attention has been given to the application of satellite-based LUE models in the region. To the best of my knowledge, no study has applied an LUE model to estimate primary production or net ecosystem exchange specifically in the HBL. For the first time, this study evaluates the suitability of LUE models for carbon flux diagnosis in the HBL. I provide estimates of LUE parameter values that are optimized to EC tower observations. This critical information on model parameters can be used by other research studies in the peatlands of the HBL.

The primary objectives of this study are to 1) evaluate a peatland-optimized LUE-based model at a fen and bog site; 2) compare an EVI-driven model and a SIF-driven model to determine which modelling approach can provide more reliable estimates of peatland photosynthesis; 3) examine how LUE and other model parameter values vary within and between different peatland types.

4.2 Methods

4.2.1 Study Sites

The two study sites are located within the HBL region and they represent the two major northern peatland types—bogs and fens (Figure 4.1). The first study site is a subarctic palsa fen (Hanis et al., 2015), near Churchill, Manitoba, Canada (58°39’57"N, 93°49’48"W), situated about 10 km inland from the coast of the Hudson Bay. The site is located in the boreal forest-tundra ecotone and within the continuous permafrost zone (Brown, 1970), where the active layer depth can extend to over 1.5 m by early fall (Hanis et al., 2015). The Churchill fen (CF) site is about 1.7 km × 1.3 km in size and is characterized by sedge lawns, hummocks, and hollows, which have about 30 to 40 cm of peat over carbonate-rich glaciomarine sediments (Rouse et al., 2002). The sedge lawns—dominated by the sedge *Carex aquatilis* Wahlenb. and an understory of the moss *Pseudocalliergon turgescens* (Jensen) Loeske—are the most widespread, covering about 55% of the fen (Raddatz et al., 2009). The hummocks—dominated by *Cladina* spp. and *Cladonia* spp of lichens and the moss *Dicranum elongatum* Schwaegr—are drier mounds that rise approximately 40 cm above the sedge-peat surface level. The hollows—with mats of P. *turgescens* and partially decomposed organic matter underneath, overlying a mineral substrate—are about 30 cm below the sedge-peat surface, and are typically filled with water except during extreme drought conditions (Hanis et al., 2013; Hanis et al., 2015).

The second study site is a treed/low shrub bog (Humphreys et al., 2014) in the Attawapiskat River area of the HBL (52°41′N, 83°56′W). The Attawapiskat River bog (ARB) site is dominated by evergreen vegetation, and mainly comprises of raised hummocks—covered equally by *Sphagnum* mosses, particularly *S. fuscum* (Schimp.) Klinggr., and the *Cladonia* spp of lichens. The bog site features a scattered overstory dominated by ericaceous shrubs, particularly

Chamaedaphne calyculata (L.) Moench, and stunted evergreen black spruce trees, mainly *Picea mariana* (Miller) Britton, Sterns & Poggenburg (Helbig et al., 2019). The peat thickness near the centre of the flux footprint area is about 2 m, and the water table ranges between approximately 0.1 m above the moss surface after snowmelt in April and 0.2 m below the moss surface in August (Harris, 2017; Helbig et al., 2019).

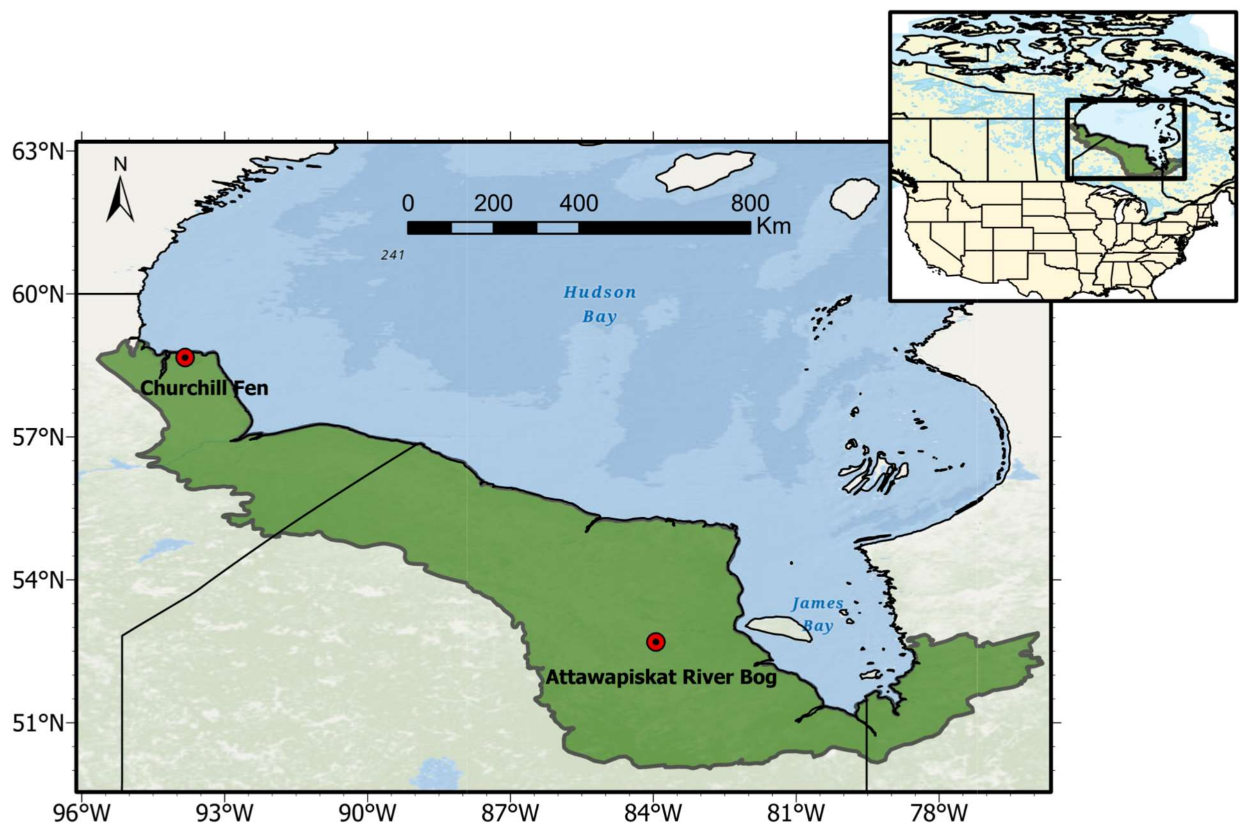

Figure 4. 1. Location of study sites in the Hudson Bay Lowlands.

4.2.2 Biospheric Carbon Flux Model

In this study, I employed two different versions of the Vegetation Photosynthesis and Respiration Model (VPRM):

1) The original VPRM (Mahadevan et al., 2008) driven by satellite-derived EVI and constrained by two different model parameterization sets using (a) model parameters calibrated by eddy covariance tower observations from the CF and ARB study sites, and (b) model parameter estimates for the peatland plant functional type (PFT) from Hilton et al. (2013).
2) A newly modified VPRM driven by satellite-derived SIF, with model parameters constrained by eddy covariance tower observations from the CF and ARB study sites.

The VPRM is an LUE-based land surface model that assimilates remote sensing, meteorological, and EC tower flux observations to provide reliable estimates of net CO_2 exchange between the terrestrial biosphere and atmosphere. Similar to other LUE models, VPRM is based on four key theoretical assumptions (Sellers, 1987; Monteith, 1972; Running et al., 2004, Xiao et al., 2004): (i) plant productivity is linearly related to the absorbed photosynthetically active radiation (APAR) by the vegetation canopies, (ii) satellite-derived vegetation indices can be used to estimate APAR, (iii) a conversion efficiency, ε (LUE), defines the efficiency with which APAR is converted to fixed carbon or plant biomass, and (iv) actual LUE may be reduced below its potential maximum value by limiting environmental factors such as temperature and water availability. Thus, LUE models can be generalized as:

$$GPP = LUE_{max} \times f(T_s, W_s, \ldots) \times FAPAR \times PAR \quad (1)$$

where LUE_{max} is the potential maximum LUE (g C m^{-2} MJ^{-1} APAR) without environment stresses, *f* are the scalars representing the effects of environmental stresses (e.g. low temperature and water scarcity) on the theoretical potential LUE, and FAPAR is the fraction of photosynthetically active radiation (PAR, MJ m^{-2}) absorbed by the photosynthetically active portion of the vegetation.

VPRM simulates NEE as the difference between the gross ecosystem exchange (GEE) and the ecosystem respiration (R or ER).

$$NEE = R - GEE \tag{2}$$

Following Mahadevan et al. (2008), GEE is modelled as

$$GEE = LUE \times FAPAR \times \frac{1}{(1 + PAR/PAR_0)} \times PAR \tag{3}$$

where PAR_0 is the half-saturation value. LUE is in μmol CO_2/ μmol PPFD, and PAR is in μmol m^{-2} s^{-1}. LUE is further decomposed into

$$LUE = \lambda \times T_{scale} \times P_{scale} \times W_{scale} \tag{4}$$

where λ is the maximum LUE (i.e. the maximum quantum yield), and T_{scale}, P_{scale}, and W_{scale} represent the effects of temperature, leaf phenology, and water stress, respectively, on LUE. They are dimensionless scaling factors that range between 0.0 and 1.0, and they vary in both time and space (Mahadevan et al., 2008).

The first scaling term T_{scale} describes the sensitivity of photosynthesis to temperature and is defined as:

$$T_{scale} = \frac{(T - T_{\min})(T - T_{\max})}{(T - T_{\min})(T - T_{\max}) - (T - T_{opt})^2} \tag{5}$$

where T is air temperature, and $T_{\min}$, $T_{\max}$, and T_{opt} are the minimum, maximum, and optimum temperatures (°C) for photosynthesis, respectively. Due to the strong relationship between temperature and PAR on a daily timescale, and to avoid instability in model parameter values caused by correlation between the parameters, T_{scale} is computed from literature values of $T_{\min}$, $T_{\max}$, and T_{opt} (Mahadevan et al., 2008).

The second scaling term P_{scale} quantifies the effects of leaf phenology on vegetation canopy photosynthesis. From bud burst to leaf full expansion, and during senescence, P_{scale} is computed as a linear function of LSWI by

$$P_{scale} = \frac{1 + LSWI}{2} \tag{6}$$

where LSWI is the satellite-derived land surface water index (Xiao et al., 2004). P_{scale} is set to 1 after leaf full expansion.

The third scaling term W_{scale} describes the regulation of LUE by canopy water content and is expressed as

$$W_{scale} = \frac{1 + LSWI}{1 + LSWI_{max}} \tag{7}$$

where $\mathrm{LSWI}_{\max}$ is the maximum LSWI in the growing season. The LSWI is calculated using the NIR (0.78–0.89 µm) and SWIR (1.58–1.75 µm) spectral bands (Xiao et al., 2002):

$$LSWI = \frac{\rho_{nir} - \rho_{swir}}{\rho_{nir} + \rho_{swir}} \tag{8}$$

The LSWI is also known as the Normalized Difference Water Index (Gao, 1996), and has been shown to be sensitive to vegetation water content (Tucker, 1980) because there is strong light absorption by liquid water in the SWIR waveband (Chandrasekar et al., 2010).

I use two different approaches to model estimates of photosynthesis by driving VPRM alternately with EVI and SIF. The first approach is based on the original VPRM (Mahadevan et al., 2008) that uses the satellite-derived EVI as a proxy for FAPAR. EVI was developed to include reflectance in the blue band to address some of the shortcomings of NDVI, including sensitivity to atmospheric contamination due to the scattering effects of aerosols, and soil background variations (Heute et al., 2002; Rahman et al., 2005; Walker et al., 2014). Previous studies have shown that EVI provides better estimates of FAPAR than NDVI, and the comparison of MODIS EVI and NDVI demonstrated that the seasonal dynamics of EVI were more strongly correlated with GPP. (Xiao et al., 2004; Schubert et., 2010).

Thus, the original VPRM GEE is given by

$$GEE = \lambda \times T_{scale} \times P_{scale} \times W_{scale} \times EVI \times \frac{1}{(1 + PAR/PAR_0)} \times PAR \tag{9}$$

In the second approach, I modified the original VPRM formulation and used satellite-derived SIF as a proxy for FAPAR. SIF is an electromagnetic signal emitted in the red and far-red spectral band by the chlorophyll-a molecules of plants. Chlorophyll fluorescence represents the re-emitted fraction of the absorbed PAR energy that was neither utilized for photochemistry nor dissipated thermally. Research studies have shown that SIF is a more direct proxy for primary production compared to VI's (Porcar-Castell et al., 2014; Yang et al., 2015), and is more responsive to changes in photosynthetic capacity caused by temperature and water stresses (Joiner et al., 2014; Rascher et al., 2015). The strong correlations between satellite-derived SIF and GPP at ecosystem to global scales have been well-documented (Frankenberg et al., 2011; Li et al., 2018b; Lu et al., 2018).

Therefore, the newly adjusted VPRM estimates the photosynthetic flux component as

$$GEE = \lambda \times T_{scale} \times W_{scale} \times \frac{SIF}{\cos(SZA)} \times \frac{1}{(1 + PAR/PAR_0)} \times PAR \qquad (10)$$

where SZA is the solar zenith angle.

Ecosystem respiration (R) is modelled as a simple linear function of observed air temperature (T):

$$R = \alpha \times T + \beta \qquad (11)$$

where α and β are the regression coefficients that describe the slope of the respiration response to air temperature and the basal rate of respiration at very cold temperatures, respectively.

4.2.3 Tower Flux Data

Eddy covariance tower observations from AmeriFlux (https://ameriflux.lbl.gov) were obtained for the CF site (Papakyriakou, 2020; Tenuta, 2020) and ARB site (Todd and Humphreys, 2018). The two sites are categorized as permanent wetlands under the International Geosphere-Biosphere Programme (IGBP) vegetation cover classification system (Loveland and Belward, 1997). It is noteworthy that the CF and ARB sites are two of the only three EC tower sites within the HBL with publicly available data on the AmeriFlux network database. Also, while a few other North American peatland sites—for example, Mer Bleue, Eastern Peatland; LaBiche, Western Peatland; and Atqasuk, Alaska—have been previously used to calibrate LUE models, this represents the first time sites within the HBL are employed to calibrate an LUE-based model.

4.2.4 Satellite Data

For this study, VPRM is driven by remote-sensing observations obtained from MODIS and OCO-2 satellite datasets. The required model input data retrieved from MODIS include EVI product MOD13Q1 at 16-day, 250m resolution (Didan, 2015); Surface Reflectance product MOD09A1 at 8-day, 500m resolution (Vermote, 2015); and Vegetation Dynamics product MCD12Q2 at annual, 500m resolution (Friedl et al., 2019). All products are from the MODIS Collection 6 dataset which implemented several improved processing algorithms from earlier versions (ORNL DAAC, 2018). Additionally, satellite-derived chlorophyll fluorescence was acquired from the global spatially contiguous SIF (CSIF) product at 4-day, 0.05° resolution (Zhang et al., 2018). The clear-sky instantaneous CSIF dataset has been shown to have high accuracy and small bias across ecosystem types.

4.2.5 Model Parameterization

VPRM parameter values were estimated using two different methods. The first method involves optimizing VPRM to EC tower observations from the CF and ARB study sites. All four user-estimated parameters (λ, PAR_0, α, and β) were computed empirically to quantify the relationship between observed tower CO_2 fluxes and climatic drivers by matching VPRM NEE estimates to the observed EC NEE. The optimum model parameter values were chosen to minimize the sum of squared errors (SSE) of the VPRM NEE residuals. The DEoptim package (Ardia et al., 2011; Mullen et al., 2011) for the R computing environment (R Core Team, 2020) which implements the Differential Evolution (DE) global optimization algorithm (Price et al., 2006) was employed to seek the best-fitting VPRM parameter values (Hilton et al., 2013).

VPRM was calibrated at the CF study site using two years (2007–2008) of EC tower observations for the study months (June–October). Model validation was carried out against another two years (2010–2011) of EC tower observations for the study months. The existence of large data gaps in 2009 caused by datalogging and power supply issues made this year unreliable and was therefore excluded from the CF dataset (Hanis et al., 2015). At the ARB study site, VPRM was calibrated and validated with EC tower observations for three years (2011–2013) and two years (2014–2015), respectively, during the study months (June–October). The half-hourly EC tower data for both study sites were filtered to remove measurements taken when the friction velocity, u* was below a threshold of 0.2 m s^{-1} (Baldocchi, 2003; Hanis et al. 2013). Only non-gap-filled tower observations were used in this study to avoid introducing another source of uncertainty to the VPRM parameter estimates (Barr et al., 2004; Lin et al., 2011). VPRM does not utilize flux or meteorological information from previous timesteps and only computes CO_2 fluxes at timesteps when the required driver data are available (Hilton et al., 2013). Thus, the NEE residuals (VPRM NEE – Observed NEE) for each 30-min period were analyzed only for complete cases, when both modelled and observed NEE were present.

In the second model parameterization method, I used the peatland PFT parameter set for VPRM provided by Hilton et al. (2013). The peatland PFT parameter estimates were determined by optimizing VPRM using four North American EC sites from the 2007 Fluxnet Synthesis dataset comprising: Mer Bleue, Eastern Peatland; LaBiche, Western Peatland; Atqasuk, Alaska; and Barrow, Alaska. Hilton et al's (2013) elegant R implementation of the VPRM (*VPRMLandSfcModel*) including tools to estimate parameter values were employed in my study.

4.3 Results

4.3.1 EVI-Based Model Calibration

VPRM was driven by EVI and model parameter values were calibrated using half-hourly EC NEE and meteorological (temperature and PAR) observations from the Churchill fen and Attawapiskat River bog sites. VPRM site-calibrated half-hourly estimates of NEE were then compared against EC tower observations. Additionally, the importance of model parameterization on the accuracy of simulated NEE estimates was assessed by comparing both the site-optimized and PFT-optimized NEE estimates against EC observations.

For the site-optimized VPRM, the half-hourly VPRM NEE residuals (model – observed) range from -2.13 to 2.15 μmol CO_2 m^{-2} s^{-1}, with a median of 0.01 μmol CO_2 m^{-2} s^{-1} at the Churchill fen during the 2007–2008 period. Using the peatland PFT parameter values, the CF half-hourly VPRM NEE residuals range between -2.61 and 2.00 μmol CO_2 m^{-2} s^{-1}, with a median of -0.28 μmol CO_2 m^{-2} s^{-1} during the same study period (Figure 4.2 and Table 4.1). The CF mean diurnal NEE estimates for the site-optimized VPRM show excellent agreement with the observed NEE (Slope = 1.05, R^2 = 0.92), and the PFT-optimized VPRM also performs reasonably well (Slope = 1.15, R^2 = 0.84) (Figure 4.3). The results show that the site-optimized VPRM better captured the mean diurnal NEE cycle compared to the PFT-optimized VPRM, particularly during the peak photosynthetically active period (Figure 4.4). Comparisons of the mean monthly (June–October) NEE estimates show that both models were able to reproduce the seasonal cycle, though the site-optimized VPRM performed better (Figure 4.5).

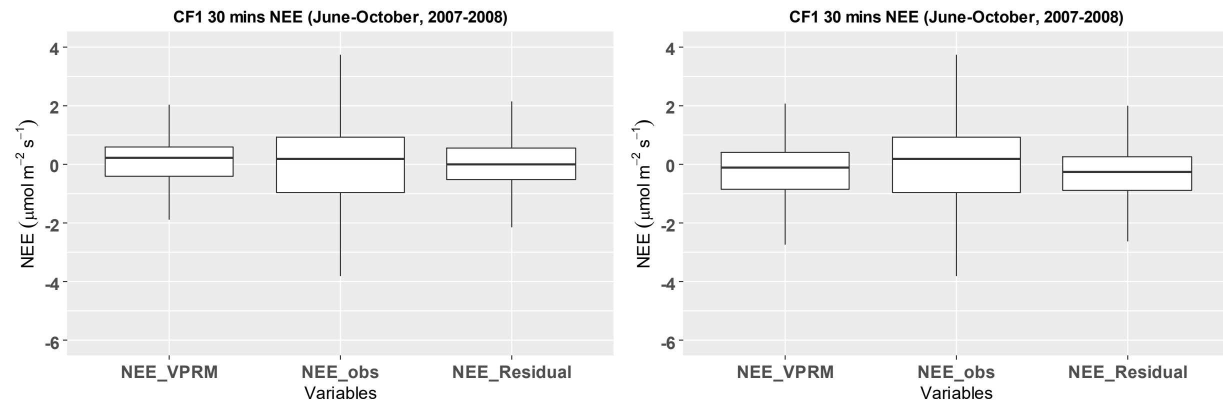

Figure 4. 2. Boxplot of mean half-hourly NEE at the Churchill fen during the 2007–2008 calibration period (CF1) for the site-optimized VPRM (left) and PFT-optimized VPRM (right). NEE_obs is the EC tower NEE observations. Residual is calculated as modelled NEE minus observed NEE.

Table 4. 1. Boxplot statistics for VPRM NEE against EC tower NEE observations at CF1 (2007 – 2008) using model parameter values from calibration site year (2007 – 2008) and Hilton et al. (2013) North American wetlands plant functional type (PFT).

(μmol CO_2 m^{-2} s^{-1})	ymin	lower	median	upper	ymax
Site-VPRM	-1.89	-0.41	0.20	0.58	2.03
PFT-VPRM	-2.73	-0.85	-0.11	0.39	2.06
EC Observations	-3.81	-0.98	0.17	0.92	3.72
Site-Residual	-2.13	-0.53	0.01	0.54	2.15
PFT-Residual	-2.61	-0.88	-0.28	0.28	2.00

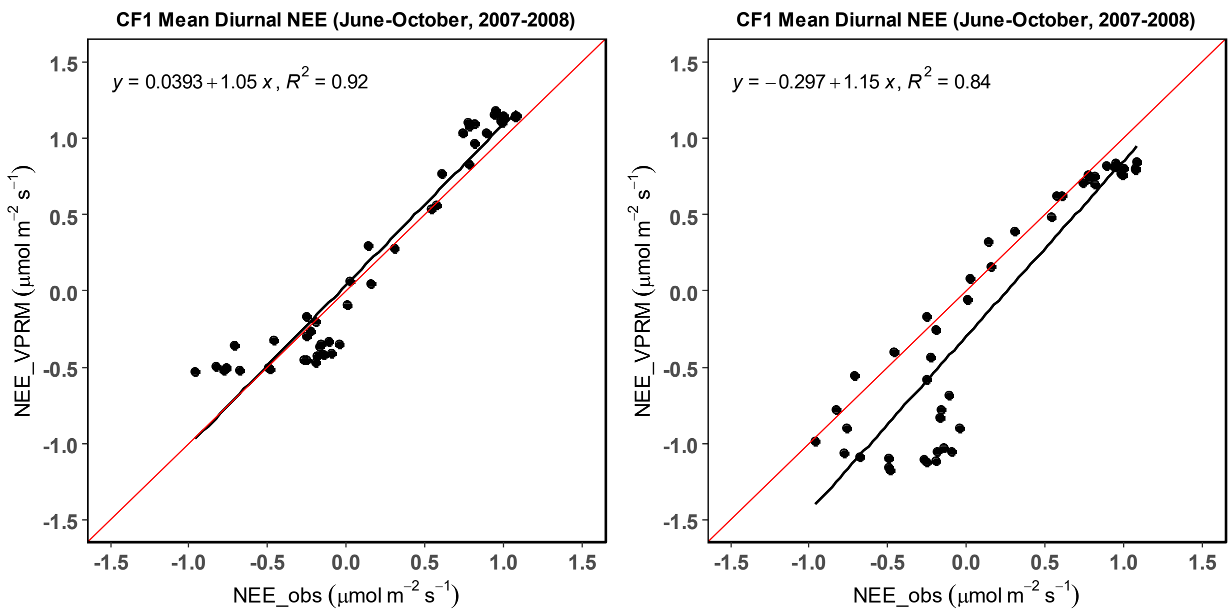

Figure 4. 3. Relationship between modelled and observed mean diurnal NEE at the Churchill fen during the 2007–2008 calibration period (CF1) for the site-optimized VPRM (left) and PFT-optimized VPRM (right). The red line is the "1:1 line".

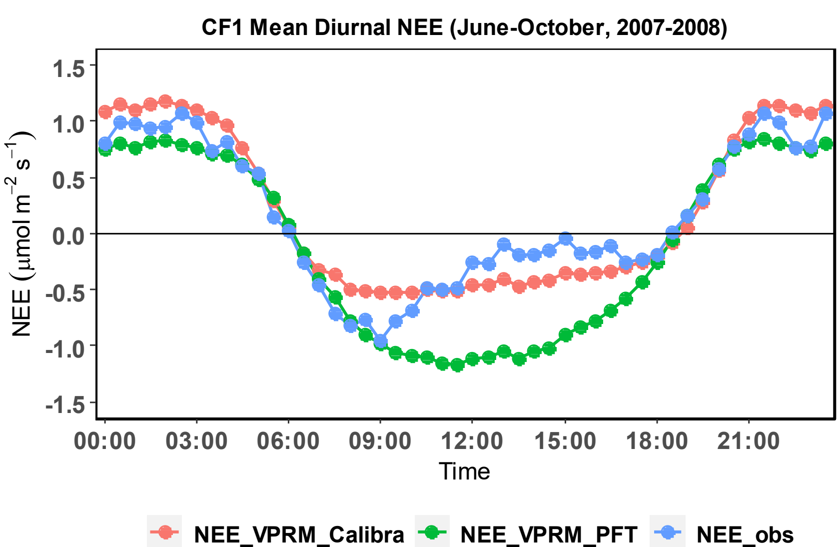

Figure 4. 4. A comparison between modelled and observed mean diurnal NEE cycle at the Churchill fen during the 2007–2008 calibration period (CF1). VPRM_Calibra is the site-optimized VPRM for the calibration period.

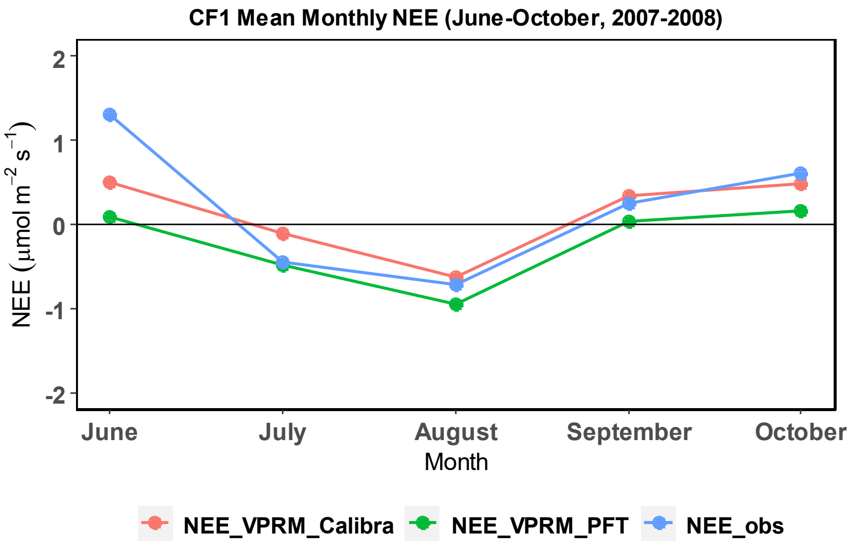

Figure 4. 5. A comparison between modelled and observed mean monthly NEE variation at the Churchill fen during the 2007–2008 calibration period (CF1). VPRM_Calibra is the site-optimized VPRM for the calibration period.

At the Attawapiskat River bog site, the half-hourly site-optimized VPRM NEE residuals range from -2.85 to 2.75 μmol CO_2 m^{-2} s^{-1}, with a median of -0.17 μmol CO_2 m^{-2} s^{-1} during the 2011–2013 period. For the PFT-optimized model at the same site, the half-hourly VPRM NEE residuals range between -2.76 and 2.69 μmol CO_2 m^{-2} s^{-1}, with a median of -0.15 μmol CO_2 m^{-2} s^{-1} during the same study period (Figure 4.6 and Table 4.2). Modelled mean diurnal estimates of NEE in Figure 4.7 show strong agreement with the observed NEE at ARB for both the site-optimized VPRM (Slope = 0.71, R^2 = 0.98) and the PFT-optimized VPRM (Slope = 0.76, R^2 = 0.99). The results demonstrate that the ARB diurnal cycles simulated by the site-optimized VPRM and PFT-optimized VPRM are remarkably similar, and have some noticeable discrepancies with the observed diurnal cycle, particularly around midday and nighttime (Figure 4.8). Comparisons of the mean monthly (June–October) NEE estimates show that while both VPRM models were able to reproduce the general seasonal cycle at the ARB site, there are large differences between the modelled NEE estimates and the NEE observations in July and September (Figure 4.9).

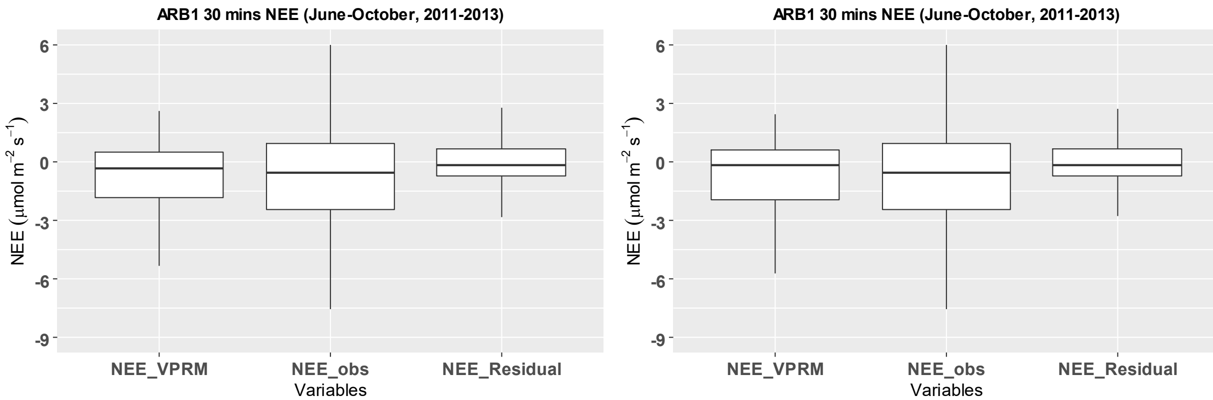

Figure 4. 6. Boxplot of mean half-hourly NEE at the Attawapiskat River bog during the 2011–2013 calibration period (ARB1) for the site-optimized VPRM (left) and PFT-optimized VPRM (right). NEE_obs is the EC tower NEE observations. Residual is calculated as modelled NEE minus observed NEE.

Table 4. 2. Boxplot statistics for VPRM NEE against EC tower NEE observations at ARB1 (2011 – 2013) using model parameter values from calibration site year (2011 – 2013) and Hilton et al. (2013) North American wetlands plant functional type (PFT).

(μmol CO_2 m^{-2} s^{-1})	ymin	lower	median	upper	ymax
Site-VPRM	-5.34	-1.83	-0.35	0.50	2.62
PFT-VPRM	-5.73	-1.93	-0.17	0.60	2.41
EC Observations	-7.55	-2.46	-0.55	0.93	5.99
Site-Residual	-2.85	-0.75	-0.17	0.65	2.75
PFT-Residual	-2.76	-0.72	-0.15	0.65	2.69

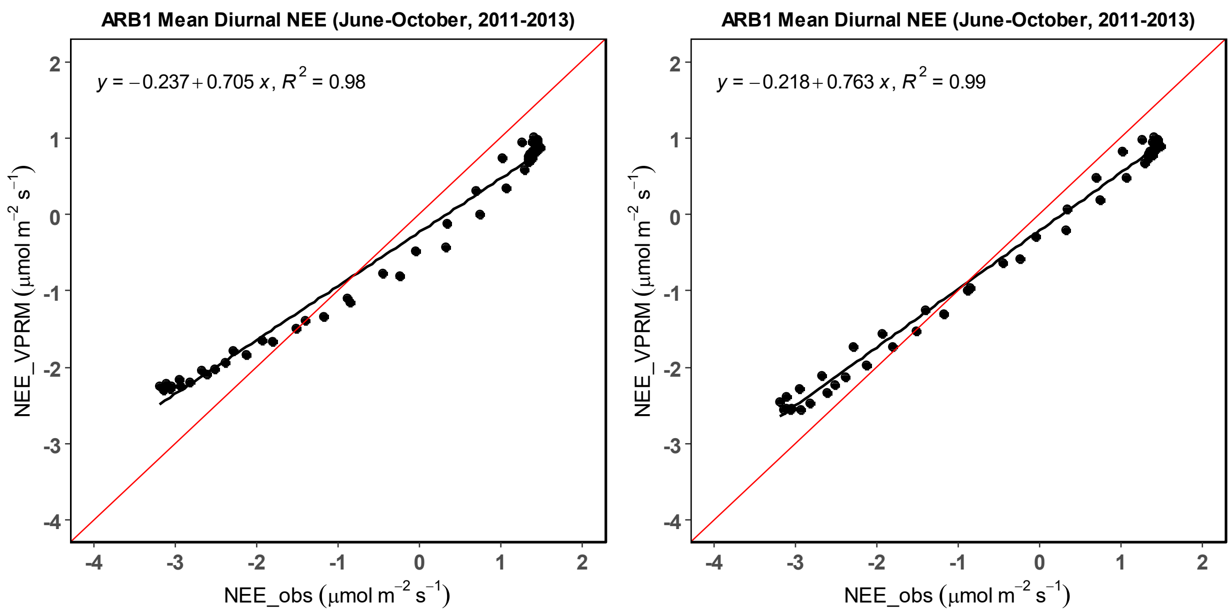

Figure 4. 7. Relationship between modelled and observed mean diurnal NEE at the Attawapiskat River bog during the 2011–2013 calibration period (ARB1) for the site-optimized VPRM (left) and PFT-optimized VPRM (right). The red line is the "1:1 line".

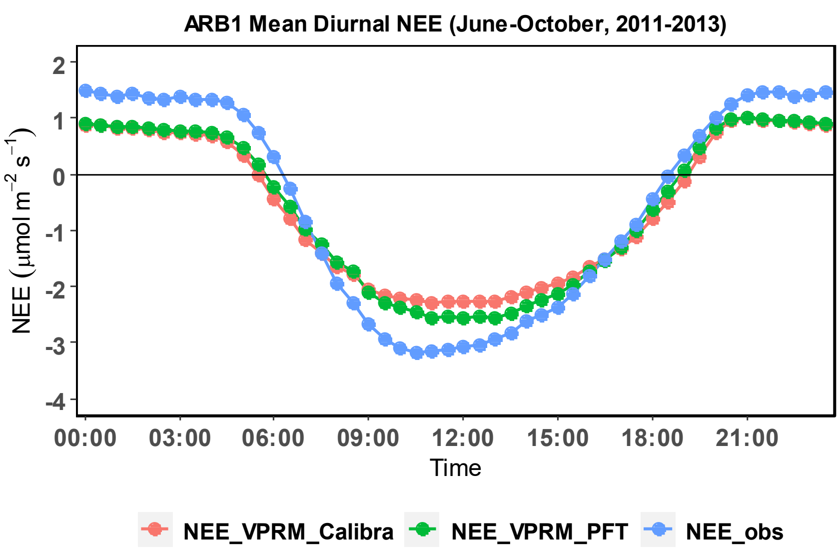

Figure 4. 8. A comparison between modelled and observed mean diurnal NEE cycle at the Attawapiskat River bog during the 2011–2013 calibration period (ARB1). VPRM_Calibra is the site-optimized VPRM for the calibration period.

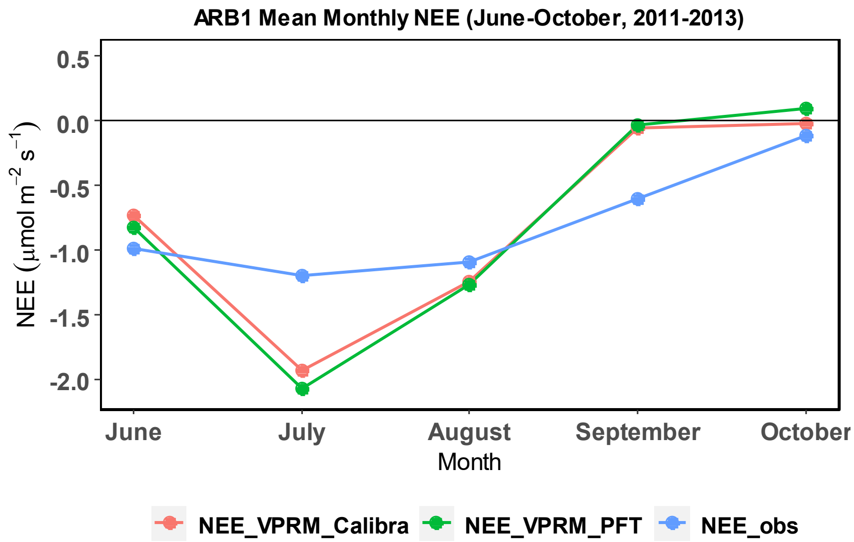

Figure 4. 9. A comparison between modelled and observed mean monthly NEE variation at the Attawapiskat River bog during the 2011–2013 calibration period (ARB1). VPRM_Calibra is the site-optimized VPRM for the calibration period.

An overall assessment of the two models indicates that the site-optimized VPRM estimates of CF mean diurnal NEE had a significantly smaller mean bias error (MBE = 0.05 μmol CO_2 m^{-2} s^{-1}) and root mean squared error (RMSE = 0.20 μmol CO_2 m^{-2} s^{-1}) compared to the PFT-optimized VPRM estimates (MBE = -0.27 μmol CO_2 m^{-2} s^{-1}, RMSE = 0.43 μmol CO_2 m^{-2} s^{-1}) (Table 4.3). Also, biases in the CF mean monthly NEE estimates were considerably lower for the site-optimized VPRM (MBE = -0.08 μmol CO_2 m^{-2} s^{-1}, RMSE = 0.40 μmol CO_2 m^{-2} s^{-1}) compared to the PFT-optimized VPRM (MBE = -0.43 μmol CO_2 m^{-2} s^{-1}, RMSE = 0.59 μmol CO_2 m^{-2} s^{-1}). Conversely, biases in NEE estimates at the ARB site were similar for both models (Table 4.3). The MBE and RMSE for the site-optimized VPRM mean diurnal NEE estimates at ARB was -0.09 μmol CO_2 m^{-2} s^{-1} and 0.57 μmol CO_2 m^{-2} s^{-1}, respectively, while the PFT-optimized VPRM had an MBE of -0.10 μmol CO_2 m^{-2} s^{-1} and an RMSE of 0.46 μmol CO_2 m^{-2} s^{-1}. The biases in the ARB mean monthly NEE estimates by the two models were also very similar.

Table 4. 3. Error statistics (MBE and RMSE in μmol CO_2 m^{-2} s^{-1}) calculated through the comparison of diurnally, daily and monthly averaged estimates of VPRM NEE against eddy covariance NEE observations at CF1 (2007 – 2008) and ARB1 (2011 – 2013).

CF1	MBE	RMSE
Diurnal		
Site-VPRM	0.05	0.20
PFT-VPRM	-0.27	0.43
Daily		
Site-VPRM	-0.07	0.62
PFT-VPRM	-0.41	0.77
Monthly		
Site-VPRM	-0.08	0.40
PFT-VPRM	-0.43	0.59
ARB1		
Diurnal		
Site-VPRM	-0.09	0.57
PFT-VPRM	-0.10	0.46
Daily		
Site-VPRM	-0.01	0.55
PFT-VPRM	-0.03	0.61
Monthly		
Site-VPRM	0.00	0.43
PFT-VPRM	-0.02	0.49

4.3.2 EVI-Based Model Validation

To evaluate the capability of VPRM-EVI to simulate NEE estimates at the Churchill fen and Attawapiskat River bog sites, modelled half-hourly estimates of NEE were validated against EC observations in years that were not used for model parameter estimation. At the CF site, validation involved comparing VPRM NEE estimates against EC observations during the 2010–2011 period (recall that the model was initially calibrated with EC data from 2007–2008). At the ARB site, validation was carried out by comparing VPRM NEE estimates against EC observations during the 2014–2015 period (recall that the model was initially calibrated with EC data from 2011–2013). Furthermore, both the site-optimized and PFT-optimized NEE estimates were evaluated during the validation years to determine which model parameterization method provided more reliable estimates of NEE at the study sites.

For the site-optimized VPRM, the CF half-hourly VPRM NEE residuals range from -2.46 to 3.56 μmol CO_2 m^{-2} s^{-1}, with a median of 0.41 μmol CO_2 m^{-2} s^{-1} during the validation years (2010–2011). Using the PFT-optimized VPRM, the CF half-hourly VPRM NEE residuals range between -2.87 and 3.26 μmol CO_2 m^{-2} s^{-1}, with a median of 0.09 μmol CO_2 m^{-2} s^{-1} during the same study period (Figure 4.10 and Table 4.4). Modelled mean diurnal NEE estimates show strong agreement with observed NEE at the CF site during the validation years (Figure 4.11). The site-optimized VPRM and PFT-optimized VPRM were able to explain 94% and 88%, respectively, of the diurnal variability in observed NEE. The results reveal that the PFT-optimized VPRM mean diurnal NEE estimates closely matched EC observations, while site-optimized VPRM NEE estimates were systematically lower (smaller carbon sink) than observed values (Figure 4.12). Comparisons of the mean monthly (June–October) NEE estimates for the validation period show that, although the two models were able to produce a seasonal cycle that was broadly consistent with EC observations at CF, the modelled mean monthly NEE estimates were smaller in magnitude, particularly for the site-optimized VPRM (Figure 4.13).

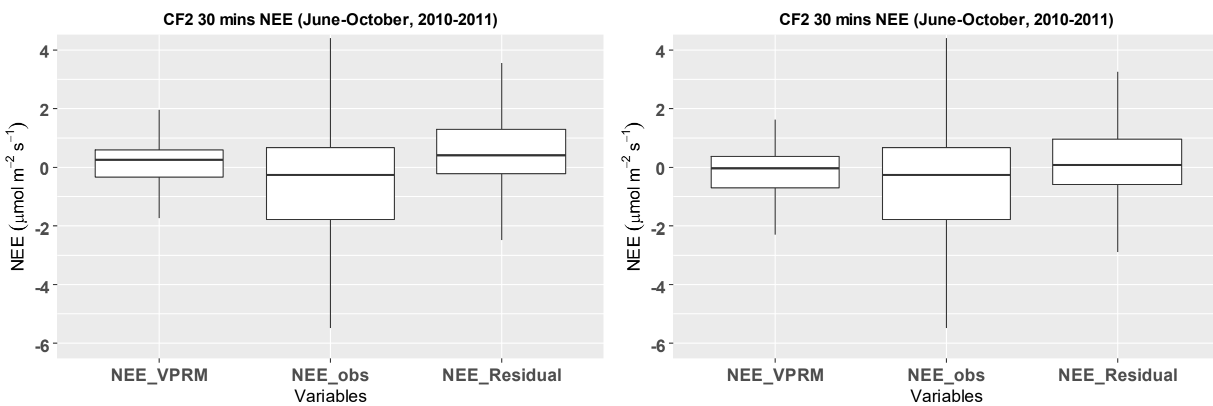

Figure 4. 10. Boxplot of mean half-hourly NEE at the Churchill fen during the 2010–2011 validation period (CF2) for the site-optimized VPRM (left) and PFT-optimized VPRM (right). NEE_obs is the EC tower NEE observations. Residual is calculated as modelled NEE minus observed NEE.

Table 4. 4. Boxplot statistics for VPRM NEE against EC tower NEE observations at CF2 (2010 – 2011) using model parameter values from calibration site year (2007 – 2008) and Hilton et al. (2013) North American wetlands plant functional type (PFT).

(μmol CO_2 m^{-2} s^{-1})	ymin	lower	median	upper	ymax
Site-VPRM	-1.75	-0.34	0.26	0.60	1.95
PFT-VPRM	-2.28	-0.70	-0.06	0.37	1.63
EC Observations	-5.47	-1.79	-0.26	0.68	4.38
Site-Residual	-2.46	-0.21	0.41	1.30	3.56
PFT-Residual	-2.87	-0.57	0.09	0.96	3.26

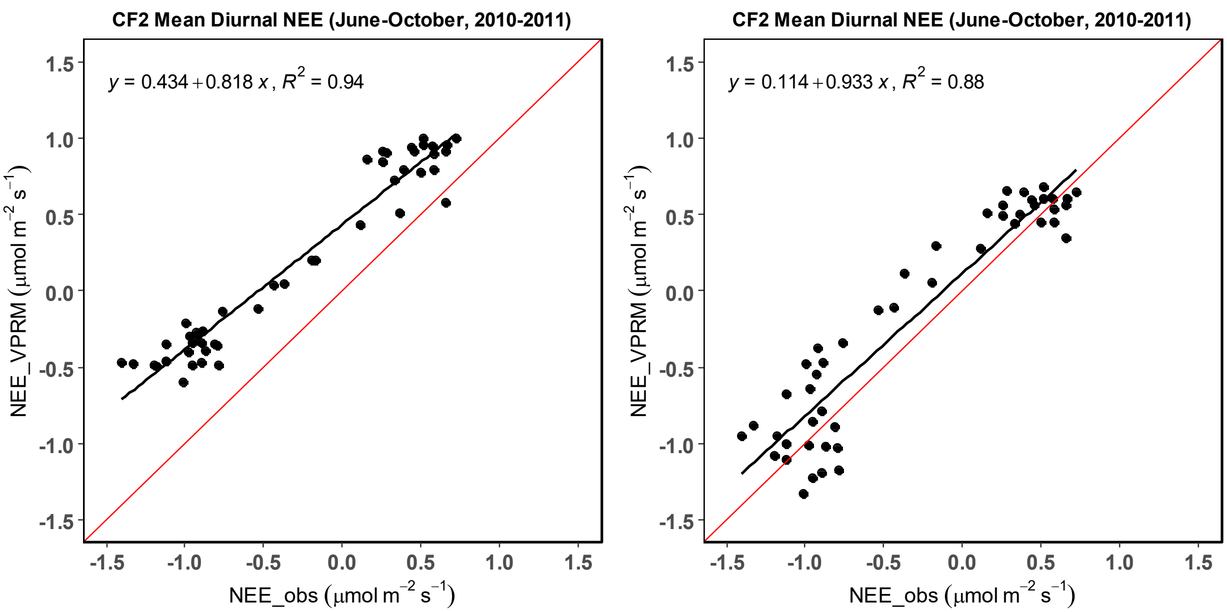

Figure 4. 11. Relationship between modelled and observed mean diurnal NEE at the Churchill fen during the 2010–2011 validation period (CF2) for the site-optimized VPRM (left) and PFT-optimized VPRM (right). The red line is the "1:1 line".

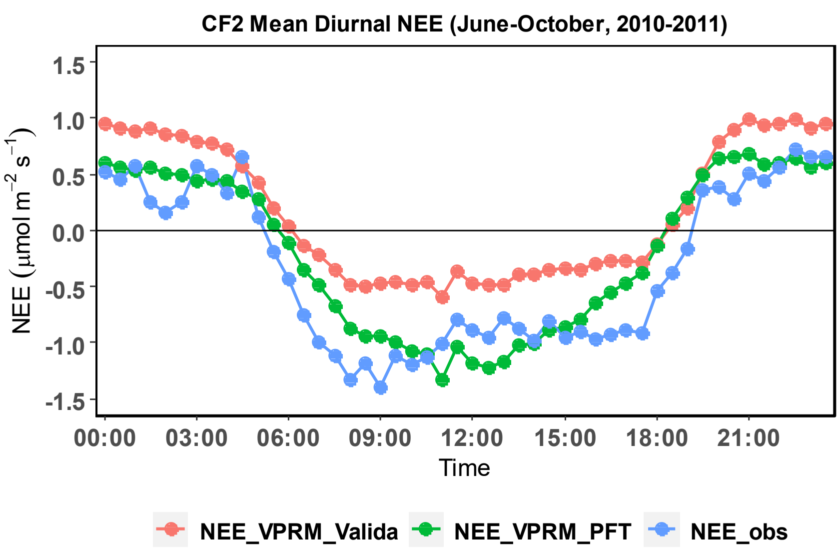

Figure 4. 12. A comparison between modelled and observed mean diurnal NEE cycle at the Churchill fen during the 2010–2011 validation period (CF2). VPRM_Valida is the site-optimized VPRM for the validation period.

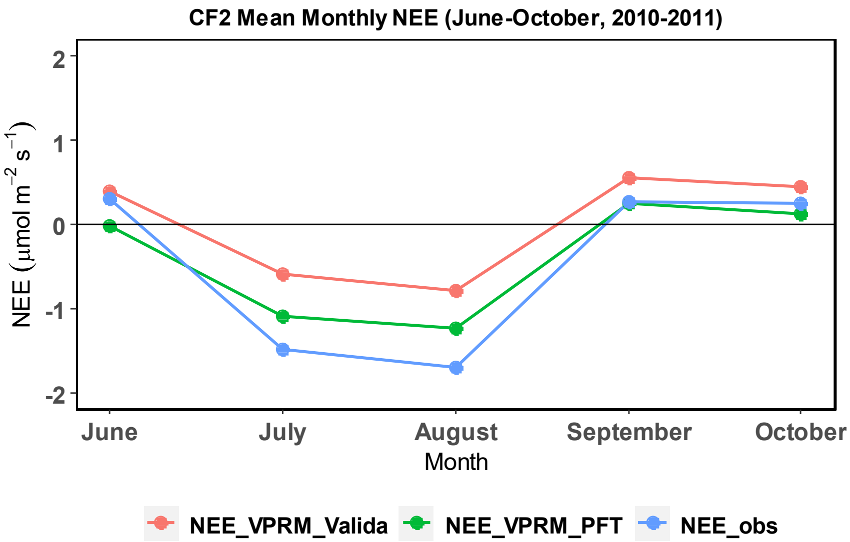

Figure 4. 13. A comparison between modelled and observed mean monthly NEE variation at the Churchill fen during the 2010–2011 validation period (CF2). VPRM_Valida is the site-optimized VPRM for the validation period.

At the Attawapiskat River bog site, the half-hourly site-optimized VPRM NEE residuals range from -2.74 to 2.61 μmol CO_2 m^{-2} s^{-1}, with a median of -0.18 μmol CO_2 m^{-2} s^{-1} during the validation years (2014–2015). For the PFT-optimized VPRM, the ARB half-hourly VPRM NEE residuals range between -2.77 and 2.66 μmol CO_2 m^{-2} s^{-1}, with a median of -0.18 μmol CO_2 m^{-2} s^{-1} during the same validation period (Figure 4.14 and Table 4.5). VPRM mean diurnal NEE estimates display excellent agreement with ARB tower observations, with both the site-optimized VPRM and PFT-optimized VPRM explaining 99% of the diurnal variability in observed EC NEE during the validation years (Figure 4.15). The results indicate that the modelled ARB diurnal cycles by the site-optimized VPRM and PFT-optimized VPRM are strikingly similar, and both models sufficiently reproduced the observed diurnal cycle, including the timing of the peak photosynthetically active period (Figure 4.16). Furthermore, both models captured the seasonal variability in ARB observed NEE with remarkable fidelity as shown in Figure 4.17.

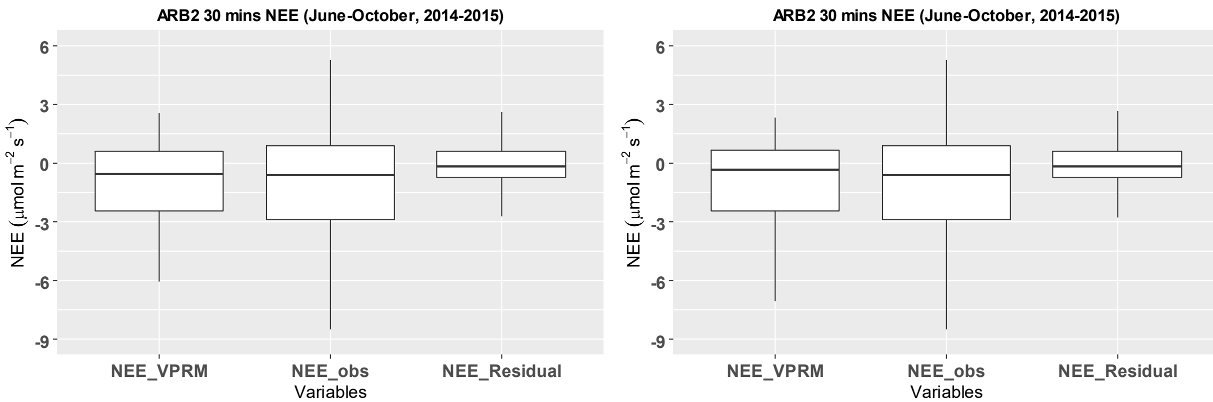

Figure 4. 14. Boxplot of mean half-hourly NEE at the Attawapiskat River bog during the 2014–2015 validation period (ARB2) for the site-optimized VPRM (left) and PFT-optimized VPRM (right). NEE_obs is the EC tower NEE observations. Residual is calculated as modelled NEE minus observed NEE.

Table 4. 5. Boxplot statistics for VPRM NEE against EC tower NEE observations at ARB2 (2014 – 2015) using model parameter values from calibration site year (2011 – 2013) and Hilton et al. (2013) North American wetlands plant functional type (PFT).

(µmol CO_2 m^{-2} s^{-1})	ymin	lower	median	upper	ymax
Site-VPRM	-6.02	-2.46	-0.58	0.59	2.56
PFT-VPRM	-7.05	-2.44	-0.35	0.68	2.35
EC Observations	-8.51	-2.89	-0.63	0.89	5.23
Site-Residual	-2.74	-0.74	-0.18	0.60	2.61
PFT-Residual	-2.77	-0.74	-0.18	0.62	2.66

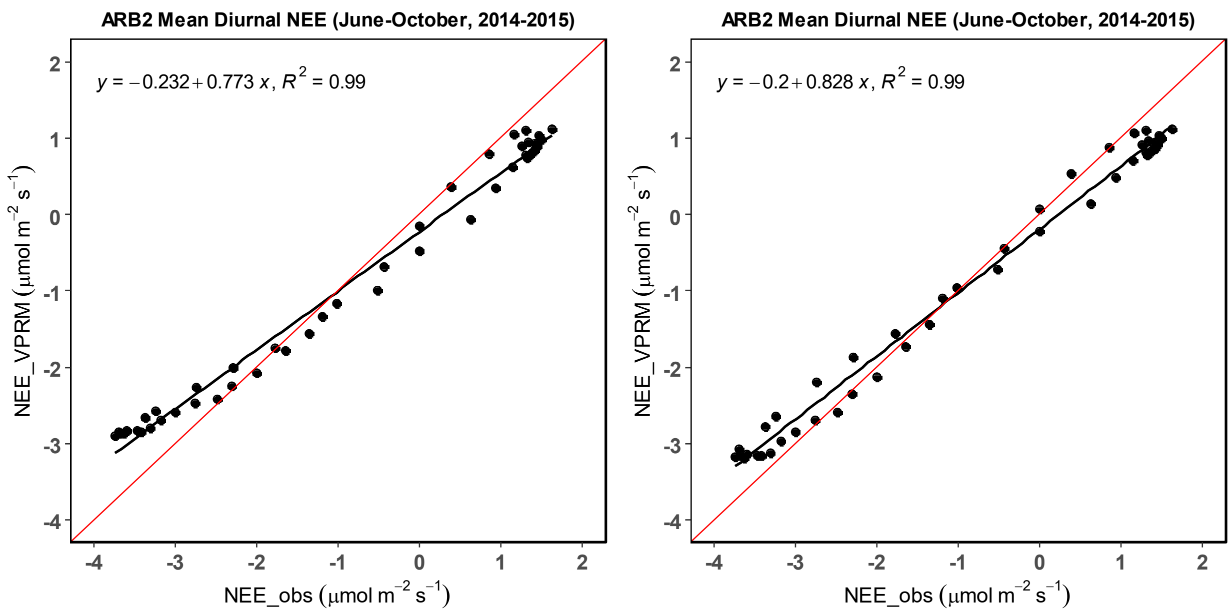

Figure 4. 15. Relationship between modelled and observed mean diurnal NEE at the Attawapiskat River bog during the 2014–2015 validation period (ARB2) for the site-optimized VPRM (left) and PFT-optimized VPRM (right). The red line is the "1:1 line".

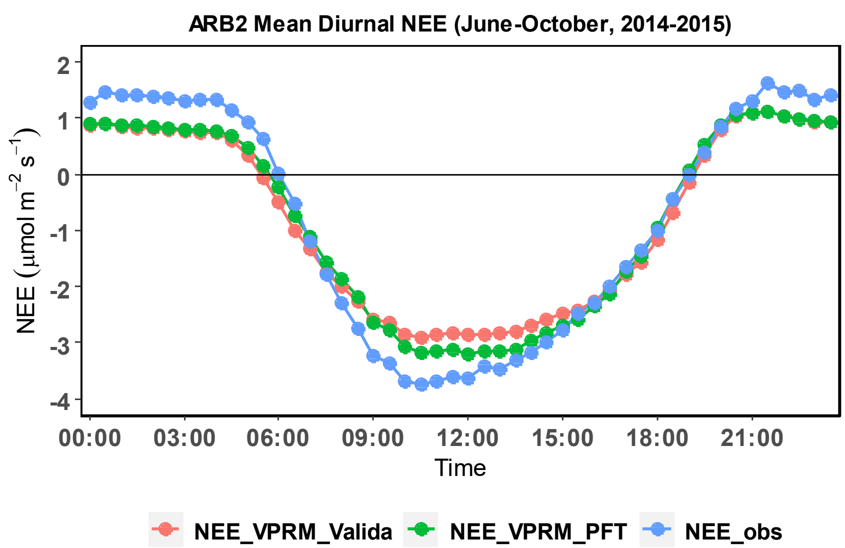

Figure 4. 16. A comparison between modelled and observed mean diurnal NEE cycle at the Attawapiskat River bog during the 2014–2015 validation period (ARB2). VPRM_Valida is the site-optimized VPRM for the validation period.

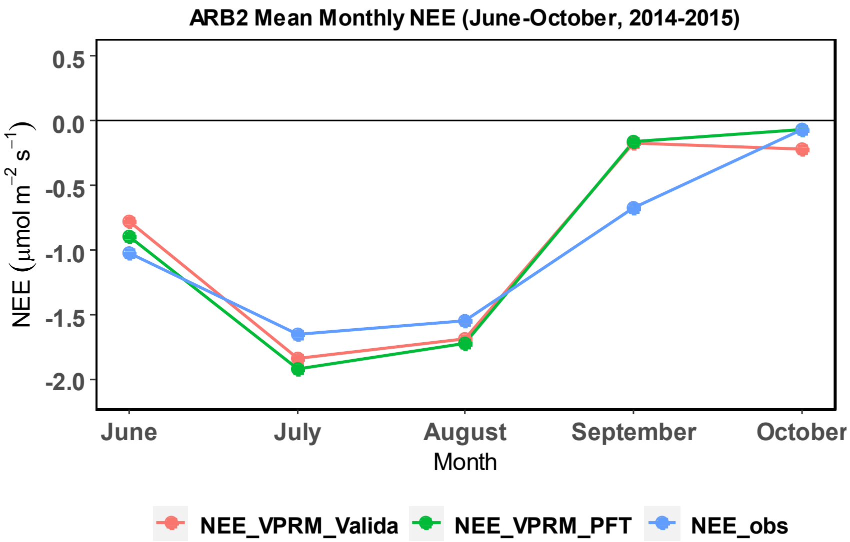

Figure 4. 17. A comparison between modelled and observed mean monthly NEE variation at the Attawapiskat River bog during the 2014–2015 validation period (ARB2). VPRM_Valida is the site-optimized VPRM for the validation period.

Model evaluation suggests that, overall, biases in PFT-optimized VPRM estimates of mean diurnal NEE were substantially smaller (MBE = 0.14 μmol CO_2 m^{-2} s^{-1}, RMSE = 0.28 μmol CO_2 m^{-2} s^{-1}) than site-optimized VPRM estimates (MBE = 0.49 μmol CO_2 m^{-2} s^{-1}, RMSE = 0.53 μmol CO_2 m^{-2} s^{-1}) at the CF site (Table 4.6). Biases in the CF mean monthly NEE estimates during the validation period (2010–2011) were also distinctly lower for the PFT-optimized VPRM (MBE = 0.08 μmol CO_2 m^{-2} s^{-1}, RMSE = 0.32 μmol CO_2 m^{-2} s^{-1}) compared to site-optimized VPRM (MBE = 0.48 μmol CO_2 m^{-2} s^{-1}, RMSE = 0.60 μmol CO_2 m^{-2} s^{-1}). Interestingly, biases in NEE estimates at the ARB site were quite similar for both models during the validation period (2014–2015). The MBE and RMSE for the site-optimized VPRM mean diurnal NEE estimates at ARB were -0.05 μmol CO_2 m^{-2} s^{-1} and 0.50 μmol CO_2 m^{-2} s^{-1}, respectively, while the PFT-optimized VPRM had an MBE of -0.07 μmol CO_2 m^{-2} s^{-1} and an RMSE of 0.39 μmol CO_2 m^{-2} s^{-1} (Table 4.6). Also, the mean monthly NEE estimates by the two models showed almost identical biases at the ARB site during the validation period.

Table 4. 6. Error statistics (MBE and RMSE in µmol CO_2 m^{-2} s^{-1}) calculated through the comparison of diurnally, daily and monthly averaged estimates of VPRM NEE against eddy covariance NEE observations at CF2 (2010 – 2011) and ARB2 (2014 – 2015).

CF2	MBE	RMSE
Diurnal		
Site-VPRM	0.49	0.53
PFT-VPRM	0.14	0.28
Daily		
Site-VPRM	0.46	1.07
PFT-VPRM	0.08	0.98
Monthly		
Site-VPRM	0.48	0.60
PFT-VPRM	0.08	0.32
ARB2		
Diurnal		
Site-VPRM	-0.05	0.50
PFT-VPRM	-0.07	0.39
Daily		
Site-VPRM	0.06	0.54
PFT-VPRM	0.05	0.59
Monthly		
Site-VPRM	0.05	0.28
PFT-VPRM	0.04	0.27

4.3.3 SIF-Based vs EVI-Based Model Calibration

VPRM was driven alternately with EVI and SIF to determine which model is better able to capture the diurnal, seasonal and inter-annual variations in peatland photosynthesis. VPRM-EVI and VPRM-SIF CO_2 fluxes were both constrained with half-hourly EC tower observations from CF and ARB for the calibration periods 2007–2008 and 2011–2013, respectively. The mean diurnal NEE estimates for both models show excellent agreement with EC tower fluxes, explaining approximately 92% and 98% of the diurnal variability in NEE observations at CF and ARB, respectively (Figure 4.18 and Figure 4.19). The seasonal NEE cycle was correctly reproduced, and both models captured peak photosynthesis in August at CF and in July at ARB (Figure 4.20 and Figure 4.21). At ARB, VPRM-SIF estimates of the mean monthly (June–October) NEE were more closely linked to observations compared to VPRM-EVI, particularly in July and September. The RMSE for the mean diurnal NEE estimates was 0.20 μmol CO_2 m^{-2} s^{-1} at CF and 0.57 μmol CO_2 m^{-2} s^{-1} at ARB for VPRM-EVI, and 0.32 μmol CO_2 m^{-2} s^{-1} at CF and 0.36 μmol CO_2 m^{-2} s^{-1} at ARB for VPRM-SIF (Table 4.7). For the mean monthly NEE estimates, VPRM-EVI had an RMSE of 0.40 μmol CO_2 m^{-2} s^{-1} and 0.43 μmol CO_2 m^{-2} s^{-1} at CF and ARB, respectively, while VPRM-SIF obtained an RMSE of 0.35 μmol CO_2 m^{-2} s^{-1} and 0.21 μmol CO_2 m^{-2} s^{-1} at CF and ARB, respectively. Overall, the results show that VPRM-SIF performed better than VPRM-EVI in simulating diurnal and monthly estimates of NEE at the study sites during the calibration period.

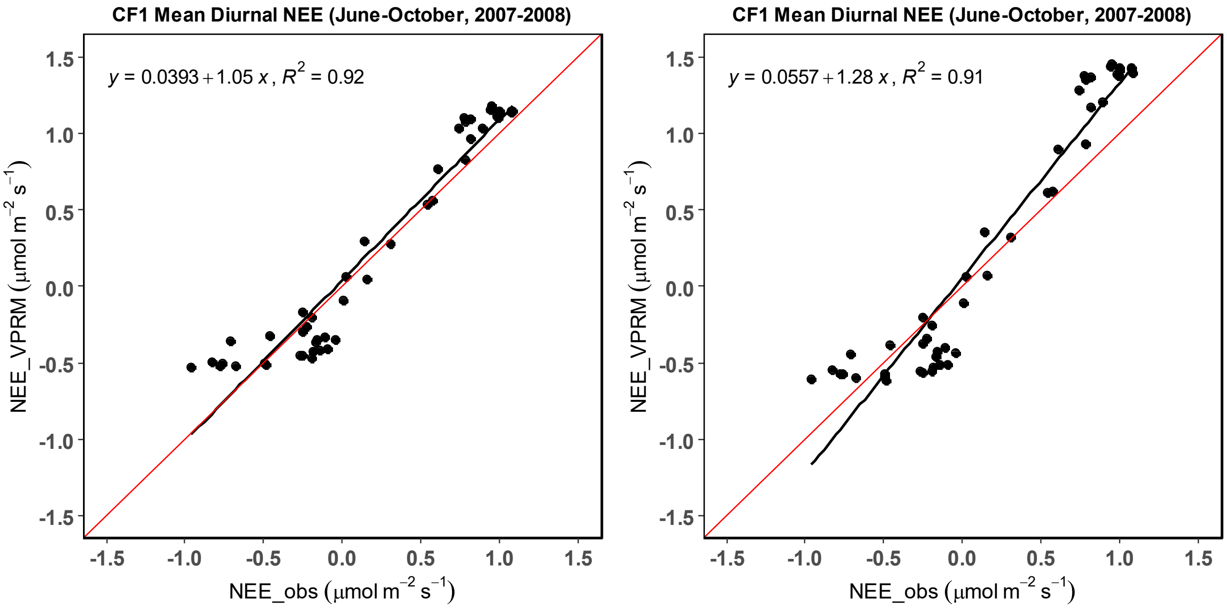

Figure 4. 18. Relationship between modelled and observed mean diurnal NEE at the Churchill fen during the 2007–2008 calibration period (CF1) for the VPRM-EVI (left) and VPRM-SIF (right). The red line is the "1:1 line".

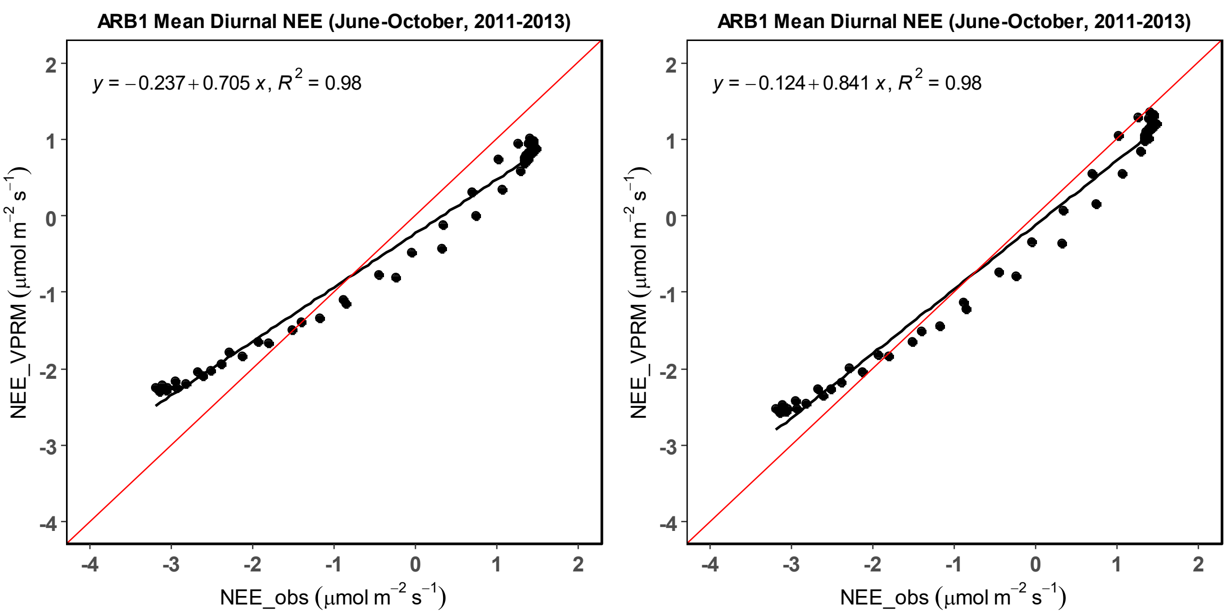

Figure 4. 19. Relationship between modelled and observed mean diurnal NEE at the Attawapiskat River bog during the 2011–2013 calibration period (ARB1) for the VPRM-EVI (left) and VPRM-SIF (right). The red line is the "1:1 line".

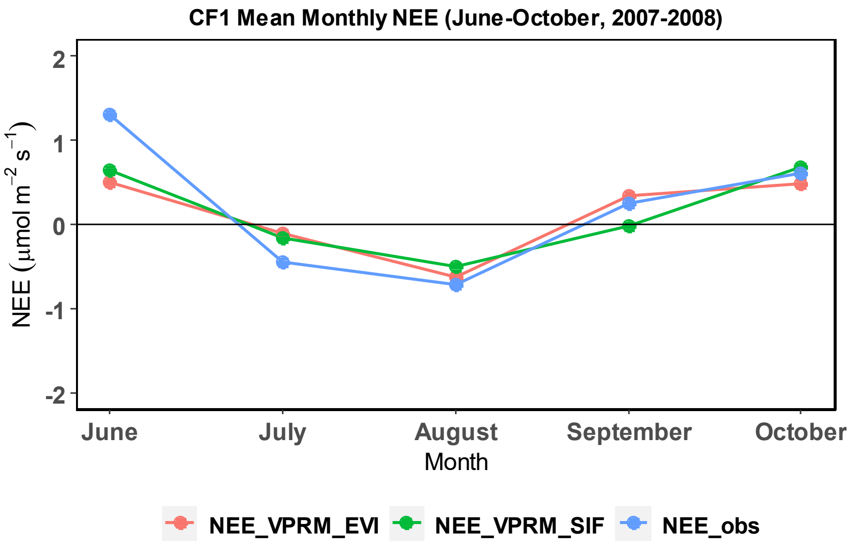

Figure 4. 20. A comparison between VPRM-EVI, VPRM-SIF, and EC observed mean monthly NEE variation at the Churchill fen during the 2007–2008 calibration period (CF1).

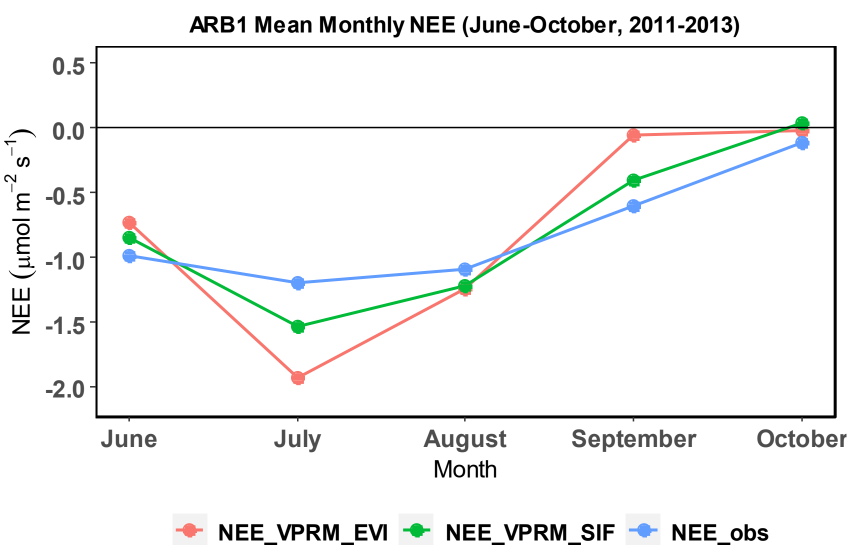

Figure 4. 21. A comparison between VPRM-EVI, VPRM-SIF, and EC observed mean monthly NEE variation at the Attawapiskat River bog during the 2011–2013 calibration period (ARB1).

Table 4. 7. Error statistics (MBE and RMSE in μmol CO_2 m^{-2} s^{-1}) calculated through the comparison of diurnally, daily and monthly averaged estimates of VPRM-EVI and VPRM-SIF NEE against eddy covariance NEE observations at CF1 (2007 – 2008) and ARB1 (2011 – 2013).

CF1	MBE	RMSE
Diurnal		
VPRM-EVI	0.05	0.20
VPRM-SIF	0.10	0.32
Daily		
VPRM-EVI	-0.07	0.62
VPRM-SIF	-0.05	0.54
Monthly		
VPRM-EVI	-0.08	0.40
VPRM-SIF	-0.07	0.35
ARB1		
Diurnal		
VPRM-EVI	-0.09	0.57
VPRM-SIF	-0.04	0.36
Daily		
VPRM-EVI	-0.01	0.55
VPRM-SIF	-0.01	0.33
Monthly		
VPRM-EVI	0.00	0.43
VPRM-SIF	0.00	0.21

4.3.4 SIF-Based vs EVI-Based Model Validation

Modelled estimates of NEE were evaluated against tower observations during the 2010–2011 validation period at CF and the 2014–2015 validation period at ARB. VPRM-EVI and VPRM-SIF mean diurnal estimates of NEE display identical and strong correlations with observed NEE at CF ($R^2 = 0.94$) and ARB ($R^2 \sim 0.99$) study sites (Figure 4.22 and Figure 4.23). Both models performed better at estimating the mean monthly NEE at ARB compared to CF, especially during the peak growing season (Figure 4.24 and Figure 4.25). Further analyses of the results reveal that VPRM-SIF estimates of NEE had smaller RMSE at both the CF and ARB sites, and at all timescales during the validation period (Table 4.8). For example, the RMSE for the mean diurnal NEE estimates was 0.51 μmol CO_2 m^{-2} s^{-1} for VPRM-SIF and 0.53 μmol CO_2 m^{-2} s^{-1} for VPRM-EVI at the CF site, and 0.36 μmol CO_2 m^{-2} s^{-1} for VPRM-SIF and 0.50 μmol CO_2 m^{-2} s^{-1} for VPRM-EVI at the ARB site.

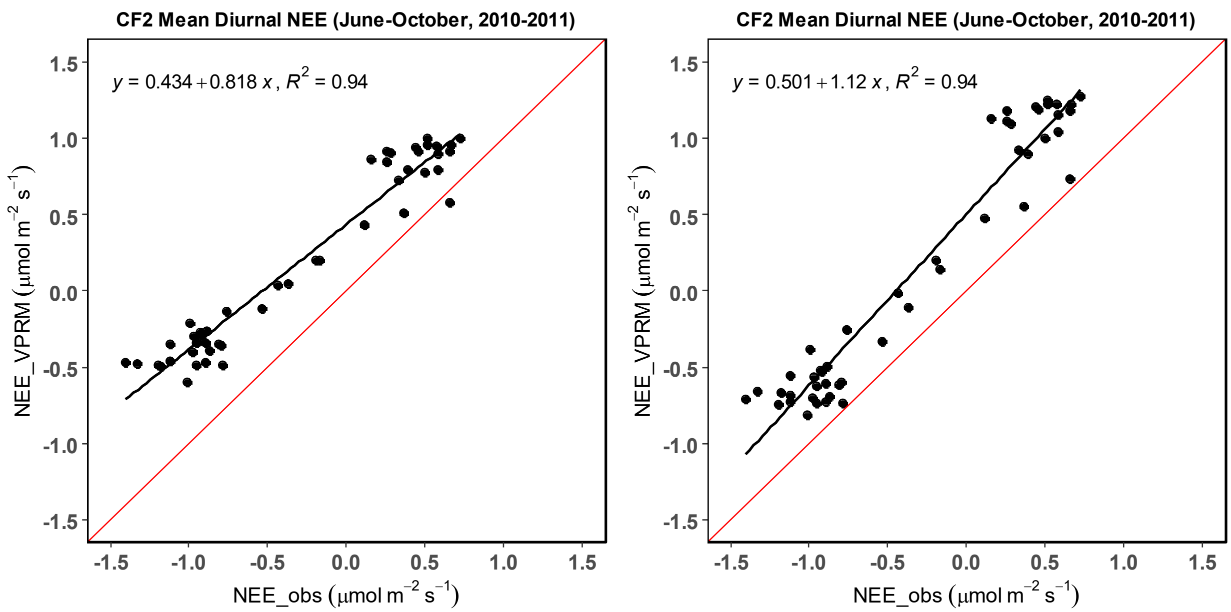

Figure 4. 22. Relationship between modelled and observed mean diurnal NEE at the Churchill fen during the 2010–2011 validation period (CF2) for the VPRM-EVI (left) and VPRM-SIF (right). The red line is the "1:1 line".

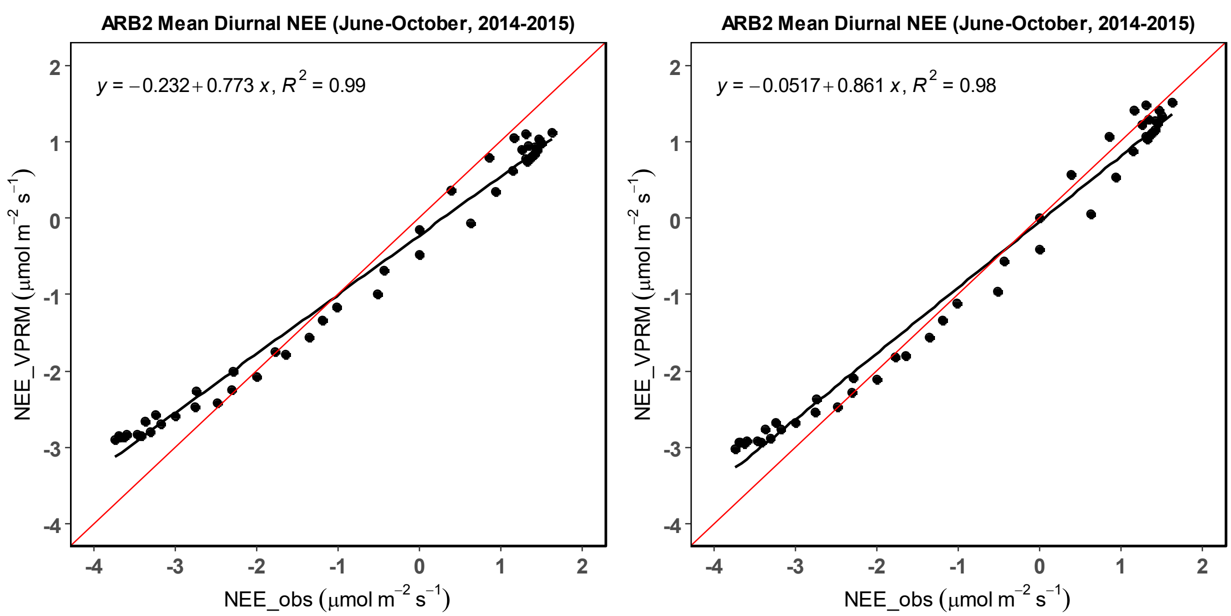

Figure 4. 23. Relationship between modelled and observed mean diurnal NEE at the Attawapiskat River bog during the 2014–2015 validation period (ARB2) for the VPRM-EVI (left) and VPRM-SIF (right). The red line is the "1:1 line".

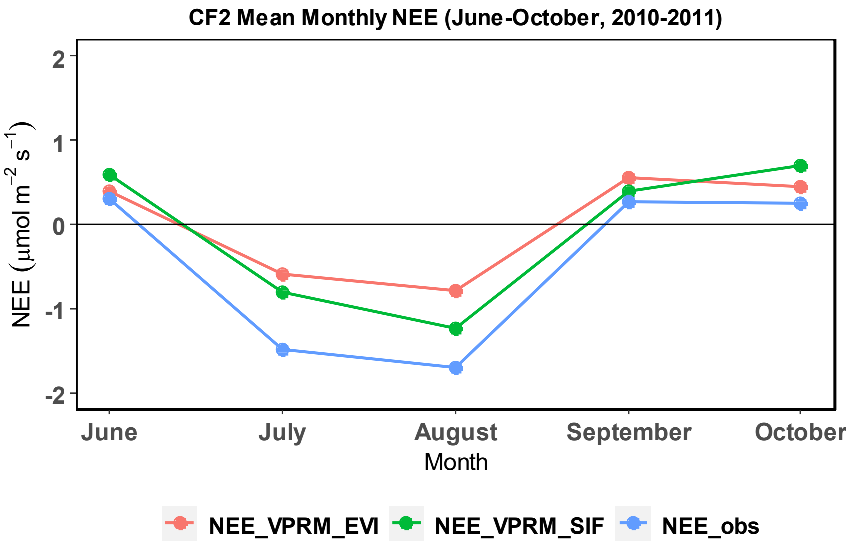

Figure 4. 24. A comparison between VPRM-EVI, VPRM-SIF, and EC observed mean monthly NEE variation at the Churchill fen during the 2010–2011 validation period (CF2).

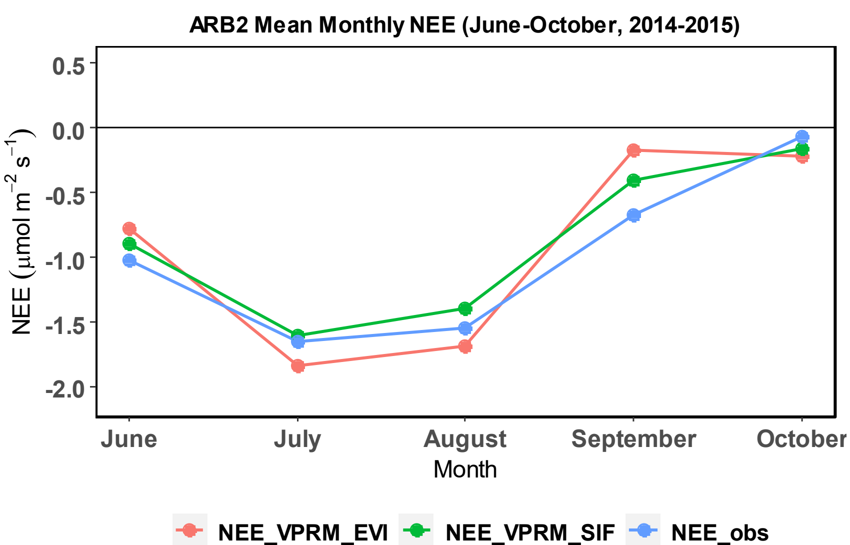

Figure 4. 25. A comparison between VPRM-EVI, VPRM-SIF, and EC observed mean monthly NEE variation at the Attawapiskat River bog during the 2014–2015 validation period (ARB2).

Table 4. 8. Error statistics (MBE and RMSE in µmol CO_2 m^{-2} s^{-1}) calculated through the comparison of diurnally, daily and monthly averaged estimates of VPRM-EVI and VPRM-SIF NEE against eddy covariance NEE observations at CF2 (2010 – 2011) and ARB2 (2014 – 2015).

CF2	MBE	RMSE
Diurnal		
VPRM-EVI	0.49	0.53
VPRM-SIF	0.46	0.51
Daily		
VPRM-EVI	0.46	1.07
VPRM-SIF	0.35	0.96
Monthly		
VPRM-EVI	0.48	0.60
VPRM-SIF	0.40	0.44
ARB2		
Diurnal		
VPRM-EVI	-0.05	0.50
VPRM-SIF	0.06	0.36
Daily		
VPRM-EVI	0.06	0.54
VPRM-SIF	0.10	0.46
Monthly		
VPRM-EVI	0.05	0.28
VPRM-SIF	0.10	0.16

4.4 Discussion

4.4.1 Does Site-Specific Parameter Optimization Improve NEE Estimates?

LUE-based models such as VPRM have been widely applied to various terrestrial ecosystems such as cropland and forests, but less attention has been given to northern peatlands (Lees et al., 2018). Most studies estimate carbon fluxes at a regional or continental scale using model parameter values calibrated at a few available EC tower sites. This is accomplished by grouping different ecosystems within the study region under vegetation classes or PFTs (e.g. Mahadevan et al., 2008; Hilton et al., 2014; Luus and Lin, 2015). Some research studies had to rely on literature-derived LUE parameter, ε, and other model parameter values to estimate site-specific carbon fluxes (Lees et al., 2018). However, it has been argued that one of the primary challenges of LUE models is that they require a well-constrained LUE parameter (ε) to provide reliable estimates of CO_2 exchange, particularly in peatland ecosystems (Kross et al., 2016). The photosynthetic LUE varies not only across biomes but also within the same PFT (Ruimy et al., 1994; Schwalm et al., 2006).

In this study, I investigate if a site-optimized LUE model provides improved estimates of peatland NEE compared to a PFT-optimized model. The results show that the site-optimized VPRM performs better than the PFT-optimized VPRM during the 2007–2008 period at the CF site. Following the sign convention that a negative NEE is a net carbon uptake by vegetation and a negative MBE is an overestimation of NEE, the PFT-optimized VPRM strongly overestimates the mean diurnal NEE flux at CF (Figure 4.3, Table 4.3), particularly between approximately 10:00 and 17:00 local time (Figure 4.4). The RMSE of the PFT-optimized mean diurnal NEE is more than a factor of two larger than that of the site-optimized VPRM (Table 4.3). The improved accuracy of the site-optimized VPRM at the CF site during the 2007–2008 period is as expected since the EC observations for that period were used in the model calibration.

Interestingly, an evaluation of the modelled NEE during the 2010–2011 validation period at CF shows that the PFT-optimized VPRM provided more reliable NEE estimates (Figure 4.11, Table 4.6). The site-optimized VPRM systematically underestimated NEE fluxes at the diurnal and monthly timescales (Figure 4.12 and Figure 4.13). The systematic bias in mean diurnal NEE estimates at CF would suggest that the site-optimized VPRM overestimated respiration both during the daytime and nighttime. It was unexpected that the PFT-optimized VPRM would perform better than the site-optimized VPRM since the PFT parameter values were from other peatland sites (i.e. Mer Bleue, LaBiche, Atqasuk, and Barrow) outside the HBL. Moreover, the EC tower observations used for the calibration and validation of the PFT parameter values (Hilton et al., 2013) were collected during years outside my study period.

One possible reason for the improved estimates of NEE by the PFT-optimized VPRM at the CF site is that the PFT parameter values were constrained with a much larger dataset, covering four different wetland sites and collectively spanning over six years (Hilton et al., 2013). In contrast, only four years of EC tower data are available for the CF site on the AmeriFlux database; two years were used for the site-optimized VPRM calibration and the other two years for model validation. The PFT-optimized VPRM also used study sites that included EC observations collected all year round, while the site-optimized VPRM used only EC data from June–October because there are no year-round EC observations available at the CF study site. Indeed, winter EC tower measurements over northern peatlands are rare, and when they do exist, are characterized by large data gaps (Lafleur et al., 2003). The site-optimized VPRM diurnal and monthly NEE estimates at CF, therefore, have RMSEs that are almost twice as large as the PFT-optimized VPRM estimates during the 2010–2011 validation period (Table 4.6). These results are similar to those of Luus and Lin (2015) who found that PolarVPRM considerably underestimated GEE during the peak growing season at Daring Lake, Northwest Territories, Canada. They reasoned that the disproportionately large model bias at Daring Lake compared to other calibration sites was due to the unavailability of year-round EC tower observations.

The biases in modelled NEE estimates at ARB were remarkably similar for the site-optimized VPRM and PFT-optimized VPRM, both during the calibration and validation periods (Table 4.3 and Table 4.6). Following the sign convention used for NEE (negative = carbon uptake, positive = carbon release), the two models tend to slightly underestimate NEE at high (negative) values and overestimate NEE at low (positive) values (Figure 4.7 and Figure 4.15). The site-optimized VPRM and PFT-optimized VPRM together underestimated the net carbon uptake between approximately 9:00 and 14:00 local time but overestimated NEE during the nighttime (i.e. underestimated respiration) at ARB during the calibration and validation periods (Figure 4.8 and Figure 4.16). Overall, NEE estimates of both models display excellent statistical agreement with observations at ARB, with reasonably low MBEs and RMSEs at all timescales.

It is noteworthy that the PFT-optimized VPRM provides comparable or arguably better NEE estimates at ARB because the model parameter values were estimated from EC tower observations outside the study region, as discussed earlier. This suggests that the VPRM environmental scalars, T_{scale}, P_{scale} and W_{scale}, which represent the effect of temperature, phenology and water content, respectively, on photosynthesis, are sufficient to determine the actual light-use efficiency of vegetation in the HBL. The results presented in this study support those of Kross et al. (2016) who argued that a unique maximum LUE parameter value, $\varepsilon_{\max}$

(denoted as λ in VPRM), may be used for peatlands as long as the LUE model is able to adequately resolve the environmental limitations on primary production. Also, Hilton et al. (2013) found that VPRM respiration parameter values, α and β, are somewhat consistent across vegetation classes in North America. Kuppel et al. (2012) demonstrated that multi-site model optimization often produced comparable seasonal and annual NEE cycles to those of single-site model optimizations in temperate deciduous broadleaf forests. However, some studies have shown contrary results and suggested that PFT classifications do not adequately capture the variation in vegetation carbon exchange across sites. For instance, Groenendijk et al. (2011) reported that using PFT-generic parameters instead of site-specific optimization to simulate photosynthesis resulted in a weaker agreement with EC tower fluxes. They concluded that model parameter values vary considerably and cannot be categorized by PFTs. In this study, I demonstrate that PFT-optimized VPRM parameterization was able to accurately capture the diurnal and seasonal variations of NEE at peatland sites in the HBL.

4.4.2 Can SIF-Based Models Produce More Reliable Estimates of Peatland NEE?

LUE models are most commonly driven by satellite-derived greenness or chlorophyll indices such as NDVI and EVI. Research studies have reported that MODIS EVI showed stronger agreement with EC tower GPP compared to MODIS NDVI (Xiao et al., 2004; Schubert et., 2010). Satellite-derived VI's should be more accurately interpreted as a measure of potential photosynthetic capacity under optimum environmental conditions rather than actual primary productivity which is regulated by temperature and moisture stress. (Xiao et al., 2019). Recent advances in remotely-sensed SIF measurements, retrievals and modelling have provided an alternative approach to determining the photosynthetic activity of terrestrial ecosystems. There is ample evidence that SIF has the potential to estimate actual primary productivity rather than the maximum photosynthetic capacity of the vegetation (Frankenberg et al., 2011; Joiner et al., 2014; Porcar-Castell et al., 2014). Despite the immense potential of satellite-based SIF, there have been some concerns in their application to modelling ecosystem productivity (Xiao et al., 2019). It has been shown that the relationship between SIF and GPP at the leaf- or canopy-scale is complex and may become nonlinear or even reverse direction under certain physiological and environmental conditions (Porcar-Castell et al., 2014; Damm et al., 2015; Verma et al., 2017; Marrs et al., 2020). Moreover, only a few studies have examined the utility of SIF-driven LUE models in estimating ecosystem production in northern peatlands (Luus et al., 2017).

In this study, I evaluate the performance of satellite-retrieved proxies for photosynthesis by driving VPRM alternately with EVI and SIF during the calibration and validation periods. At the CF site, both the EVI-based and SIF-based modelled NEE estimates had strong correlations with EC tower observations. Table 4.7 and Table 4.8 show NEE biases for the two VPRM models when evaluated against EC tower observations at CF and ARB during calibration and validation years. VPRM-SIF estimates of CF NEE during the 2007–2008 calibration period had lower RMSEs at the daily and monthly timescales, while VPRM-EVI had a lower RMSE at the diurnal timescale. During the 2010–2011 validation period at CF, VPRM-SIF had smaller RMSEs at the diurnal, daily and monthly timescales compared to VPRM-EVI. At the ARB site, VPRM-SIF provided more reliable estimates of NEE at all timescales throughout the study period.

The overall better performance of VPRM-SIF demonstrates that SIF is a more direct proxy for photosynthesis in the peatland sites of the HBL. Previous studies in other terrestrial ecosystems such as forests, croplands, and savannas have shown that SIF provided improved estimates of remotely-sensed GPP (Guanter et al., 2014; Pérez-Priego et al., 2015; Walther et al., 2016). It has been suggested that satellite-derived SIF should be employed in land surface models since they are more effective than satellite-derived VI's in capturing the response of GPP to environmental stress (Lee et al., 2013). A global analysis of the relationship between OCO-2 SIF and GPP from EC tower sites showed that satellite-retrieved SIF had a strong agreement with observed GPP across various biomes and that OCO-2 SIF provided far more reliable estimates of GPP than MODIS-derived VIs. (Li et al., 2018a). Luus et al. (2017) found that the SIF-based modelling approach produced better estimates of the timing of spring photosynthetic onset and duration of the growing season in the Alaskan tundra ecosystem. They reported that the EVI-driven seasonal cycle showed that the growing season started approximately 9 days earlier than the SIF-driven model, resulting in an overestimation of carbon uptake by arctic vegetation. Similarly, Yang et al. (2015) found that the SIF-GPP relationship is significantly strong and SIF is more closely related to GPP than VI's in temperate deciduous forests. They further argued that SIF is not just simply a proxy for APAR but also contains critical information about vegetation LUE. Here, I demonstrate that while both the EVI-driven VPRM and SIF-driven VPRM NEE estimates display strong agreement with EC tower observations, VPRM-SIF provides more reliable estimates of peatland NEE in the HBL. This suggests that despite the complex and dynamic environmental control on the SIF-GPP relationship at leaf and canopy scales (Marrs et al., 2020), their linear correlation remains robust at the ecosystem scale (Verma et al., 2017).

4.4.3 How Do LUE and Other Model Parameters Vary Within and Between Sites?

The relatively simple mathematical structure of the VPRM makes it possible to evaluate model sensitivities to parameter estimates and diagnose errors in simulated NEE (Lin et al., 2011). As described earlier, only four parameters are used for the computation of NEE in VPRM: two parameters (λ and PAR_0) are used to calculate GEE, and two parameters (α and β) are used to calculate respiration. The biases in the mean diurnal and monthly estimates of VPRM NEE can be diagnosed by:

(i) Comparing model parameter values constrained by EC tower observations during the calibration period at the CF (2007–2008) and ARB (2011–2013) study sites, against the wetland PFT parameter values from Hilton et al. (2013).

(ii) Analyzing model parameter values estimated during the calibration period against optimal parameter values for the validation period at CF (2010–2011) and ARB (2014 – 2015).

The different model parameter sets used to run the EVI-based VPRM are shown in Table 4.9.

First, I compare the model parameter values used for the site-optimized VPRM (*Calibra_Param*) during the calibration period against those parameter values used in the PFT-optimized VPRM (*PFT-Param*). The difference between *Calibra_Param* and *PFT_Param* explains why the PFT-optimized VPRM strongly overestimated the mean diurnal NEE around afternoon at the CF site. The PFT-optimized VPRM has a much higher PAR_0 (half-saturation value), though λ (LUE) is much lower. In addition, β (basal rate of respiration) is very small for *PFT_Param* compared to *Calibra_Param*. As a result, the PFT-optimized VPRM overestimated photosynthesis and underestimated respiration at CF during the 2007–2008 calibration period (Figure 4.3 – 4.5). At the ARB site, the differences between the *Calibra_Param* and *PFT_Param* are considerably smaller compared to the CF site (Table 4.9). Thus, the estimated mean diurnal and monthly NEE are remarkably similar at ARB during the 2011–2013 calibration period (Figure 4.7 –4. 9).

Table 4. 9. VPRM parameter sets*. *Calibra_Param* are parameter values estimated from associations found between meteorological and EC NEE tower observations (June–October) during the calibration period at CF (2007–2008) and ARB (2011–2013). *Optimiza_Param* are recalculated optimal parameter values using meteorological and EC NEE observations during the validation period at CF (2010–2011) and ARB (2014 – 2015). *PFT_Param* are the PFT parameter values for North American wetlands from Hilton et al. (2013).

CF	lambda (λ)	alpha (α)	beta (β)	PAR_0
Calibra_Param	0.29	0.08	0.40	105
Optimiza_Param	0.18	0.09	-0.16	200
PFT_Param	0.08	0.09	0.04	618
ARB				
Calibra_Param	0.12	0.10	-0.13	323
Optimiza_Param	0.16	0.11	-0.05	240
PFT_Param	0.08	0.09	0.04	618

*Units are in: λ: µmole CO_2 m^{-2} s^{-1}/µmole PAR m^{-2} s^{-1}; α: µmole CO_2 m^{-2} $s^{-1}/^0C$; β: µmole CO_2 m^{-2} s^{-1}; PAR_0: µmole m^{-2} s^{-1}

Second, I analyze the model parameter values used for the site-optimized VPRM (*Calibra_Param*) during the validation period against the optimal parameter values for the validation period (*Optimiza_Param*). As described earlier, EC tower observations during the calibration years were used to constrain *Calibra_Param*, and then *Calibra_Param* was used to run the site-optimized VPRM during the validation period. For comparison, the optimal parameter values (*Optimiza_Param*) for the validation period were computed by constraining the model with EC tower observations collected during the validation period.

At the CF site, a comparison between *Calibra_Param* and *Optimiza_Param* shows that a relatively high value of λ is partially offset by a relatively low value of PAR_0 for *Calibra_Param* (Table 4.9). This suggests that the main discrepancy between *Calibra_Param* and *Optimiza_Param* at the CF site is in the β parameter value (*Calibra_Param* $\beta = 0.40$, *Optimiza_Param* $\beta = -0.16$). Thus, the biases in the mean diurnal NEE estimates at CF during the 2010–2011 period can be attributed to the difference between the *Calibra_Param* and *Optimiza_Param* β values (0.56 μmole CO_2 m^{-2} s^{-1}) as shown in Figure 4.12. It is apparent that *Calibra_Param* caused the site-optimized VPRM to systematically overestimate respiration both during the day and nighttime, resulting in an underestimation of NEE at the CF site for the 2010–2011 period. When the optimal parameter values (*Optimiza_Param*) were instead used to run the site-optimized VPRM, the biases in respiration and NEE were eliminated (Figure 4.26).

Luus et al. (2017) previously published model parameter values of 0.15 for λ and 241 for PAR_0 for Alaskan wetland sites. These parameter values are more consistent with *Optimiza_Param* ($\lambda = 0.18$ and $PAR_0 = 200$) than *Calibra_Param* ($\lambda = 0.29$ and $PAR_0 = 105$) at CF. This suggests that the 2007–2008 calibration years at CF may have been rather unusual, which could also explain the overall better performance of VPRM at the ARB site. Indeed, *Calibra_Param* and *Optimiza_Param* have a stronger agreement at ARB, and there is no major improvement to the mean diurnal NEE estimates when the site-optimized VPRM is recalibrated with *Optimiza_Param* during the 2014–2015 validation period at ARB (not shown).

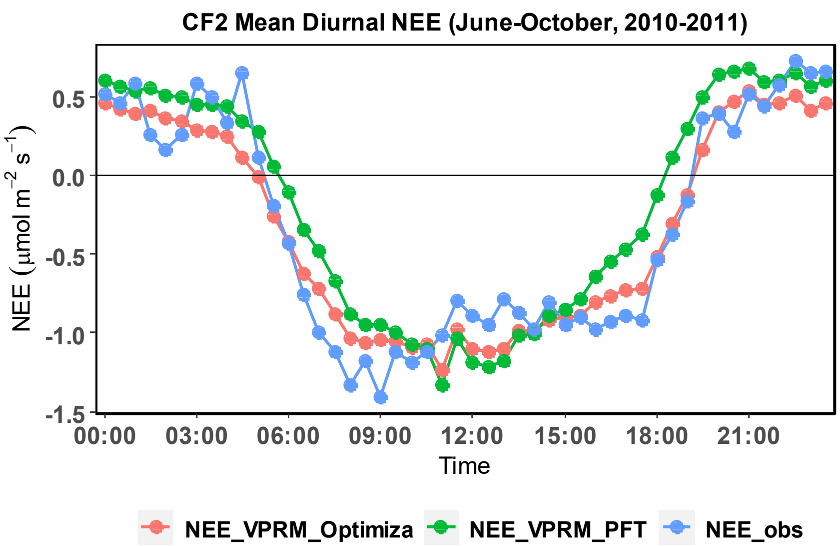

Figure 4. 26. A comparison between modelled and observed mean diurnal NEE cycle at the Churchill fen during the 2010–2011 validation period (CF2). VPRM_Optimiza is the site-optimized VPRM using the recalculated optimal parameter values constrained by EC tower observations during the 2010–2011 validation period.

4.5 Conclusion

The reliability of LUE-based model estimates of carbon fluxes largely depends on their ability to accurately compute the LUE parameter, ε, and other model parameters. This is particularly important in peatland ecosystems which have received less attention in LUE-model calibration and validation, compared to other major biomes such as forests and grassland (Kross et al., 2016; Lees et al., 2018). In most LUE models, ε is often estimated from a constant ε_{max} which is derived from site-specific EC tower observations and adjusted by limiting environmental factors such as temperature and water stress (Hilker et al., 2008; Yuan et al., 2014). The estimated ε_{max} values are then applied to regional or continental scale carbon studies based on vegetation classes or PFTs.

There are still large uncertainties in the reliability of the aforementioned approach to estimating LUE-based model parameter values. For instance, some studies have found that LUE varied significantly between plants and across different ecosystems (Gamon et al., 1995; Turner et al., 2003), while other studies have suggested that LUE parameter values were constant or relatively invariant across several PFTs (Yuan et al., 2007; Hilton et al., 2013). Kuppel et al. (2012) and Hilton et al. (2013) showed that model respiration parameter values, such as VPRM's α and β, only vary slightly across biomes. It has also been argued that vegetation functional type and the presence of non-vascular plant cover such as understory moss have considerable impacts on the photosynthetic LUE in high-latitude tundra ecosystems (Huemmrich et al., 2010). Moreover, few studies have investigated the variability and controls of ε in northern peatlands (Schubert et al., 2010; Harris and Dash, 2011; Kross et al., 2013), and no studies have evaluated the applicability of LUE-based models in the HBL region of Canada.

Moreover, satellite-derived EVI has been widely used as a proxy for FAPAR in LUE-based models to estimate GPP. It has been shown that in comparison to MODIS GPP, MODIS EVI produced similar or better statistical relationships with observed GPP over North American EC tower sites (Rahman et al., 2005; Sims et al., 2006). Recently, SIF retrieved from the OCO-2 satellite has provided an independent approach for estimating plant primary production (Frankenberg et al., 2014; Mohammed et al., 2019). Nevertheless, the ability of SIF to correctly capture short-term and landscape-scale variations in photosynthetic carbon uptake in response to ecological stresses still remains uncertain (Middleton et al., 2018; Helm et al., 2020; Marrs et al., 2020).

In this study, I evaluated a site-optimized and a PFT-optimized VPRM at the Churchill fen and Attawapiskat River bog sites in the HBL, and compared an EVI-driven VPRM and a SIF-driven VPRM to determine which modelling approach provided more reliable estimates of peatland photosynthesis. I also investigated the variation in LUE and other model parameter values within and between the study sites. The results showed that the site-optimized VPRM produced improved NEE estimates at the Churchill fen during the 2007–2008 period compared to the PFT-optimized VPRM. The biases in model NEE estimates suggest that the PFT-optimized VPRM performed better than the site-optimized VPRM during the 2010–2011 period at the Churchill fen. In contrast, mean NEE estimates at the Attawapiskat River bog were remarkably comparable for the site-optimized VPRM and PFT-optimized VPRM throughout the study period (2011–2015). The two models generally overestimated NEE during the calibration period but underestimated NEE during the validation period at both study sites. Furthermore, the SIF-driven VPRM overall produced more reliable estimates of NEE in the HBL compared to the EVI-driven VPRM.

The site-optimized model parameter values for the calibration and validation periods varied considerably within the Churchill fen, as well as between the Churchill fen and Attawapiskat River bog. It was found that the biases in site-optimized VPRM NEE estimates at the Churchill fen during the 2010–2011 validation period were primarily due to unsuitable β parameter values which resulted in an overestimation of respiration. Also, the VPRM parameter values for the calibration period at the Churchill fen were substantially different compared to those from the Attawapiskat River bog and previously studied Alaskan tundra sites. This may suggest that 2007–2008 were atypical years at the Churchill fen.

The PFT-optimized VPRM was able to capture the mean diurnal and monthly variations in NEE at the study sites, with an overall similar performance to the site-optimized VPRM. In particular, the PFT-optimized VPRM estimates of NEE showed strong agreement with EC tower observed NEE at the Attawapiskat bog throughout the study period. This impressive performance of the PFT-optimized VPRM can be interpreted in two opposing ways. On the one hand, it implies that the relatively simple structure of the VPRM, its effective environmental scalars, (T_{scale}, P_{scale} and W_{scale}), and its superb ability to integrate satellite-based surface reflectance, phenology and FAPAR proxy data make it robust to intra-PFT and inter-annual variations in model parameter values. On the other hand, it suggests that the VPRM uses different and somewhat inconsistent combinations of model parameter values to arrive at comparable mean diurnal and monthly NEE estimates within and across study sites. Nevertheless, it is clear that the VPRM can serve as a valuable tool for studying long-term CO_2 exchange in peatland sites, and the model parameter values can be applied on a larger scale to the entire HBL region.

Chapter 5

Long-term response of peatland carbon exchange to climatic changes in the Hudson Bay Lowlands

Abstract

Northern peatlands have been a persistent net sink of atmospheric carbon due to the greater rates of plant photosynthesis compared to ecosystem respiration in these regions. Recent global warming and the associated Arctic amplification have raised serious concerns about the carbon (C) sink strength of northern peatlands. In the vast peatlands of the Hudson Bay Lowlands region of Canada, the potential changes in the carbon balance could be even more important. Warming-induced changes in sea ice dynamics and the surface energy balance over the Hudson Bay have altered its advective influence on the adjacent lowlands. Despite our knowledge of the short-term carbon exchange in the peatlands of the HBL, there remain large uncertainties about the long-term combined response of net plant productivity and soil respiration to these climatic changes. In this study, the satellite data-driven Vegetation Photosynthesis and Respiration Model (VPRM) was employed to investigate the response of gross photosynthesis (GPP), ecosystem respiration (ER), and net ecosystem exchange (NEE) to climate warming and moisture changes at a fen and bog in the HBL. The results show contrasting net CO_2 exchange in the peatland sites over the last 20 years, with the fen acting as a net C source (+24 g C m^{-2}) to the atmosphere and the bog serving as a net C sink (-130 g C m^{-2}). Strong anomalies in GPP and ER were associated with climatic trends in temperature and moisture between the 2000–2019 study period. There is ample evidence that a warmer and wetter climate enhanced GPP much more than ER, while cooler temperatures weakened the peatland net C sink regardless of the moisture conditions. Additionally, an examination of the advective influence of the Hudson Bay on the adjacent HBL reveals markedly different carbon dynamics between offshore and onshore winds, with higher respiration rates (12%–26%) during offshore winds. The implications for peatland C balance under increased frequency of onshore winds in the HBL are discussed.

5.1 Introduction

Peatlands are estimated to cover only about 3% (4×10^6 km^2) of the global landmass yet store approximately 400-600 Pg of carbon (Gorham, 1991, 1995; Maltby & Immirzi, 1993; Yu et al., 2010). The mid- and high-latitude peatlands represent over half of the world's wetlands and account for the majority of the global peatland soil organic carbon (C) stocks. They store an estimated 500 Pg C, which is equivalent to one-third of the world's soil organic carbon pool (Limpens et al., 2008; Gorham et al., 2012; Yu, 2012).

Canadian peatlands cover about 12% of the total land area and account for about one-quarter of the world's peatlands (Webster et al., 2018). Here, peatlands store approximately 150 Pg of organic C (Tarnocai et al., 2006), of which 67% occurs in the Boreal and 30% in the Subarctic peatland regions (Zoltai, 1980; Webster et al., 2018). The largest peat-accumulating complex in Canada—and the second largest in the world—is located in the Hudson Bay Lowlands (HBL). The HBL region is mainly found in Ontario, extending northwest to Manitoba and east to Quebec. It covers an area of ~250,000 km^2, comprising 25% of Canada's wetlands, and roughly 6% of the northern C reservoir (Riley, 2011; McLaughlin and Webster, 2014; Packalen et al., 2014). The average peat thickness in the HBL is about 0.5 m but can extend up to 4 m in inland locations, particularly in the northern part of the region (Dredge and Mott 2003; Riley 2011). Peat initiation in the HBL started during the mid-Holocene following the final retreat of the Laurentide Ice Sheet. The region was initially inundated by the post-glacial Tyrrell Sea until around 8,500 years ago, after which extensive peatland development occurred as new land emerged from the Hudson Bay due to glacial isostatic adjustment (Packalen et al., 2014). Although isostatic uplift has since slowed, the coastal HBL is still rising today at a rate of 5–12 mm per year (Peltier, 2004). Differential rates of peat accumulation over low relief deposits of glacio-marine sediments (Martini, 2006) and the spatial variations in the rate of isostatic adjustment across the HBL (Packalen et al., 2014) have promoted the development of different hydrogeomorphic features including microforms (hummocks, lawns and hollows) within fens and bogs (Belyea and Clymo 2001; Harris et al., 2020).

Northern peatlands play a crucial role in the global carbon cycle and have served as an important sink of carbon dioxide (CO_2) since the Last Glacial Maximum (Bridgham et al., 2006; Jones and Yu, 2010; Zhuang et al., 2020). Long-term carbon accumulation in peatlands has occurred as a result of the persistent imbalance between gross primary production (GPP) and ecosystem respiration (R or ER). Here, carbon uptake by vegetation exceeds carbon loss from microbial decomposition due to cool and anerobic environmental conditions. The slow but sustained removal of atmospheric carbon by northern peatlands has traditionally had a net cooling effect on the global climate. However, recent climatic changes across the world have raised serious concerns about the stability of the northern peatland carbon reservoir and its ability to continue to act as a net sink of carbon. Significant changes in temperatures in permafrost regions since the early 1900s are likely to have major implications on peatland carbon balance (Roulet et al., 2007; Price et al., 2013; Meredith et al., 2019). Global warming, which is amplified by the snow- and sea ice-albedo feedback effects in the Arctic and Subarctic regions could result in an increased microbial breakdown of previously frozen peat (Gorham et al., 2012; Chaudhary et al., 2020).

The potential reduction in northern peatland resilience under climate change may be further exacerbated by drier conditions associated with an increase in evapotranspiration (ET), changes in precipitation patterns and the anthropogenic drainage of peatlands for infrastructure development (Shukla et al., 2019; Harris et al., 2020; Yuan et al., 2019). Recent studies have shown that warming over peatland regions increases the atmospheric vapour pressure deficit (VPD) and ET rates, as well as permafrost thaw depth, thus accelerating the decomposition of organic matter (Novick et al., 2016; Gill et al., 2017; Helbig et al., 2020). Furthermore, peatland drainage due to land-use changes from agriculture, mining, and forestry may increase carbon loss in northern peatlands as a result of more intense and widespread wildfires (Turetsky et al., 2011; Kettridge et al., 2015). Granath et al. (2016) found that climate and land-use change caused a considerable increase in wildfire risks across managed peatlands in Canada and northern Europe. The response of arctic and subarctic peatlands to a warming climate will be largely influenced by their sensitivity to changes in water table depth.

Despite the importance of peatlands in regulating climate and their vulnerability to global warming, the long-term (decadal) impact of changes in temperature and moisture conditions on northern peatlands remain uncertain. There is strong evidence that northern high latitudes will continue to experience the greatest warming throughout the 21st century with temperatures rising faster during winter than summer (IPCC, 2021). Yet, it is still unclear whether warmer temperatures would lead to an increase in peatland net ecosystem exchange (NEE) due to greater photosynthetic CO_2 uptake by plants, or if such an increase in plant production will be offset by greater decomposition rates (Qiu et al., 2020) and on what time-scales. There is also considerable uncertainty in projected moisture changes in northern peatland regions. Although it is expected that precipitation will increase in the Arctic and Subarctic regions (IPCC, 2021), it is possible that higher evapotranspiration from warming will lead to the drying of peatlands (Green et al., 2019; Helbig et al., 2020).

Ise et al. (2008) and Dorrepaal et al. (2009) argued that ecosystem respiration is typically more sensitive to temperature changes than primary production in northern environments. They showed that the increase in carbon losses from peatlands was stronger than the enhancement in carbon assimilation rates under warmer temperatures. On the other hand, some research studies have demonstrated that a warmer climate will likely favour peat accumulation in most northern peatlands over the next century, except under excessive dry conditions (Charman et al., 2013; Charman et al., 2015; Packalen et al., 2016). It has been shown that climate change results in higher photosynthetic C uptake by northern ecosystems due to the CO_2 fertilization effect (Bastos et al., 2019; Piao et al., 2020), increase in growing season length (Pedlar et al., 2015; IPCC, 2021), and expansion of shrub extent across the region (Myers-Smith et al., 2011; Martin et al., 2017; Myers-Smith et al., 2020). In contrast, other researchers found that the enhanced photosynthesis of terrestrial ecosystems driven by higher atmospheric CO_2 concentrations has declined considerably in recent decades (Peñuelas et al., 2017; Wang et al., 2020), and the expansion of woody shrubs in peatlands under warmer conditions was inhibited by the rapid vertical growth of *Sphagnum* mosses (Dorrepaal et al., 2009). Indeed, the unresolved fate of peatland carbon stability under climate change is due to the complex, non-linear response of photosynthesis and respiration to higher atmospheric CO_2 concentrations, warmer temperatures, and changes in soil water availability. Besides, peatland ecosystems in different parts of the Arctic and Subarctic region will have varying responses to these climatic changes and feedbacks.

Paleoclimatic studies of peatland carbon stocks in North America showed that the greatest C accumulation rates in northern peatlands occurred during the Holocene Thermal Maximum from the period 10,000 to 8,000 years ago (Zhuang et al., 2020). The higher temperatures and moisture conditions during this period accelerated peat growth through enhanced vegetation production. However, continued warmer temperatures during the late Holocene resulted in a decline in peat accumulation due to increased moisture loss and heterotrophic respiration. This suggests that current global warming may initially promote a net increase in carbon uptake by peatland vegetation over the next few decades; however, a further rise in temperatures, permafrost degradation and changes in wetland dynamics during the latter part of the 21st century may considerably reduce the capacity of northern peatlands to sequester carbon (Gallego-Sala et al., 2018; Chaudhary et al., 2020). Additionally, Qiu et al. (2020) showed that peatland extent in western Canada and western Europe may shrink, and these regions may shift from being carbon sinks to sources, particularly under rapid global warming scenarios. The study found that peatlands of the Western Siberian Lowlands and the HBL were relatively more resilient to climate warming, with both their areal extent and carbon sink capacity increasing over the 21st century.

The short-term carbon dynamics of peatlands in the HBL region has been well-studied (Humphreys et al., 2014; Hanis et al., 2015; Helbig et al., 2019; Nwaishi et al., 2020), yet the longer-term (decadal) fate of the HBL peatlands NEE in response to climate change is still poorly understood (McLaughlin and Packalen, 2021). Moreover, different peatland types and permafrost features in the HBL have exhibited varied responses to warmer temperatures and moisture changes (McLaughlin and Webster, 2014; Webster et al., 2018). The impact of global warming on the NEE of the HBL is further complicated by the negative trends in sea ice extent and a lengthening of the ice-free season over the Hudson Bay (Hochheim and Barber, 2014), as well as the recent changes in the surface radiation and energy budget over the Bay (Bello and Higuchi, 2019).

It has been shown that the Hudson Bay exerts a strong advective influence on the surface energy balance in the HBL (Rouse and Bello, 1985; Lafleur and Rouse, 1988; Delidjakova et al., 2016). The onshore winds blowing from the Bay towards the HBL are relatively cold and moist compared to the warm and dry offshore winds. A comprehensive long-term analysis of the mesoscale wind and temperature trends across approximately 200 grid locations in the HBL revealed that recent global warming and trends in Hudson Bay sea-ice have caused significant changes in the mesoscale wind regimes and the advective role of the Bay on the surface energy balance in the HBL region (Chapter 2). The study found a strong increasing trend in onshore wind frequency of about 7% over the last 40 years. The largest changes occur in June when the onshore winds have increased by 17%, resulting in a shift from offshore to onshore winds dominance in June over the HBL region as a whole. It was also shown that the rise in temperatures during offshore wind regimes was stronger than those during onshore winds, with the most rapid temperature increase occurring in June and September.

The impacts of these climatic changes in the mesoscale wind and temperature regimes on the surface energy balance of the HBL have been extensively investigated (Chapter 2 and 3), but their effects on the terrestrial ecosystem carbon dynamics have not yet been examined. Delidjakova et al. (2016) provided the first and only known quantitative evidence of the advective influence of Hudson Bay on the net ecosystem exchange of the HBL. Although they provided valuable insights into the interactions between mesoscale wind regimes and carbon fluxes in the HBL, the study was limited to a single eddy covariance (EC) measurement tower site over one growing season.

The current study attempts to reduce these important research gaps and address the uncertainties in the long-term response of peatland carbon exchange to climatic changes in the HBL. Additionally, this study aims to advance our understanding of the advective impacts of the Hudson Bay on the NEE in the adjacent lowlands under global warming. The main objectives of this study are to 1) extend the limited EC carbon flux data over a fen and bog site in the HBL and examine the net CO_2 exchange during the growing season; 2) investigate the 20-year response of peatland C balance to changes in temperature and moisture conditions; 3) quantify the relative importance of environmental controls on peatland C balance; and 4) assess the advective influence of the Hudson Bay on the C dynamics of the HBL under global warming.

5.2 Methods

5.2.1 Study Sites and EC Tower Flux Data

Fens and bogs are the two most common peatland types in boreal North America. Two sites that represent these major peatland types in the HBL were selected for this study based on EC flux data availability. The first study site (58°39’57"N, 93°49’48"W) is a fen located on the western shore of the Hudson Bay in northern Manitoba. The site is about 12 km south of the Churchill Northern Studies Centre, which is approximately 23 km east of the town of Churchill. (Figure 5.1). The closest major settlement to Churchill is Thompson, about 400 km to the south. The study area is underlain by continuous permafrost where the active layer can be over 1.5 m deep (Brown, 1970; Hanis et al., 2013). It is situated at the intersection of three major ecosystems consisting of marine, boreal forest and tundra. The Churchill fen (CF) features microforms dominated by sedge lawns, hummocks and hollows, which have up to 0.4 m of peat over carbonate-rich glaciomarine sediments (Rouse et al., 2002). The sedge lawns cover roughly 55% of the fen and are dominated by *Carex aquatilis* Wahlenb. and an understory of the moss *Pseudocalliergon turgescens* (Jensen) Loeske (Raddatz et al., 2009). The hummocks are dominated by *Cladina* spp. and *Cladonia* spp of lichens and the moss *Dicranum elongatum* Schwaegr. The hollows are characterized by mats of *P. turgescens*, underlain with peat which overlies a mineral substrate (Hanis et al., 2013; Hanis et al., 2015). The climate of Churchill is subarctic and the daily average temperature ranges from a minimum of -26.0 °C in January to a maximum of 12.7 °C in July, with an annual average of -6.5 °C (Environment Canada, 2020). Over the 1981–2010 climate normal period, the area received average annual precipitation of approximately 453 mm, with about 44% of the annual precipitation falling as snow in all months except July and August (Environment Canada, 2020).

The second study site (52°41′N, 83°56′W) is a treed/low shrub ombrotrophic bog (Humphreys et al., 2014) located in the southern part of the HBL approximately 100 km west of the town of Attawapiskat, at the mouth of the Attawapiskat River on James Bay in northern Ontario. Attawapiskat is home to the Attawapiskat First Nation, a small Mushkegowuk community with a population of about 2,000. The study site is located roughly 13 km south of De Beers Canada Victor Mine; a 15-hectare open pit kimberlite where commercial diamond production began in 2008 (AMEC, 2004). The Attawapiskat River bog (ARB) features raised hummocks covered equally by *Sphagnum* mosses and lichens. A sporadic overstory dominated by ericaceous shrubs and stunted evergreen black spruce trees is also present (Helbig et al., 2019). The area surrounding the study site is estimated to store about 100 kg C m^{-2}, with peat thickness ranging from about 1–4 m (Akumu and McLaughlin, 2014). The water table depth fluctuates between 0.1 m above the moss surface in April and 0.2 m below the moss surface in August (Harris, 2017; Helbig et al., 2019). The nearest weather station with a long-term climate record is at Moosonee, 160 km south of Attawapiskat. There, the daily average temperature ranges from a minimum of -20.0 °C in January to a maximum of 15.8 °C in July, with an annual average of -0.5 °C. The area received average annual precipitation of approximately 704 mm over the 1981–2010 climate normal period, with about 71% of the annual precipitation falling as rain particularly between June and October (Environment Canada, 2020).

EC tower observations from AmeriFlux (https://ameriflux.lbl.gov) were obtained for the CF site (Papakyriakou, 2020; Tenuta, 2020) and ARB site (Todd and Humphreys, 2018). The two sites are categorized as permanent wetlands under the International Geosphere-Biosphere Programme (IGBP) vegetation cover classification system (Loveland and Belward, 1997). Four years of EC flux measurements are available for the CF site (2007, 2008, 2010, 2011) and five years of data for the ARB site (2011–2015). It is noteworthy that the CF and ARB sites are two of the only three EC tower sites within the HBL with publicly available data on the AmeriFlux network. Further details about the EC flux instrumentation and measurements at the CF and ARB sites have been provided by Hanis et al. (2015) and Humphreys et al. (2014), respectively.

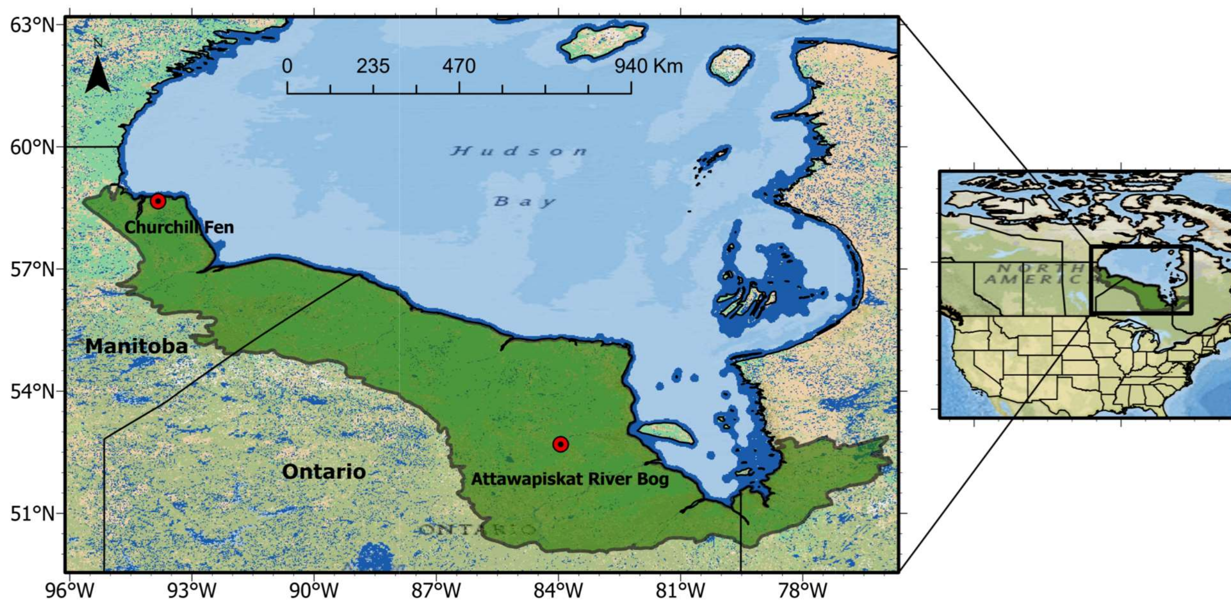

Figure 5. 1. Map showing the locations of study sites in the Hudson Bay Lowlands

5.2.2 Terrestrial Carbon Flux Model

This study employs a modified version of the Vegetation Photosynthesis and Respiration Model (VPRM, Mahadevan et al., 2008) driven by satellite-derived solar-induced chlorophyll fluorescence (SIF), and constrained by EC tower observations from the CF and ARB study sites. As a light-use efficiency (LUE)-based land surface model, VPRM has been shown to provide reliable estimates of terrestrial CO_2 fluxes across various ecosystems in North America, including peatlands (Hilton et al., 2014; Luus and Lin, 2015).

VPRM simulates NEE as the difference between the gross ecosystem exchange (GEE) and the ecosystem respiration (R or ER).

$$NEE = R - GEE \tag{1}$$

Following Mahadevan et al. (2008), GEE is modelled as

$$GEE = LUE \times FAPAR \times \frac{1}{(1 + PAR/PAR_0)} \times PAR \tag{2}$$

where LUE is the light-use efficiency in μmol CO_2/ μmol PPFD, FAPAR is the fraction of photosynthetically active radiation (PAR, in μmol m^{-2} s^{-1}) absorbed by the photosynthetically active portion of the vegetation, and PAR_0 is the half-saturation value of PAR.

LUE is further decomposed into

$$LUE = \lambda \times T_{scale} \times P_{scale} \times W_{scale} \tag{3}$$

where λ is the maximum LUE (i.e. the maximum quantum yield), and T_{scale}, P_{scale}, and W_{scale} are the scaling factors that represent the effects of temperature, leaf phenology, and water stress, respectively, on LUE. These scalers range from 0.0 to 1.0 and vary in both time and space (Mahadevan et al., 2008).

The first scaling term T_{scale} describes the sensitivity of photosynthesis to temperature and is expressed as:

$$T_{scale} = \frac{(T - T_{\min})(T - T_{\max})}{(T - T_{\min})(T - T_{\max}) - (T - T_{opt})^2} \tag{4}$$

where T is air temperature, and T_{min}, T_{max}, and T_{opt} are the minimum, maximum, and optimum temperatures (°C) for photosynthesis, respectively. To prevent instability in model parameter values caused by correlation between the parameters, T_{scale} is computed from literature values of T_{min}, T_{max}, and T_{opt} (Mahadevan et al., 2008).

The second scaling term P_{scale} represents the effects of leaf phenology on canopy photosynthesis. From bud burst to leaf full expansion and during senescence, P_{scale} is computed by

$$P_{scale} = \frac{1 + LSWI}{2} \tag{5}$$

where LSWI is the satellite-derived land surface water index (Xiao et al., 2004). P_{scale} is not required in VPRM-SIF and was therefore not included in this study.

The third scaling term W_{scale} describes the regulation of LUE by canopy moisture content and is calculated as

$$W_{scale} = \frac{1 + LSWI}{1 + LSWI_{max}} \tag{6}$$

where $LSWI_{max}$ is the maximum LSWI during the growing season. The LSWI is estimated using the NIR (0.78–0.89 μm) and SWIR (1.58–1.75 μm) spectral bands (Xiao et al., 2002) as

$$LSWI = \frac{\rho_{nir} - \rho_{swir}}{\rho_{nir} + \rho_{swir}} \tag{7}$$

Studies have shown that the LSWI is sensitive to canopy water content (Tucker, 1980) due to the strong light absorption by liquid water in the SWIR waveband (Chandrasekar et al., 2010).

To model photosynthesis, I use satellite-derived SIF as a proxy for FAPAR. SIF is an electromagnetic signal emitted by assimilating plants. This chlorophyll fluorescence represents a fraction of the light energy that is absorbed by vegetation but not utilized during photosynthesis. SIF is therefore a photo-protective mechanism by which excess energy is re-emitted at longer wavelengths from approximately 650 to 850 nm, with two peaks at 685 nm (red) and 740 nm (far-red). It has been shown that SIF is a more accurate proxy for plant productivity compared to the Normalized Difference Vegetation Index (NDVI) and Enhanced Vegetation Index (EVI) (Porcar-Castell et al., 2014; Yang et al., 2015; Chapter 4). SIF is also more sensitive to changes in photosynthetic capacity resulting from temperature and moisture stresses (Joiner et al., 2014; Rascher et al., 2015). Furthermore, the strong relationship between satellite-derived SIF and GPP at various spatial scales have been widely reported (Frankenberg et al., 2011; Li et al., 2018b; Lu et al., 2018).

The modified VPRM thus simulates the gross ecosystem exchange as

$$GEE = \lambda \times T_{scale} \times W_{scale} \times \frac{SIF}{\cos(SZA)} \times \frac{1}{(1 + PAR/PAR_0)} \times PAR \tag{8}$$

where SZA is the solar zenith angle.

Ecosystem respiration (R) is modelled as a simple linear function of air temperature (T):

$$R = \alpha \times T + \beta \tag{9}$$

where α and β are the regression coefficients representing the slope or the sensitivity of respiration to air temperature and the basal rate of respiration under very low temperatures, respectively.

Hilton et al's (2013) elegant R implementation of the VPRM (*VPRMLandSfcModel*) which includes tools to estimate parameter values was employed in this study.

5.2.3 Remote-Sensing Observations

VPRM is driven by remotely sensed measurements derived from MODIS and OCO-2 satellite datasets. Surface Reflectance product MOD09A1 at 8-day, 500m resolution (Vermote, 2015) was retrieved from MODIS Collection 6 dataset which implemented several improved processing algorithms from earlier versions (ORNL DAAC, 2018). In addition, satellite-derived chlorophyll fluorescence was acquired from the global spatially contiguous SIF (CSIF) product at 4-day, 0.05° resolution (Zhang et al., 2018). The clear-sky instantaneous CSIF dataset has been shown to have high accuracy and small bias across various terrestrial ecosystems.

5.2.4 Meteorological Observations

To run VPRM outside of the available EC tower measurement period, meteorological observations were obtained from NOAA's North American Regional Reanalysis (NARR) model, produced by the National Centers for Environmental Prediction (NCEP). NARR is a long-term, dynamically consistent, high-resolution, atmospheric and land surface hydrology dataset for the entire North American domain (Mesinger et al., 2006). VPRM was driven by NARR 3-hourly air temperature and downward shortwave radiation (PAR = 1.98 × SW; Lin et al., 2011) to compute 3-hourly CO_2 fluxes for CF and ARB over the study period (June to October 2000–2019). Additional meteorological data including wind direction, precipitation, humidity, evaporation, and soil moisture were used to examine the sensitivity of NEE, GPP and ER to environmental factors. To assess the advective influence of the Hudson Bay on the HBL, the VPRM CO_2 fluxes and NARR meteorological observations were subsequently partitioned into onshore and offshore wind regimes based on the wind direction.

5.2.5 Model Parameterization

All four VPRM parameters (λ, PAR_0, α, and β) were initially estimated using different approaches as discussed previously in Chapter 4. Briefly, one method involved using model parameter estimates that have been optimized for peatland plant functional types (PFT) in North America (Hilton et al., 2013). Another method involved optimizing VPRM to EC tower flux observations from the CF and ARB study sites, and driving the model alternatively with EVI and SIF. The DEoptim package (Ardia et al., 2011; Mullen et al., 2011) for the R computing environment (R Core Team, 2020) which implements the Differential Evolution (DE) global optimization algorithm (Price et al., 2006) was used to find the best-fitting VPRM parameter values (Hilton et al., 2013). Overall, model validation and error analysis established that though the NEE estimates simulated by the VPRM-PFT, EVI-driven VPRM and SIF-driven VPRM all showed strong agreements with EC tower observations, VPRM-SIF provided the most reliable estimates of peatland NEE in the HBL. Additional details on model calibration and validation have been discussed in Chapter 4.

In this study, VPRM was recalibrated using the full range of available half-hourly EC tower flux data at the CF (2007, 2008, 2010, and 2011) and ARB (2011–2015) study sites from June to October. The presence of large data gaps in 2009 caused by datalogging and power supply issues made this year unreliable and was therefore excluded from the CF dataset (Hanis et al., 2015). The half-hourly EC flux data for the study sites were filtered to remove measurements taken when the friction velocity, u^* was below a threshold of 0.2 m s^{-1} (Baldocchi, 2003; Hanis et al. 2013). Only non-gap-filled EC tower observations were used here to avoid introducing another source of uncertainty to the VPRM parameter estimates (Barr et al., 2004; Lin et al., 2011). Model parameter values optimized using the half-hourly EC tower observations were then used to run VPRM from June to October during the 2000–2019 study period. This VPRM run was driven by MODIS surface reflectance, OCO-2 CSIF, and NARR meteorology.

5.2.6 Statistical Analysis

The Shapiro–Wilk (Shapiro and Wilk, 1965) and Kolmogorov-Smirnov (Massey, 1951) tests for normality and Q-Q plots were used to determine whether the data were normally distributed. When the datasets were not normally distributed (Kolmogorov–Smirnov, $p < 0.05$; Shapiro–Wilk, $p < 0.05$), non-parametric statistical methods were employed to analyze the study results. Linear regression was used to examine the relationships between modelled and observed CO_2 fluxes or meteorological variables. Either Pearson correlation or Spearman rank correlation was employed, when applicable, to investigate the response of NEE, GPP and ER to environmental factors. Due to the correlation between the environmental variables (i.e. multicollinearity), partial correlation analysis (R package *ppcor*; Kim, 2015) was applied to examine the relationships between daily CO_2 fluxes and environmental factors during offshore and onshore winds. The annual relationships between environmental variables and C fluxes were investigated using stepwise regression (R package *MASS*; Ripley et al., 2013). Furthermore, the relative influences of the environmental controls on peatland C exchange variability were quantified by computing the relative importance of each of the predictors in the linear regression model (R package *relaimpo*; Grömping, 2006). Also, the Mann-Kendall test (McLeod, 2011) was used for the detection of trends in the time series, while the Theil-Sen slope approach (TSA; Sen, 1968; Hirsch et al., 1982) was used to calculate the magnitude of the trend. The Mann-Whitney U test was employed to test for statistically significant differences between the means of onshore and offshore wind variables. All statistical analyses were carried out using R programming (R Core Team, 2020).

5.3 Results

5.3.1 Validation of VPRM Meteorological Inputs

Air temperature and PAR from NARR were needed to run VPRM over the 2000–2019 study period. The reliability of the NARR meteorological variables was first determined by comparing them to the EC tower meteorological observations at the study sites. The results show that the 3-hourly NARR temperatures and PAR show strong agreement with EC tower observations at the CF study site both on a diurnal (Figure 5.2) and monthly timescale (Figure 5.3). The NARR model captured approximately 90% and 80% of the variability in the observed daily averaged temperatures and PAR, respectively, at CF (not shown). However, it can be seen that NARR overestimates both meteorological variables at the CF site during the validation period. At the ARB site, the relationships between NARR and EC observed temperatures and PAR are likewise strong, with NARR reproducing about 95% and 80% of the variability in the observed daily averaged temperatures and PAR, respectively, during the validation period (not shown). Overall, the results suggest that though NARR (at 32 km resolution) overestimates measured air temperature and PAR at these HBL peatland sites, it does provide reliable estimates of the meteorological inputs required to drive the VPRM CO_2 fluxes.

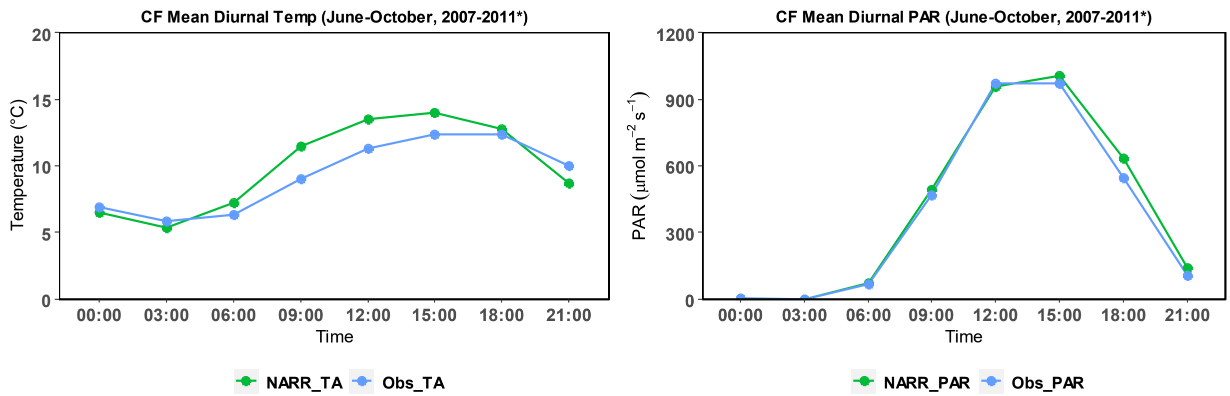

Figure 5. 2. Diurnal NARR air temperatures and PAR compared against EC tower observations at the Churchill fen during the 2007–2011 recalibration period. *Excluding 2009.*

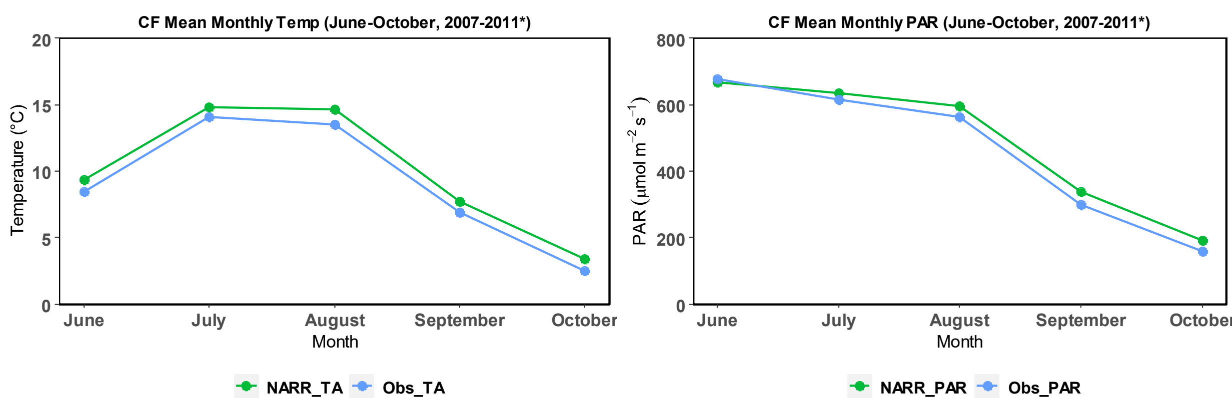

Figure 5. 3. Monthly NARR air temperatures and PAR compared against EC tower observations at the Churchill fen during the 2007–2011 recalibration period. *Excluding 2009*

To further evaluate the accuracy of the NARR meteorological data, VPRM net CO_2 exchange simulated using 3-hourly temperatures and PAR from NARR were compared against EC tower NEE observations at the two study sites. The results indicate that the NARR-driven VPRM was able to capture both the diurnal and monthly cycle of NEE at the CF (Figure 5.4) and

ARB (Figure 5.5) study sites during the NARR validation period. Nevertheless, the model performed better at CF than ARB, especially in the evening and during the peak of the growing season. The biases in NARR-VPRM estimates of mean diurnal NEE fluxes at CF had considerably smaller biases (MBE = 0.00 μmol CO_2 m^{-2} s^{-1}, RMSE = 0.20 μmol CO_2 m^{-2} s^{-1}) compared to biases at ARB (MBE = -0.35 μmol CO_2 m^{-2} s^{-1}, RMSE = 0.64 μmol CO_2 m^{-2} s^{-1}) over their respective validation periods (Table 5.1). Also, the overall decrease in VPRM performance as a result of the NARR meteorology is evident in the modelled NEE biases at ARB, and, to a lesser extent, the CF site. For the mean diurnal NEE estimates, the VPRM driven by EC tower meteorology at ARB had an MBE of -0.04 μmol CO_2 m^{-2} s^{-1} (RMSE = 0.35 μmol CO_2 m^{-2} s^{-1}), while the NARR-VPRM had a larger MBE of -0.35 μmol CO_2 m^{-2} s^{-1} (RMSE = 0.64 μmol CO_2 m^{-2} s^{-1}). The results indicate that VPRM overestimates the net CO_2 sink by the peatlands of the HBL, particularly when the model is driven by NARR temperatures and PAR.

5.3.2 Environmental Conditions

NARR meteorological variables including air temperature, PAR, precipitation, evaporation, VPD, and soil moisture provide insights into environmental conditions at the CF and ARB sites over the 2000–2019 study period. The mean daily temperature between June and October at CF was 8.9 °C, with July (13.6 °C) being the warmest month (Table 5.2). The CF site received a mean daily PAR of 386 μmol m^{-2} s^{-1} over the study period, with PAR peaking in June at about 565 μmol m^{-2} s^{-1} and declining through the remainder of the season (Figure 5.6). Total precipitation from June to October at CF was about 303 mm far exceeding evaporation amounts of 172 mm. The CF mean daily vapour pressure deficit (VPD) was roughly 0.40 kPa and the mean soil moisture content was 759 mm over the study period.

At ARB, the mean daily temperature between June and October was 12.2 °C, with July also having the warmest temperature (16.9 °C). The mean daily PAR incident at ARB was about 401 μmol m^{-2} s^{-1} and the highest light levels of 547 μmol m^{-2} s^{-1} occurred in June. The bog received about 391 mm and 367 mm of total precipitation and evaporation, respectively, between June and October. The mean daily VPD was approximately 0.40 kPa, while the mean soil moisture was 611 mm, reaching a minimum of about 590 mm in September (Figure 5.7).

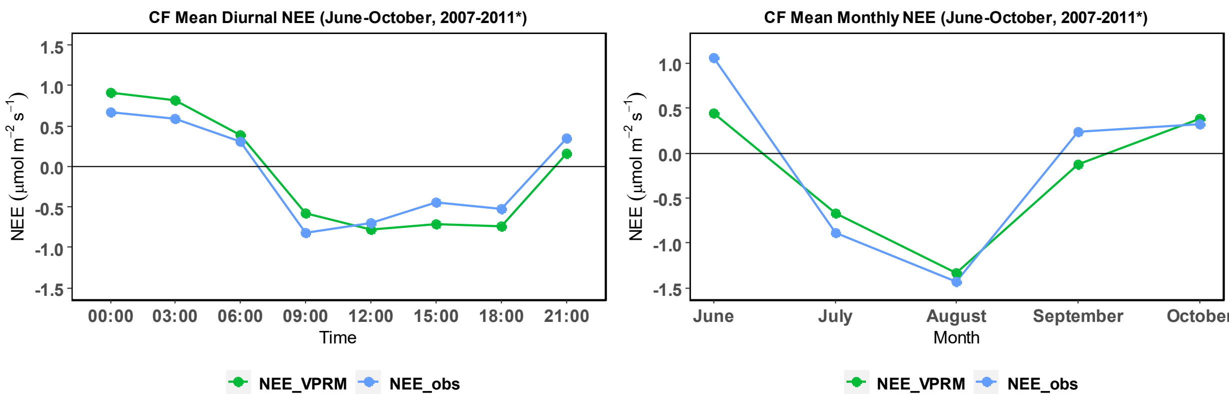

Figure 5. 4. A comparison between NARR-driven VPRM NEE and observed mean NEE cycles on a diurnal and monthly timescale at the Churchill fen during the 2007–2011 recalibration period. *Excluding 2009.*

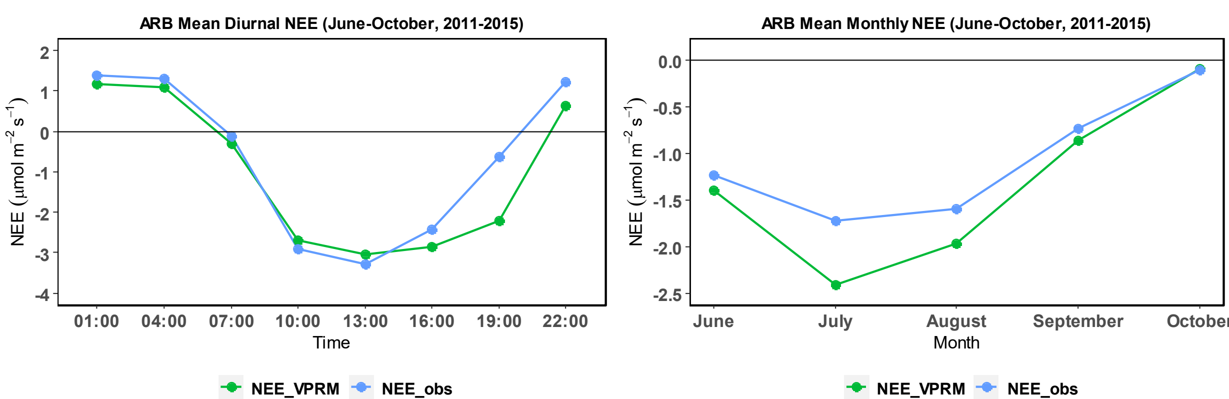

Figure 5. 5. A comparison between NARR-driven VPRM NEE and observed mean NEE cycles on a diurnal and monthly timescale at the Attawapiskat River bog during the 2011–2015 recalibration period.

Table 5. 1. Error Statistics (MBE and RMSE in μmol CO_2 m^{-2} s^{-1}) calculated through the comparison of diurnally, daily and monthly averaged estimates of VPRM NEE against eddy covariance NEE observations at CF (2007–2011*) and ARB (2011–2015). VPRM was driven alternatively with EC site meteorology (EC Met-VPRM) and NARR (NARR-VPRM). *Excludes 2009.

CF	MBE	RMSE
Diurnal		
EC Met-VPRM	0.08	0.27
NARR-VPRM	0.00	0.20
Daily		
EC Met-VPRM	-0.06	0.67
NARR-VPRM	-0.11	0.73
Monthly		
EC Met-VPRM	-0.06	0.31
NARR-VPRM	-0.12	0.34
ARB		
Diurnal		
EC Met-VPRM	-0.04	0.35
NARR-VPRM	-0.35	0.64
Daily		
EC Met-VPRM	0.01	0.26
NARR-VPRM	-0.28	0.47
Monthly		
EC Met-VPRM	0.01	0.15
NARR-VPRM	-0.27	0.37

Table 5. 2. Monthly environmental conditions at the Churchill fen (CF) and Attawapiskat River Bog (ARB) from June to October during the study period (2000–2019). All values are averages except for total precipitation and evaporation.

CF	Temperature (°C)	PAR (μmol m^{-2} s^{-1})	Precipitation (mm)	Evaporation (mm)	VPD (kPa)	Soil Moisture (mm)
June	8.8	565	42	44	0.50	781
July	13.6	544	61	53	0.61	752
August	13.0	411	76	37	0.46	739
September	7.8	273	57	24	0.24	749
October	1.1	139	67	15	0.10	774
Season	8.9	386	303	172	0.38	759
ARB						
June	13.5	547	73	98	0.55	649
July	16.9	528	87	107	0.55	613
August	15.7	436	88	87	0.43	593
September	10.9	311	79	52	0.27	590
October	4.0	183	65	23	0.15	611
Season	12.2	401	391	367	0.39	611

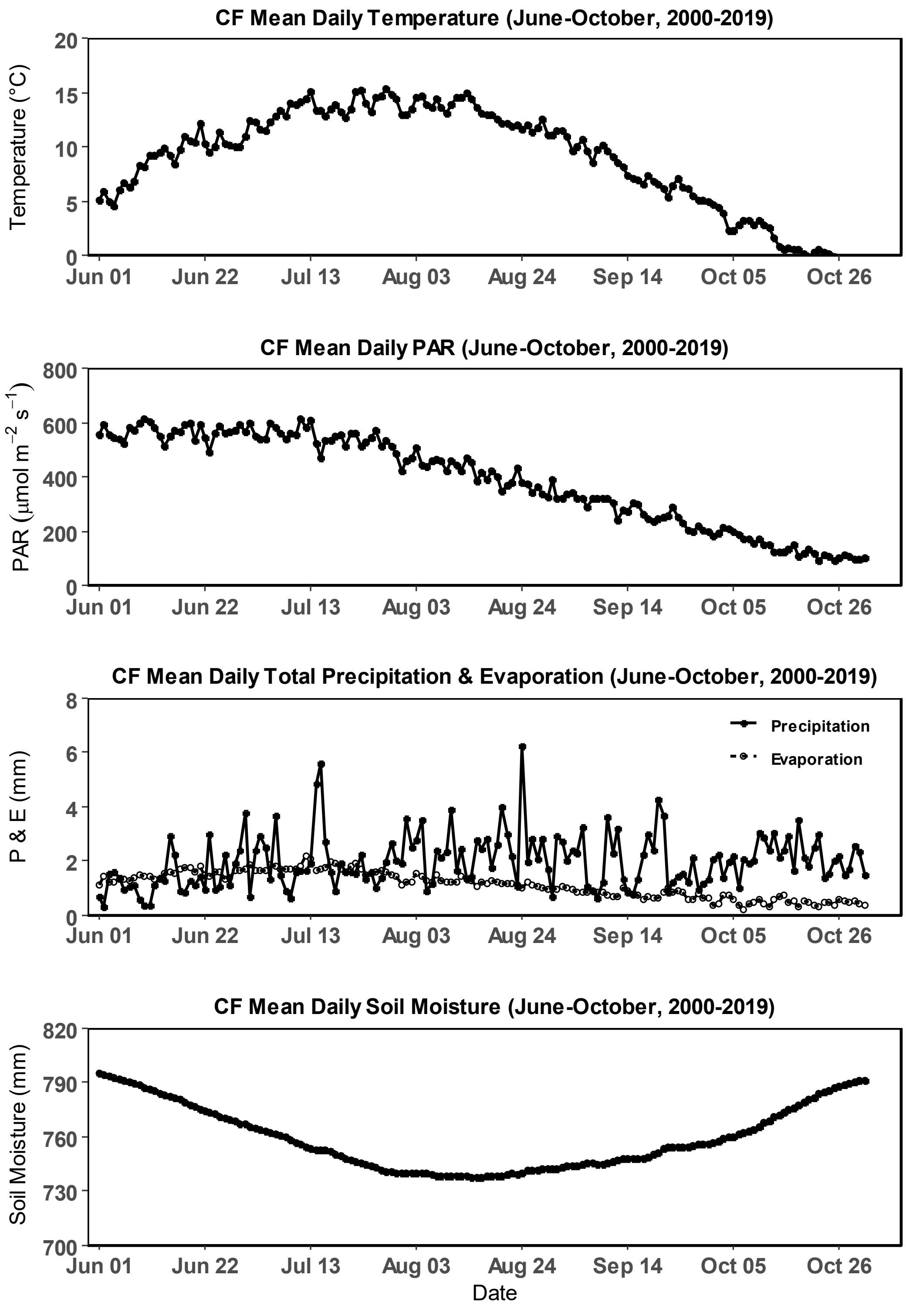

Figure 5. 6. Daily environmental conditions at the Churchill fen (CF) from June to October during the study period (2000–2019).

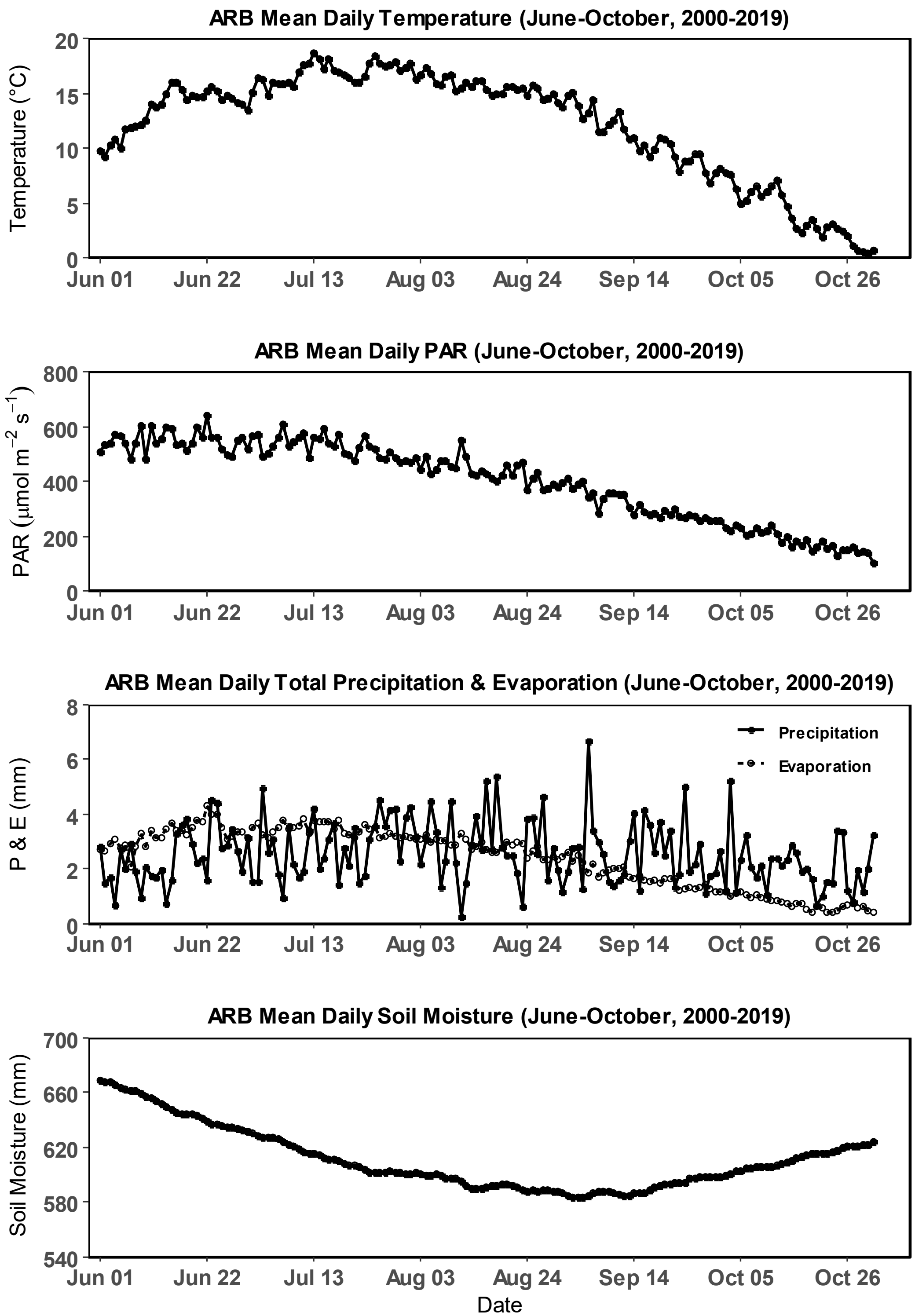

Figure 5. 7. Daily environmental conditions at the Attawapiskat River Bog (ARB) from June to October during the study period (2000–2019).

5.3.3 Net Ecosystem Exchange at Peatland Sites

VPRM estimates of GPP, ER, and NEE from 2000 to 2019 show noticeable seasonal and spatial variations between the CF and ARB sites. At the Churchill fen, mean GPP was 1.14 µmol m^{-2} s^{-1} (181 g C m^{-2}) during the study period (Table 5.3), with the largest productivity occurring in July (1.97 µmol m^{-2} s^{-1}) and August (2.02 µmol m^{-2} s^{-1}). The mean ER ranged from 1.86 µmol m^{-2} s^{-1} in July to 0.36 µmol m^{-2} s^{-1} in October, with a seasonal mean of 1.29 µmol m^{-2} s^{-1} (205 g C m^{-2}). Ecosystem respiration rates at the fen initially exceeded plant productivity resulting in a net CO_2 emission of about 0.53 µmol m^{-2} s^{-1} in June (Figure 5.8). By mid-July, the fen had become a net sink of CO_2, but the maximum plant C uptake (approximately -0.50 µmol m^{-2} s^{-1}) did not occur until around late July to early August. The rates of ER exceeded GPP in September and October at the CF site. Overall, the fen was a net C source of 24 g C m^{-2} to the atmosphere during the 2000–2019 study period.

Table 5. 3. Monthly average CO_2 fluxes at the Churchill fen (CF) and Attawapiskat River Bog (ARB) from June to October during the study period (2000–2019).

CF	NEE_VPRM (µmol m^{-2} s^{-1})	GPP_VPRM (µmol m^{-2} s^{-1})	ER_VPRM (µmol m^{-2} s^{-1})
June	0.53	0.76	1.29
July	-0.11	1.97	1.86
August	-0.23	2.02	1.79
September	0.31	0.86	1.16
October	0.26	0.11	0.36
Season	0.15	1.14	1.29
ARB			
June	-0.78	2.43	1.65
July	-1.52	3.60	2.08
August	-1.29	3.21	1.92
September	-0.50	1.82	1.32
October	0.00	0.48	0.47
Season	-0.82	2.31	1.49

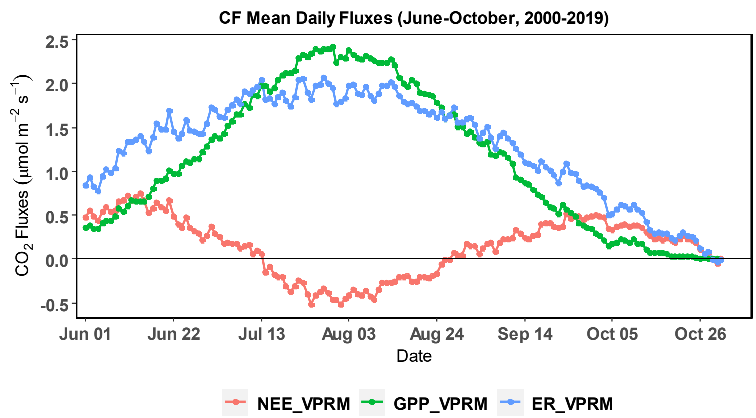

Figure 5. 8. Daily average CO_2 fluxes at the Churchill fen from June to October during the study period (2000–2019).

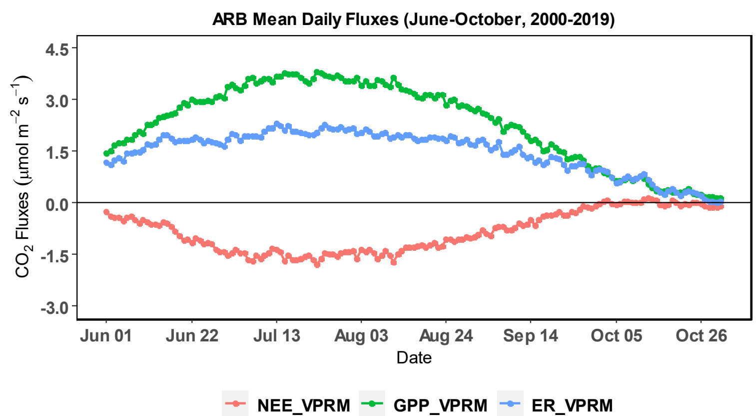

Figure 5. 9. Daily average CO_2 fluxes at the Attawapiskat River Bog from June to October during the study period (2000–2019).

The carbon fluxes at the bog site were much larger than at the fen. Here, the mean GPP ranged from a maximum of 3.60 μmol m^{-2} s^{-1} in July to a minimum of 0.48 μmol m^{-2} s^{-1} in October (Table 5.3). The gross photosynthetic CO_2 uptake was about 2.31 μmol m^{-2} s^{-1} (367 g C m^{-2}) at the bog during the study period. The mean ER was around 1.49 μmol m^{-2} s^{-1} (236 g C m^{-2}) for the study season, with the highest mean respiration occurring in July (2.08 μmol m^{-2} s^{-1}). GPP exceeded ER in all months except October (Figure 5.9), and as a result, the bog was mostly a consistent net sequester of carbon. The maximum mean NEE at ARB occurred in July (-1.52 μmol m^{-2} s^{-1}) and the site was carbon neutral in October. Overall, the bog was a net CO_2 sink during the study period, seasonally removing approximately 130 g C m^{-2} from the atmosphere.

5.3.4 Trends in CO_2 Fluxes and Climate Anomalies

The 2000–2019 study period is characterized by interannual variations in carbon exchange over the HBL peatlands. VPRM estimates of the annual (June–October) CO_2 fluxes at CF show that the site was a carbon source in all years except 2011, 2012, and 2018 (Figure 5.10). The fen experienced strong anomalies (relative to the study period average) in annual GPP and ER, which coincided with large anomalies in climatic conditions. During the first half of the study period, there were strong negative temperature anomalies (> 1°C cooling) in 2000, 2002, 2004, 2009 (Figure 5.11b), which were correlated with the largest negative trends in GPP and ER at the fen (Figure 5.11a). This suggests that the lower temperatures during those anomalous years resulted in a decrease in both photosynthesis and respiration at the CF site. Except for 2002, GPP was more sensitive to these changes in temperature. Consequently, the fen had a positive NEE anomaly (stronger C source) in 2000, 2004 and 2009, releasing an additional 13–18 g C m^{-2} to the atmosphere, compared to the average for the entire study period. In a year when respiration was more sensitive to a decrease in temperatures such as occurred in 2002, the trend in NEE was negative (weaker C source) at the CF site.

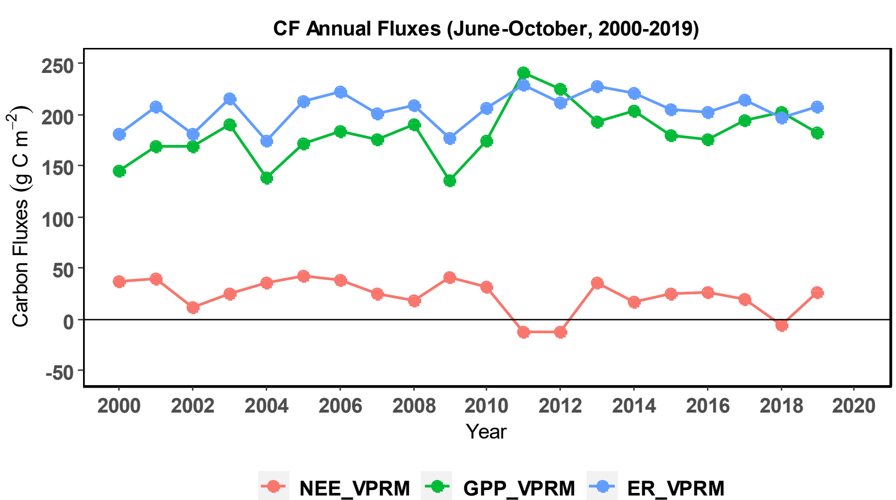

Figure 5. 10. Annual average CO_2 fluxes at the Churchill fen during the study period (2000–2019).

Other years during the first half of the study period at the fen were characterized by moderate positive temperature anomalies (< 1°C warming) accompanied by strong negative soil moisture anomalies (Figure 5.11c). These years—particularly 2005 and 2006—were associated with relatively small changes in GPP and ER, yet produced strong positive NEE anomalies. The warmer and drier conditions either increased ER and decreased GPP (i.e. 2005) or increased ER far more than GPP (i.e. 2006). In both cases, the net effect on the fen was a greater C release to the atmosphere.

The second half of the study period was mostly characterized by positive temperature anomalies over the fen, with the largest trends (> 1°C warming) occurring in 2011 and 2013. The warmer temperatures during those anomalous years were correlated with substantially higher photosynthesis and respiration at the Churchill peatland site. The results indicate that the annual GPP at the fen was more sensitive to the increase in temperatures in 2011 compared to ER. In contrast, the sensitivity of the annual ER was greater than that of GPP in 2013. Therefore, the annual NEE anomaly at the fen was negative (enhanced C uptake) in 2011, but positive (higher C emission) in 2013, relative to the study period average. Moreover, 2011 is noteworthy because the strong temperature anomalies were also accompanied by considerable changes in soil moisture conditions at the fen site. The year 2011 and the preceding year (2010) were exceptionally wet, with positive precipitation anomalies of about 60 mm and 125 mm, respectively (Figure 5.11d). The soil moisture content at CF was considerably high in 2011, with a positive anomaly of approximately 40 mm. In the following year (2012), the highest soil moisture anomaly of 62 mm was recorded for the study period. The strong positive anomalies in soil moisture persisted through 2013 and 2014.

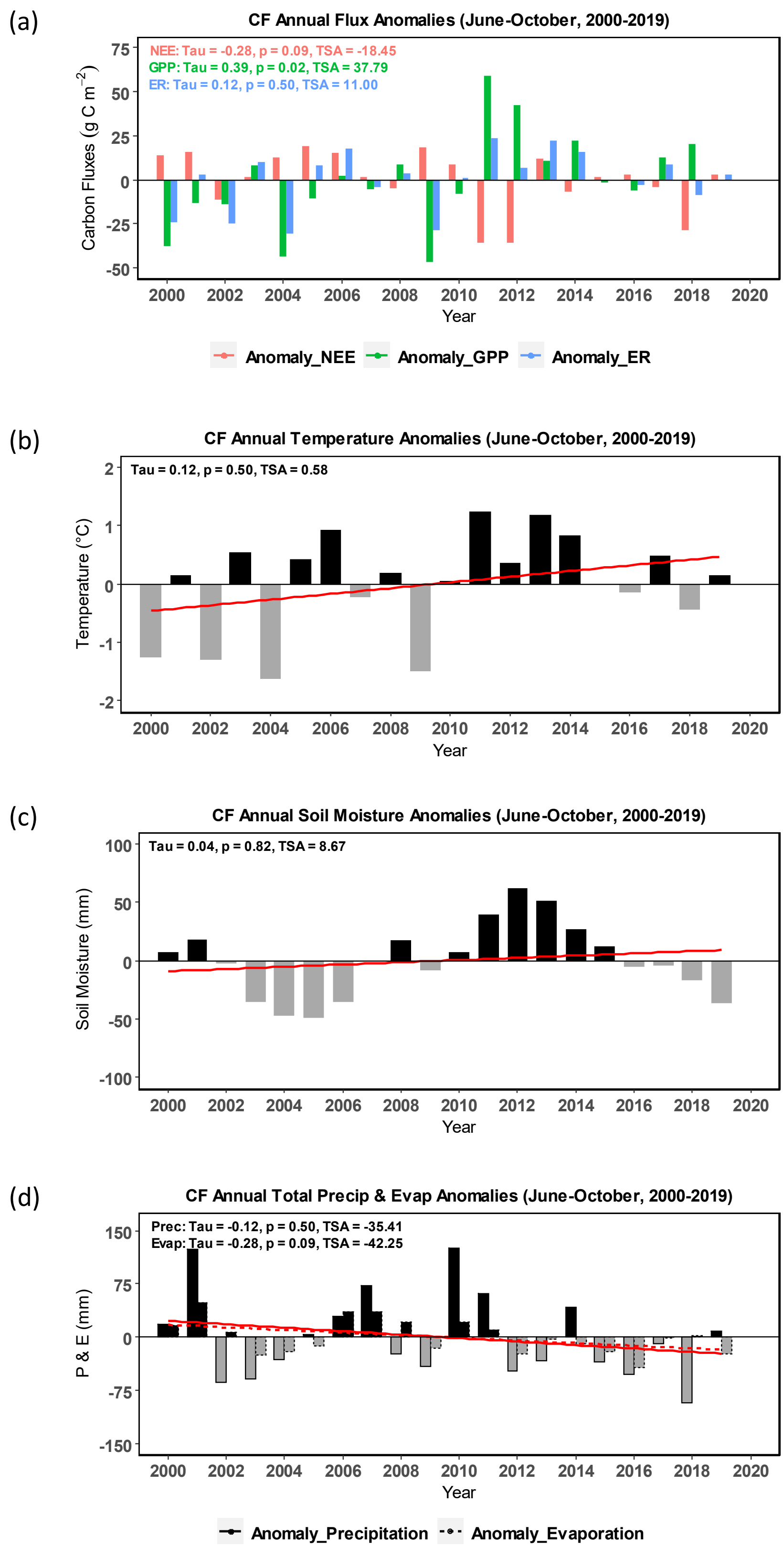

Figure 5. 11. Anomalies in annual CO_2 fluxes and climatic factors at the Churchill fen during the study period (2000–2019). (a) CO_2 fluxes, (b) Temperature, (c) Soil moisture, d) Precipitation & Evaporation.

It is important to note that the exceptionally warmer and wetter climatic conditions in 2011 and 2012 temporarily shifted the fen into a net CO_2 sink (NEE anomaly of -36 g C m^{-2}) as the gains in photosynthesis far surpassed the increase in respiration during this period. The only other year when this fen was a net sink of CO_2 was 2018, though climatic conditions and NEE carbon dynamics were quite different from those in 2011 and 2012. The strong negative NEE trend (-29 g C m^{-2}) at the fen in 2018 was associated with drier conditions and cooler temperatures. The fen received the smallest amount of precipitation in 2018, with a negative anomaly of 92 mm. However, the corresponding decrease in soil moisture was relatively modest (-17 mm), and temperatures were only about 0.4 °C cooler. The combined effect of the climatic conditions in 2018 on the fen was a substantial increase in photosynthetic uptake and a slight decrease in respiration rates (net C sink). When these climatic anomalies were reversed (highest precipitation, modest increase in soil moisture, and small warming) in 2001 and 2010, the directions of the CO_2 fluxes were also reversed (greater C losses).

Overall, the results show a significant ($p = 0.02$) positive trend in annual GPP at the Churchill fen, with an increase of approximately 38 g C m^{-2} over the 2000–2019 study period (Figure 5.11a). On the other hand, there is no significant trend in annual ER at the fen over the study period. This has given rise to an increase (C sink) in annual NEE of approximately 18 g C m^{-2} at the fen over the study period, though this trend is not significant ($p = 0.09$). However, strong significant trends were found in July for GPP (24 g C m^{-2}, $p = 0.01$), ER (8 g C m^{-2}, $p = 0.03$) and NEE (-14 g C m^{-2}, $p = 0.02$), and in August for GPP (19 g C m^{-2}, $p = 0.02$) and NEE (-17 g C m^{-2}, $p = 0.005$) at the CF site (Figure not shown).This suggests that, on balance, the anomalies in temperature and moisture conditions during the study period have had a stronger influence on peatland photosynthesis than respiration at the CF site.

At the Attawapiskat River bog in the southern part of the HBL, the VPRM estimates of the annual (June–October) CO_2 fluxes show a net carbon sink in all years during the 2000–2019 study period (Figure 5.12). Ecosystem CO_2 exchange over the bog is characterized by large interannual anomalies, particularly in the first half of the study period (Figure 5.13a). The strongest annual anomalies are found in GPP and NEE at the bog, with both showing significant increasing trends ($p = 0.02$) of about 61 g C m^{-2} and 42 g C m^{-2}, respectively, over the 2000–2019 study period. Moreover, there are significant positive anomalies in GPP in July (22 g C m^{-2}, $p = 0.001$) and August (19 g C m^{-2}, $p = 0.02$). Since there are no significant trends in ER, GPP anomalies have resulted in enhanced NEE of approximately 16 g C m^{-2} in both July ($p = 0.004$) and August ($p = 0.06$) at the bog (Figure not shown).

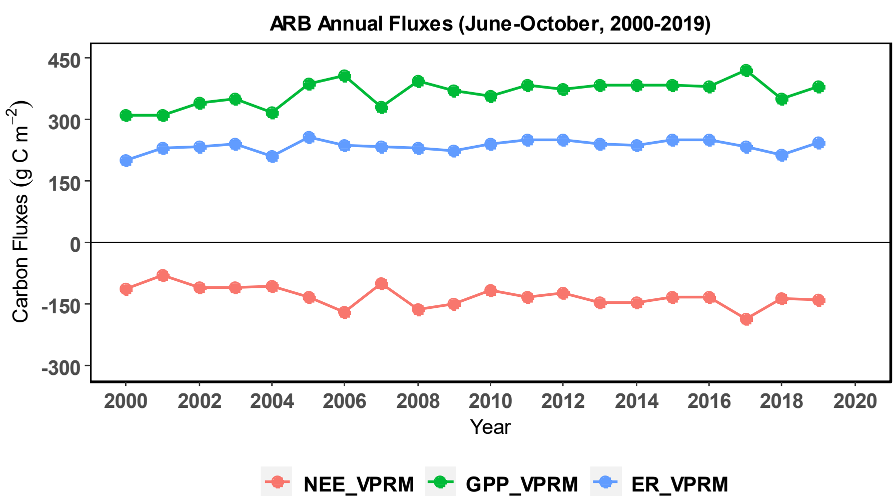

Figure 5. 12. Annual average CO_2 fluxes at the Attawapiskat River Bog during the study period (2000–2019).

It can be seen that the NEE anomalies were all positive (reduced C uptake) during the first five years at the ARB site, though the climatic trends were rather different among those years. NARR climatological analyses (Figure 5.13b-d) show that lower temperatures and precipitation (negative anomalies) prevailed from 2000–2002, and were associated with a strong decline in photosynthesis but a relatively modest decrease in respiration at ARB. The coldest year during the study period was in 2000 when temperatures dropped by about -1.8 °C, accompanied by a precipitation decrease of -77 mm at the bog site. These anomalous climatic conditions in 2000 likely resulted in a considerable reduction in both GPP (-54 g C m^{-2}) and ER (-36 g C m^{-2}), producing a net CO_2 release of around 19 g C m^{-2} from the bog. Photosynthesis was equally suppressed in 2001, possibly influenced by the strong temperature anomaly from the previous year. On the other hand, respiration had largely recovered, though still slightly lower. This massive imbalance between GPP and ER resulted in a large positive anomaly in NEE, with a reduction in carbon uptake of 51 g C m^{-2} at the bog in 2001, compared to the study period average.

Although the bog was characterized by positive NEE anomalies (lower C uptake) during the first five years (2000–2004), the climatic trends were somewhat different in 2003 and 2004. The amount of precipitation received over the bog was still unusually low in 2003, but temperatures were now warmer. This was probably responsible for the shift to a positive ER anomaly at ARB as the higher temperatures slightly enhanced respiration, though dry conditions continued to constrain plant productivity. In 2004, a strong negative temperature anomaly of around -1.3 °C (second coldest year) occurred at the bog, along with a large positive precipitation anomaly of about 97 mm (second wettest year). Despite the contrasting precipitation anomalies in 2000 and 2004, the bog displayed remarkably similar trends in GPP, ER, and NEE.

The bog temporarily shifted from predominantly positive NEE anomalies (reduced C uptake) to a negative anomaly (greater C uptake) in 2006, and again in 2008. An increase in GPP (mean anomaly of 35 g C m^{-2}) rather than changes in ER (mean anomaly of -1 g C m^{-2}) appear to have been responsible for this shift in NEE trends during those years. Since there are no major climate anomalies in 2006, the trends in NEE may be related to other non-climatic factors at the bog. The only noticeable climate anomaly at ARB in 2008 was the persistence of a very high soil moisture level, most likely due to the excessive precipitation (accompanied by limited peatland productivity) during the previous year. Indeed, the bog site was exceptionally moist in 2007 (wettest year) and similar to 2004, there was a substantial decrease in GPP which more than offset the decline in ER. The largest CO_2 sink at the ARB site occurred in 2017 when a strong positive anomaly in GPP with no detectable change in ER resulted in a NEE anomaly of -54 g C m^{-2}. It seems unlikely that a modest positive anomaly in PAR (Figure not shown) in 2017 could have had such a large influence on photosynthetic uptake at the bog.

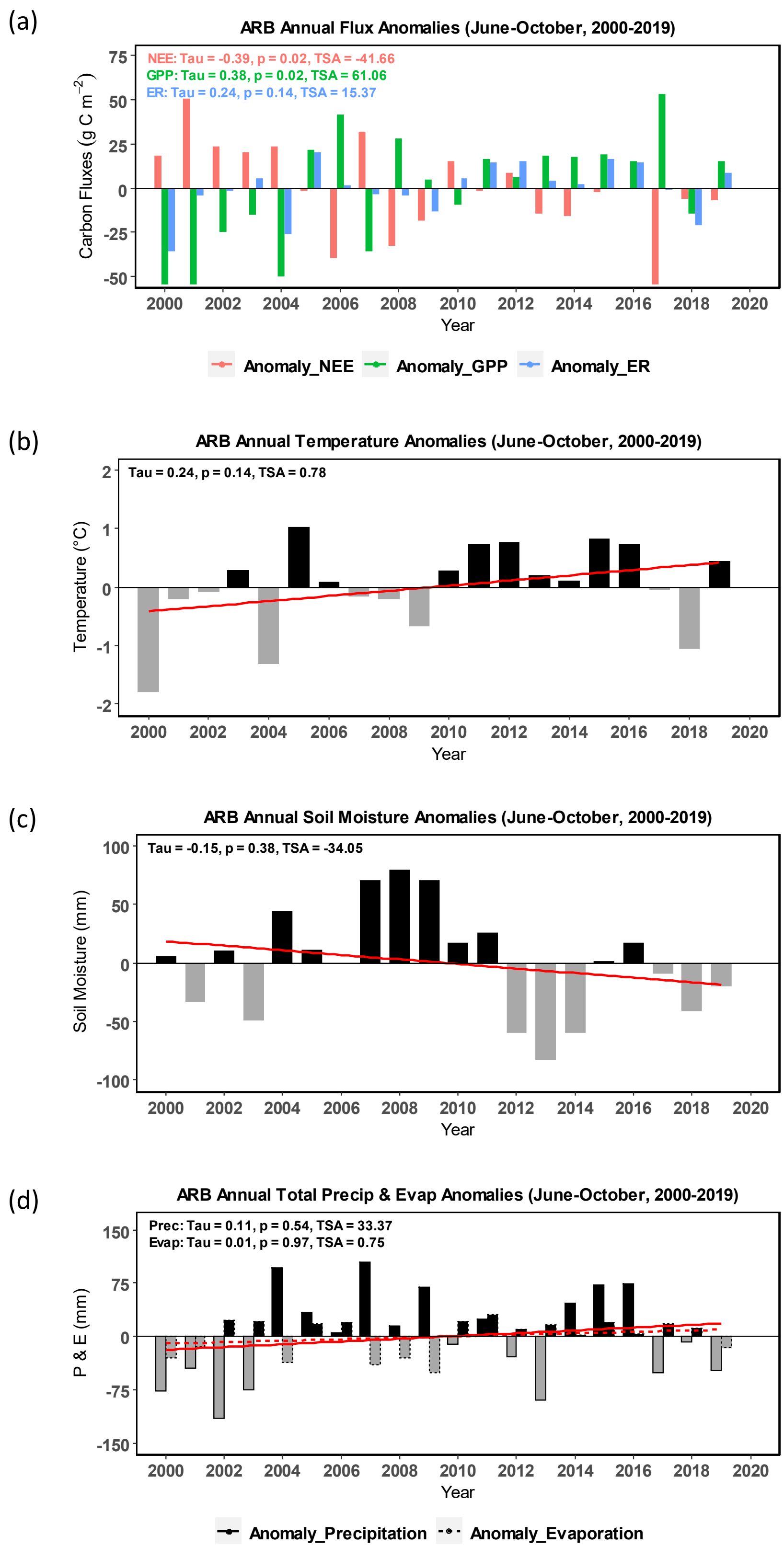

Figure 5. 13. Anomalies in annual CO_2 fluxes and climatic factors at the Attawapiskat River Bog during the study period (2000–2019). (a) CO_2 fluxes, (b) Temperature, (c) Soil moisture, d) Precipitation & Evaporation.

5.3.5 Advective Influence of the Hudson Bay on the Peatlands

Meteorological and CO_2 flux data were classified into two wind regimes based on the prevailing wind direction. Onshore winds were defined as winds blowing from the Hudson Bay while offshore winds originate from inland. It was found that the offshore winds were significantly more dominant during the study period occurring approximately 60% of the time at both CF and ARB (Figure not shown). The dominance of offshore winds persisted in all the study months except June when the occurrence of the two wind regimes was essentially equal. The results show that air temperature, PAR and VPD were considerably different between the two wind regimes at both the CF (Figure 5.14) and ARB (Figure 5.15) sites. At the Churchill fen, temperatures were significantly higher (1.2 °C, $p < 0.0001$) during offshore winds than onshore. The mean temperature from June to October was about 9.4 °C for offshore winds and 8.1 °C for onshore winds over the 2000–2019 study period (Table 5.4). The mean PAR was 353 μmol m^{-2} s^{-1} during offshore winds and 438 μmol m^{-2} s^{-1} during onshore winds, indicating that light levels were significantly lower (-85 μmol m^{-2} s^{-1}, $p < 0.0001$) during periods of offshore winds. The atmospheric demand for moisture (VPD) was significantly larger (0.15 kPa, $p < 0.0001$) during offshore winds (0.44 kPa) compared to onshore winds (0.29 kPa).

At the bog, the average temperature difference between offshore and onshore winds over the study period was much higher at around 2.7 °C ($p < 0.0001$), reaching 4.4 °C in June (Table 5.5). Here, the mean PAR was 406 μmol m^{-2} s^{-1} during offshore and 392 μmol m^{-2} s^{-1} during onshore winds. This indicates that, unlike the fen site, light levels were slightly higher (14 μmol m^{-2} s^{-1}) for offshore than onshore winds at the bog, though the difference is not statistically significant. The atmospheric vapour deficit was significantly stronger (0.13 kPa, $p < 0.0001$) during offshore winds (0.44 kPa) compared to onshore winds (0.31 kPa) at the bog. These results provide strong evidence about the advective influence of the Hudson Bay on the adjacent lowlands.

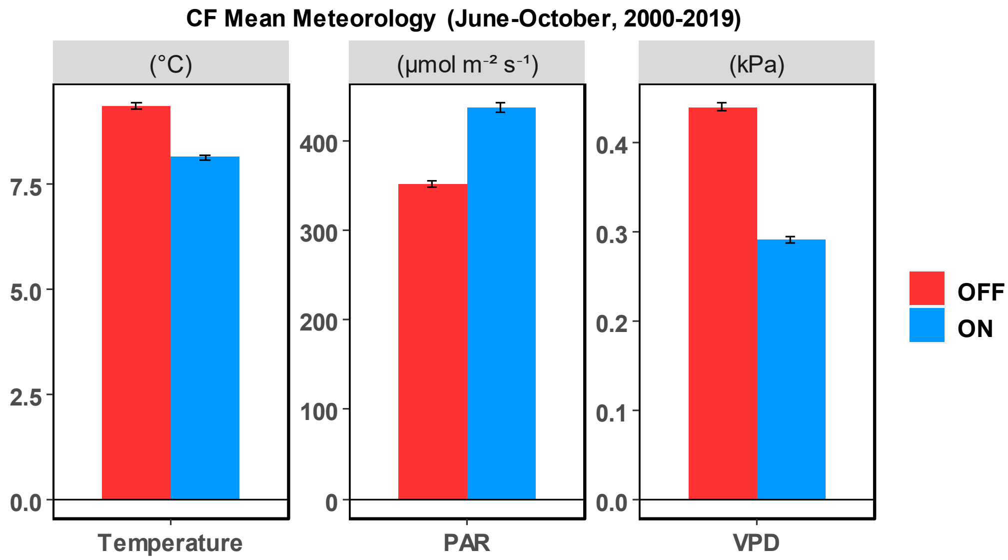

Figure 5. 14. Offshore and onshore winds environmental conditions at the Churchill fen (CF) during the study period (2000–2019).

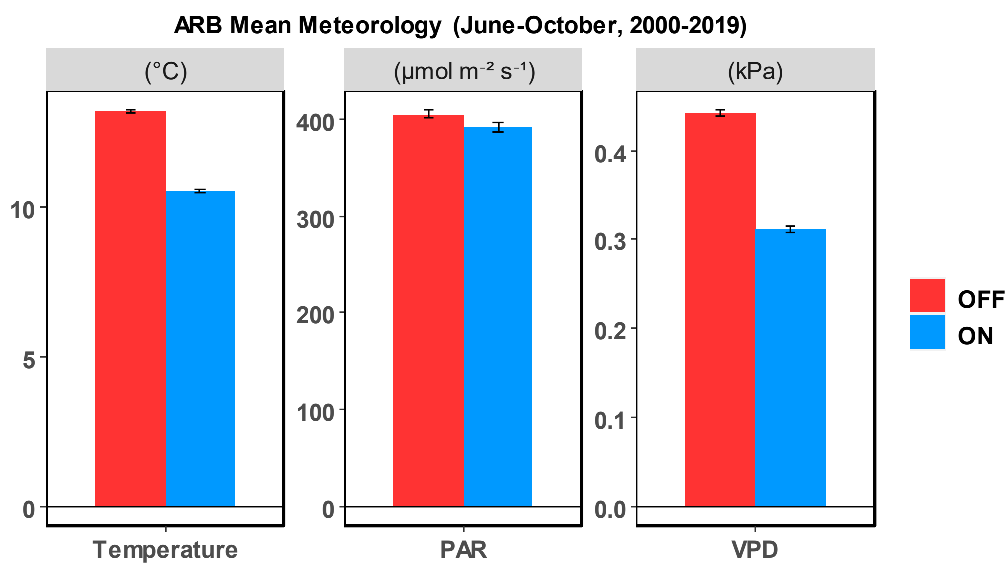

Figure 5. 15. Offshore and onshore winds environmental conditions at the Attawapiskat River Bog (ARB) during the study period (2000–2019).

Table 5. 4. Offshore and onshore winds environmental conditions and CO_2 fluxes at the Churchill fen (CF) from June to October during the study period (2000–2019).

Temperature (°C)	OFF	ON	OFF–ON	OFF/ON	p value
June	10.5	7.2	3.4	1.47	0.000
July	15.2	11.3	3.9	1.34	0.000
August	13.7	11.8	1.9	1.16	0.000
September	7.9	7.5	0.4	1.06	0.797
October	0.7	1.9	-1.1	0.40	0.000
Season	9.4	8.1	1.2	1.15	0.000
PAR (µmol m^{-2} s^{-1})					
June	508	622	-115	0.82	0.000
July	509	592	-83	0.86	0.000
August	401	427	-25	0.94	0.000
September	265	287	-22	0.92	0.000
October	144	127	17	1.13	0.846
Season	353	438	-85	0.81	0.000
VPD (kPa)					
June	0.63	0.37	0.26	1.70	0.000
July	0.73	0.43	0.30	1.71	0.000
August	0.54	0.33	0.21	1.64	0.000
September	0.28	0.17	0.11	1.64	0.000
October	0.11	0.07	0.04	1.61	0.000
Season	0.44	0.29	0.15	1.51	0.000
GPP (µmol m^{-2} s^{-1})					
June	0.80	0.73	0.07	1.10	0.077
July	1.97	1.97	0.00	1.00	0.944
August	1.98	2.07	-0.09	0.96	0.047
September	0.82	0.93	-0.11	0.88	0.000
October	0.11	0.10	0.01	1.13	0.170
Season	1.12	1.18	-0.06	0.95	0.000
ER (µmol m^{-2} s^{-1})					
June	1.49	1.09	0.40	1.37	0.000
July	2.06	1.59	0.47	1.29	0.000
August	1.88	1.65	0.23	1.14	0.000
September	1.18	1.13	0.05	1.04	0.797
October	0.32	0.46	-0.14	0.70	0.000
Season	1.35	1.20	0.15	1.12	0.000
NEE (µmol m^{-2} s^{-1})					
June	0.69	0.36	0.33	1.93	0.000
July	0.08	-0.38	0.47	-0.22	0.000
August	-0.11	-0.43	0.32	0.25	0.000
September	0.36	0.20	0.16	1.79	0.000
October	0.21	0.36	-0.15	0.59	0.000
Season	0.23	0.02	0.21	11.26	0.000

Table 5. 5. Offshore and onshore winds environmental conditions and CO_2 fluxes at the Attawapiskat River Bog (ARB) from June to October during the study period (2000–2019).

Temperature (°C)	OFF	ON	OFF–ON	OFF/ON	p value
June	15.7	11.2	4.4	1.39	0.000
July	18.5	14.6	3.9	1.27	0.000
August	16.6	13.7	2.9	1.21	0.000
September	11.7	9.1	2.6	1.29	0.000
October	4.4	3.3	1.2	1.36	0.000
Season	13.2	10.5	2.7	1.25	0.000
PAR (µmol m^{-2} s^{-1})					
June	571	522	49	1.09	0.095
July	547	500	47	1.09	0.088
August	441	427	14	1.03	0.898
September	328	275	52	1.19	0.016
October	193	165	28	1.17	0.064
Season	406	392	14	1.04	0.571
VPD (kPa)					
June	0.68	0.42	0.26	1.62	0.000
July	0.64	0.42	0.23	1.55	0.000
August	0.48	0.33	0.14	1.43	0.000
September	0.31	0.20	0.11	1.52	0.000
October	0.17	0.12	0.05	1.38	0.000
Season	0.44	0.31	0.13	1.42	0.000
GPP (µmol $m^{-}2$ $s^{-}1$)					
June	2.57	2.29	0.28	1.12	0.000
July	3.65	3.52	0.13	1.04	0.106
August	3.22	3.19	0.03	1.01	0.494
September	1.91	1.64	0.28	1.17	0.003
October	0.52	0.38	0.14	1.36	0.001
Season	2.35	2.25	0.10	1.04	0.319
ER (µmol m^{-2} s^{-1})					
June	1.92	1.37	0.55	1.40	0.000
July	2.27	1.78	0.48	1.27	0.000
August	2.04	1.68	0.36	1.22	0.000
September	1.43	1.10	0.33	1.30	0.000
October	0.52	0.38	0.15	1.39	0.000
Season	1.61	1.28	0.33	1.26	0.000
NEE (µmol m^{-2} s^{-1})					
June	-0.65	-0.92	0.27	0.70	0.000
July	-1.38	-1.74	0.36	0.80	0.000
August	-1.18	-1.51	0.33	0.78	0.000
September	-0.48	-0.53	0.05	0.91	0.029
October	0.00	-0.01	0.01	0.16	0.798
Season	-0.74	-0.97	0.23	0.76	0.000

Moreover, it was found that ecosystem carbon exchange over the peatlands was strongly regulated by the presence of the Bay (Figure 5.16 and 5.17). The seasonal productivity of the fen was slightly enhanced by about 5% ($p < 0.0001$) during onshore winds compared to offshore winds (Table 5.4). This increase in onshore GPP mainly occurred in September when it was about 13% higher than offshore GPP. The results also reveal that peatland respiration was significantly enhanced (12%, $p < 0.0001$) during offshore winds at CF over the study period. An increase in offshore ER is found in all the study months except October, and it ranges from 4% in September to 37% in June. The net impact of the wind regimes on the carbon dynamics of the fen is a significant reduction ($p < 0.0001$) in CO_2 emissions during onshore winds, with a seasonal offshore NEE of about 0.23 µmol m^{-2} s^{-1}, and onshore NEE of only 0.02 µmol m^{-2} s^{-1}, over the study period.

The advective influence of the Bay on peatland net C exchange was similar further south at ARB where the seasonal offshore NEE (-0.74 µmol m^{-2} s^{-1}) was about 24% lower ($p < 0.0001$) than the onshore NEE (-0.97 µmol m^{-2} s^{-1}) over the study period (Table 5.5). However, the offshore GPP at the bog was significantly larger ($p < 0.005$) than its onshore counterpart in June (12%), September (17%) and October (36%), although the seasonal difference was not significant. The results demonstrate that although photosynthesis was higher at the bog during offshore wind conditions, the C gains were more than offset by increased ER (22%–40%, $p < 0.0001$) during offshore winds. For the 2000–2019 study period as a whole and accounting for the wind frequency, offshore winds (onshore winds) at CF contributed about 60% (40%), 64% (36%) and 95% (5%) to the total GPP, ER and NEE, respectively. At ARB, offshore winds (onshore winds) accounted for approximately 63% (37%), 68% (32%) and 56% (44%) of the total GPP, ER and NEE, respectively.

The relative amount of PAR available during offshore and onshore wind regimes may influence their relative contributions to the net C balance over the study sites. Onshore winds occur more frequently during the day than at nighttime. Moreover, the frequency and duration of the wind regimes can be influenced by the diurnal cycle of the sea-breeze circulation which often becomes dominant by mid-afternoon in the HBL (Rouse and Bello, 1985).

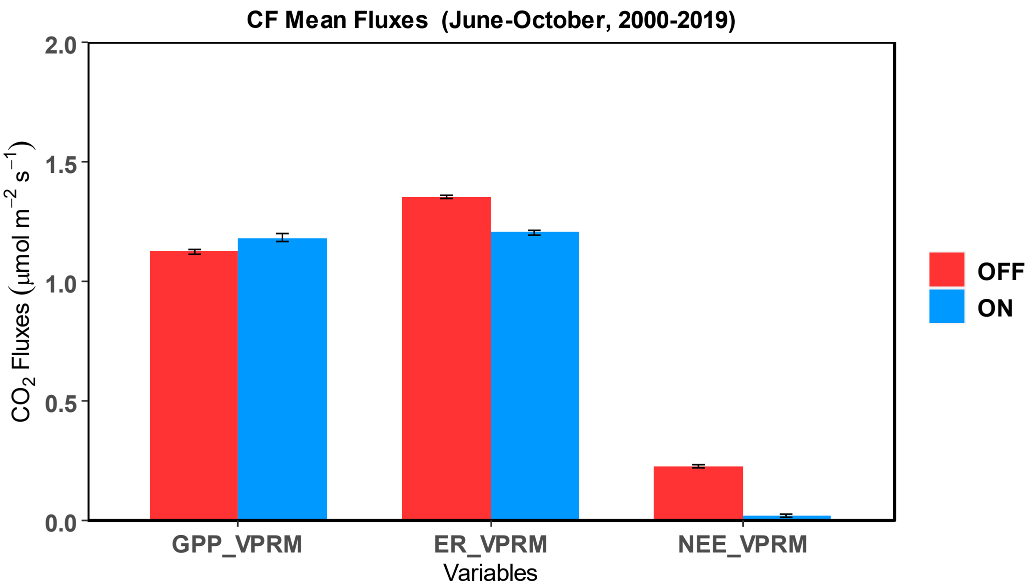

Figure 5. 16. Offshore and onshore winds CO_2 fluxes at the Churchill fen (CF) during the study period (2000–2019).

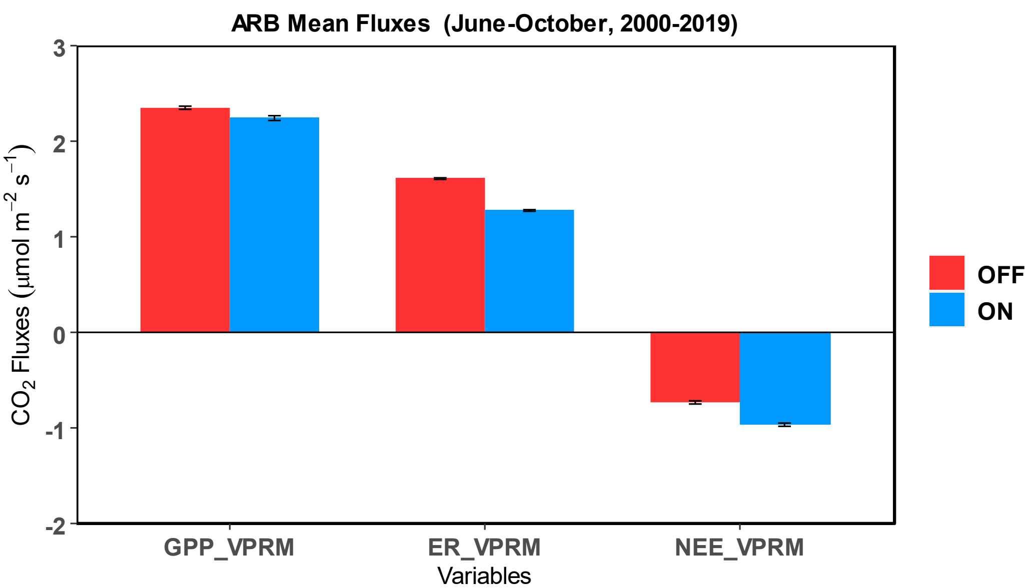

Figure 5. 17. Offshore and onshore winds CO_2 fluxes at the Attawapiskat River Bog (ARB) during the study period (2000–2019).

The higher rates of photosynthesis during onshore winds at the CF site may be due to the significantly higher light levels for onshore compared to offshore winds. When onshore and offshore GPP at the fen were normalized by PAR, it was found that the seasonal photosynthetic efficiency of the fen was greater during offshore winds compared to onshore winds, but the difference was not statistically significant (not shown). At the bog site, there is neither a significant difference in PAR nor photosynthetic efficiency between offshore and onshore wind regimes.

To examine if trends in peatland C exchange are impacted by the advective wind direction in the HBL, GPP, ER and NEE anomalies were partitioned between onshore and onshore winds. The results show that over the June–October study period, there was a significant trend ($p = 0.02$) in onshore NEE at the fen, with increased CO_2 uptake of approximately 13 g C m^{-2} (Figure 5.18) from 2000 to 2019. There was no significant trend in the offshore NEE at the fen since the increase in GPP was largely offset by higher ER. In addition, monthly analysis (not shown) indicates that a significant increase in June respiration occurred only during offshore winds (7 g C m^{-2}, $p = 0.03$), which resulted in a positive trend (decrease) in NEE (6 g C m^{-2}, $p = 0.03$) at the CF site. This trend in offshore ER in June was most likely due to a large temperature anomaly of approximately 4 °C ($p = 0.03$) only during offshore winds, which was not present at the fen in other months (not shown). There were significant and comparable trends in offshore and onshore GPP and NEE (greater C uptake) at the fen in July and August. The anomalies in offshore and onshore CO_2 exchange are markedly different over the bog site. There, the results show that there were significant trends ($p < 0.03$) in offshore GPP (54 g C m^{-2}) and NEE (30 g C m^{-2}), but no significant trends in the onshore CO_2 fluxes over the June–October study period (Figure 5.19). The increasing trends in photosynthetic C uptake at ARB during offshore winds mostly occurred in July and August (not shown). In those months, the C gains during onshore wind regimes were relatively small and marginally significant (on average, $p = 0.05$). Interestingly, neither the June warming trend nor the accelerated ER at CF was found at the ARB site.

5.3.6 Correlations Between Environmental Factors and Carbon Fluxes

It has been demonstrated that the contrasting thermal and moisture properties of the wind regimes influence the carbon balance of the peatland sites. To further examine these effects, partial correlation analysis was applied between carbon fluxes and environmental variables during offshore and onshore winds. The results show that GPP, ER and NEE showed significant correlations with daily temperatures, PAR and VPD at the CF and ARB sites over the study season (Table 5.6). The highest correlation coefficients were found between temperature and CO_2 fluxes, with increasing temperatures promoting greater GPP, ER and NEE. The relationship between VPD and GPP was negative suggesting that increases in atmospheric water demand constrained plant productivity. In contrast with temperature and VPD, the magnitude and significance of PAR appear to differ between the study sites. The carbon fluxes at the CF site showed relatively weak correlations with PAR in comparison to the ARB site. There were no noticeable differences in the correlations between CO_2 fluxes and environmental factors during offshore and onshore winds.

On an annual scale, the net (non-directional) effects of the variability in temperature, PAR, precipitation, evaporation, VPD, and soil moisture were investigated using stepwise regression analysis. The results show that the most important factors explaining the interannual variability in GPP are temperature, PAR, soil moisture and VPD ($R^2 = 0.76$, $p < 0.001$) at the fen site (Table 5.7). At the bog, the best regression model for GPP consisted of temperature, PAR, precipitation and VPD ($R^2 = 0.62$, $p < 0.005$). Temperature was excluded from the stepwise regression since VPRM stimulated ER as a linear function of temperature. A regression model comprising of precipitation and VPD explained 70% ($p < 0.001$) of the variability in ER at CF, while PAR and soil moisture had to be added to that model at ARB to capture 76% ($p < 0.001$) of the variability in ER. Overall, the best combination of environmental variables that best predicted NEE at CF was PAR, soil moisture and VPD ($R^2 = 0.40$, $p < 0.05$), while temperature, PAR, precipitation and VPD were the best predictor variables of NEE at ARB ($R^2 = 0.43$, $p = 0.06$).

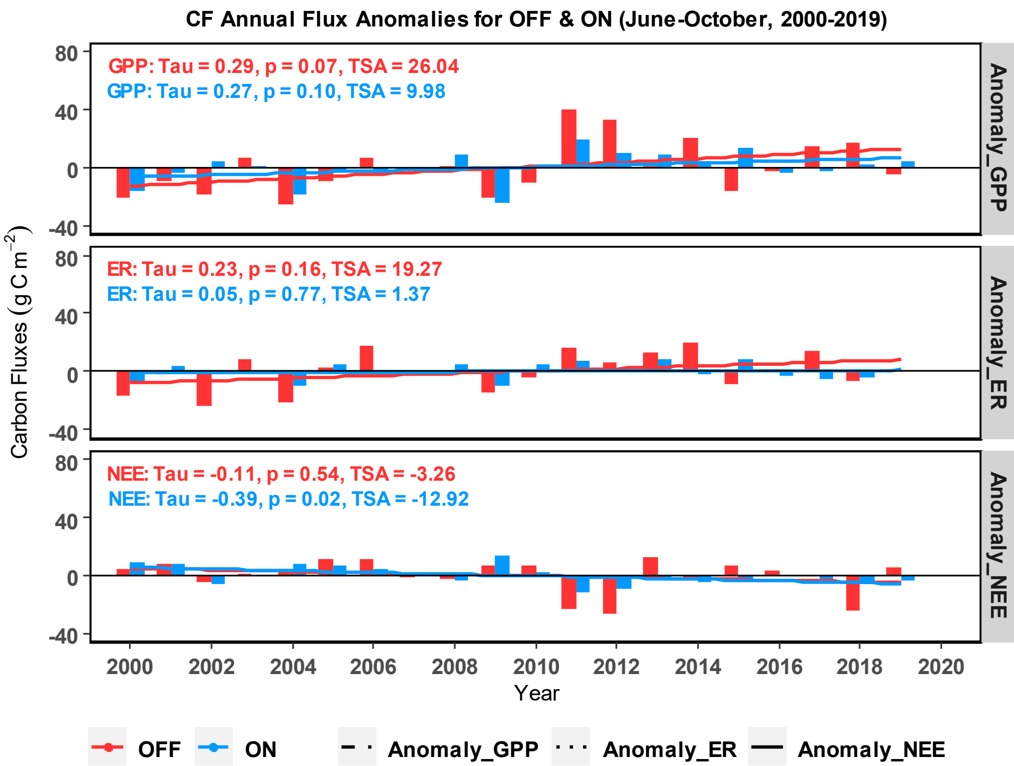

Figure 5. 18. Anomalies in annual CO_2 fluxes for offshore and onshore winds at the Churchill fen (2000–2019).

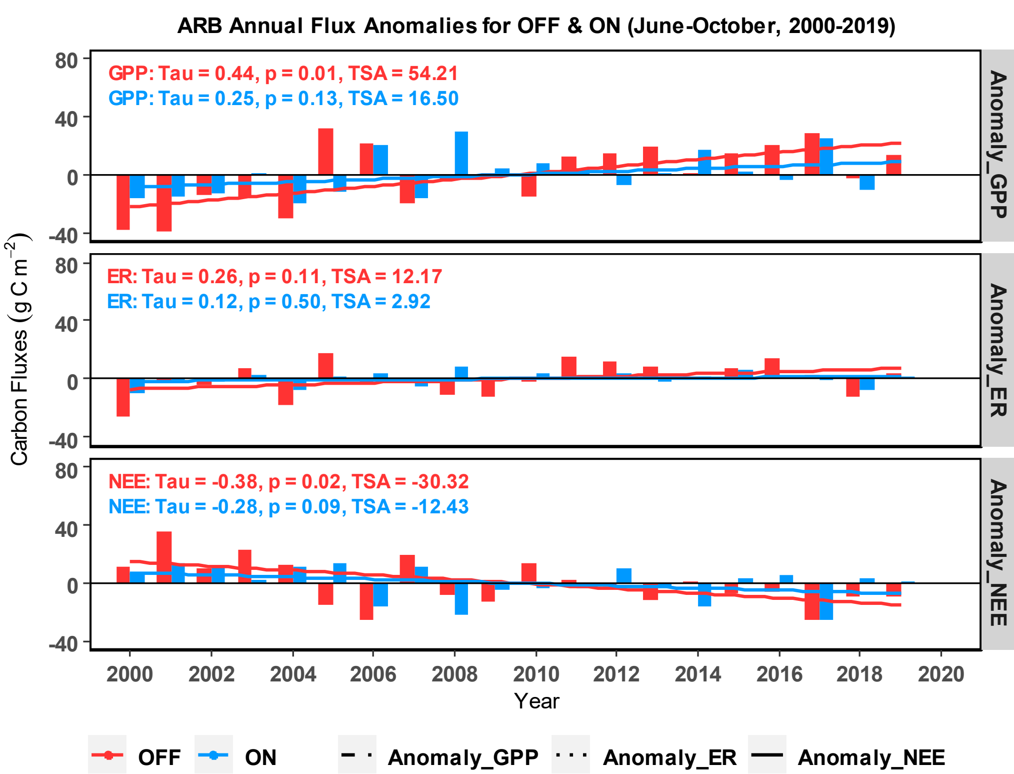

Figure 5. 19. Anomalies in annual CO_2 fluxes for offshore and onshore winds at the Attawapiskat River Bog (2000–2019).

Table 5. 6. Partial correlation coefficients between daily carbon fluxes and environmental variables for offshore and onshore winds at the Churchill Fen and Attawapiskat River Bog (June to October, 2000–2019).

CO_2 Flux	OFF			ON		
CF	Temperature	PAR	VPD	Temperature	PAR	VPD
GPP	0.91 ***	0.24 **	-0.54 ***	0.93 ***	0.21 **	-0.26 ***
ER	1.00 ***	0.02	0.55 ***	1.00 ***	-0.08	0.50 ***
NEE	-0.70 ***	-0.04	0.46 ***	-0.68 ***	0.03	0.13
ARB						
GPP	0.91 ***	0.56 ***	-0.56 ***	0.93 ***	0.60 ***	-0.50 ***
ER	1.00 ***	0.13 *	0.33 ***	1.00 ***	0.16 **	0.31 ***
NEE	-0.79 ***	-0.52 ***	0.53 ***	-0.84 ***	-0.56 ***	0.46 ***

* Significant at the 0.05 level; ** Significant at the 0.01 level; *** Significant at the 0.001 level

Table 5. 7. Stepwise regression between annual carbon fluxes and environmental factors at the Churchill Fen and Attawapiskat River Bog (June to October, 2000–2019).

CO_2 Fluxes	GPP				ER		NEE		
CF	Temperature	PAR	S. Moisture	VPD	Precipitation	VPD	PAR	S. Moisture	VPD
Coefficient	0.094	-0.004	0.002	1.477	0.001	1.517	0.004	-0.002	-1.191
p-value	0.02	0.10	0.02	0.05	0.01	0.00	0.10	0.02	0.05
R^2(p-value)	0.76 (<0.001)				0.70 (<0.001)		0.40 (<0.05)		
Adjusted R^2	0.69				0.67		0.29		

CO_2 Fluxes	GPP				ER				NEE			
ARB	Temperature	PAR	Precipitation	VPD	PAR	Precipitation	S. Moisture	VPD	Temperature	PAR	Precipitation	VPD
estimate	0.301	0.010	-0.001	-7.086	-0.002	0.001	0.001	3.556	-0.177	-0.010	0.001	7.086
p-value	0.00	0.01	0.15	0.01	0.04	0.01	0.16	0.00	0.04	0.01	0.15	0.01
R^2(p-value)	0.62 (<0.005)				0.76 (<0.001)				0.43 (0.06)			
Adjusted R^2	0.52				0.70				0.28			

5.4 Discussion

5.4.1 Contrasting Net CO_2 Exchange over Peatlands in the HBL

The HBL is a climatologically and ecologically diverse wetland region that is moderated by the Hudson Bay. The advective influence of the Hudson Bay is crucial during the growing season when the persistence of sea ice over the Bay regulates both the energy and carbon balance. In this study covering the June to October (2000–2019) period, I examine the seasonal and interannual CO_2 exchange of two diverse peatland types (eutrophic fen vs ombrogenous bog) in different parts of the HBL. The Churchill fen in the northern section of the region has relatively lower temperatures, light levels, precipitation and evaporation, but higher soil moisture conditions, compared to the Attawapiskat River bog in the south. The contrasting climatic, hydrological and vegetation characteristics of these two study sites make them ideal for investigating the long-term variations and trends in peatland NEE over the HBL.

This study found that plant productivity and ecosystem respiration were higher at ARB compared to the CF site from June to October. More importantly, the results revealed that the CF site was a net source of CO_2 to the atmosphere while ARB was a net CO_2 sink over the study period. The differences in C exchange between fens and bogs due to their contrasting water supply, nutrient availability and vegetation community has been previously reported (Rydin and Jeglum, 2006; Bauer et al., 2009). Other studies in the Churchill area of the HBL have shown that different peatland types and permafrost landforms have varied growing season CO_2 dynamics. Delidjakova et al. (2016) demonstrated that a peat plateau consistently removed CO_2 from the atmosphere over their study period. On the other hand, Nwaishi et al. (2020) found at a nearby site that peat plateaus were a steady net CO_2 source to the atmosphere, while fens acted as persistent sinks of CO_2 over the growing season. This is in contrast to the present study where the CF site was a net C source and ARB was a net CO_2 sink. The modelled NEE estimates at ARB and CF are consistent with EC tower measurements that showed an annual NEE of about –80 g C m^{-2} over a five-year period at ARB (Helbig et al., 2019), and a growing season NEE of approximately +16 g C m^{-2} in 2008 and 2010 at CF (Hanis et al. (2015). Different studies at the same Churchill fen between 1993 and 1999 (average of 67 measurement days, June–August) recorded cumulative NEE ranging from −64 to +22 g C m^{-2} (Burton et al., 1996; Schreader et al., 1998; Griffis et al., 2000; Lafleur et al., 2001). The combined probability of northern bogs and fens being net emitters of CO_2 is estimated to be approximately 30% (McLaughlin and Webster, 2014). Also, it has been demonstrated that about 14% and 23% of bogs and fens were net CO_2 sources, respectively, across boreal and subarctic peatlands (McLaughlin and Packalen, 2021).

5.4.2 Response of Peatland Net CO_2 Exchange to Climate Anomalies

It is still uncertain how the carbon dynamics of northern environments will be influenced by global warming and changes in moisture conditions. The overall stability of northern peatland net C balance will be determined by the combined long-term (decadal) sensitivity of GPP and ER to climatic changes. Warmer temperatures, earlier snowmelt and longer growing seasons may stimulate plant photosynthesis (Aurela et al., 2004; Churkina et al., 2005) and increase biomass, but such gains could be mostly offset by higher carbon losses from soil respiration (Mack et al., 2004; Dorrepaal et al., 2009). It is believed that these potential trends in the C balance of the arctic and subarctic terrestrial ecosystem will vary in different subregions and among peatland types (McLaughlin and Webster, 2014; Webster et al., 2018). In this study, I found considerable interannual variations in GPP and ER at both the fen and bog sites, with conflicting impacts on peatland NEE over the past 20 years. The trends in peatland CO_2 exchange coincide with strong climate anomalies that are associated with temperature and moisture stress.

The CF site experienced cooler conditions in some years during the first half of the study period, particularly in 2000, 2002, 2004, and 2009. The relatively cold climate inhibited both photosynthesis and respiration in all four years, with GPP displaying greater sensitivity to temperature anomalies in all but one year. The fen was, therefore, a stronger C source in 2000, 2004 and 2009 and a weaker C source in 2002. It is unlikely that the unique response of the fen to the temperature anomaly in 2002 is due to the lower precipitation received in that year, since other years (e.g. 2004, 2009) also experienced a slight decrease in precipitation. Besides, the soil water level remained high at the fen in 2002, somewhat similar to 2009. It seems a negative temperature trend was the main climatic driver of the large anomalies in GPP and ER at the fen in the first half of the study period. Also, it can be seen that at ARB negative temperature trends resulted in an overall decrease in the net C uptake of the bog, regardless of whether the lower temperatures occurred along with drier (e.g. 2000–2002) or wetter (e.g. 2004 and 2007) conditions.

These results contrast with some previous studies that suggested that a cooler climate enhanced GPP and limited ER, thus stimulating C sequestration over boreal fens (Peichl et.al., 2014). It was generally assumed that ecosystem respiration is more sensitive to temperature changes than photosynthesis and that global warming would decrease the C sink strength of northern peatlands (Ise et al., 2008; Dorrepaal et al., 2009). In contrast, this present study found that lower temperatures generally reduced the net CO_2 uptake of the fen and bog, since GPP decreased considerably more than ER. This is consistent with other research findings that demonstrated that peat core records over the last 1000 years indicate C sequestration in peatlands reduced during the Little Ice Age (LIA, 1425–1850 AD,) due to shorter, colder growing seasons and increased cloudiness (Lamarre et al., 2012; Charman et al., 2013; Garneau et al., 2014), as well as a drier climate (Zhao et al., 2014). They argued that warmer temperatures will promote longer growing seasons and increase the net C sink strength of peatland ecosystems.

In the current study, there is ample evidence that positive temperature anomalies could indeed enhance GPP much more than ER. It was found that warmer and wetter conditions over the fen in 2011 and 2012 were associated with strong negative NEE anomalies as the increase in plant productivity was considerably higher than the increase in respiration. A major precipitation event in 2010 produced about 110 mm of rain within 24 hours, raising the water table position by about 12 cm above the peat surface (Hanis et al., 2015). Initially, the flooding of the fen site abruptly decreased GPP and ER, but both fluxes later recovered. A considerably warmer temperature the following year, coupled with moderately higher-than-normal precipitation and soil moisture stimulated GPP more than ER, such that the fen briefly shifted from a net CO_2 source to sink between 2011 and 2012. Remarkably, this was the first time the fen was a net sink of CO_2 since the beginning of the study period in 2000.

Previous studies have suggested that the response of GPP to climate variability plays a more crucial role than ER in regulating the long-term C accumulation rates over peatlands (Charman et al., 2013; Charman et al., 2015). It has been shown that the fastest C accumulation rates in northern peatlands occurred during the Holocene Thermal Maximum when warmer temperatures and higher moisture accelerated net ecosystem productivity and peat C accumulation (Zhuang et al., 2020). These results suggest that future climate warming—provided it is accompanied by wetter conditions—will likely lead to increased peatland C sequestration, at least over the next several decades (Packalen et al., 2016). Under such a scenario, northern peatlands will serve as a negative feedback to climate change, though their response to warming may shift to a positive climate feedback (i.e. decreased carbon sink with warming) by the end of the 21st century (Gallego-Sala et al., 2018; Chaudhary et al., 2020). This present study shows that both the fen and bog sites in the HBL may benefit from higher temperatures and precipitation in the future, and the fen could possibly shift from a CO_2 source to sink.

On the other hand, should future climatic conditions become warmer and drier as occurred in 2005-2006 at the CF site and 2003 at ARB, these peatlands will release more CO_2 to the atmosphere. Such conditions may increase soil respiration and suppress plant productivity due to higher VPD (Aurela et al., 2007). Warming also increases permafrost thaw depth which may further accelerate organic matter decomposition and release CO_2 and CH_4 (Lund et al., 2010; Gill et al., 2017). Climate projections suggest that Arctic and Subarctic regions will likely experience increases in precipitation over the 21st century (Kirtman et a., 2013; IPCC, 2021), but higher rates of evapotranspiration due to warming may lead to the drying of peatlands (Green et al., 2019; Helbig et al., 2020).

The occurrence of strong positive precipitation anomalies during the study period (e.g. 2001 and 2010 in CF, and 2007 in ARB) coincides with positive NEE anomalies. It has been previously shown that extended flooding abruptly decreases both photosynthesis and respiration due to the sudden rise in the peatland water table (Hanis et al., 2015). The increase in net C emissions during the flood years at CF demonstrates that GPP decreased while ER increased slightly. At ARB, prolonged flooding decreased GPP and, to a lesser extent, ER. This may suggest that after the large precipitation event, soil respiration recovered rapidly as the water table receded, but photosynthesis remained low for longer periods. Larmola et al. (2004) showed that extended flooding over wetlands in eastern Finland delayed the seasonal maximum productivity by nearly 8 weeks, resulting in a decrease in the net ecosystem production. They found an increase in decomposition rates after the lowering of the water table.

Overall, the CF and ARB sites have both experienced significant increases in plant productivity over the last 20 years. There is however no significant trend in ecosystem respiration at the study sites. This indicates that the enhancement in net CO_2 uptake over the peatlands, particularly in July and August, has been primarily driven by changes in GPP and not ER. It suggests that plant productivity may be more sensitive than respiration to future climate warming in the HBL region. These research findings support the view that global warming may strengthen carbon sequestration in northern peatlands and act as a small negative feedback to climate change (Charman et al., 2013; Gallego-Sala et al., 2018). The significant trends in GPP and NEE at ARB exceed those at the CF site. We can expect therefore that the magnitude of the trends in net CO_2 exchange will vary across the HBL depending on peatland type and location. The fen site in this study could eventually become a net CO_2 sink if the current trend persists over the next decades and provided the plant community remains the same.

5.4.3 Relative Influences of Environmental Controls on Carbon Fluxes

The net C exchange in peatlands depends on the interplay of several abiotic (e.g. temperature and water table depth) and biotic factors (e.g. vegetation composition and litter quality) acting at different spatial and temporal scales (Griffis et al., 2000; Ward et al., 2013). The complex and nonlinear influences of environmental variables give rise to considerable interannual variability in peatland CO_2 exchange (Bubier et al., 2003; Lafleur et al., 2003). In this study, the relationships between environmental factors and GPP, ER and NEE variability were examined using stepwise regression. Additionally, the unique influences of the environmental controls on the variability in peatland carbon exchange were quantified by computing the relative importance of each of the predictors in the linear regression model. The results demonstrate that soil moisture, VPD, and PAR were the most important environmental factors controlling annual net CO_2 exchange at the fen, accounting for 54%, 34%, and 13%, respectively, of the total explained variability ($R^2 = 0.40$) (Table 5.7 and Figure 5.20). At the bog, PAR, VPD, temperature and, to a less extent, precipitation captured about 52%, 27%, 15%, and 6%, respectively, of the total explained variability ($R^2 = 0.43$) in annual NEE (Table 5.7 and Figure 5.21). This suggests that the environmental factors considered here explained approximately 40% of the interannual variability in net CO_2 exchange in the peatlands.

Previous studies have shown that temperature, PAR, precipitation and soil moisture are critical factors controlling wetland photosynthesis and respiration during the growing season, though their overall effects on peatland C balance have varied among studies (Flanagan and Syed, 2011; Hao et al., 2011; Zhu et al., 2020). It has been previously reported that fens and bogs may respond differently to environmental stresses due to their distinctive vegetation and hydrologic characteristics (Bridgham et al., 2008; Wu and Roulet, 2014). Hao et al. (2011) found that precipitation and temperature were the most important controls on ecosystem CO_2 cycling in wetlands of southwest China. Lafleur et al. (2003) suggested that water table position was the dominant factor determining the interannual variations in NEE during the growing season at an ombrotrophic bog near Ottawa, Canada.

Using a multiple linear regression model at this same ARB site, Helbig et al. (2019) showed that temperature, soil moisture, and PAR explained as much as 60% of the variability in NEE between 2011 and 2015. They indicated that temperature alone accounted for about 40% of the NEE variation, particularly around the peak growing season. In this present study, PAR accounted for the majority (52%) of the explained variability in NEE at ARB between 2000 and 2019, with temperature accounting for only 15% of the total variance. Also, the contrasting importance of soil moisture and precipitation at CF and ARB underscores the different moisture dynamics of peatland types. Bogs are raised and depend on precipitation for water and nutrient supply. On the other hand, groundwater-connected fens are relatively rich in nutrients in comparison to ombrogenous bogs. The results of this study show that soil moisture strongly influenced GPP and NEE at the CF site, explaining up to 54% of the annual variability. In contrast, soil moisture does not appear to be an important determinant of the interannual variation in GPP and NEE at the ARB site, where precipitation has a small but noticeable influence. *Sphagnum* moss is a dominant vegetation type in bogs and it plays an important role in peat sequestration (Beilman et al., 2009; Loisel et al., 2014; Packalen et al., 2016). As a non-vascular plant, *Sphagnum* is heavily dependent on regular moisture supply to avoid dehydration, and their productivity has been shown to be adversely affected by a lower water table (McNeil and Waddington, 2003; Tuittila et al., 2004; Strack et al., 2009). Nevertheless, it has been previously demonstrated that *Sphagnum* is actually more influenced by lack of precipitation than a low water table position since small or periodic rain events can be captured by the moss surface without contributing to the water table level. (Robroeck et al., 2009; Strack and Price, 2009). This is in agreement with the results at the ARB site that suggests precipitation was relatively more important than soil moisture in controlling interannual variations in net CO_2 exchange.

The results of this study demonstrate that climatic factors explained about 40% of the interannual variability in the net CO_2 exchange over peatlands of the HBL, and therefore other non-climatic factors must be responsible for the unexplained variance. Armstrong et al. (2015) argued that biotic factors also played a vital role in driving C fluxes in northern peatlands. They demonstrated that interactions between and within biotic and abiotic controls—including PFT biomass, peat temperature and nutrient content—explained a significant percentage of variation in C exchange. The presence of specific plant functional traits in boreal forests and tundra has been shown to strongly regulate photosynthetic and decomposition rates in these ecosystems (Nilsson and Wardle 2005; De Deyn et al., 2008).

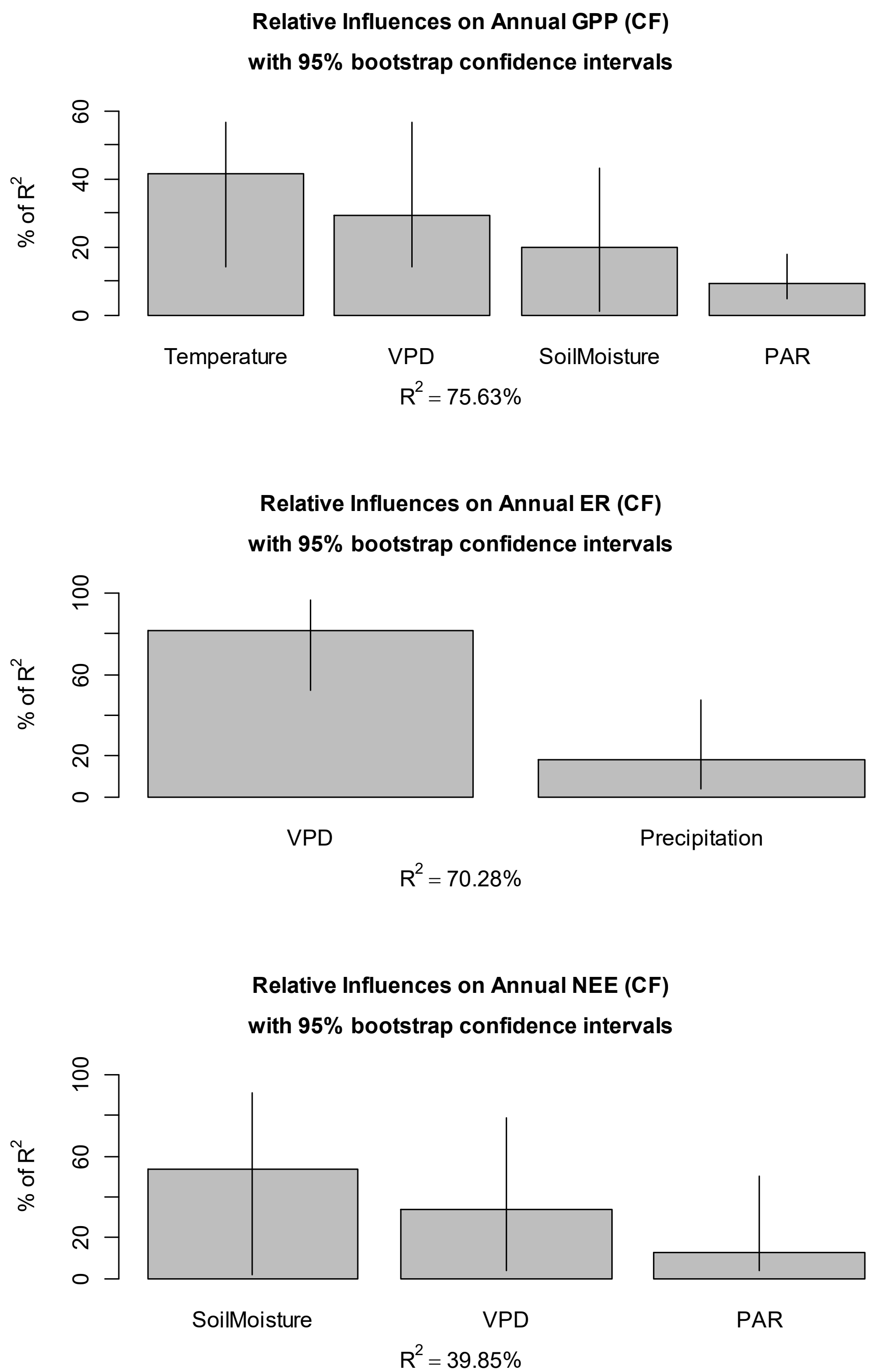

Figure 5. 20. Relative importance of environmental predictors in the regression model for Churchill fen (2000–2019).

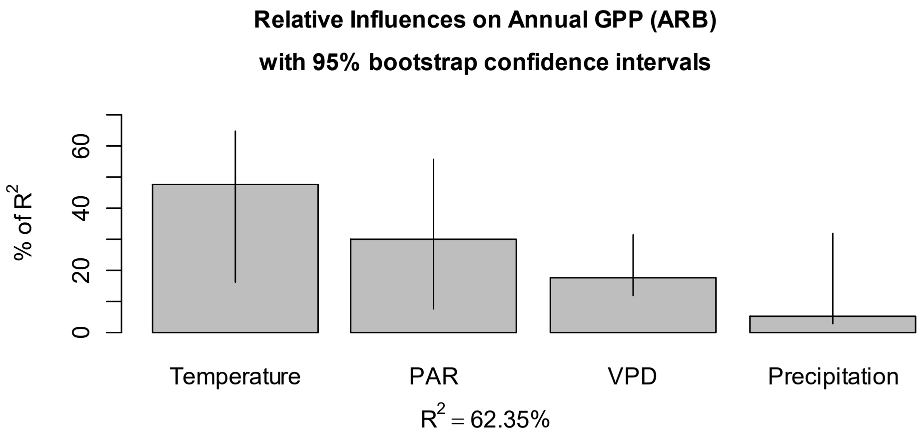

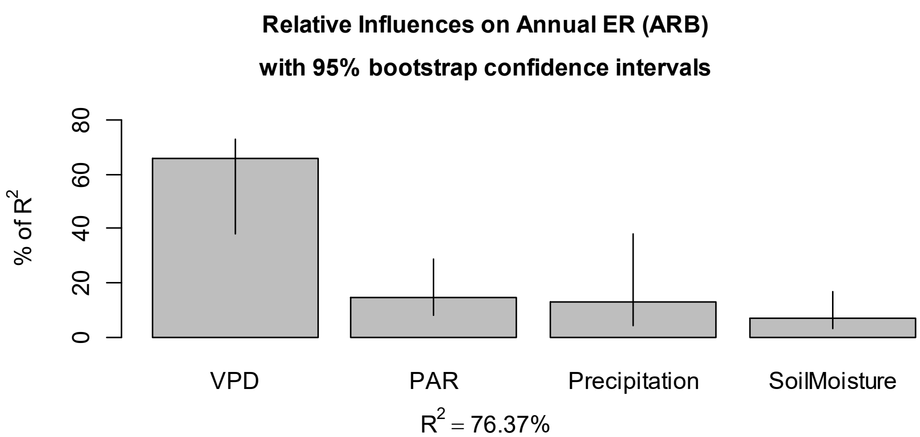

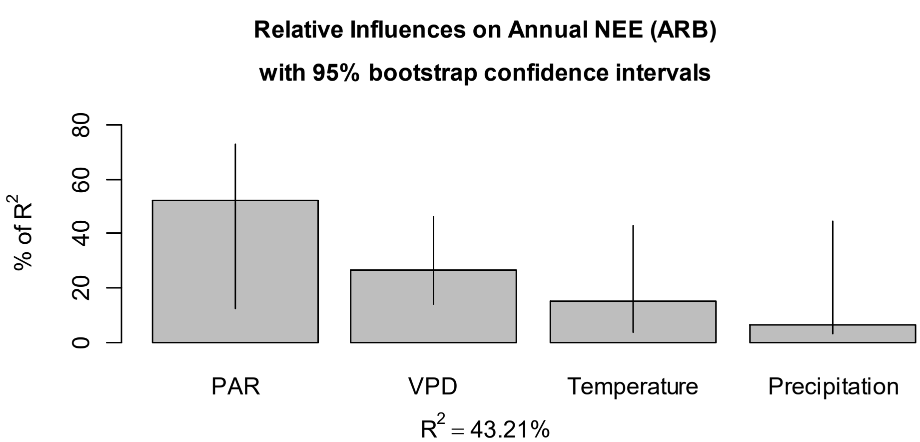

Figure 5. 21. Relative importance of environmental predictors in the regression model for Attawapiskat River Bog (2000–2019).

5.4.4 Enhanced Net CO_2 Uptake During Onshore Wind Conditions

The diurnal cycle of GPP, ER and NEE is primarily regulated by the diurnal variation in temperature, PAR and VPD. In general, photosynthesis and respiration increase with higher temperatures and light levels, until optimum conditions are exceeded (Yamori et al., 2014). Photosynthetic rates are also constrained by increasing VPD as the stomata close to reduce moisture loss by transpiration (Lin et al., 2012; Bonan, 2015). The offshore and onshore CO_2 fluxes at the study sites display comparable functional relationships with environmental controls, though some key features are noteworthy. Onshore GPP over the study sites were higher than offshore GPP at any given temperature since onshore PAR was higher for the same temperature (Figure 5.22 and Figure 5.23). In contrast, the light-response curve indicates that at a given PAR, offshore GPP was similar even though the offshore temperature was higher for the same PAR. This suggests that the lower (higher) temperatures during onshore (offshore) winds do not appear to limit (enhance) photosynthetic rates at the fen.

The response of offshore and onshore NEE to temperature and PAR are analogous to those of GPP. The results show good congruence with a previous study which suggested that the environmental control on ER played a more important role in NEE differences between onshore and offshore winds (Delidjakova et al. (2016). The effect of VPD on GPP is evident, particularly during offshore winds (which have greater VPD), as photosynthesis begins to level off somewhat at relatively high VPD. This suggests that climate warming-induced increases in VPD may constrain GPP and offset the enhanced C gains from higher temperatures and the CO_2 fertilization effect. (Novick et al., 2016; Yuan et al., 2019; Helbig et al., 2020). This will exert a strong upper limit on northern peatlands to act as carbon sinks.

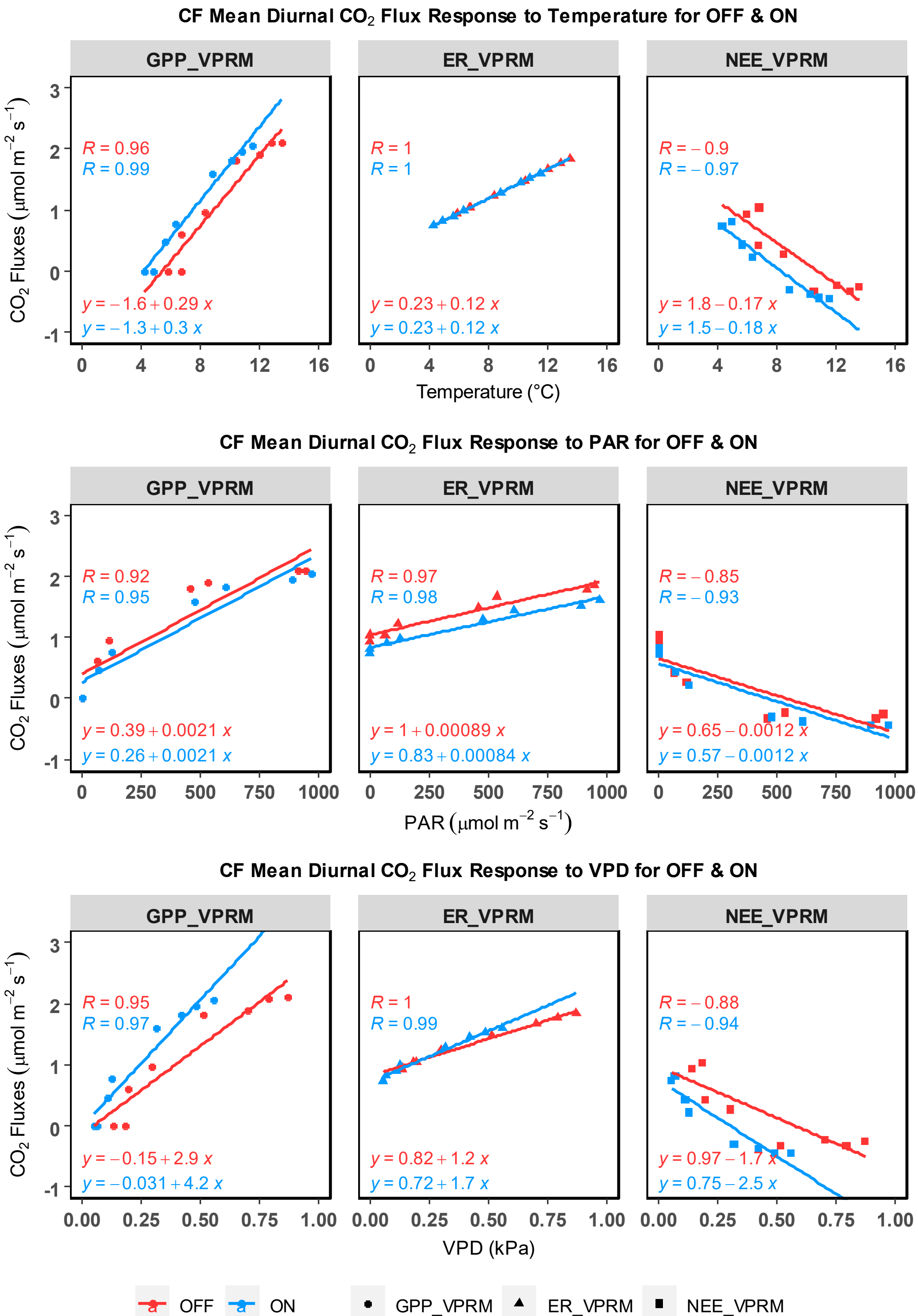

Figure 5. 22. Relationships between environmental controls and CO_2 fluxes during offshore and onshore winds at the Churchill fen (CF) during the study period (2000–2019).

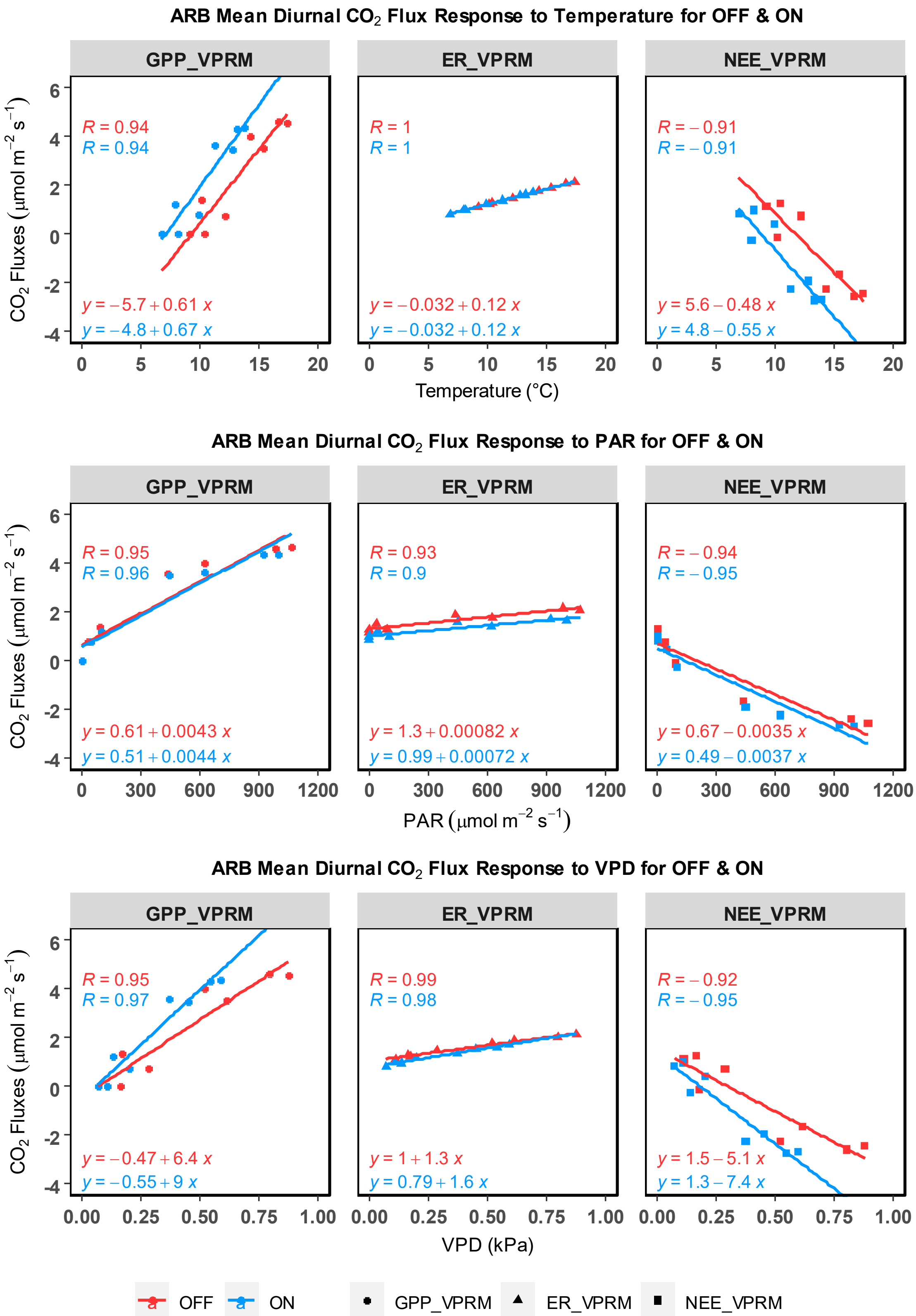

Figure 5. 23. Relationships between environmental controls and CO_2 fluxes during offshore and onshore winds at the Attawapiskat River Bog (ARB) during the study period (2000–2019).

Climate change has been disproportionately greater in the Arctic and Subarctic regions as a result of polar amplification, which is dominated by surface-albedo feedback and other local forcings (Serreze and Simmonds, 2010; Taylor et al., 2013; Stuecker et al., 2018). The annual mean temperatures in northern environments have risen at over twice the global average rate (Screen and Simmonds, 2010; Cowtan and Way, 2013; Richter-Menge et al., 2019), and there is strong evidence that the region will continue to undergo the fastest-warming throughout the 21st century (IPCC, 2021). In the HBL, climate change could be further amplified by changes in the sea-ice dynamics and energy budget of the Hudson Bay (Hochheim and Barber, 2014; Bello and Higuchi, 2019). This present study demonstrates that the Hudson Bay exerts a strong advective influence on the carbon dynamics of the adjacent lowlands due to the contrasting temperature and moisture properties between offshore and onshore winds.

The results show that the offshore winds were significantly more dominant (60%) than the onshore winds over the peatland sites during the 2000–2019 study period. The offshore winds were significantly warmer and drier than the onshore winds at both CF and ARB. This is consistent with other research findings that have examined the advective role of Hudson Bay on the surface energy balance in HBL (Rouse and Bello, 1985; Lafleur and Rouse, 1988; Delidjakova et al., 2016). A previous study revealed that the climatic changes over the Hudson Bay have caused significant trends in the mesoscale wind regimes and the advective role of the Bay on the HBL surface energy balance over the last 40 years (Chapter 2). It was found that the frequency of onshore winds has increased by about 7% between 1979 and 2018, with the largest increase of 17% occurring in June. This has resulted in a shift from offshore to onshore winds dominance in June over the HBL region. Also, it was shown that the temperatures during offshore winds have risen faster than onshore temperatures, with the most rapid increase occurring in June and September. Here, no significant trends were found in the wind frequency over the last 20 years (not shown), though it is striking that the onshore and offshore winds have roughly equal contributions in June.

The advective influence of the Hudson Bay on the adjacent peatlands is evident in the differences in net C exchange between offshore and onshore winds. The results show that photosynthetic rates were slightly higher during onshore winds than offshore winds only at the CF site. Conversely, ecosystem respiration was significantly greater during offshore than onshore winds at both CF and ARB. This suggests that the most important determinant of the differences in NEE between offshore and onshore wind regimes was respiration and not photosynthesis. The net advective effect of the Hudson Bay on the C dynamics over the fen (a net C source) was a significant reduction in CO_2 emissions at the fen due to the onshore winds. Since the bog is a net C sink, the overall impact of the onshore winds has been to significantly strengthen CO_2 removal from the atmosphere. Delidjakova et al. (2016) found similar advective effects on the net C balance at a peat plateau near Churchill, Manitoba during the 2007 growing season. They also showed that there was no significant difference between the seasonal offshore and onshore GPP, but the photosynthetic efficiency (GPP/PAR) was significantly higher during offshore winds. While this present study also found no significant difference in GPP between the two wind regimes at ARB, this was not the case at the CF site where onshore GPP was higher. I found no statistically significant differences in photosynthetic efficiency between offshore and onshore winds at both CF and ARB. However, the photosynthetic efficiency of ARB was greater than CF due to the more favourable temperature conditions in southern HBL.

5.5 Conclusion

5.5.1 Implications for Climate Change

The net C sinks of northern peatlands may be strengthened, diminished or unchanged in response to future global warming. The potential outcome would depend on the net impact of climatic changes on photosynthesis and respiration; basically, the question on our minds is: "Will photosynthesis (continue to) increase more than respiration?". This study shows that under recent climate warming in the HBL region, GPP has significantly increased more than ER, and therefore, resulted in a strengthening of the net C sink of the peatlands over the last 20 years. Whether this NEE trend continues in the future remains an uncertainty that requires further research.

For researchers in the HBL region, another question that frequently arises is: "What will be the impact of sea-ice changes in the Hudson Bay and shifts in wind regimes on peatland C sequestration?". It was previously believed that the HBL will undergo a shift towards an increased frequency of offshore winds, which would be associated with a weakened C sink in peatlands (Rouse and Bello, 1985; Delidjakova et al., 2016). This is because GPP is similar during offshore and onshore winds, but ER is much higher for offshore winds. However, it has been demonstrated that there has been an increase in the frequency of onshore winds across the HBL over the past forty years and a shift towards onshore dominance in June (Chapter 2 and 3). In this present study, the trends in CO_2 fluxes at the fen—which has traditionally been a net C source—show that increased C gains during offshore winds were largely offset by increased C losses from ER, resulting in no significant changes in NEE over the past 20 years. In contrast, the increase in onshore GPP is accompanied by a much smaller increase in ER, resulting in a significant reduction in net C losses from the fen. At the bog site—which has always been a net

C sink—the trends in CO_2 fluxes show that increased C gains during offshore winds far exceed increased C losses from ER, resulting in a significant enhancement in the net C sink over the past 20 years. Similar trends are found for the onshore winds, though the magnitude and significance are much lower.

The overall implication is that peatlands in the HBL that are traditionally CO_2 sinks will become stronger sequesters of carbon under future climate warming. Additionally, peatlands which are currently CO_2 sources will release less carbon into the atmosphere in the future and will benefit more from the increased frequency of onshore winds in the HBL, assuming current ice conditions on Hudson Bay persist. It should also be noted the both the CF site and ARB site are situated in locations with larger changes in the surface energy budget. The long-term impact of future climate change on peatlands is likely to be more complicated. Indeed, the fate of northern ecosystems in response to global warming will depend on changes in plant community composition (Breeuwer et al., 2009; Turetsky et al., 2012; Dieleman et al., 2015), nutrient availability (Heijmans et al., 2008; Melillo et al., 2011; Fan et al., 2013), permafrost thaw (Payette et al., 2004; Camill, 2005) and methane emissions (Cooper et al., 2017; Jones et al., 2017). There is a need for further research to understand the combined effects of the wide variety of changes on the net carbon balance in peatlands of the HBL.

Chapter 6

Conclusions

6.1 Summary

The Hudson Bay Lowlands (HBL) is the largest peatland region in Canada and the second largest in the world. The accumulation of a globally significant frozen peat C pool in the HBL is partly due to the chilling influence of the Hudson Bay. While the long-term fate of northern peatlands, in general, will depend on global warming and regional Arctic amplification, the peatlands of the HBL will also be uniquely influenced by climate change in the Hudson Bay. Prior to this research study, we had a very limited understanding of the long-term changes in the HBL surface energy balance and net ecosystem exchange in response to climatic trends on the Bay. Indeed, many previous studies were constrained by short-term field observations over a few growing seasons at a single site, which was insufficient to provide a clear and thorough analysis of climatic changes in the HBL.

To overcome these challenges, I use a combined model and assimilated climate dataset (NARR) to study the mesoscale wind and temperature changes in the entire HBL and their impacts on the surface energy balance over the past 40 years. Additionally, I employ a satellite data-driven light-use efficiency model (MODIS, OCO-2, VPRM), calibrated and validated with EC tower observations at two distinct peatland types to investigate the response of GPP, ER and

NEE to climatic changes between 2000 and 2019. The central aim of this research work was to improve our understanding of the long-term warming-induced changes in the surface energy balance and net CO_2 exchange over peatlands of the HBL, and how they have been influenced by climate change in the Hudson Bay.

The first step in achieving the central research aim was to investigate if there have been changes in the advective influence of the Bay on the adjacent lowlands. I found that both the offshore and onshore wind temperatures have increased significantly, but more importantly, the offshore winds were warming at a faster rate than the onshore winds. The differential rate of warming between the two wind regimes produced significant changes in the advective role of the Hudson Bay which has been superimposed on global warming. The study results indicate that the higher trends in the offshore temperatures have strengthened the horizontal temperature and pressure gradients between the HBL and the Bay and therefore increased the frequency and strength of onshore winds. In June, the rapid warming and strong land–sea surface warming contrast (1 °C), combined with the highest mean temperature difference between offshore and onshore winds (5.1 °C) has resulted in the largest and most significant upward trend in onshore wind frequency (17.4%) over the study period. Further evidence of the linkage between climate change in the Hudson Bay and the adjacent HBL was found in June and September. These transition months during the study period have experienced the most rapid increase in temperatures which is consistent with trends towards earlier sea ice breakup and later freeze-up on the Bay.

The next step was to examine the spatial variations in the climatic changes over the HBL. I found significant spatial heterogeneity across the region, with several prominent hotspots mostly along the coast and at the mouths of rivers such as Churchill, Severn and Winisk, as well as in an extensive narrow belt along the Ekwan and Attawapiskat Rivers in southern HBL. These locations coincide with areas with severe ice loss and enhanced energy budget over the Hudson Bay. The disproportionately larger warming at the mouths of rivers is due to an earlier onset of upstream discharge and accelerated river ice breakup during the spring period. Furthermore, it was shown that the advective influence of the Bay has extended further inland, suggesting that a broader area of the HBL is now being regulated by the comparatively cool and wet onshore winds. These climatic changes have produced significant positive trends in sensible heat, evaporation and ground warming that are markedly different between offshore and onshore winds.

Having established the trends in the temperatures and surface energy balance over the HBL and their linkage with the changing advective influence of the Bay, I proceeded to investigate the long-term response of peatland C exchange in the HBL to changes in both the global climate and the moderating influence of the Hudson Bay. First, I evaluated different parametrization methods and modelling approaches to find the most suitable LUE model version to estimate NEE at the peatland sites. It was found that overall the site-optimized, SIF-driven VPRM produced the most reliable estimates of NEE in the HBL. Accordingly, VPRM was run over a 20-year period using the most reliable model version and best available input datasets.

I found contrasting net CO_2 exchange in the peatland sites, with the Churchill fen acting as a net C source to the atmosphere and the Attawapiskat River bog serving as a consistent net C sink. This underscores the differences in carbon dynamics among diverse peatlands types in the HBL. It was revealed that large anomalies in GPP and ER were associated with strong trends in temperature and moisture over the study period. To my surprise, I found evidence that a warmer and wetter climate enhanced GPP much more than ER, while cooler temperatures weakened the peatland net C sink irrespective of the moisture conditions. These results were in agreement with some previous studies but in contrast to others.

Also, it was shown that the Hudson Bay had a more pronounced advective influence on peatland ER than GPP, with onshore winds having lower ER rates and thus greater net C uptake. Under recent climate warming at the fen, the increasing trend in offshore GPP was largely offset by increased offshore ER, resulting in no significant changes in NEE over the past 20 years. On the other hand, the increasing trend in onshore GPP was accompanied by a considerably smaller increase in onshore ER, resulting in a significant decrease in net C losses from the fen. This suggests that the recent changes in the moderating effect of the Hudson Bay as evident in the increased frequency and strength of onshore winds will favour the Churchill fen. At the Attawapiskat River, climate warming has resulted in an increase in C uptake by plants that far exceed the increase in C losses from ER during both offshore and onshore winds. This has resulted in a significant enhancement in the net C sink over the study period, with a greater magnitude during offshore winds compared to onshore winds.

This research work provides a unique contribution to the limited literature on the warming-induced changes in the advective influence of the Hudson Bay and its relationship with the changes in the surface energy and carbon balance in the HBL. The spatio-temporal analyses of the climate warming signals during offshore and onshore winds in the region delivers the most comprehensive research findings on the topic to date. The peatland-optimized VPRM parameters for the HBL can be used by fellow researchers working at other study sites where EC tower observations are unavailable for model calibration and validation.

6.2 Future Directions

The present research study demonstrated that satellite data-driven LUE models such as VPRM can serve as a valuable tool for studying the long-term net CO_2 exchange in peatland sites. The relatively simple structure of the VPRM and its ability to integrate satellite information and adequately resolve the environmental constraints on photosynthesis makes it robust to inter-site and inter-annual variations in model parameter values. Therefore, VPRM can be applied to the entire HBL using the optimized parameter values from the Churchill and Attawapiskat River peatlands. These study sites are located in distinct parts (northern and southern) of the HBL and represent the two main peatland types (fen vs bog) in the region, with contrasting carbon dynamics (source vs sink). Moreover, Churchill and Attawapiskat were revealed as prominent hotspots in the study region during the spatial analysis of the wind and temperature changes in Chapter 3. Coincidentally, the current network of AmeriFlux EC tower sites only includes the Churchill and Attawapiskat River peatland sites. This makes the study sites ideal for examining the changes in the carbon balance of the HBL under climate warming. Nevertheless, it will be important to extend the study in Chapter 5 to the entire HBL region and investigate the spatial variations in the response of peatland C exchange to both global warming and changes in the advective influence of the Hudson Bay.

There is likely to be an opportunity in the future for me to apply a process-based model such as CLASSIC to the entire HBL region to further improve our understanding of the long-term changes in peatland carbon balance. CLASSIC model outputs specifically optimized for the peatlands of the HBL are currently unavailable and was therefore not included in this research study. It will be valuable in the near future to compare the VPRM estimates of NEE for the entire

HBL region with those of CLASSIC since the two models have contrasting structural complexity and computational requirements.

In addition, my previous experience with the Stochastic Time-Inverted Lagrangian Transport (STILT) model and past collaboration with Environment and Climate Change Canada, may provide an opportunity in the future to work on identifying anthropogenic sources of CO_2 across Canada using biospheric flux estimates from VPRM.

During this research study, a lot of work went into developing extensive R scripts with several thousand lines of code to automate the extraction of model input data and reproduce temporal and spatial data analyses of climate, surface energy and carbon fluxes in the HBL. The original Hilton's VPRM package in R was also improved with the newly modified SIF approach. I will be making my R scripts and documentation, along with the NARR and VPRM output datasets (hereafter, HBL R collection) from this research study available to other researchers. More importantly, the HBL R collection will be made available to upper-level undergraduate and graduate students who are either interested in learning R in general or are working on research in the HBL. Since my future goal is to pursue an academic career in university teaching and research, I will use these resources to teach upper-level courses to facilitate student learning and engagement, as well as promote student interest in scientific research in general and HBL research in particular. Upon publication of the manuscripts, the HBL R collection will be made available via www.hblresearch.science and www.hblresearch.com, and may also be put on GitHub later as a complete R package. Future work may also be undertaken to develop web and mobile applications with interactive activities and tools for teaching and research in the HBL region.

References

Akumu, C. E., & McLaughlin, J. W. (2014). Modeling peatland carbon stock in a delineated portion of the Nayshkootayaow river watershed in Far North, Ontario using an integrated GIS and remote sensing approach. *Catena*, *121*, 297-306.

AMEC (2004). Environment and Infrastructure 2004 Environmental Baseline Study, Victor Diamond Project, Section 5.3.6.2. https://www.ceaa.gc.ca/80C30413-docs/report_e.pdf

Arctic Monitoring, Assessment Programme, ACIA-Arctic Climate Impact Assessment, Program for the Conservation of Arctic Flora, & International Arctic Science Committee. (2005). Arctic Climate Impact Assessment-Scientific Report. Cambridge University Press.

Ardia, D., Boudt, K., Carl, P., Mullen, K.M., Peterson, B.G. (2011). Differential Evolution with 'DEoptim': An Application to Non-Convex Portfolio Optimization. R Journal, 3(1), 27-34. doi:10.32614/RJ-2011-005.

Armstrong, A., Waldron, S., Ostle, N. J., Richardson, H., & Whitaker, J. (2015). Biotic and abiotic factors interact to regulate northern peatland carbon cycling. *Ecosystems*, *18*(8), 1395-1409.

Arora, V. K., Boer, G. J., Friedlingstein, P., Eby, M., Jones, C. D., Christian, J. R., ... & Wu, T. (2013). Carbon–concentration and carbon–climate feedbacks in CMIP5 Earth system models. *Journal of Climate*, 26(15), 5289-5314.

Aurela, M., Laurila, T., & Tuovinen, J. P. (2004). The timing of snow melt controls the annual CO_2 balance in a subarctic fen. *Geophysical research letters*, *31*(16).

Aurela, M., Riutta, T., Laurila, T., Tuovinen, J. P., Vesala, T., Tuittila, E. S., ... & Laine, J. (2007). CO_2 exchange of a sedge fen in southern Finland-The impact of a drought period. *Tellus B: Chemical and Physical Meteorology*, *59*(5), 826-837.

Baldocchi, D. D. (2003). Assessing the eddy covariance technique for evaluating carbon dioxide exchange rates of ecosystems: past, present and future. *Global change biology*, *9*(4), 479-492.

Barr, A. G., Black, T. A., Hogg, E. H., Kljun, N., Morgenstern, K., & Nesic, Z. (2004). Inter-annual variability in the leaf area index of a boreal aspen-hazelnut forest in relation to net ecosystem production. *Agricultural and forest meteorology*, *126*(3-4), 237-255.

Bastos, A., Ciais, P., Chevallier, F., Rödenbeck, C., Ballantyne, A. P., Maignan, F., ... & Zhu, D. (2019). Contrasting effects of CO_2 fertilization, land-use change and warming on seasonal amplitude of Northern Hemisphere CO_2 exchange. *Atmospheric chemistry and physics*, *19*(19), 12361-12375.

Batjes, N. H. (1996). Total carbon and nitrogen in the soils of the world. *European journal of soil science*, 47(2), 151-163.

Bauer, I. E., Bhatti, J. S., Swanston, C., Wieder, R. K., & Preston, C. M. (2009). Organic Matter Accumulation and Community Change at the Peatland–Upland Interface: Inferences from 14 C and 210 Pb Dated Profiles. *Ecosystems*, *12*(4), 636-653.

Bayazit, M., & Önöz, B. (2007). To prewhiten or not to prewhiten in trend analysis?. Hydrological Sciences Journal, 52(4), 611-624. doi:10.1623/hysj.52.4.611

Bayazit, M., & Önöz, B. (2007). To prewhiten or not to prewhiten in trend analysis? Hydrological Sciences Journal, 52(4), 611-624. doi:10.1623/hysj.52.4.611

Beilman, D. W., MacDonald, G. M., Smith, L. C., & Reimer, P. J. (2009). Carbon accumulation in peatlands of West Siberia over the last 2000 years. *Global biogeochemical cycles*, *23*(1).

Bello, R., & Higuchi, K. (2019). Changing surface radiation and energy budgets of the Hudson Bay Complex using the North American regional reanalysis (NARR) model. Arctic Science, 5(4), 218-239.

Belyea, L. R., & Clymo, R. S. (2001). Feedback control of the rate of peat formation. *Proceedings of the Royal Society of London. Series B: Biological Sciences*, *268*(1473), 1315-1321.

Bindof, N. L. et al. in Climate Change 2013: The Physical Science Basis (eds Stocker, T. F. et al.) 867–952 (IPCC, Cambridge Univ. Press, 2013).

Boer, G. J., & Arora, V. (2009). Temperature and concentration feedbacks in the carbon cycle. *Geophysical Research Letters*, 36(2).

Bonan, G. (2015). Ecological climatology: concepts and applications. Cambridge University Press.

Bonan, G. (2019). Climate change and terrestrial ecosystem modeling. Cambridge University Press.

Braganza, K., Karoly, D. J., Hirst, A. C., Stott, P., Stouffer, R. J., & Tett, S. F. (2004). Simple indices of global climate variability and change Part II: attribution of climate change during the twentieth century. Climate Dynamics, 22(8), 823-838.

Braganza, K., Karoly, D., Hirst, A., Mann, M., Stott, P., Stouffer, R., & Tett, S. (2003). Simple indices of global climate variability and change: Part I–variability and correlation structure. Climate Dynamics, 20(5), 491-502.

Breeuwer, A., Robroek, B. J., Limpens, J., Heijmans, M. M., Schouten, M. G., & Berendse, F. (2009). Decreased summer water table depth affects peatland vegetation. *Basic and Applied Ecology*, *10*(4), 330-339.

Bridgham, S. D., Megonigal, J. P., Keller, J. K., Bliss, N. B., & Trettin, C. (2006). The carbon balance of North American wetlands. *Wetlands*, *26*(4), 889-916.

Bridgham, S. D., Pastor, J., Dewey, B., Weltzin, J. F., & Updegraff, K. (2008). Rapid carbon response of peatlands to climate change. *Ecology*, *89*(11), 3041-3048.

Brown, R. (1970). Permafrost in Canada: its influence on Northern development. University of Toronto Press, Toronto, Ont.

Bubier, J. L., Bhatia, G., Moore, T. R., Roulet, N. T., & Lafleur, P. M. (2003). Spatial and temporal variability in growing-season net ecosystem carbon dioxide exchange at a large peatland in Ontario, Canada. *Ecosystems*, 353-367.

Bunbury, J., Finkelstein, S. A., & Bollmann, J. (2012). Holocene hydro-climatic change and effects on carbon accumulation inferred from a peat bog in the Attawapiskat River watershed, Hudson Bay Lowlands, Canada. Quaternary Research, 78(2), 275-284.

Burton, K. L., Rouse, W. R., & Boudreau, L. D. (1996). Factors affecting the summer carbon dioxide budget of subarctic wetland tundra. *Climate research, 6*(3), 203-213.

Camill, P. (2005). Permafrost thaw accelerates in boreal peatlands during late-20th century climate warming. Climatic Change, 68(1), 135-152.

Canadell, J. G., Kirschbaum, M. U., Kurz, W. A., Sanz, M. J., Schlamadinger, B., & Yamagata, Y. (2007). Factoring out natural and indirect human effects on terrestrial carbon sources and sinks. environmental science & policy, 10(4), 370-384.

Chandrasekar, K., Sesha Sai, M. V. R., Roy, P. S., & Dwevedi, R. S. (2010). Land Surface Water Index (LSWI) response to rainfall and NDVI using the MODIS Vegetation Index product. *International Journal of Remote Sensing*, *31*(15), 3987-4005.

Charman, D. J., Amesbury, M. J., Hinchliffe, W., Hughes, P. D., Mallon, G., Blake, W. H., ... & Mauquoy, D. (2015). Drivers of Holocene peatland carbon accumulation across a climate gradient in northeastern North America. *Quaternary Science Reviews*, *121*, 110-119.

Charman, D. J., Beilman, D. W., Blaauw, M., Booth, R. K., Brewer, S., Chambers, F. M., ... & Zhao, Y. (2013). Climate-related changes in peatland carbon accumulation during the last millennium. *Biogeosciences*, *10*(2), 929-944.

Chaudhary, N., Miller, P. A., & Smith, B. (2017). Modelling past, present and future peatland carbon accumulation across the pan-Arctic region. *Biogeosciences*, 14(18), 4023-4044.

Chaudhary, N., Westermann, S., Lamba, S., Shurpali, N., Sannel, A. B. K., Schurgers, G., ... & Smith, B. (2020). Modelling past and future peatland carbon dynamics across the pan-Arctic. *Global change biology*, *26*(7), 4119-4133.

Churkina, G., Schimel, D., Braswell, B. H., & Xiao, X. (2005). Spatial analysis of growing season length control over net ecosystem exchange. *Global Change Biology*, 11(10), 1777-1787.

Comiso, J.C. (2002). A rapidly declining perennial sea ice cover in the Arctic. Geophysical Research Letters, 29(20):1956, doi:10.1029/2002GL015650.

Connolly, J., Roulet, N. T., Seaquist, J. W., Holden, N. M., Lafleur, P. M., Humphreys, E. R., ... & Ward, S. M. (2009). Using MODIS derived fPAR with ground based flux tower measurements to derive the light use efficiency for two Canadian peatlands. *Biogeosciences*, *6*(2), 225-234.

Cooley, S. W., & Pavelsky, T. M. (2016). Spatial and temporal patterns in Arctic river ice breakup revealed by automated ice detection from MODIS imagery. Remote Sensing of Environment, 175, 310-322.

Cooper, M. D., Estop-Aragonés, C., Fisher, J. P., Thierry, A., Garnett, M. H., Charman, D. J., ... & Hartley, I. P. (2017). Limited contribution of permafrost carbon to methane release from thawing peatlands. *Nature Climate Change*, *7*(7), 507-511.

Cowtan, K. and Way, R. G. (2013). Coverage bias in the HadCRUT4 temperature series and its impact on recent temperature trends. Q. J. R. Meteorol. Soc. 133, 459–77.

Cox, P. M., Betts, R. A., Bunton, C. B., Essery, R. L. H., Rowntree, P. R., & Smith, J. (1999). The impact of new land surface physics on the GCM simulation of climate and climate sensitivity. Climate Dynamics, 15(3), 183-203.

Cubasch, U., Meehl, G.A., Boer, G.J., Stouffer, R.J., Dix, M., Noda, A., Senior, C.A., Raper, S. and Yap, K.S. (2001). Projections of future climate change. In Climate Change 2001: The scientific basis. Contribution of WG1 to the Third Assessment Report of the IPCC (TAR) (pp. 525-582). Cambridge University Press.

Damm, A., Guanter, L., Paul-Limoges, E., Van der Tol, C., Hueni, A., Buchmann, N., ... & Schaepman, M. E. (2015). Far-red sun-induced chlorophyll fluorescence shows ecosystem-specific relationships to gross primary production: An assessment based on observational and modeling approaches. *Remote Sensing of Environment*, *166*, 91-105.

Davidson, E. A., & Janssens, I. A. (2006). Temperature sensitivity of soil carbon decomposition and feedbacks to climate change. *Nature*, *440*(7081), 165-173.

De Deyn, G. B., Cornelissen, J. H., & Bardgett, R. D. (2008). Plant functional traits and soil carbon sequestration in contrasting biomes. *Ecology letters*, *11*(5), 516-531.

Delidjakova, K. K., Bello, R. L., Higuchi, K., & Pokharel, B. (2016). Influence of Hudson Bay on the carbon dynamics of a Hudson Bay Lowlands coastal site. Arctic Science, 2(3), 142-163.

Derksen, C., Burgess, D., Duguay, C., Howell, S., Mudryk, L., Smith, S., Thackeray, C., & Kirchmeier-Young, M. (2018). Changes in snow, ice, and permafrost across Canada: Chapter 5. In E. Bush & D. S. Lemmen (Eds.), Canada's Changing Climate Report (pp. 194–260). Ottawa, Ontario: Government of Canada.

Déry, S. J., Mlynowski, T. J., Hernández-Henríquez, M. A., & Straneo, F. (2011). Interannual variability and interdecadal trends in Hudson Bay streamflow. Journal of Marine Systems, 88(3), 341-351.

Didan, K. (2015). MOD13Q1 MODIS/Terra Vegetation Indices 16-Day L3 Global 250m SIN Grid V006. NASA EOSDIS Land Processes DAAC. https://doi.org/10.5067/MODIS/MOD13Q1.006.

Dieleman, C. M., Branfireun, B. A., McLaughlin, J. W., & Lindo, Z. (2015). Climate change drives a shift in peatland ecosystem plant community: implications for ecosystem function and stability. *Global change biology*, *21*(1), 388-395.

Dorrepaal, E., Toet, S., Van Logtestijn, R. S., Swart, E., Van De Weg, M. J., Callaghan, T. V., & Aerts, R. (2009). Carbon respiration from subsurface peat accelerated by climate warming in the subarctic. *Nature*, *460*(7255), 616-619.

Dredge, L., & Mott, R. (2003). Holocene pollen records and peatland development, northeastern Manitoba. *Géographie physique et Quaternaire*, *57*(1), 7-19.

Ecological Stratification Working Group (1995) A National Ecological Framework for Canada. Agriculture and Agri-Food Canada, Research Branch, Centre for Land and Biological Resources Research and Environment Canada, State of the Environment Directorate, Ecozone Analysis Branch, Ottawa/Hull. Report and national map at 1:7500 000 scale.

Environment Canada (2020). Canadian Climate Normals 1981-2010. Station Data: CHURCHILL A, Manitoba; MOOSONEE UA, Ontario. http://climate.weather.gc.ca/climate_normals/index_e.html#1981

Etkin, D. A. (1991). Break-up in Hudson Bay: its sensitivity to air temperatures and implications for climate warming. Climatological Bulletin, 25: 21–34.

Euskirchen, E. S., Edgar, C. W., Turetsky, M. R., Waldrop, M. P., & Harden, J. W. (2014). Differential response of carbon fluxes to climate in three peatland ecosystems that vary in the presence and stability of permafrost. *Journal of Geophysical Research: Biogeosciences*, 119(8), 1576-1595.

Euskirchen, E. S., McGuire, A. D., Kicklighter, D. W., Zhuang, Q., Clein, J. S., Dargaville, R. J., ... & Romanovsky, V. E. (2006). Importance of recent shifts in soil thermal dynamics on growing season length, productivity, and carbon sequestration in terrestrial high-latitude ecosystems. Global Change Biology, 12(4), 731-750.

Fan, Z., David McGuire, A., Turetsky, M. R., Harden, J. W., Michael Waddington, J., & Kane, E. S. (2013). The response of soil organic carbon of a rich fen peatland in interior Alaska to projected climate change. *Global change biology*, 19(2), 604-620.

Flanagan, L. B., & Syed, K. H. (2011). Stimulation of both photosynthesis and respiration in response to warmer and drier conditions in a boreal peatland ecosystem. *Global Change Biology*, *17*(7), 2271-2287.

Francis, J. A., & Vavrus, S. J. (2012). Evidence linking Arctic amplification to extreme weather in mid-latitudes. Geophysical research letters, 39(6), L06801.

Francis, J. A., & Vavrus, S. J. (2015). Evidence for a wavier jet stream in response to rapid Arctic warming. Environmental Research Letters, 10(1), 014005.

Frankenberg, C., Fisher, J. B., Worden, J., Badgley, G., Saatchi, S. S., Lee, J. E., ... & Yokota, T. (2011). New global observations of the terrestrial carbon cycle from GOSAT: Patterns of plant fluorescence with gross primary productivity. *Geophysical Research Letters*, *38*(17).

Frankenberg, C., O'Dell, C., Berry, J., Guanter, L., Joiner, J., Köhler, P., ... & Taylor, T. E. (2014). Prospects for chlorophyll fluorescence remote sensing from the Orbiting Carbon Observatory-2. *Remote Sensing of Environment*, *147*, 1-12.

Friedl, M., Gray, J., Sulla-Menashe, D. (2019). MCD12Q2 MODIS/Terra+Aqua Land Cover Dynamics Yearly L3 Global 500m SIN Grid V006 [Data set]. NASA EOSDIS Land Processes DAAC. https://doi.org/10.5067/MODIS/MCD12Q2.006.

Friedlingstein, P., Cox, P., Betts, R., Bopp, L., von Bloh, W., Brovkin, V., ... & Zeng, N. (2006). Climate–carbon cycle feedback analysis: results from the C4MIP model intercomparison. *Journal of climate*, 19(14), 3337-3353.

Gagnon, A. S., and Gough, W. A. (2005). Trends in the dates of ice freeze-up and breakup over Hudson Bay, Canada. Arctic, 58: 370–382.

Gallego-Sala, A. V., Charman, D. J., Brewer, S., Page, S. E., Prentice, I. C., Friedlingstein, P., ... & Zhao, Y. (2018). Latitudinal limits to the predicted increase of the peatland carbon sink with warming. *Nature climate change*, *8*(10), 907-913.

Gamon, J. A., Field, C. B., Goulden, M. L., Griffin, K. L., Hartley, A. E., Joel, G., ... & Valentini, R. (1995). Relationships between NDVI, canopy structure, and photosynthesis in three Californian vegetation types. *Ecological Applications*, *5*(1), 28-41.

Gao, B. C. (1996). NDWI—A normalized difference water index for remote sensing of vegetation liquid water from space. *Remote sensing of environment*, *58*(3), 257-266.

Garneau, M., van Bellen, S., Magnan, G., Beaulieu-Audy, V., Lamarre, A., & Asnong, H. (2014). Holocene carbon dynamics of boreal and subarctic peatlands from Québec, Canada. *The Holocene*, *24*(9), 1043-1053.

Gill, A. L., Giasson, M. A., Yu, R., & Finzi, A. C. (2017). Deep peat warming increases surface methane and carbon dioxide emissions in a black spruce-dominated ombrotrophic bog. *Global change biology*, *23*(12), 5398-5411.

Gorham, E. (1991). Northern peatlands: role in the carbon cycle and probable responses to climatic warming. *Ecological applications*, *1*(2), 182-195.

Gorham, E. (1995). The biogeochemistry of northern peatlands and its possible responses to global warming. *Biotic feedbacks in the global climatic system: will the warming feed the warming*, 169-187.

Gorham, E., Lehman, C., Dyke, A., Clymo, D., & Janssens, J. (2012). Long-term carbon sequestration in North American peatlands. *Quaternary Science Reviews*, *58*, 77-82.

Gough, W. A. and Leung, A. (2002). Nature and fate of Hudson Bay permafrost, Reg. Environ. Change 2, 177–184.

Granath, G., Moore, P. A., Lukenbach, M. C., & Waddington, J. M. (2016). Mitigating wildfire carbon loss in managed northern peatlands through restoration. *Scientific reports*, *6*(1), 1-9.

Graversen, R. G., & Wang, M. (2009). Polar amplification in a coupled climate model with locked albedo. *Climate Dynamics*, 33(5), 629-643.

Green, J. K., Seneviratne, S. I., Berg, A. M., Findell, K. L., Hagemann, S., Lawrence, D. M., & Gentine, P. (2019). Large influence of soil moisture on long-term terrestrial carbon uptake. *Nature*, *565*(7740), 476-479.

Griffis, T. J., Rouse, W. R., & Waddington, J. M. (2000). Interannual variability of net ecosystem CO_2 exchange at a subarctic fen. *Global Biogeochemical Cycles*, *14*(4), 1109-1121.

Groenendijk, M., Dolman, A. J., Van der Molen, M. K., Leuning, R., Arneth, A., Delpierre, N., ... & Wohlfahrt, G. (2011). Assessing parameter variability in a photosynthesis model within and between plant functional types using global Fluxnet eddy covariance data. *Agricultural and forest meteorology*, *151*(1), 22-38. doi:10.1016/j.agrformet.2010.08.013.

Grömping, U. (2006). Relative importance for linear regression in R: the package relaimpo. Journal of statistical software, 17(1), 1-27.

Grosse, G., Harden, J., Turetsky, M., McGuire, A. D., Camill, P., Tarnocai, C., ... & Romanovsky, V. (2011). Vulnerability of high-latitude soil organic carbon in North America to disturbance. Journal of Geophysical Research: Biogeosciences, 116(G4).

Guanter, L., Zhang, Y., Jung, M., Joiner, J., Voigt, M., Berry, J. A., ... & Griffis, T. J. (2014). Global and time-resolved monitoring of crop photosynthesis with chlorophyll fluorescence. *Proceedings of the National Academy of Sciences*, *111*(14), E1327-E1333.

Hall, A. (2004). The role of surface albedo feedback in climate. J. Clim. 17, 1550–1568.

Hanis, K. L., Amiro, B. D., Tenuta, M., Papakyriakou, T., & Swystun, K. A. (2015). Carbon exchange over four growing seasons for a subarctic sedge fen in northern Manitoba, Canada. *Arctic Science*, *1*(2), 27-44.

Hanis, K. L., Tenuta, M., Amiro, B. D., & Papakyriakou, T. N. (2013). Seasonal dynamics of methane emissions from a subarctic fen in the Hudson Bay Lowlands. *Biogeosciences*, *10*(7), 4465-4479.

Hannah, C. G., Dupont, F., & Dunphy, M. (2009). Polynyas and tidal currents in the Canadian Arctic Archipelago. Arctic, 62(1): 83-95.

Hao, Y. B., Cui, X. Y., Wang, Y. F., Mei, X. R., Kang, X. M., Wu, N., ... & Zhu, D. (2011). Predominance of precipitation and temperature controls on ecosystem CO_2 exchange in Zoige alpine wetlands of Southwest China. *Wetlands*, *31*(2), 413-422.

Harris, A., & Dash, J. (2011). A new approach for estimating northern peatland gross primary productivity using a satellite-sensor-derived chlorophyll index. *Journal of Geophysical Research: Biogeosciences*, *116*(G4).

Harris, L. I. (2017). The structure and function of peatlands in the Hudson Bay Lowland: response to environmental change. PhD thesis. 242p. McGill University (Canada).

Harris, L. I., Roulet, N. T., & Moore, T. R. (2020). Drainage reduces the resilience of a boreal peatland. *Environmental Research Communications*, *2*(6), 065001.

Harvey, J.G. (1978). Atmosphere and ocean: our fluid environment. Artemis Press, Sussex, UK. 78 pp.

Heijmans, M. M., Mauquoy, D., Van Geel, B., & Berendse, F. (2008). Long-term effects of climate change on vegetation and carbon dynamics in peat bogs. *Journal of Vegetation Science*, *19*(3), 307-320.

Helbig, M., Humphreys, E. R., & Todd, A. (2019). Contrasting temperature sensitivity of CO_2 exchange in peatlands of the Hudson Bay Lowlands, Canada. *Journal of Geophysical Research: Biogeosciences*, *124*(7), 2126-2143.

Helbig, M., Waddington, J. M., Alekseychik, P., Amiro, B. D., Aurela, M., Barr, A. G., ... & Zyrianov, V. (2020). Increasing contribution of peatlands to boreal evapotranspiration in a warming climate. *Nature Climate Change*, *10*(6), 555-560.

Helm, L. T., Shi, H., Lerdau, M. T., & Yang, X. (2020). Solar-induced chlorophyll fluorescence and short-term photosynthetic response to drought. *Ecological Applications*, *30*(5), e02101.

Henry, M. (2011). Sea ice trends in Canada. EnviroStats Serv Bull, 5, 3-13.

Hilker, T., Coops, N. C., Wulder, M. A., Black, T. A., & Guy, R. D. (2008). The use of remote sensing in light use efficiency based models of gross primary production: A review of current status and future requirements. *Science of the Total Environment*, *404*(2-3), 411-423.

Hilton, T. W., Davis, K. J., & Keller, K. (2014). Evaluating terrestrial CO_2 flux diagnoses and uncertainties from a simple land surface model and its residuals. *Biogeosciences*, *11*(2), 217-235.

Hilton, T. W., Davis, K. J., Keller, K., & Urban, N. M. (2013). Improving North American terrestrial CO_2 flux diagnosis using spatial structure in land surface model residuals. *Biogeosciences*, *10*(7), 4607-4625.

Hirsch, R. M., Slack, J. R., & Smith, R. A. (1982). Techniques of trend analysis for monthly water quality data. Water resources research, 18(1), 107-121.

Hochheim, K. P., & Barber, D. G. (2014). An update on the ice climatology of the Hudson Bay system. Arctic, Antarctic, and Alpine Research, 46(1), 66-83.

Holmquist, J. R., MacDonald, G. M., & Gallego-Sala, A. (2014). Peatland initiation, carbon accumulation, and 2 ka depth in the James Bay Lowland and adjacent regions. Arctic, antarctic, and alpine research, 46(1), 19-39.

Holton, J. R. (1992). An introduction to dynamic meteorology (International geophysics series, San Diego, New York.

Huang, J., Zhang, X., Zhang, Q., Lin, Y., Hao, M., Luo, Y., ... & Zhang, J. (2017). Recently amplified arctic warming has contributed to a continual global warming trend. Nature Climate Change, 7(12), 875-879.

Huang, X., Xiao, J., & Ma, M. (2019). Evaluating the performance of satellite-derived vegetation indices for estimating gross primary productivity using FLUXNET observations across the globe. *Remote Sensing*, *11*(15), 1823.

Huemmrich, K. F., Gamon, J. A., Tweedie, C. E., Oberbauer, S. F., Kinoshita, G., Houston, S., ... & Oechel, W. C. (2010). Remote sensing of tundra gross ecosystem productivity and light use efficiency under varying temperature and moisture conditions. *Remote Sensing of Environment*, *114*(3), 481-489.

Huete, A., Didan, K., Miura, T., Rodriguez, E. P., Gao, X., & Ferreira, L. G. (2002). Overview of the radiometric and biophysical performance of the MODIS vegetation indices. *Remote sensing of environment*, *83*(1-2), 195-213.

Humphreys, E. R., Charron, C., Brown, M., & Jones, R. (2014). Two bogs in the Canadian Hudson Bay Lowlands and a temperate bog reveal similar annual net ecosystem exchange of CO2. *Arctic, Antarctic, and Alpine Research*, *46*(1), 103-113.

Humphreys, E. R., Lafleur, P. M., Flanagan, L. B., Hedstrom, N., Syed, K. H., Glenn, A. J., & Granger, R. (2006). Summer carbon dioxide and water vapor fluxes across a range of northern peatlands. *Journal of Geophysical Research: Biogeosciences*, *111*(G4).

Huntingford, C., Lowe, J. A., Booth, B. B., Jones, C. D., Harris, G. R., Gohar, L. K., & Meir, P. (2009). Contributions of carbon cycle uncertainty to future climate projection spread. Tellus B: Chemical and Physical Meteorology, 61(2), 355-360.

IPCC (2021): Summary for Policymakers. In: Climate Change 2021: The Physical Science Basis. Contribution of Working Group I to the Sixth Assessment Report of the Intergovernmental Panel on Climate Change [Masson-Delmotte, V., P. Zhai, A. Pirani, S. L. Connors, C. Péan, S. Berger, N. Caud, Y. Chen, L. Goldfarb, M. I. Gomis, M. Huang, K. Leitzell, E. Lonnoy, J.B.R. Matthews, T. K. Maycock, T. Waterfield, O. Yelekçi, R. Yu and B. Zhou (eds.)]. Cambridge University Press. In Press.

Ise, T., Dunn, A. L., Wofsy, S. C., & Moorcroft, P. R. (2008). High sensitivity of peat decomposition to climate change through water-table feedback. *Nature Geoscience*, *1*(11), 763-766.

Jia, G., Shevliakova, E., Artaxo, N., De Noblet-Ducoudré, N., Houghton, R., and House, J. (2019). Climate Change and Land: an IPCC special report on climate change, desertification, land degradation, sustainable land management, food security, and greenhouse gas fluxes in terrestrial ecosystems. In Press

Joiner, J., Yoshida, Y., Vasilkov, A. P., Schaefer, K., Jung, M., Guanter, L., ... & Marchesini, L. B. (2014). The seasonal cycle of satellite chlorophyll fluorescence observations and its relationship to vegetation phenology and ecosystem atmosphere carbon exchange. *Remote Sensing of Environment*, *152*, 375-391.

Jones, M. C., & Yu, Z. (2010). Rapid deglacial and early Holocene expansion of peatlands in Alaska. *Proceedings of the National Academy of Sciences*, *107*(16), 7347-7352.

Jones, M. C., Harden, J., O'Donnell, J., Manies, K., Jorgenson, T., Treat, C., & Ewing, S. (2017). Rapid carbon loss and slow recovery following permafrost thaw in boreal peatlands. *Global change biology*, *23*(3), 1109-1127.

Joshi, M. M., Gregory, J. M., Webb, M. J., Sexton, D. M., & Johns, T. C. (2008). Mechanisms for the land/sea warming contrast exhibited by simulations of climate change. Climate Dynamics, 30(5), 455-465.

Joshi, M., & Gregory, J. (2008). Dependence of the land-sea contrast in surface climate response on the nature of the forcing. Geophysical Research Letters, 35(24).

Kalnay, E., Kanamitsu, M., Kistler, R., Collins, W., Deaven, D., Gandin, L., Iredell, M., Saha, S., White, G., Woollen, J. and Zhu, Y. (1996). The NCEP/NCAR 40-year reanalysis project. Bulletin of the American meteorological Society, 77(3), 437-472.

Kanamitsu, M., Ebisuzaki, W., Woollen, J., Yang, S. K., Hnilo, J. J., Fiorino, M., & Potter, G. L. (2002). Ncep–doe amip-ii reanalysis (r-2). Bulletin of the American Meteorological Society, 83(11), 1631-1644.

Keeling, C. D., Bacastow, R. B., Bainbridge, A. E., Ekdahl Jr, C. A., Guenther, P. R., Waterman, L. S., & Chin, J. F. (1976). Atmospheric carbon dioxide variations at Mauna Loa observatory, Hawaii. *Tellus*, 28(6), 538-551.

Keeling, C. D., Bacastow, R. B., Carter, A. F., Piper, S. C., Whorf, T. P., Heimann, M., ... & Roeloffzen, H. (1989). A three-dimensional model of atmospheric CO_2 transport based on observed winds: 1. Analysis of observational data. *Aspects of climate variability in the Pacific and the Western Americas*, 55, 165-236.

Keenan, T. F., Baker, I., Barr, A., Ciais, P., Davis, K., Dietze, M., ... & Richardson, A. D. (2012). Terrestrial biosphere model performance for inter-annual variability of land-atmosphere CO_2 exchange. *Global Change Biology*, *18*(6), 1971-1987.

Kettridge, N., Turetsky, M. R., Sherwood, J. H., Thompson, D. K., Miller, C. A., Benscoter, B. W., ... & Waddington, J. M. (2015). Moderate drop in water table increases peatland vulnerability to post-fire regime shift. *Scientific reports*, *5*(1), 1-4.

Kim Seongho (2015). ppcor: Partial and Semi-Partial (Part) Correlation. R package version 1.1. https://CRAN.R-project.org/package=ppcor

Kirtman, B., Power, S. B., Adedoyin, A. J., Boer, G. J., Bojariu, R., Camilloni, I., ... & Wang, H. J. (2013). Near-term climate change: projections and predictability. Climate Change 2013: the Physical Science Basis. Contribution of Working Group I to the Fifth Assessment Report of the Intergovernmental Panel on Climate Change. Cambridge University Press, Cambridge, pp. 953e1028.

Kistler, R., Kalnay, E., Collins, W., Saha, S., White, G., Woollen, J., Chelliah, M., Ebisuzaki, W., Kanamitsu, M., Kousky, V. and van den Dool, H. (2001). The NCEP–NCAR 50-year reanalysis: monthly means CD-ROM and documentation. Bulletin of the American Meteorological society, 82(2), 247-268.

Kittler, F., Burjack, I., Corradi, C. A. R., Heimann, M., Kolle, O., Merbold, L., ... & Göckede, M. (2016). Impacts of a decadal drainage disturbance on surface–atmosphere fluxes of carbon dioxide in a permafrost ecosystem.

Koven, C. D., Hugelius, G., Lawrence, D. M., & Wieder, W. R. (2017). Higher climatological temperature sensitivity of soil carbon in cold than warm climates. *Nature Climate Change*, 7(11), 817-822.

Koven, C. D., W. J. Riley, and A. Stern, (2013). Analysis of permafrost thermal dynamics and response to climate change in the CMIP5 Earth System Models. J. Clim., 26, 1877-1900.

Kowal, S., Gough, W. A., & Butler, K. (2017). Temporal evolution of Hudson Bay sea ice (1971–2011). Theoretical and Applied Climatology, 127(3-4), 753-760.

Kross, A., Seaquist, J. W., & Roulet, N. T. (2016). Light use efficiency of peatlands: Variability and suitability for modeling ecosystem production. *Remote Sensing of Environment*, *183*, 239-249.

Kross, A., Seaquist, J. W., Roulet, N. T., Fernandes, R., & Sonnentag, O. (2013). Estimating carbon dioxide exchange rates at contrasting northern peatlands using MODIS satellite data. *Remote sensing of environment*, *137*, 234-243.

Kuppel, S., Peylin, P., Chevallier, F., Bacour, C., Maignan, F., & Richardson, A. D. (2012). Constraining a global ecosystem model with multi-site eddy-covariance data. *Biogeosciences*, *9*(10), 3757-3776. doi:10.5194/bg-9-3757-2012.

Lafleur, P. M., & Rouse, W. R. (1988). The influence of surface cover and climate on energy partitioning and evaporation in a subarctic wetland. Boundary-Layer Meteorology, 44(4), 327-347.

Lafleur, P. M., Griffis, T. J., & Rouse, W. R. (2001). Interannual variability in net ecosystem CO_2 exchange at the arctic treeline. Arctic, Antarctic, and Alpine Research, 33(2), 149-157.

Lafleur, P. M., Roulet, N. T., Bubier, J. L., Frolking, S., & Moore, T. R. (2003). Interannual variability in the peatland-atmosphere carbon dioxide exchange at an ombrotrophic bog. Global Biogeochemical Cycles, 17(2).

Lamarre, A., Garneau, M., & Asnong, H. (2012). Holocene paleohydrological reconstruction and carbon accumulation of a permafrost peatland using testate amoeba and macrofossil analyses, Kuujjuarapik, subarctic Québec, Canada. *Review of Palaeobotany and Palynology*, *186*, 131-141.

Larmola, T., Alm, J., Juutinen, S., Saarnio, S., Martikainen, P. J. N., & Silvola, J. (2004). Floods can cause large interannual differences in littoral net ecosystem productivity. *Limnology and Oceanography*, *49*(5), 1896-1906.

Le Quéré, C., Andrew, R. M., Friedlingstein, P., Sitch, S., Hauck, J., Pongratz, J., ... & Zheng, B. (2018). Global carbon budget 2018. *Earth System Science Data*, *10*(4), 2141-2194.

Lee, J. E., Frankenberg, C., van der Tol, C., Berry, J. A., Guanter, L., Boyce, C. K., ... & Saatchi, S. (2013). Forest productivity and water stress in Amazonia: Observations from GOSAT chlorophyll fluorescence. *Proceedings of the Royal Society B: Biological Sciences*, *280*(1761), 20130171.

Lees, K. J., Quaife, T., Artz, R. R. E., Khomik, M., & Clark, J. M. (2018). Potential for using remote sensing to estimate carbon fluxes across northern peatlands–A review. *Science of the Total Environment*, *615*, 857-874.

Lemordant, L., Gentine, P., Swann, A. S., Cook, B. I., & Scheff, J. (2018). Critical impact of vegetation physiology on the continental hydrologic cycle in response to increasing CO_2. *Proceedings of the National Academy of Sciences*, 115(16), 4093-4098.

Leung, A., & Gough, W. (2016). Air mass distribution and the heterogeneity of the climate change signal in the Hudson Bay/Foxe Basin region, Canada. Theoretical and applied climatology, 125(3-4), 583-592.

Li, X., & Xiao, J. (2019). A global, 0.05-degree product of solar-induced chlorophyll fluorescence derived from OCO-2, MODIS, and reanalysis data. *Remote Sensing*, *11*(5), 517.

Li, X., Xiao, J., & He, B. (2018b). Chlorophyll fluorescence observed by OCO-2 is strongly related to gross primary productivity estimated from flux towers in temperate forests. *Remote Sensing of Environment*, *204*, 659-671.

Li, X., Xiao, J., He, B., Altaf Arain, M., Beringer, J., Desai, A. R., ... & Varlagin, A. (2018a). Solar-induced chlorophyll fluorescence is strongly correlated with terrestrial photosynthesis for a wide variety of biomes: First global analysis based on OCO-2 and flux tower observations. *Global change biology*, *24*(9), 3990-4008.

Limpens, J., Berendse, F., Blodau, C., Canadell, J. G., Freeman, C., Holden, J., ... & Schaepman-Strub, G. (2008). Peatlands and the carbon cycle: from local processes to global implications–a synthesis. *Biogeosciences*, *5*(5), 1475-1491.

Lin, J. C., Pejam, M. R., Chan, E., Wofsy, S. C., Gottlieb, E. W., Margolis, H. A., & McCaughey, J. H. (2011). Attributing uncertainties in simulated biospheric carbon fluxes to different error sources. *Global Biogeochemical Cycles*, *25*(2).

Lin, Y. S., Medlyn, B. E., & Ellsworth, D. S. (2012). Temperature responses of leaf net photosynthesis: the role of component processes. *Tree physiology*, *32*(2), 219-231.

Loisel, J., & Yu, Z. (2013). Recent acceleration of carbon accumulation in a boreal peatland, south central Alaska. Journal of Geophysical Research: Biogeosciences, 118(1), 41-53.

Loisel, J., Yu, Z., Beilman, D. W., Camill, P., Alm, J., Amesbury, M. J., ... & Zhou, W. (2014). A database and synthesis of northern peatland soil properties and Holocene carbon and nitrogen accumulation. *the Holocene*, *24*(9), 1028-1042.

Loveland, T. R., & Belward, A. S. (1997). The IGBP-DIS global 1km land cover data set, DISCover: first results. *International Journal of Remote Sensing*, *18*(15), 3289-3295.

Lu, X., Cheng, X., Li, X., Chen, J., Sun, M., Ji, M., ... & Tang, J. (2018). Seasonal patterns of canopy photosynthesis captured by remotely sensed sun-induced fluorescence and vegetation indexes in mid-to-high latitude forests: A cross-platform comparison. *Science of the total environment*, *644*, 439-451.

Lund, M., Lafleur, P. M., Roulet, N. T., Lindroth, A., Christensen, T. R., Aurela, M., ... & Nilsson, M. B. (2010). Variability in exchange of CO_2 across 12 northern peatland and tundra sites. *Global Change Biology*, *16*(9), 2436-2448.

Luus, K. A., & Lin, J. C. (2015). The Polar Vegetation Photosynthesis and Respiration Model: a parsimonious, satellite-data-driven model of high-latitude CO_2 exchange. *Geoscientific Model Development*, *8*(8), 2655-2674.

Luus, K. A., Commane, R., Parazoo, N. C., Benmergui, J., Euskirchen, E. S., Frankenberg, C., ... & Lin, J. C. (2017). Tundra photosynthesis captured by satellite-observed solar-induced chlorophyll fluorescence. *Geophysical Research Letters*, *44*(3), 1564-1573.

Mack, M. C., Schuur, E. A., Bret-Harte, M. S., Shaver, G. R., & Chapin, F. S. (2004). Ecosystem carbon storage in arctic tundra reduced by long-term nutrient fertilization. *Nature*, *431*(7007), 440-443.

Mahadevan, P., Wofsy, S. C., Matross, D. M., Xiao, X., Dunn, A. L., Lin, J. C., ... & Gottlieb, E. W. (2008). A satellite-based biosphere parameterization for net ecosystem CO_2 exchange: Vegetation Photosynthesis and Respiration Model (VPRM). *Global Biogeochemical Cycles*, *22*(2).

Maltby, E., & Immirzi, P. (1993). Carbon dynamics in peatlands and other wetland soils regional and global perspectives. *Chemosphere*, *27*(6), 999-1023.

Manabe, S., Stouffer, R. J., Spelman, M. J., & Bryan, K. (1991). Transient responses of a coupled ocean–atmosphere model to gradual changes of atmospheric CO2. Part I. Annual mean response. Journal of Climate, 4(8), 785-818.

Markham, W. E. (1986) The ice cover, in Martini, I. P. (ed.), Canadian Inland Seas. Elsevier, Amsterdam.

Marrs, J. K., Reblin, J. S., Logan, B. A., Allen, D. W., Reinmann, A. B., Bombard, D. M., ... & Hutyra, L. R. (2020). Solar-induced fluorescence does not track photosynthetic carbon assimilation following induced stomatal closure. *Geophysical Research Letters*, *47*(15), e2020GL087956.

Martin, A. C., Jeffers, E. S., Petrokofsky, G., Myers-Smith, I., & Macias-Fauria, M. (2017). Shrub growth and expansion in the Arctic tundra: an assessment of controlling factors using an evidence-based approach. *Environmental Research Letters*, *12*(8), 085007.

Martini, I. P. (2006). The cold climate peatlands of the Hudson Bay Lowland, Canada: brief overview of recent work. In Martini, I. P., Cortizas, A. M., and Chesworth, W. (eds.), Peatlands: evolution and records of environmental and climatic changes. Amsterdam: Elsevier, 53–84.

Marushchak, M. E., Kiepe, I., Biasi, C., Elsakov, V., Friborg, T., Johansson, T., ... & Martikainen, P. J. (2013). Carbon dioxide balance of subarctic tundra from plot to regional scales. *Biogeosciences*, *10*(1), 437-452.

Massey Jr, F. J. (1951). The Kolmogorov-Smirnov test for goodness of fit. Journal of the American statistical Association, 46(253), 68-78.

Maxwell, J. B. (1986) A climate overview of the Canadian inland seas, in Martini, I. P. (ed.), Canadian Inland Seas. Elsevier, Amsterdam.

McLaughlin, J. W., & Packalen, M. (2021). Peat carbon vulnerability to projected climate warming in the Hudson Bay Lowlands, Canada: A decision support tool for land use planning in peatland dominated landscapes. *Frontiers in Earth Science*, *9*, 608.

McLaughlin, J., & Webster, K. (2014). Effects of climate change on peatlands in the far north of Ontario, Canada: A synthesis. *Arctic, Antarctic, and Alpine Research*, *46*(1), 84-102.

McLeod, A. I. (2011). Kendall rank correlation and Mann-Kendall trend test. R Package Kendall. https://CRAN.R-project.org/package=Kendall.

McNeil, P., & Waddington, J. M. (2003). Moisture controls on Sphagnum growth and CO_2 exchange on a cutover bog. *Journal of applied ecology*, *40*(2), 354-367.

Melillo, J. M., Butler, S., Johnson, J., Mohan, J., Steudler, P., Lux, H., ... & Tang, J. (2011). Soil warming, carbon–nitrogen interactions, and forest carbon budgets. *Proceedings of the National Academy of Sciences*, *108*(23), 9508-9512.

Melton, J. R., Arora, V. K., Wisernig-Cojoc, E., Seiler, C., Fortier, M., Chan, E., & Teckentrup, L. (2020). CLASSIC v1. 0: the open-source community successor to the Canadian Land Surface Scheme (CLASS) and the Canadian Terrestrial Ecosystem Model (CTEM)–Part 1: Model framework and site-level performance. Geoscientific Model Development, 13(6), 2825-2850.

Meredith, M., Sommerkorn, M., Cassotta, S., Derksen, C., Ekaykin, A., Hollowed, A., ... & Schuur, E. A. (2019). Polar Regions. Chapter 3, IPCC Special Report on the Ocean and Cryosphere in a Changing Climate.

Mesinger, F., DiMego, G., Kalnay, E., Mitchell, K., Shafran, P. C., Ebisuzaki, W., ... & Ek, M. B. (2006). North American regional reanalysis. Bulletin of the American Meteorological Society, 87(3), 343-360.

Middleton, E.M., Huemmrich, K.F., Zhang, Q., Campbell, P.K., and Landis, D.R. (2018). Spectral bio-indicators of photosynthetic efficiency and vegetation stress, chap. 5. In: Thenkabail, P.S., Lyon, J.G., Huete, A. (Eds.), Hyperspectral Remote Sensing of Vegetation, 2nd edition. Vol. III: Biophysical and Biochemical Characterization and Plant Species Studies Taylor & Francis, New York, pp. 133–179.

Mohammed, G. H., Colombo, R., Middleton, E. M., Rascher, U., van der Tol, C., Nedbal, L., ... & Zarco-Tejada, P. J. (2019). Remote sensing of solar-induced chlorophyll fluorescence (SIF) in vegetation: 50 years of progress. *Remote sensing of environment*, *231*, 111177.

Monteith, J. L. (1972). Solar radiation and productivity in tropical ecosystems. *Journal of applied ecology*, *9*(3), 747-766.

Mudryk, L.R., Derksen, C., Howell, S., Laliberté, F., Thackeray, C., Sospedra-Alfonso, R., Vionnet, V., Kushner, P.J. and Brown, R. (2018). Canadian snow and sea ice: historical trends and projections. The Cryosphere, 12(4), 1157. doi:10.5194/tc-12-1157-2018

Mullen, K., Ardia, D., Gil, D. L., Windover, D., & Cline, J. (2011). DEoptim: An R package for global optimization by differential evolution. Journal of Statistical Software, 40(6), 1-26. doi:10.18637/jss.v040.i06.

Myers-Smith, I. H., Forbes, B. C., Wilmking, M., Hallinger, M., Lantz, T., Blok, D., ... & Hik, D. S. (2011). Shrub expansion in tundra ecosystems: dynamics, impacts and research priorities. *Environmental Research Letters*, *6*(4), 045509.

Myers-Smith, I. H., Kerby, J. T., Phoenix, G. K., Bjerke, J. W., Epstein, H. E., Assmann, J. J., ... & Wipf, S. (2020). Complexity revealed in the greening of the Arctic. *Nature Climate Change*, *10*(2), 106-117.

NCAR Command Language (Version 6.6.2) [Software]. (2019). Boulder, Colorado: UCAR/NCAR/CISL/TDD. http://dx.doi.org/10.5065/D6WD3XH5

Nilsson, M. C., & Wardle, D. A. (2005). Understory vegetation as a forest ecosystem driver: evidence from the northern Swedish boreal forest. *Frontiers in Ecology and the Environment*, *3*(8), 421-428.

Novick, K. A., Ficklin, D. L., Stoy, P. C., Williams, C. A., Bohrer, G., Oishi, A. C., ... & Phillips, R. P. (2016). The increasing importance of atmospheric demand for ecosystem water and carbon fluxes. *Nature climate change*, *6*(11), 1023-1027.

Nwaishi, F. C., Morison, M. Q., Van Huizen, B., Khomik, M., Petrone, R. M., & Macrae, M. L. (2020). Growing season CO_2 exchange and evapotranspiration dynamics among thawing and intact permafrost landforms in the Western Hudson Bay lowlands. *Permafrost and Periglacial Processes*, *31*(4), 509-523.

Nzotungicimpaye, C.-M., K. Zickfeld (2017). The contribution from methane to the permafrost carbon feedback, Current Climate Change Reports, 3, 58–68, doi:10.1007/s40641-017-0054-1.

ORNL DAAC. (2018). MODIS and VIIRS Land Products Global Subsetting and Visualization Tool. ORNL DAAC, Oak Ridge, Tennessee, USA. https://doi.org/10.3334/ORNLDAAC/1379.

Packalen, M. S., Finkelstein, S. A., & McLaughlin, J. W. (2014). Carbon storage and potential methane production in the Hudson Bay Lowlands since mid-Holocene peat initiation. *Nature communications*, *5*(1), 1-8.

Packalen, M. S., Finkelstein, S. A., & McLaughlin, J. W. (2016). Climate and peat type in relation to spatial variation of the peatland carbon mass in the Hudson Bay Lowlands, Canada. *Journal of Geophysical Research: Biogeosciences*, *121*(4), 1104-1117.

Papakyriakou, T. (2020). *AmeriFlux CA-CF1 Churchill Fen Site 1*. Lawrence Berkeley National Lab.(LBNL), Berkeley, CA (United States). AmeriFlux; University of Manitoba. https://doi.org/10.17190/AMF/1660336.

Parkinson, C. L., Cavalieri, D. J., Gloersen, P., Zwally, H. J., & Comiso, J. C. (1999). Arctic sea ice extents, areas, and trends, 1978–1996. Journal of Geophysical Research: Oceans, 104(C9), 20837-20856.

Parmentier, F. J. W., Van Der Molen, M. K., Van Huissteden, J., Karsanaev, S. A., Kononov, A. V., Suzdalov, D. A., ... & Dolman, A. J. (2011). Longer growing seasons do not increase net carbon uptake in the northeastern Siberian tundra. *Journal of Geophysical Research: Biogeosciences*, 116(G4).

Payette, S., Delwaide, A., Caccianiga, M., & Beauchemin, M. (2004). Accelerated thawing of subarctic peatland permafrost over the last 50 years. *Geophysical research letters*, *31*(18).

Pedlar, J. H., McKenney, D. W., Lawrence, K., Papadopol, P., Hutchinson, M. F., & Price, D. (2015). A comparison of two approaches for generating spatial models of growing-season variables for Canada. *Journal of Applied Meteorology and Climatology*, *54*(2), 506-518.

Peichl, M., Öquist, M., Löfvenius, M. O., Ilstedt, U., Sagerfors, J., Grelle, A., ... & Nilsson, M. B. (2014). A 12-year record reveals pre-growing season temperature and water table level threshold effects on the net carbon dioxide exchange in a boreal fen. *Environmental Research Letters*, *9*(5), 055006.

Peltier, W. R. (2004). Global glacial isostasy and the surface of the ice-age Earth: the ICE-5G (VM2) model and GRACE. *Annu. Rev. Earth Planet. Sci.*, *32*, 111-149.

Peñuelas, J., Ciais, P., Canadell, J. G., Janssens, I. A., Fernández-Martínez, M., Carnicer, J., ... & Sardans, J. (2017). Shifting from a fertilization-dominated to a warming-dominated period. *Nature ecology & evolution*, *1*(10), 1438-1445.

Perez-Priego, O., Guan, J., Rossini, M., Fava, F., Wutzler, T., Moreno, G., ... & Migliavacca, M. (2015). Sun-induced chlorophyll fluorescence and photochemical reflectance index improve remote-sensing gross primary production estimates under varying nutrient availability in a typical Mediterranean savanna ecosystem. *Biogeosciences*, *12*(21), 6351-6367.

Piao, S., Wang, X., Park, T., Chen, C., Lian, X. U., He, Y., ... & Myneni, R. B. (2020). Characteristics, drivers and feedbacks of global greening. *Nature Reviews Earth & Environment*, *1*(1), 14-27.

Pithan, F., & Mauritsen, T. (2014). Arctic amplification dominated by temperature feedbacks in contemporary climate models. Nature geoscience, 7(3), 181-184.

Polvani, L. M., Previdi, M., England, M. R., Chiodo, G., & Smith, K. L. (2020). Substantial twentieth-century Arctic warming caused by ozone-depleting substances. Nature Climate Change, 10(2), 130-133.

Porcar-Castell, A., Tyystjärvi, E., Atherton, J., Van der Tol, C., Flexas, J., Pfündel, E. E., ... & Berry, J. A. (2014). Linking chlorophyll a fluorescence to photosynthesis for remote sensing applications: mechanisms and challenges. *Journal of experimental botany*, *65*(15), 4065-4095.

Potter, C. S., Randerson, J. T., Field, C. B., Matson, P. A., Vitousek, P. M., Mooney, H. A., & Klooster, S. A. (1993). Terrestrial ecosystem production: a process model based on global satellite and surface data. *Global Biogeochemical Cycles*, *7*(4), 811-841.

Prentice, I. C., Farquhar, G. D., Fasham, M. J. R., Goulden, M. L., Heimann, M., Jaramillo, V. J., ... & Johnson, C. A. (2001). The carbon cycle and atmospheric carbon dioxide. Chapter 3. In Climate change 2001: the scientific basis. Contribution of working group I to the third assessment report of the Intergovernmental Panel on Climate Change (pp. 183-237). Cambridge University Press.

Price, D. T., Alfaro, R. I., Brown, K. J., Flannigan, M. D., Fleming, R. A., Hogg, E. H., ... & Venier, L. A. (2013). Anticipating the consequences of climate change for Canada's boreal forest ecosystems. *Environmental Reviews*, *21*(4), 322-365.

Price, K., Storn, R. M., & Lampinen, J. A. (2006). *Differential evolution: a practical approach to global optimization*. Springer Science & Business Media.

Prinsenberg, S. J. (1986). The circulation pattern and current structure of Hudson Bay. In Martini, E. P. (ed.), Canadian Inland Seas. Oceanography Series 44. New York: Elsevier, 187–203.

Qiu, C., Zhu, D., Ciais, P., Guenet, B., & Peng, S. (2020). The role of northern peatlands in the global carbon cycle for the 21st century. *Global Ecology and Biogeography*, *29*(5), 956-973.

R Core Team (2019). R: A language and environment for statistical computing. R Foundation for Statistical Computing, Vienna, Austria. https://www.R-project.org/.

R Core Team (2020). R: A language and environment for statistical computing. R Foundation for Statistical Computing, Vienna, Austria. https://www.R-project.org/.

Raczka, B. M., Davis, K. J., Huntzinger, D., Neilson, R. P., Poulter, B., Richardson, A. D., ... & Viovy, N. (2013). Evaluation of continental carbon cycle simulations with North American flux tower observations. *Ecological Monographs*, *83*(4), 531-556.

Raddatz, R. L., Papakyriakou, T. N., Swystun, K. A., & Tenuta, M. (2009). Evapotranspiration from a wetland tundra sedge fen: Surface resistance of peat for land-surface schemes. *Agricultural and Forest Meteorology*, *149*(5), 851-861.

Rahman, A. F., Sims, D. A., Cordova, V. D., & El-Masri, B. Z. (2005). Potential of MODIS EVI and surface temperature for directly estimating per-pixel ecosystem C fluxes. *Geophysical Research Letters*, *32*(19).

Rascher, U., Alonso, L., Burkart, A., Cilia, C., Cogliati, S., Colombo, R., ... & Zemek, F. (2015). Sun-induced fluorescence–a new probe of photosynthesis: First maps from the imaging spectrometer HyPlant. *Global change biology*, *21*(12), 4673-4684.

Richter-Menge, J., Druckenmiller, M. L., and Jeffries, M., Eds. (2019). Arctic Report Card 2019. https://www.arctic.noaa.gov/Report-Card.

Riley, J. (2011). Wetlands of the Hudson Bay Lowlands. Nature Conservancy of Canada and the Ontario Ministry of Natural Resources, Toronto, Ont.

Ripley, B., Venables, B., Bates, D. M., Hornik, K., Gebhardt, A., Firth, D., & Ripley, M. B. (2013). Package 'mass'. Cran r, 538, 113-120.

Robroek, B. J., Schouten, M. G., Limpens, J., Berendse, F., & Poorter, H. (2009). Interactive effects of water table and precipitation on net CO_2 assimilation of three co-occurring Sphagnum mosses differing in distribution above the water table. *Global Change Biology*, *15*(3), 680-691.

Rothrock, D.A., Y.Yu and Maykut, G.A. (1999).Thinning of the Arctic sea-ice cover. Geophysical Research Letters, 26:3469–3472.

Roulet, N. T., Lafleur, P. M., Richard, P. J., Moore, T. R., Humphreys, E. R., & Bubier, J. I. L. L. (2007). Contemporary carbon balance and late Holocene carbon accumulation in a northern peatland. *Global Change Biology*, *13*(2), 397-411.

Rouse, W. R., Bello, R. L., D'Souza, A., Griffis, T. J., & Lafleur, P. M. (2002). The annual carbon budget for fen and forest in a wetland at Arctic treeline. Arctic, 229-237.

Rouse, W. R., Hardill, S. G., & Lafleur, P. (1987). The energy balance in the coastal environment of James Bay and Hudson Bay during the growing season. Journal of Climatology, 7(2), 165-179.

Rouse, W.R., and Bello, R.L. (1985). Impact of Hudson Bay on the energy balance in the Hudson Bay Lowlands and the potential for climatic modification. Atmos. Ocean. 23: 375–392. doi: 10.1080/07055900.1985.9649234.

Ruimy, A., Saugier, B., & Dedieu, G. (1994). Methodology for the estimation of terrestrial net primary production from remotely sensed data. *Journal of Geophysical Research: Atmospheres*, *99*(D3), 5263-5283.

Running, S. W., Nemani, R. R., Heinsch, F. A., Zhao, M., Reeves, M., & Hashimoto, H. (2004). A continuous satellite-derived measure of global terrestrial primary production. *Bioscience*, *54*(6), 547-560.

Rydin, H., & Jeglum, J. (2006). The biology of peatlands. Biology of Habitats Series, Oxford University Press.

Saucier, F. J. and Dionne, J. (1998). A 3-D coupled ice-ocean model applied to Hudson Bay, Canada: The seasonal cycle and time-dependent climate response to atmospheric forcing and runoff. J. Geophys. Res. 103, 27689–27705.

Schädel, C., Bader, M. K. F., Schuur, E. A., Biasi, C., Bracho, R., Čapek, P., ... & Wickland, K. P. (2016). Potential carbon emissions dominated by carbon dioxide from thawed permafrost soils. *Nature climate change*, 6(10), 950-953.

Schreader, C. P., Rouse, W. R., Griffis, T. J., Boudreau, L. D., & Blanken, P. D. (1998). Carbon dioxide fluxes in a northern fen during a hot, dry summer. *Global Biogeochemical Cycles, 12*(4), 729-740.

Schubert, P., Eklundh, L., Lund, M., & Nilsson, M. (2010). Estimating northern peatland CO_2 exchange from MODIS time series data. *Remote Sensing of Environment*, *114*(6), 1178-1189.

Schuur, E.A.G., McGuire, A.D., Schädel, C., Grosse, G., Harden, J.W., Hayes, D.J., Hugelius, G., Koven, C.D., Kuhry, P., Lawrence, D.M., Natalo, S.M., Olefeldt, D., Romanovsky, V.E., Schaefer, K., Turetsky, M.R., Treat, C.C., Vonk, J.E. (2015). Climate change and the permafrost carbon feedback. Nature 520, 171–179.

Schwalm, C. R., Black, T. A., Amiro, B. D., Arain, M. A., Barr, A. G., Bourque, C. P. A., ... & Wofsy, S. C. (2006). Photosynthetic light use efficiency of three biomes across an east–west continental-scale transect in Canada. *Agricultural and Forest Meteorology*, *140*(1-4), 269-286.

Screen, J. A. and Simmonds, I. (2010). The central role of diminishing sea ice in recent Arctic temperature amplification. Nature 464, 1334–1337.

Screen, J. A., Deser, C., & Simmonds, I. (2012). Local and remote controls on observed Arctic warming. Geophysical Research Letters, 39(10).

Sellers, P. J. (1987). Canopy reflectance, photosynthesis, and transpiration, II. The role of biophysics in the linearity of their interdependence. *Remote sensing of Environment*, *21*(2), 143-183.

Sellers, P.J., Bounoua, L., Collatz, G.J., Randall, D.A., Dazlich, D.A., Los, S.O., Berry, J.A., Fung, I., Tucker, C.J., Field, C.B. and Jensen, T.G. (1996). Comparison of radiative and physiological effects of doubled atmospheric CO_2 on climate. Science, 271(5254), 1402-1406.

Sen, P. K. (1968). Estimates of the regression coefficient based on Kendall's tau. Journal of the American statistical association, 63(324), 1379-1389.

Serreze, M. C. and Francis, J. A. (2006). The arctic amplification debate. Climatic Change 76, 241–264.

Serreze, M. C., Barrett, A. P., Stroeve, J. C., Kindig, D. M. & Holland, M. M. (2009). The emergence of surface-based Arctic amplification. Cryosphere 3, 11–19.

Serreze, M. C., Barry, R. G. (2011). Processes and impacts of Arctic amplification: a research synthesis. Global Planet Chang 77:85–96.

Shafran, P. C., Woollen, J., Ebisuzaki, W., Shi, W., Fan, Y., Grumbine, R. W., & Fennessy, M. (2004). Observational data used for assimilation in the NCEP North American Regional Reanalysis.

Shapiro, S. S., & Wilk, M. B. (1965). An analysis of variance test for normality (complete samples). Biometrika, 52(3/4), 591-611.

Shindell, D., & Faluvegi, G. (2009). Climate response to regional radiative forcing during the twentieth century. *Nature Geoscience*, 2(4), 294-300.

Shukla, P. R., Skea, J., Calvo Buendia, E., Masson-Delmotte, V., Pörtner, H. O., Roberts, D. C., ... & Malley, J. (2019). IPCC, 2019: Climate Change and Land: an IPCC special report on climate change, desertification, land degradation, sustainable land management, food security, and greenhouse gas fluxes in terrestrial ecosystems.

Sim, T. G., Swindles, G. T., Morris, P. J., Baird, A. J., Cooper, C. L., Gallego-Sala, A. V., ... & Gałka, M. (2021). Divergent responses of permafrost peatlands to recent climate change. *Environmental Research Letters*, 16(3), 034001.

Sims, D. A., Rahman, A. F., Cordova, V. D., El-Masri, B. Z., Baldocchi, D. D., Bolstad, P. V., ... & Xu, L. (2008). A new model of gross primary productivity for North American ecosystems based solely on the enhanced vegetation index and land surface temperature from MODIS. *Remote sensing of Environment*, *112*(4), 1633-1646.

Sims, D. A., Rahman, A. F., Cordova, V. D., El-Masri, B. Z., Baldocchi, D. D., Flanagan, L. B., ... & Xu, L. (2006). On the use of MODIS EVI to assess gross primary productivity of North American ecosystems. *Journal of Geophysical Research: Biogeosciences*, *111*(G4).

South, Andy. (2011). rworldmap: A new R package for mapping global data. The R Journal Vol. 3(1), 35-43. http://journal.r-project.org/archive/2011-1/RJournal_2011-1_South.pdf

South, Andy. (2012). rworldxtra: Country boundaries at high resolution. R package version 1.01. https://CRAN.R-project.org/package=rworldxtra

Spielhagen, R. F., Werner, K., Sørensen, S. A., Zamelczyk, K., Kandiano, E., Budeus, G., ... & Hald, M. (2011). Enhanced modern heat transfer to the Arctic by warm Atlantic water. *Science*, 331(6016), 450-453.

St-Hilaire, F., Wu, J., Roulet, N. T., Frolking, S., Lafleur, P. M., Humphreys, E. R., & Arora, V. (2010). McGill wetland model: evaluation of a peatland carbon simulator developed for global assessments. *Biogeosciences*, 7(11), 3517-3530.

Strack, M., & Price, J. S. (2009). Moisture controls on carbon dioxide dynamics of peat-Sphagnum monoliths. *Ecohydrology: Ecosystems, Land and Water Process Interactions, Ecohydrogeomorphology*, *2*(1), 34-41.

Strack, M., Waddington, J. M., Lucchese, M. C., & Cagampan, J. P. (2009). Moisture controls on CO_2 exchange in a Sphagnum-dominated peatland: results from an extreme drought field experiment. *Ecohydrology: Ecosystems, Land and Water Process Interactions, Ecohydrogeomorphology*, *2*(4), 454-461.

Stuecker, M. F., Bitz, C. M., Armour, K. C., Proistosescu, C., Kang, S. M., Xie, S. P., ... & Jin, F. F. (2018). Polar amplification dominated by local forcing and feedbacks. Nature Climate Change, 8(12), 1076-1081

Sun, Y., Frankenberg, C., Jung, M., Joiner, J., Guanter, L., Köhler, P., & Magney, T. (2018). Overview of Solar-Induced chlorophyll Fluorescence (SIF) from the Orbiting Carbon Observatory-2: Retrieval, cross-mission comparison, and global monitoring for GPP. *Remote Sensing of Environment*, *209*, 808-823.

Sutton, R. T., Dong, B., & Gregory, J. M. (2007). Land/sea warming ratio in response to climate change: IPCC AR4 model results and comparison with observations. Geophysical Research Letters, 34(2).

Swindles, G. T., Morris, P. J., Mullan, D., Watson, E. J., Turner, T. E., Roland, T. P., ... & Galloway, J. M. (2015). The long-term fate of permafrost peatlands under rapid climate warming. *Scientific reports*, 5(1), 1-6.

Tarnocai, C. (2006). The effect of climate change on carbon in Canadian peatlands. *Global and planetary Change*, *53*(4), 222-232.

Tarnocai, C., Canadell, J. G., Schuur, E. A., Kuhry, P., Mazhitova, G., & Zimov, S. (2009). Soil organic carbon pools in the northern circumpolar permafrost region. *Global biogeochemical cycles*, *23*(2).

Taylor, P. C. et al. (2013). A decomposition of feedback contributions to polar warming amplification. J. Clim. 26, 7023–7043.

Tenuta, M. (2020). *AmeriFlux CA-CF2 Churchill Fen Site 2*. Lawrence Berkeley National Lab.(LBNL), Berkeley, CA (United States). AmeriFlux; University of Manitoba. https://doi.org/10.17190/AMF/1634879.

Thackeray, C. W., Fletcher, C. G., Mudryk, L. R., & Derksen, C. (2016). Quantifying the uncertainty in historical and future simulations of Northern Hemisphere spring snow cover. Journal of Climate, 29(23), 8647-8663.

Tivy, A., Howell, S. E., Alt, B., McCourt, S., Chagnon, R., Crocker, G., ... & Yackel, J. J. (2011). Trends and variability in summer sea ice cover in the Canadian Arctic based on the Canadian Ice Service Digital Archive, 1960–2008 and 1968–2008. Journal of Geophysical Research: Oceans, 116(C3).

Todd, A., & Humphreys, E. (2018). *AmeriFlux CA-ARF Attawapiskat River Fen*. Lawrence Berkeley National Lab.(LBNL), Berkeley, CA (United States). AmeriFlux; Carleton University; Ministry of Environment and Climate Change. https://doi.org/10.17190/AMF/1480319.

Treat, C. C., Wollheim, W. M., Varner, R. K., Grandy, A. S., Talbot, J., & Frolking, S. (2014). Temperature and peat type control CO_2 and CH_4 production in Alaskan permafrost peats. *Global Change Biology*, 20(8), 2674-2686.

Tucker, C. J. (1980). Remote sensing of leaf water content in the near infrared. *Remote sensing of Environment*, *10*(1), 23-32.

Tuittila, E. S., Vasander, H., & Laine, J. (2004). Sensitivity of C sequestration in reintroduced Sphagnum to water-level variation in a cutaway peatland. *Restoration Ecology*, *12*(4), 483-493.

Turetsky, M. R., Bond-Lamberty, B., Euskirchen, E., Talbot, J., Frolking, S., McGuire, A. D., & Tuittila, E. S. (2012). The resilience and functional role of moss in boreal and arctic ecosystems. *New Phytologist*, *196*(1), 49-67.

Turetsky, M. R., Donahue, W., & Benscoter, B. W. (2011). Experimental drying intensifies burning and carbon losses in a northern peatland. *Nature Communications*, *2*(1), 1-5.

Turner, D. P., Urbanski, S., Bremer, D., Wofsy, S. C., Meyers, T., Gower, S. T., & Gregory, M. (2003). A cross-biome comparison of daily light use efficiency for gross primary production. *Global Change Biology*, *9*(3), 383-395.

Vallée, S., & Payette, S. (2007). Collapse of permafrost mounds along a subarctic river over the last 100 years (northern Quebec). Geomorphology, 90(1), 162-170.

van Wijngaarden, W. A. (2008). Climate change during 1953–2007 in the Canadian Arctic, The Pacific and Arctic Oceans: New Oceanographic Research, Nova Science.

Vavrus, S. (2004). The impact of cloud feedbacks on Arctic climate under greenhouse forcing. *Journal of Climate*, 17(3), 603-615.

Verma, M., Schimel, D., Evans, B., Frankenberg, C., Beringer, J., Drewry, D. T., ... & Eldering, A. (2017). Effect of environmental conditions on the relationship between solar-induced fluorescence and gross primary productivity at an OzFlux grassland site. *Journal of Geophysical Research: Biogeosciences*, *122*(3), 716-733.

Vermote, E. (2015). MOD09A1 MODIS/Terra Surface Reflectance 8-Day L3 Global 500m SIN Grid V006. NASA EOSDIS Land Processes DAAC. https://doi.org/10.5067/MODIS/MOD09A1.006.

Vincent, L.A., Zhang, X., Brown, R.D., Feng, Y., Mekis, E., Milewska, E.J., Wan, H. and Wang, X.L. (2015). Observed trends in Canada's climate and influence of low-frequency variability modes. Journal of Climate, 28(11), 4545-4560.

Von Storch H. (1995). Misuses of statistical analysis in climate research. In: Storch HV, Navarra A (eds) Analysis of climate variability: applications of statistical techniques. Springer-Verlag, Berlin, pp 11–26.

Walker, J. J., De Beurs, K. M., & Wynne, R. H. (2014). Dryland vegetation phenology across an elevation gradient in Arizona, USA, investigated with fused MODIS and Landsat data. *Remote Sensing of Environment*, *144*, 85-97.

Walsh, J. E., Overland, J. E., Groisman P. Y., Rudolf B. (2011). Ongoing climate change in the arctic. Ambio 40:6–16

Walther, S., Voigt, M., Thum, T., Gonsamo, A., Zhang, Y., Köhler, P., ... & Guanter, L. (2016). Satellite chlorophyll fluorescence measurements reveal large-scale decoupling of photosynthesis and greenness dynamics in boreal evergreen forests. *Global change biology*, *22*(9), 2979-2996. doi:10.1111/gcb.13200.

Wang, S., Zhang, Y., Ju, W., Chen, J. M., Ciais, P., Cescatti, A., ... & Peñuelas, J. (2020). Recent global decline of CO_2 fertilization effects on vegetation photosynthesis. *Science*, *370*(6522), 1295-1300.

Ward, S. E., Ostle, N. J., Oakley, S., Quirk, H., Henrys, P. A., & Bardgett, R. D. (2013). Warming effects on greenhouse gas fluxes in peatlands are modulated by vegetation composition. *Ecology letters*, *16*(10), 1285-1293.

Webster, K. L., Bhatti, J. S., Thompson, D. K., Nelson, S. A., Shaw, C. H., Bona, K. A., ... & Kurz, W. A. (2018). Spatially-integrated estimates of net ecosystem exchange and methane fluxes from Canadian peatlands. *Carbon balance and management*, *13*(1), 1-21.

Weick, E. J., & Rouse, W. R. (1991). Advection in the coastal Hudson Bay lowlands, Canada. I. The terrestrial surface energy balance. Arctic and Alpine Research, 328-337.

Woo, M. K. (2012). Permafrost hydrology. Springer Science & Business Media.

Wu, J., & Roulet, N. T. (2014). Climate change reduces the capacity of northern peatlands to absorb the atmospheric carbon dioxide: The different responses of bogs and fens. *Global Biogeochemical Cycles*, *28*(10), 1005-1024.

Xiao, J., & Moody, A. (2004). Photosynthetic activity of US biomes: responses to the spatial variability and seasonality of precipitation and temperature. *Global Change Biology*, *10*(4), 437-451.

Xiao, J., Chevallier, F., Gomez, C., Guanter, L., Hicke, J. A., Huete, A. R., ... & Zhang, X. (2019). Remote sensing of the terrestrial carbon cycle: A review of advances over 50 years. *Remote Sensing of Environment*, *233*, 111383.

Xiao, X., Boles, S., Liu, J. Y., Zhuang, D. F., & Liu, M. L. (2002). Characterization of forest types in Northeastern China, using multitemporal SPOT-4 VEGETATION sensor data. Remote Sensing of Environment, 82, 335– 348.

Xiao, X., Hollinger, D., Aber, J., Goltz, M., Davidson, E. A., Zhang, Q., & Moore III, B. (2004). Satellite-based modeling of gross primary production in an evergreen needleleaf forest. *Remote sensing of environment*, *89*(4), 519-534.

Yamori, W., Hikosaka, K., & Way, D. A. (2014). Temperature response of photosynthesis in C3, C4, and CAM plants: temperature acclimation and temperature adaptation. *Photosynthesis research*, *119*(1), 101-117.

Yang, X., Tang, J., Mustard, J. F., Lee, J. E., Rossini, M., Joiner, J., ... & Richardson, A. D. (2015). Solar-induced chlorophyll fluorescence that correlates with canopy photosynthesis on diurnal and seasonal scales in a temperate deciduous forest. *Geophysical Research Letters*, *42*(8), 2977-2987.

Yu, Z. C. (2012). Northern peatland carbon stocks and dynamics: a review. *Biogeosciences*, *9*(10), 4071-4085.

Yu, Z., Loisel, J., Brosseau, D. P., Beilman, D. W., & Hunt, S. J. (2010). Global peatland dynamics since the Last Glacial Maximum. *Geophysical research letters*, *37*(13).

Yuan, W., Cai, W., Xia, J., Chen, J., Liu, S., Dong, W., ... & Wohlfahrt, G. (2014). Global comparison of light use efficiency models for simulating terrestrial vegetation gross primary production based on the LaThuile database. *Agricultural and Forest Meteorology*, *192*, 108-120.

Yuan, W., Liu, S., Yu, G., Bonnefond, J. M., Chen, J., Davis, K., ... & Verma, S. B. (2010). Global estimates of evapotranspiration and gross primary production based on MODIS and global meteorology data. *Remote Sensing of Environment*, *114*(7), 1416-1431.

Yuan, W., Liu, S., Zhou, G., Zhou, G., Tieszen, L. L., Baldocchi, D., ... & Wofsy, S. C. (2007). Deriving a light use efficiency model from eddy covariance flux data for predicting daily gross primary production across biomes. *Agricultural and Forest Meteorology*, *143*(3-4), 189-207.

Yuan, W., Zheng, Y., Piao, S., Ciais, P., Lombardozzi, D., Wang, Y., ... & Yang, S. (2019). Increased atmospheric vapor pressure deficit reduces global vegetation growth. *Science advances*, *5*(8), eaax1396.

Yue, S. & Wang, C. Y. (2004a). The Mann-Kendall test modified by effective sample size to detect trend in serially correlated hydyrological series. Water Resour. Manage. 18, 201–218.

Yue, S. & Wang, C. Y. (2004b). Reply to comment by M. Bayazit & B. Önöz on "Applicability of prewhitening to eliminate the influence of serial correlation on the Mann-Kendall test." Water Resour. Res. 40(8), W08802.

Yue, S., & Wang, C. Y. (2002). Applicability of prewhitening to eliminate the influence of serial correlation on the Mann-Kendall test. Water resources research, 38(6), 4-1.

Yue, S., Pilon, P., Phinney, B., & Cavadias, G. (2002). The influence of autocorrelation on the ability to detect trend in hydrological series. Hydrological processes, 16(9), 1807-1829.

Zhang, H., Gallego-Sala, A. V., Amesbury, M. J., Charman, D. J., Piilo, S. R., & Väliranta, M. M. (2018). Inconsistent response of Arctic permafrost peatland carbon accumulation to warm climate phases. *Global Biogeochemical Cycles*, 32(10), 1605-1620.

Zhang, X., Tan, B., & Yu, Y. (2014). Interannual variations and trends in global land surface phenology derived from enhanced vegetation index during 1982–2010. International journal of biometeorology, 58(4), 547-564.

Zhang, Y., Joiner, J., Alemohammad, S. H., Zhou, S., & Gentine, P. (2018). A global spatially contiguous solar-induced fluorescence (CSIF) dataset using neural networks. *Biogeosciences*, *15*(19), 5779-5800.

Zhao, Y., Tang, Y., Yu, Z., Li, H., Yang, B., Zhao, W., ... & Li, Q. (2014). Holocene peatland initiation, lateral expansion, and carbon dynamics in the Zoige Basin of the eastern Tibetan Plateau. *The Holocene*, *24*(9), 1137-1145.

Zhu, J., Zhang, F., Li, H., He, H., Li, Y., Yang, Y., ... & Luo, F. (2020). Seasonal and Interannual Variations of CO_2 Fluxes Over 10 Years in an Alpine Wetland on the Qinghai-Tibetan Plateau. *Journal of Geophysical Research: Biogeosciences*, *125*(11), e2020JG006011.

Zhuang, Q., Wang, S., Zhao, B., Aires, F., Prigent, C., Yu, Z., ... & Bridgham, S. (2020). Modeling Holocene peatland carbon accumulation in North America. *Journal of Geophysical Research: Biogeosciences*, *125*(11), e2019JG005230.

Zimov, S. A., Schuur, E. A., & Chapin III, F. S. (2006). Permafrost and the global carbon budget. *Science(Washington)*, 312(5780), 1612-1613.

Zoltai, S. C. (1980). outline of the wetland regions of Canada. In *Proc. of a workshop on Canadian wetlands: meeting of the Natl. Wetl. Work. Group, Saskatoon, Saskat., 11-13 June 1979/comp., ed. CDA Rubec, FC Pollett= Compte-rendu d'un atelier sur les terres humides du Canada*. [Ottawa]: Environment Canada, Lands Directorate, c1980.